Electrodeposited Electrocatalysts For Rechargeable Zinc-air Batteries

by

Ming Xiong

A thesis submitted in partial fulfillment of the requirements for the degree of

Doctor of Philosophy

in

MATERIALS ENGINEERING

Department of Chemical and Materials Engineering

University of Alberta

Abstract

Rechargeable zinc-air (Zn-air) batteries have gained renewed interest among the various technologies available with their high theoretical energy density and low cost. However, large-scale industrial deployment of Zn-air batteries is limited by several issues; the most concerning of these are low round-trip energy efficiency and performance degradation. Both problems are intimately related to the low activity and stability of electrocatalysts at the air electrode for catalyzing the oxygen reduction reaction (ORR) and oxygen evolution reaction (OER). Many transition metal-based catalysts have been developed to replace precious metal catalysts. However, most of them require complex procedures to fabricate and need to be mixed with additives to work as electrodes. These processes can add extra cost and are difficult to scale-up. Therefore, a simple way to prepare air electrodes with active catalysts is desired.

The purpose of this work was to electrodeposit transition metal (Co, Fe, Mn) based ORR/OER active catalysts on a gas diffusion layer (GDL) as the air electrode of Zn-air batteries. The as-deposited samples were characterized by several techniques including scanning electron microscopy (SEM), transmission electron microscopy (TEM), Auger electron spectroscopy (AES), X-ray diffraction (XRD) and X-ray photoelectron spectroscopy (XPS). The electrochemical properties were investigated by a variety of electrochemical tests, such as cyclic voltammetry (CV), linear sweep voltammetry (LSV) and electrochemical impedance spectroscopy (EIS). Samples with the best performance were assembled into a Zn-air battery for further evaluation.

The first study involved electrodeposition of cobalt-iron (Co-Fe) OER catalysts on GDL as the air electrode. The morphology and mass loading were directly controlled by adjusting deposition time and the deposits evolved from single crystal nanocubes into continuous films. The Co-Fe catalysts

exhibited a low overpotential (0.29 V at 10 mA cm^{-2}) and good durability during testing. A Zn-air battery using Co-Fe showed the same cycling efficiency as one using Pt/Ru catalysts.

The second study followed up the first study to various deposit Co-Fe solid solutions. Different electrolyte compositions were explored so that deposits with a full range of compositions, from pure Co to pure Fe, were obtained. Electron microscopy and AES were used to investigate the morphology and composition of the electrodeposits. The Fe content in the deposits increased with increasing Fe concentration in the electrolyte and Fe segregated to the particle surfaces. Electrochemical tests demonstrated that the deposit Co/Fe ratio influences OER activity by altering the electrochemically active surface area (ECSA) and charge transfer resistance. The OER activity increased with increasing Fe content up to ~65 at% Fe, with a minimum overpotential of 0.33 V at 10 mA cm^{-2}.

In the third study, manganese oxide (MnOx) and Co-Fe were sequentially electrodeposited onto a GDL as bifunctional electrocatalysts for rechargeable Zn-air batteries. The fabricated material was characterized by SEM, TEM, XRD and XPS. The sequentially deposited MnOx/Co-Fe catalysts, tested using CV, showed activity for both the ORR and OER, with better performance than either MnOx or Co-Fe alone. A Zn-air battery fabricated using MnOx/Co-Fe catalysts exhibited good performance and a cycling efficiency of 59.6% at 5 mA cm^{-2}, which is comparable to Pt/C catalysts. In addition, the electrodeposited MnOx/Co-Fe layer showed strong adhesion to the GDL and was structurally stable throughout 40 h of battery cycling.

In the fourth study, a horizontal Zn-air battery has been designed to enable the use of physically decoupled ORR and OER electrodes for discharge and charge, respectively. The horizontal design features a horizontally positioned ORR electrode and a vertically positioned OER electrode, allowing effective management of oxygen transport and pressure. The ORR catalyst (MnOx) and

OER catalyst (Co-Fe alloy) are fabricated via one-step electrodeposition on carbon paper and Ni foam, respectively. MnOx was identified as a combination of Mn_3O_4 nanorods and α-Mn_2O_3 spheres. Co-Fe was deposited as a solid solution film with an oxidized surface. Electrochemical tests showed that both catalysts have comparable or even better activity than their commercial Pt-Ru catalyst counterpart. Cycling tests at 20 mA cm^{-2} show that the potential affects catalyst durability, with improved lifetime under separate ORR and OER conditions compared with the full ORR-OER voltage range. The fabricated catalysts were tested in Zn-air battery and show the same average efficiency (58%) as Pt-Ru catalysts at 10 mA cm^{-2}.

Preface

This thesis is focused on the synthesis, characterization and electrochemical testing of electrodeposited transition metal catalysts for rechargeable Zn-air batteries. The research presented in Chapter 3, Chapter 4, Chapter 5 and Chapter 6 along with their supporting information is my original work.

Chapter 6 summarizes the research conducted in collaboration work with Michael Clark (PhD student), Matthew Labbe (undergraduate student) and Mehdi Alipour (postdoctoral fellow) of our group. Michael Clark performed the TEM analysis. Matthew Labbe performed part of the materials synthesis. The implementation and interpretation of materials characterization as well as electrochemical tests were done solely by myself. Modeling was done with COMSOL Multiphysics® software. Mehdi Alipour assisted with designing the geometrical grid of the Zn-air battery in COMSOL. I was responsible for the simulation and parameter optimization.

Versions of Chapter 3, Chapter 4, Chapter 5 and Chapter 6 of this thesis have been published as:

Chapter 3: M. Xiong, D.G. Ivey, Electrodeposited Co-Fe as an oxygen evolution catalyst for rechargeable Zn-air batteries, *Electrochemistry Communications*, 75 (2017) 73-77. (10.1016/j.elecom.2016.12.018)

Chapter 4: M. Xiong, D.G. Ivey, Composition effects of electrodeposited Co-Fe as electrocatalysts for the oxygen evolution reaction, *Electrochimica Acta*, 260 (2017) 872-881. (10.1016/j.electacta.2017.12.059)

Chapter 5: M. Xiong, D.G. Ivey, Electrodeposited MnOx-CoFe as Bifunctional Electrocatalysts for Rechargeable Zinc-Air Batteries, *ECS Transactions*, 75 (2017) 1-7. (10.1149/07536.0001ecst)

M. Xiong, D.G. Ivey, Sequentially Electrodeposited MnOx/Co-Fe as Bifunctional Electrocatalysts for Rechargeable Zinc-Air Batteries, *Journal of The Electrochemical Society*, 164 (2017) A1012-A1021. (10.1149/2.0481706jes)

Chapter 6: M. Xiong, M.P. Clark, M. Labbe, D.G. Ivey, A horizontal zinc-air battery with physically decoupled oxygen evolution/reduction reaction electrodes, *Journal of Power Sources*, 393 (2018) 108-118. (10.1016/j.jpowsour.2018.05.004)

Supporting information have been added at the end of each chapter for further confirmation of the results and conclusions or for more comprehensive studies. The data in the supporting information were not included in journal papers due to the word limitations.

Dedication

I dedicate this work to my parents, who have always been there to offer unconditional love and support for me. Thank you so much.

Acknowledgments

Firstly, I would like to express sincere gratitude to my supervisor Dr. Douglas Ivey for giving me the opportunity to study for this PhD. His wisdom and passion for material science always inspires me. His support, guidance and tolerance helped me overcome numerous difficulties in my research. I am really proud to be his student.

I would like to thank our group members for supporting me. I am particularly grateful to Michael Clark, Elaheh Davari and Mehdi Alipour for their support and contributions. I also want to thank Matthew Labbe and Aliesha Johnson for helping me with some of the experiments. Wei Qu, Xinge Zhang and Xiao-Zi Yuan of NRC Canada are acknowledged for valuable discussions.

I would like to thank Dr. Anqiang He, Dr. Shihong Xu and Mrs. Diane Caird for their technical support.

Financial support from the Natural Sciences and Engineering Research Council (NSERC) of Canada, the Faculty of Graduate Studies and Research (FGSR), the Graduate Student's Association (GSA) and the Chinese Scholarship Council (CSC) is gratefully acknowledged.

Table of Contents

List of Tables

List of Figures

List of abbreviations

AC	Alternating Current
AES	Auger Electron Spectroscopy
BF	Bright Field
CE	Counter Electrode
CMC	Carboxymethyl Cellulose
CNT	Carbon Nanotube
CPE	Constant Phase Element
CTAB	Hexadecyl Trimethyl Ammonium Bromide
CV	Cyclic Voltammetry
DI	Deionized
ECSA	Electrochemically Active Surface Area
EDX	Energy Dispersive Spectroscopy
EIS	Electrochemical Impedance Spectroscopy
EMD	Electrochemical Manganese Dioxide
FESEM	Field Emission Scanning Electron Microscopy
GDL	Gas Diffusion Layer
HER	Hydrogen Evolution Reaction
HR	High Resolution
LDH	Layered Double Hydroxides
LSV	Linear Sweep Voltammetry
MOF	Metal-organic Frameworks
MPL	Microporous Layer
OCV	Open Circuit Voltage
OER	Oxygen Evolution Reaction
ORR	Oxygen Reduction Reaction
PAA	Poly(Acrylic Acid)
PE	Polyethylene

PEI	Polyetherimide
PEO	Poly(Ethylene Oxide)
PP	Polypropylene
PTFE	Polytetrafluoroethylene
PVA	Poly(Vinyl Alcohol)
Redox	Reduction And Oxidation Reactions
RE	Reference Electrode
RS	Raman Spectroscopy
SAED	Selected Area Electron Diffraction
SDS	Sodium Dodecyl Sulfate
SE	Secondary Electron
SEM	Scanning Electron Microscope(y)
SHE	Standard Hydrogen Electrode
STEM	Scanning Transmission Electron Microscope(y)
TBAB	Tetrabutylammonium Bromide
TEM	Transmission Electron Microscope(y)
WE	Working Electrode
XPS	X-ray Photoelectron Spectroscopy
XRD	X-ray Diffraction

List of symbols

Symbol	Meaning	Units
F	Faraday Constant	96485 C mol^{-1}
n	Number of Electrons Transferred	dimensionless
T	Temperature	K
η	Overpotential	V
j_0	Exchange Current Density	mA cm^{-2}
j	Current Density	mA cm^{-2}
q	Charge	mC cm^{-2}
E	Potential	V
R_s	Solution Resistance	Ω cm^2
R_f	Catalyst Interlayer Resistance	Ω cm^2
R_{ct}	Charge Transfer Resistance	Ω cm^2
C_{dl}	Double-layer capacitance	mF cm^{-2}
C_p	Pseudo capacitance	mF cm^{-2}
C_t	Total Capacitance	mF cm^{-2}

Chapter 1 : Introduction

Clean, but abundant energy, is desired by every nation in the world. In the past several years, solar and wind power have experienced great growth. They are ideal energy sources because they are almost inexhaustible and do not generate hazardous by-products which can occur in nuclear power stations. However, these clean power sources have their own issues. Their output relies heavily on environmental conditions. For example, a solar power station can only output energy during the daytime if there are no energy storage devices. Thus, the storage of solar power energy is crucial to the application of solar power. Similar issues hold for wind farms.

The rapid growth of renewable energy production requires an economical and efficient way to store and deliver the electricity. Currently, large-scale energy storage remains a serious problem. The most common way is pumped hydroelectric energy storage (PHES). Using solar power as an example, pumps running on solar power draw water from a lower reservoir during the daytime. At night, the water is released to produce electric power. However, even though the system has an efficiency between 65% and 80%, it requires a special site with both geographical height and water availability, and can cause ecological problems.[1] Other mechanical energy storage systems such as compressed air energy storage (CAES) face the same problem of selecting favorable locations.

Batteries convert chemical energy into electrical energy by electrochemical reactions. There are different types of batteries according to the nature of the electrochemical reactions, in which rechargeable or secondary batteries are the most useful for energy storage. Table 1-1 lists the rechargeable batteries that have been commercialized in recent years. Among this list, Ni-MH (metal hydride) and lead-acid are commonly used in household applications because of their low cost, good reliability and high power density. However, their application in grid-scale energy

storage is limited by their relatively low energy densities, ranging from 30 to 70 Wh/kg. Sodium-sulfur (Na-S) batteries are capable of providing a prompt response in distribution grid support but need to work at 300-350℃. The high temperature for Na and S to stay as molten salts also makes them more corrosive and reactive than their solid-state counterparts, introducing safety problems.[2] Flow batteries, especially vanadium redox flow batteries (VRB) have the advantage of low maintenance cost, flexible physical design (power output and capacity are independent) and long cycle life.[3] However, their low energy densities and the potential shortage of V are obstacles for widespread application. Lithium-ion batteries are an ideal candidate for grid storage with their balanced performance and they have been applied in grid-level energy storage projects globally.[4] The major drawback is their low tolerance to abuse such as overcharging, short-circuiting and high temperatures, which can lead to critical failures like fires or explosion.

The Zn-air battery is a member of metal-air battery group, which includes aluminum-air, magnesium-air and lithium-air batteries. Metal-air batteries make use of metal (Zn, Al, Mg and Li) and oxygen from the air to generate electricity. Among all metal-air batteries, Zn-air is the most promising one for use in large-scale energy storage. Al and Mg are difficult to be deposit from aqueous electrolytes, resulting in a low current efficiency during charging of the cell. Mechanical recharging by changing spent Al/Mg anodes with fresh anodes is a more realistic approach for these cells.[5] Lithium-air batteries are able to be charged by using a hybrid electrolyte, i.e., a non-aqueous electrolyte for the metal electrode and an aqueous electrolyte for the air electrode, separated by a solid-state electrolyte. However, the low ionic conductivity of the hybrid electrolyte significantly impairs its current density (in the range of 0.1-1 mA/cm^2).[6] Zinc-air batteries can be charged with a higher current efficiency than Al/Mg counterparts, because Zn has a higher reduction potential and a large overpotential for hydrogen evolution. Zinc is the 24^{th} most abundant

element in the earth and is 100% recyclable. Table 1-1 shows that a Zn-air battery can provide a higher energy density than a Li-ion battery at half the price. Other advantages of the Zn-air battery include safe operation and environmental friendliness, because they do not contain flammable and hazardous organic electrolytes.

Compared with their high energy density, the power density and round-trip efficiency of Zn-air batteries are not satisfying, due to the sluggish reactions at the air cathode. The development of electrically rechargeable Zn-air batteries has been impeded by the lack of highly efficient catalysts. Transition metal oxides as catalysts have received much attention due to their stable performance as well as their much lower cost compared with noble metals such as Pt and Ru. However, transition metal oxides have problems such as low conductivity and catalyst activity. Thus, it is necessary to develop an air cathode with highly active transition metal oxides for Zn-air batteries.

Table 1-1. Performance and cost comparison for battery technologies.[7-9]

Battery type	Power density W kg^{-1}	Energy density Wh kg^{-1}	Cycle life number	Efficiency %	Cost \$ $kW\ h^{-1}$
Ni-MH	150-300	50-70	500-3000	50-80	150-200
Lead-acid	200-400	30-50	2000-4500	70-90	120-150
Sodium-sulfur	120	100	2500-4500	75-90	250-500
Redox-flow	100	30-50	>12000	60-85	150-1000
Lithium-ion	315	155	>1200	80-90	250-350
Zn-air	105	230	100-300*	50-65*	90-120

* Some companies (EOS energy) have achieved 5000 cycles and 75% efficiency.

Chapter 2 : Literature review and experimental methodology

2.1 Zinc-air batteries

2.1.1 Primary Zn-air battery

Primary Zn-air batteries have been commercially available for several years, mostly in hearing aids. Due to their high energy density, Zn-air batteries can supply power for hearing aids for 2-3 weeks. The high energy density derives from the fact that the reactant in the cathode is oxygen, which can be supplied from air. A primary Zn-air battery is composed of a Zn negative electrode, an air positive electrode and a separator together with electrolyte between them. The electrolyte in Zn-air batteries is a KOH solution with a concentration of 30 wt% or more.

When discharged, the following reactions happen:[10, 11]

Zinc negative electrode: $Zn + 2OH^- \rightarrow Zn(OH)_2 + 2e^-$ (2-1)

$Zn(OH)_2 + 2OH^- \rightarrow Zn(OH)_4^{2-}(soln)$ (2-2)

When zincate ions ($Zn(OH)_4^{2-}$) are saturated, they will decompose into zinc oxide:

$Zn(OH)_4^{2-}(soln) \rightarrow ZnO(s) + H_2O + 2OH^-$ (2-3)

Parasitic reaction: $Zn + 2H_2O \rightarrow Zn(OH)_2 + H_2\uparrow$ (2-4)

Air positive electrode: $O_2 + 2H_2O + 4e^- \rightarrow 4OH^-$ (2-5)

Parasitic reaction: $2KOH + CO_2 \rightarrow K_2CO_3 + H_2O$ (2-6)

The overall reaction of (2-1), (2-2), (2-3) and (2-5) is: $2Zn + O_2 \rightarrow 2ZnO$ (2-7)

The standard electrode potential for reaction (2-1) is -1.25 V vs. SHE (standard hydrogen electrode), while the standard electrode potential for oxygen reduction in reaction (2-5) is 0.4 V vs. SHE.[12] The standard cell potential of the Zn-air battery is 0.4 V - (-1.25 V) = 1.65 V.

The energy density of a Zn-air battery is limited by many factors, especially the quantity of Zn and the concentration of KOH in the electrolyte. Discharge will stop when all the Zn is consumed. ZnO will accumulate in the cell during the discharge process. As shown in Reaction (2-3), the dissolved Zn species will gradually precipitate as ZnO when zincate ions are saturated.[13] ZnO is an insulator and will increase the internal resistance of the battery. Thus, the current and potential will gradually decrease. The solubility of the Zn species increases with increasing KOH concentration up to ~30 wt% KOH in the electrolyte.[11]

Even though a Zn-air battery has a standard cell potential of 1.65 V, the actual working voltage is significantly lower, normally around 1.2 V depending on the catalyst and discharge current density. A commercial Zn-air battery has an open-circuit voltage (OCV) of 1.4 V, due to corrosion of Zn which can move the electrode away from the equilibrium state. In contrast, lead-acid batteries have an OCV of 2 V and Li-ion batteries have an OCV of 3.3 V-3.7 V.[14]

The large overpotential caused by the sluggish oxygen reduction reaction (ORR) is the main reason for the decreased battery voltage, as shown in Fig. 2-1.

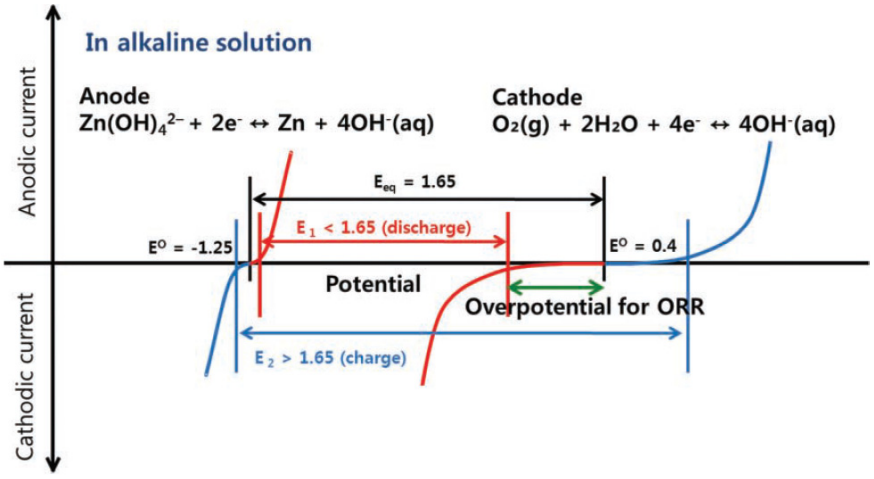

Fig. 2-1. Schematic polarization curves for a Zn-air cell.[15]

(Reproduced by permission of John Wiley and Sons.)

As shown in Fig. 2-1, the electrochemical polarization at the air electrode (cathode) is much higher than the polarization at the Zn electrode (anode), leading to a decreased cell potential ($E_1 < 1.65$ V). The air electrode contains a gas diffusion layer (GDL) as the substrate and a catalyst layer. It is the activity of the catalyst together with the conductivity of the whole electrode that controls the degree of polarization. There are two types of polarization in the electrode, ohmic polarization caused by the electrical resistance of electrode and electrochemical polarization of ORR. The resistance of the electrode is from the substrate, the catalyst itself and the contact between the substrate and catalyst. The electrochemical polarization of ORR is determined by the activity of the catalyst, which is mainly influenced by its composition and morphology.

Currently, the best ORR catalyst is Pt/C, which has been used in fuel cells for many years. However, the performance of Pt/C will gradually decrease over time due to its aggregation on the substrate.[16] Also, the high price of Pt is a significant obstacle to its widespread application. Thus, the most commonly used catalyst in commercially available Zn-air batteries is an oxide of manganese.[14]

ORR happens at the interface of oxygen, catalyst and electrolyte. Therefore, the design of the air electrode plays an important role in cell performance. The air electrode is comprised of a gas diffusion layer, a current collector and a layer of catalysts as the major functional components. The air electrode can be a metal mesh (current collector) compressed with catalyst paste, followed by a PTFE layer (to prevent leakage of electrolyte while allowing oxygen to pass) in a Zn-air button cell, or a conductive carbon paper containing PTFE particles as a binder and waterproofing agent.[14] The porosity in the GDL controls the diffusion rate of oxygen. Higher rates of oxygen diffusion will create higher current densities. However, higher porosity can also lead to a higher degree of flooding, which means the electrolyte permeates through the GDL and clogs the pores for oxygen diffusion.

Like other electrochemical power sources, parasitic reactions exist in Zn-air batteries. The Zn metal will gradually corrode due to its reaction with water, producing hydrogen gas. This hydrogen evolution reaction (HER) consumes the Zn metal in the battery and causes self-discharge, shortening its lifetime. One way to suppress this corrosion is to add 0.25%-2.5% mercury into Zn, which increases the hydrogen evolution overpotential.[17]

Another detrimental reaction in the Zn-air battery is the production of K_2CO_3 at the air electrode, according to reaction (2-6). The generated K_2CO_3 accumulates in the pores of the air electrode and clogs them, hampering oxygen diffusion. In addition, the carbonate can reduce the electrolyte conductivity.[14] A 409-1000 ppm CO_2 concentration in air can decrease the lifetime of a Zn-air battery by 90%.[18] A filtering system is required to remove CO_2 from the air supplied, although it will increase the volume of the battery system.[19]

2.1.2 Secondary Zn-air battery

The application of Zn-air batteries to other areas, besides hearing aids, is also desirable; e.g., in portable electronics, electric cars and energy storage for solar/wind power stations. All these applications can benefit from rechargeable Zn-air batteries. One option is a Zn-air battery that can be recharged by replacing Zn and the electrolyte with new ones. The recovered ZnO is then electrolyzed and Zn is recycled. In this case, only an ORR catalyst is needed in the Zn-air battery. Another way to recharge a Zn-air battery is using electrochemical methods, i.e., by reversing the discharge reaction, just like rechargeable lithium-ion batteries. During recharging, Zn metal is reduced from zincate ions and plated at the Zn electrode. At the same time, the oxygen evolution reaction (OER) happens at the air electrode. Since an electrochemical rechargeable Zn-air battery is the focus of this study, all subsequent discussions are constrained to this type of battery.

One of the main problems in electrochemical rechargeable Zn-air batteries derives from the high solubility of zincate ions. It is difficult for the zincate ions to remain in the same location and be reduced on the electrode surface. In fact, the redistribution of Zn is influenced by many factors, including a non-uniform current density distribution and preferential nucleation of Zn.[20] Therefore, the surface of the electrode will experience a morphology change or dendrite growth during discharge-recharge cycling. Dendrites are detrimental to battery performance by lowering battery capacity and they can penetrate the separator, causing a short circuit.[21]

Another challenge in developing rechargeable Zn-air batteries is the selection of catalysts that can facilitate either ORR or OER, or a bifunctional catalyst that can catalyze both reactions. The key to making an applicable secondary Zn-air battery is active and stable catalysts. The current density at a certain potential is determined by the catalyst activity. Batteries with more active catalysts can discharge at higher potential or recharge at lower potential for a given current density. In

galvanostatic discharge/recharge cycling, the efficiency is decided by discharge potential over recharge potential. Thus, batteries with more active catalysts will have higher efficiency. As shown in Fig. 2-1, the large overpotential associated with OER increases the recharge potential to around 2 V.[22] Therefore, the discharge-recharge efficiency of Zn-air battery is normally less than 1.2 V/2 V= 60%. In contrast, lead-acid batteries have an efficiency of over 70% and Li-ion batteries have an efficiency of around 80%-90% (Table 1-1).[14, 23] In addition to the cycling efficiency, the cycle life of a rechargeable Zn-air battery is a serious issue. In contrast to Li-ion batteries that can be sealed in a metal case or an aluminum-plastic film, Zn-air batteries must work as an open system. The impurities in air can cause poisoning of the catalyst. In addition, many catalysts are vulnerable during repeated ORR and OER cycling. For example, noble metals such as Pt are not stable during cycling because of oxidation problems, even though they are highly active for ORR. In fact, all catalysts face this degradation problem. **Therefore, highly efficient, yet stable catalysts, are key to an applicable secondary Zn-air battery.**

Components of secondary Zn-air batteries

2.1.2.1 Air electrode and catalyst

The air electrode is the place where electrocatalysts are loaded (Fig. 2-2). The ORR and OER processes happen at the air electrode and the electrode has to be in contact with both air and the electrolyte. Therefore, the electrode should be able to prevent leakage of electrolyte, while allowing oxygen to pass. Its structure should contain a high density of pores for the transfer of oxygen and have some hydrophobicity. This unique function is achieved in two ways. One way is to use a metal mesh as a current collector and then press into it a mixture of carbon, catalyst and

PTFE particles. Another way is to use a hydrophobic (Teflon-coated) carbon paper as the gas diffusion layer (GDL) and then coat catalyst paste onto it (Fig. 2-2). PTFE acts as the binder and hydrophobic agent in these structures.

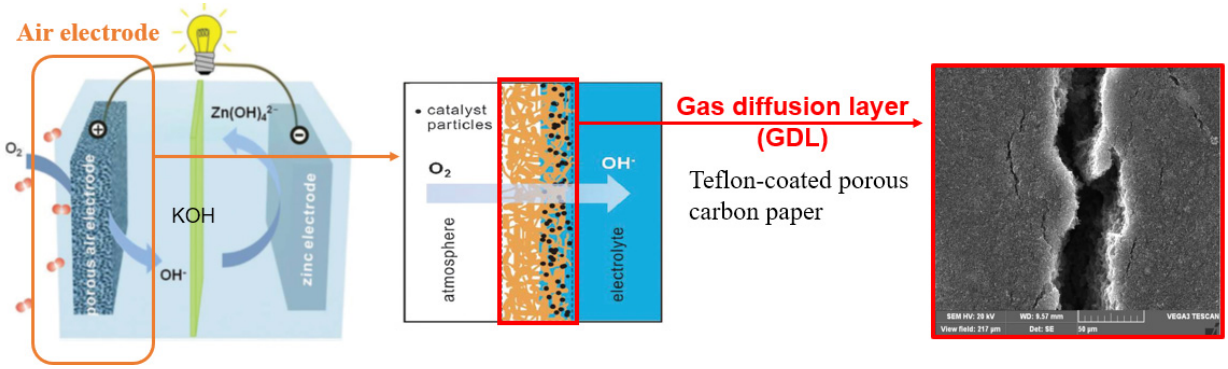

Fig. 2-2. Structure of a rechargeable Zn-air battery and its air electrode.[24]
(Reproduced by permission of the Royal Society of Chemistry; figure has been modified.)

2.1.2.2 Electrolyte

There are three types of electrolytes that can be used in Zn-air batteries: aqueous, ionic-liquid and solid-state electrolyte. Highly concentrated aqueous alkaline electrolytes are generally used in Zn-air batteries to suppress anodic passivation and to increase the solubility of Zn species.[25] The room temperature ionic conductivity varies with KOH concentration, reaching a maximum value of 0.63 S cm^{-1} at 6 M KOH.[26] Solubility of Zn species reaches a peak value on the order of 1 mol L^{-1} at the same KOH concentration.[11] Therefore, 6 M KOH is used in most research on Zn-air batteries. Some additives are used in the electrolyte to solve problems associated with the Zn anode, namely dendrite formation, Zn corrosion and hydrogen evolution. For example, bismuth chloride ($BiCl_3$) and tetrabutylammonium bromide (TBAB) are added to an alkaline zincate solution to suppress dendrite growth at a cathodic overpotential of 0.2 V.[27] A polymer additive polyethyleneimine

shows the ability to suppress dendritic morphology evolution during Zn deposition-dissolution cycles.[28] The additive functions as an adsorbent onto the Zn surface and slows Zn electrodeposition kinetics. Several acids can be added to suppress the hydrogen evolution by increasing the reaction overpotential; these show a decreased effectiveness in the order of tartaric acid > succinic acid > phosphoric acid > citric acid.[29] Surfactants, such as hexadecyl trimethyl ammonium bromide (CTAB) and perfluorosurfactants have been reported to decrease the rate of HER as well as the corrosion of Zn.[30] HER overpotential is raised due to surfactant adsorption on the Zn electrode. An appropriate amount of carboxymethyl cellulose (CMC) can reduce the corrosion current as well as suppress Zn dendrite growth.[31] ZnO can be added to inhibit the corrosion of Zn but should be controlled at an optimum concentration below its solubility limit.[32]

Aqueous electrolytes can easily permeate the air electrode and cause air electrode flooding, blocking the pores for air diffusion.[24] KOH in the electrolyte can react with CO_2 in air and precipitate as K_2CO_3 in air electrode as well. Also, the electrolyte can evaporate gradually during long-term operation. As such, room-temperature ionic liquids or solid-state electrolytes have been developed as a replacement for aqueous electrolytes. Ionic liquids are salts in a liquid state, consisting of large organic cations and anions. The wide electrochemical window and high thermal stability make them good candidates as electrolytes in various batteries.[33] They exhibit low vapor pressure and are, therefore, not easily vaporized in an open battery system. Zinc dendrite growth can be suppressed by using ionic liquids as the electrolyte.[34, 35] However, their high intrinsic viscosity and low ionic conductivity limit their application in Zn-air batteries.[36] Also, the ORR and OER processes, which rely on diffusion of oxygen and the presence of OH^-, cannot proceed easily in a pure aprotic ionic liquid electrolyte.[37] This problem can be solved by adding protic additives like water.[38]

Solid-state electrolytes in Zn-air batteries are normally gel polymers with KOH solutions. Solid-state electrolytes use gel polymers as the framework to provide support for the conductive KOH solution. Examples of gel polymers are poly(vinyl alcohol) (PVA),[39-42] poly(acrylic acid) (PAA),[43-45] poly(ethylene oxide) (PEO) or a mixture of them.[46, 47] The ionic conductivity of these solid-state electrolytes can be as high as 0.3 S cm^{-1} at room temperature, which is close to the conductivity of 6 M KOH aqueous electrolyte.[47] Other materials, such as hydroponics gel,[48, 49] gelatin[50] and cellulose,[51, 52] have also been used as solid-state electrolytes in Zn-air batteries. Solid-state electrolytes are useful in portable or flexible Zn-air batteries since they can change their shapes with different battery designs and will not leak like aqueous electrolytes. In addition, they can inhibit dendritic growth of the Zn electrode during the charge process.[53] The disadvantages of solid-state electrolytes come from their poor interfacial contact with electrodes. Catalysts particles are much harder to be fully accessed by an "immobilized" solid-state electrolyte compared with aqueous electrolytes, resulting in a lower three-phase boundary for ORR.[54] The poor contact between the solid-state electrolyte and electrode can generate a high interfacial resistance and significantly reduce the reaction current.[55] Solid-state electrolytes also act as separators in batteries. However, their poor mechanical strength may result in an internal short-circuit.

2.1.2.3 Separators

Separators are used to prevent short circuits between electrodes in Zn-air batteries. As such, they must have enough mechanical strength and be chemically inert in a concentrated alkaline electrolyte. To lower the ohmic loss in a battery, the ionic conductivity of separators should be as high as possible. Their electrochemical window should be wider than the working potential of Zn-air batteries (0.8 to 2.4 V). Commercial separators for Zn-air batteries include Celgard 5550 and

Celgard 4560, which are laminated microporous polyolefin membranes.[56] There are two ways to improve the performance of separators. The first is to increase the wettability of the aqueous electrolyte on separators to allow them to hold more electrolyte in their pores. This is done by a sulfonation treatment of polypropylene (PP)/polyethylene (PE) membrane providing an increase in ionic conductivity of 132%.[57, 58] The improvement is attributed to an enhancement of the hydrophilicity and amorphous characteristics after the sulfonation process. Another way is to add an ion selection function to separators by preventing zincate ions from moving to the air electrode. Zincate ions ($Zn(OH)_4^{2-}$) produced during discharge can migrate to the air electrode through the microporous separator, forming Zn and mixed phase deposits in the catalyst layer.[59] This ion selective function is normally achieved by coating a commercial separator with a barrier layer. For example, an ionic liquid induced copolymer was coated on a PP membrane, and showed 96% reduction in zincate ion crossover.[60] An electrospun PVA/PAA nanofiber mat was impregnated with Nafion to form a $Zn(OH)_4^{2-}$-repelling continuous phase, to allow for the selective transport of OH^- ions.[61] Electrospun polyetherimide (PEI) was coated with PVA, which provides ion size (OH^- vs. $Zn(OH)_4^{2-}$) dependent conductive pathways, to reduce crossover of zincate ions.[62] In addition to polyolefin membranes, other materials such as surface-modified Nylon filter or filter paper,[63, 64] inorganic MCM-41 membrane or sodium superionic conductors (NASICON) have been studied as separators in Zn-air batteries.[65, 66]

2.1.2.4 Zn electrode

The Zn electrode is an important part of Zn-air batteries. It limits the lifetime of batteries in the long-term. Most energy storage devices such as primary Zn-air batteries and alkaline batteries use porous Zn electrodes for a large electrode-electrolyte interface. However, a Zn foil is used in our

battery tests for easy assembly of the cell. The dissolution of Zn happens readily near its equilibrium potential and forms $Zn(OH)_4^{2-}$ as the predominant species in alkaline solutions, which leads to the corrosion of the Zn electrode in the open circuit voltage (OCV) state.

A typical I (current) -V (voltage) curve for a Zn electrode in an alkaline electrolyte is presented in Fig. 2-3. The plot shows that the deposition of Zn during charging will be accompanied by the hydrogen evolution reaction (HER). This occurs because the standard electrode potential of $Zn/Zn(OH)_2$ is -1.25 V vs. SHE, while that of HER is -0.83 V vs. SHE at pH=14.[54] However, the exchange current density (j_0) for the HER on the Zn surface is on the order of 10^{-9} A cm^{-2}, which is much lower than j_0 for Zn electrodeposition (on the order of 0.1 A cm^{-2}). This feature means that the Zn electrode has a high overpotential for HER and therefore a high current efficiency during the charging process of Zn-air batteries.[11]

During the discharge process of a Zn-air battery, the Zn will dissolve into the electrolyte. Fig. 2-3 shows that Zn dissolution process includes an anodic current peak followed by a drastic current drop due to the occurrence of passivation. Passivation is due to the formation of a solid ZnO film on the Zn surface after the electrolyte is saturated with zincate ions.[11] The ZnO film increases the resistance, leading to a decreased anode capacity and finally causes the cell to stop discharging.[67]

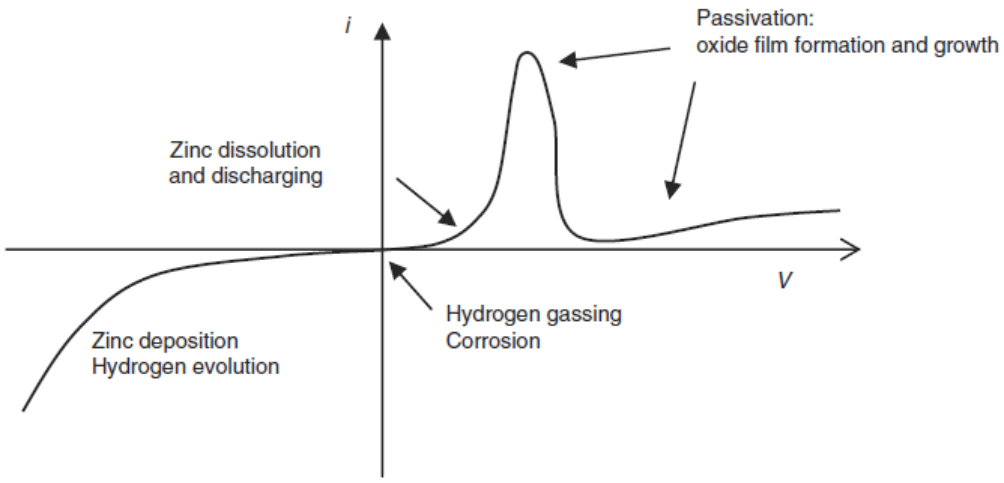

Fig. 2-3. Typical I-V curve of Zn electrode in alkaline electrolyte.[11]

(Reproduced by permission of Elsevier.)

During the charging process, five types of Zn deposits can be formed in the order of increasing current: mossy, layered, granular, dendritic and clustered.[68] Dendrites are detrimental to the cycling of rechargeable Zn-air batteries, since their tree-like shape can penetrate separators and short-circuit the cell. The growth of Zn dendrites is initiated at a critical overpotential of 75-82 mV where the deposition is under diffusion control.[69] Zinc dendrites can also be formed at a low overpotential of 40-60 mV if enough time is given during deposition.[70]

The shape of the Zn electrode can change gradually during repeated dissolution-deposition cycling. This happens when the Zn species transported across the electrode is smaller in amount during charge than it is during discharge.[71] In other words, it is caused by insufficient mass transport carried out by electrolytes. This phenomenon also occurs when Zn dissolves or deposits preferentially in certain regions like edges and corners due to a non-uniform distribution of current density along the Zn electrode surface.[72] Therefore, the layout of physically decoupled electrodes for charge and discharge may have an impact on the uniformity of current distribution. A proper

design of electrode structure or the use of enhanced mass transport (e.g., flowing electrolyte) can help mitigate the problem of shape change.[73]

A number of methods have been developed to solve the above problems of corrosion, HER, passivation and dendrites. Additives in electrolytes can provide a solution to these problems. Some examples have been discussed in the above sections on aqueous electrolyte. These additives, such as cellulose and oxides of lead and bismuth, function by depositing on the Zn surface during charging or discharging, providing a high overpotential for HER or inhibiting dendrite formation and corrosion.[74, 75] Modification of the Zn electrode is another effective solution. Reduced dendrite formation and increased HER potential were achieved by alloying Zn with nickel (Ni) and indium (In)[76]. A Li_2O-$2B_2O_3$ glass was coated on Zn to prevent its direct contact with the KOH electrolyte, thereby decreasing HER and inhibiting corrosion.[77] Other coatings such as Al_2O_3 and polyaniline are reported to have similar effects on the Zn electrode as well.[78, 79] Coatings like SiO_2 and Bi_2O_3 are reported to help reduce the formation of the ZnO passive layer and improve the discharge capacity by constructing an amorphous gel layer outside of Zn.[80, 81]

2.2 Electrocatalysts for Zn-air batteries

2.2.1 Catalyst function and mechanism for catalyzing ORR/OER

The function of the catalyst in ORR/OER is to provide a different reaction pathway with a lowered activation energy, as shown in Fig. 2-4. The activation energy is the energy barrier for a reaction to proceed. With the help of a catalyst, some intermediates are produced with reduced energy barriers, facilitating the reaction.

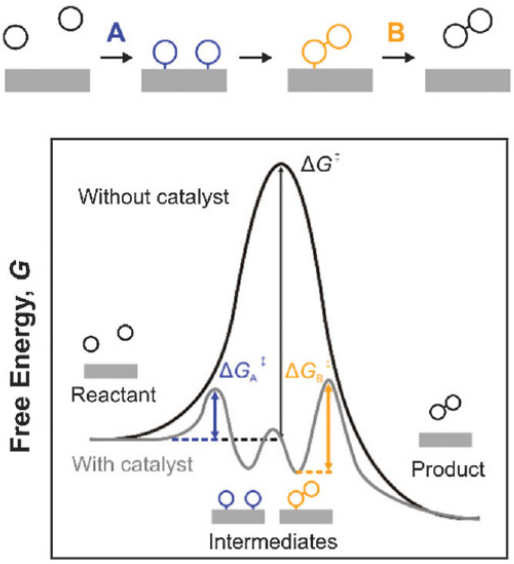

Fig. 2-4. The reaction mechanism with a catalyst.[82]

(Reproduced by permission of the Royal Society of Chemistry.)

2.2.1.1 Mechanism for ORR in alkaline electrolytes

There are two paths for the ORR process in an alkaline solution which depend on the surface properties of the catalysts, i.e., four-electron or two-step, two-electron transfer, as shown below.[83]

Four-electron pathway (e.g., on Pt/C): $O_2 + 2H_2O + 4e^- \rightarrow 4OH^-$ (2-8)

Two-step, two-electron pathway (e.g., on graphite): $O_2 + H_2O + 2e^- \rightarrow OOH^- + OH^-$ (2-9)

$OOH^- + H_2O + 2e^- \rightarrow 3OH^-$ (2-10)

The four-electron pathway is more desired than the two-electron one, because it produces hydroxide rather than peroxide species (OOH^-), which can cause carbon corrosion and performance degradation.[84] For ORR catalyzed by transition metal oxides such as Mn oxide

(MnOx), including Mn_2O_3, Mn_3O_4, Mn_5O_8 and MnOOH, chemical disproportionation of peroxide following reaction (2-9) was proposed by Mao et al:[85]

$$2OOH^- \rightarrow O_2 + 2OH^- \quad (2\text{-}11)$$

For some MnOx phases like MnO_2, it is difficult to explain the mechanism by simply using the above four-electron or two-electron mechanism. ORR on MnO_2 surface proceeds through the chemical oxidation of surface Mn^{3+} in the following way:[86]

(1) Mn^{4+} in MnO_2 is reduced to Mn^{3+} during discharge:

$$Mn^{IV}O_2 + H_2O + e^- \rightarrow Mn^{III}OOH + OH^- \quad (2\text{-}12)$$

(2) O_2 is adsorbed on surface Mn^{3+} and chemically reduced, generating intermediates:

$$2Mn^{III}OOH + O_2 \rightarrow 2\left(Mn^{IV}OOH \cdot O^-\right) \quad (2\text{-}13)$$

(3) The intermediates are reduced back to MnO_2, releasing OH^-:

$$\left(Mn^{IV}OOH \cdot O^-\right) + e^- \rightarrow Mn^{IV}O_2 + OH^- \quad (2\text{-}14)$$

The total reaction is still $O_2 + 2H_2O + 4e^- \rightarrow 4OH^-$.

Since Mn^{4+} must be first reduced to Mn^{3+} for the whole ORR reaction to proceed, the Mn^{4+}/Mn^{3+} redox kinetics will influence the ORR activity of different manganese oxides. It has been reported that MnOx with a higher surface Mn^{4+}/Mn^{3+} redox potential would also produce a higher ORR onset potential, while the ORR activity increases exponentially with the number of available active Mn^{3+} sites.[87] Stoerzinger et al. proposed that the presence of surface Mn^{4+}/Mn^{3+} mixed valence states can promote cleavage of bound oxygen and complete reduction to OH^-, with an improved charge transfer ability to oxygen brought about by Mn^{4+} ions.[88]

2.2.1.2 Mechanism for OER in alkaline electrolytes

The OER process on non-noble metal oxides such as Ni, Co and Mn oxides and perovskites proceeds via the following steps:[89, 90]

(1) Discharge of hydroxide ions on active sites (M), generating intermediate species:

$$M + OH^- \rightarrow MOH + e^- \quad (2\text{-}15)$$

(2) Deprotonation of intermediate species MOH:

$$MOH + OH^- \rightarrow MO^- + H_2O \quad (2\text{-}16)$$

(3) Intermediate species discharge:

$$MO^- \rightarrow MO + e^- \quad (2\text{-}17)$$

(4) Oxygen formation and desorption, with two different routes to form oxygen:

route (a) $$2MO \rightarrow 2M + O_2 \quad (2\text{-}18)$$

route (b) $$MO + OH^- \rightarrow MOOH + e^- \quad (2\text{-}19)$$

$$MOOH + OH^- \rightarrow M + O_2 + H_2O + e^- \quad (2\text{-}20)$$

In the first step (2-15), the multi-valent transition metal oxides increase the valence state to form bonds with oxygenated species. As such, the adsorption energy of the oxygen species will change with different metal cations, leading to different OER kinetics.[91] Any of steps (1) - (4) could be rate-determining depending on the type of oxide materials.[92] The OER activity has been found to be inversely related to the oxide surface bond energy of OH^-, making the desorption of OH^- or the oxygenated species a rate-determining step.[93]

Extensive research on Co-/Fe-/Ni-based catalysts has been reported with the aim to improve their OER activity in alkaline media.[94] Considerable effort has been devoted to making highly efficient catalysts from Co-containing materials. These are classified into five categories: Co oxides/hydroxides, Co chalcogenides, Co phosphides and Co phosphates.[95] Co oxides/hydroxides are easy to prepare through electrodeposition. Specifically, when CoO undergoes the OER process, reactions happen through the following steps:[96]

$$CoO + OH^- \rightarrow CoOOH + e^- \quad (2\text{-}21)$$

$$CoOOH + OH^- \rightarrow CoO_2^- + H_2O \quad (2\text{-}22)$$

$$CoO_2^- \rightarrow CoO_2 + e^- \quad (2\text{-}23)$$

$$CoO_2 \rightarrow CoO + O_{ad} \quad (2\text{-}24)$$

$$2O_{ad} \rightarrow O_2 \quad (2\text{-}25)$$

It has been suggested the rate of oxygen evolution becomes significant when potentials corresponding to Co(IV) formation are attained (Step (2-23)).[97] The potential of surface oxidation from Co(III) to Co(IV) is around 0.6 V vs. Hg/HgO in 1 M KOH,[98] which is also the potential where the OER current starts to arise in our experiments on Co-Fe catalysts (Fig. 3-2(a) in Chapter 3 and Fig. 4-2(a) in Chapter 4).

Based on the role of the catalyst in ORR/OER reactions, the catalyst should have the following properties for good performance:

1. High surface area to provide more active sites; highly active lattice planes with the appropriate oxidation state should be exposed to the reactants.

2. Appropriate interaction with redox species, i.e., neither too weak nor too strong. If the binding is too weak, adsorption is difficult and if the binding is too strong, separation is difficult.[99]

3. Stable during the electrochemical reaction. The catalyst should not be oxidized nor reduced by reactants under the operating potential. For Zn-air batteries, catalysts must be stable in strong alkaline solutions.

4. High electronic conductivity to allow fast electron transfer and facilitate redox reactions.

Catalysts for ORR/OER can be classified to three categories: noble metal catalysts, transition metal compounds catalysts and carbonaceous catalysts, which will be discussed in the following sections.

2.2.2 Noble metal catalysts

Platinum is chosen as the benchmark material when assessing other types of catalysts due to its superior performance in ORR. Nano-sized Pt particles are dispersed on a carbon support with high surface area in a commercial product.[100] However, the cost of Pt is a major issue for its application. There are two ways to reduce the cost of using Pt. One method is to produce a nano-structured Pt-based catalyst with high surface area and maximize the highly active crystal planes.[101] Another way is to alloy Pt with other cheap metals such as Ni, Fe or Co to develop intermetallic compounds with good performance.[102-104]

Other noble metals like Pd and Ag have also been studied as ORR catalysts because of their relatively low cost and reasonable performance. The ORR activity of Pd catalysts increases by 10-fold and becomes comparable to that of Pt by changing the morphology from nanoparticles to nanorods.[105] The ORR on Ag/C catalysts proceeds mainly through a four-electron pathway.[106]

The benchmark for OER is Ru- and Ir-based catalysts. Tobias et al. compared the OER capability of Ru, Ir and Pt catalysts, indicating that their OER activities in nano-particle form decreased in the following order: oxidized Ru > oxidized Ir > oxidized Pt.[107]

2.2.3 Transition metal compound catalysts

ORR/OER catalysts based on noble metals are not a good choice for widespread application of Zn-air batteries. Other cheaper alternatives must be found to replace them. Earth-abundant transition metal elements include Ti, V, Cr, Mn, Fe, Co, Ni, Cu, Zn, Zr, Nb, Mo and W.[108] Some of them are believed to have good ORR and OER catalyst ability. Transition metals such as Mn, Fe, Co and Ni are inexpensive and abundant in the Earth's crust. They can exist in many forms as catalysts, such as metal oxides/sulfides/phosphides/carbides/nitrides, spinel-type mixed oxides or perovskites.

2.2.3.1 Metal oxides, sulfides, phosphides, carbides and nitrides

Transition metal oxides are quite stable in alkaline solutions and thus suitable to be used in Zn-air batteries. Because transition metals have multiple valences, there are a variety of oxides for each element. For example, Mn has various valence states of Mn(II), Mn(III), Mn(IV), etc., leading to a series of oxides like MnO, Mn_2O_3, MnO_2 and Mn_3O_4 as well as others. The ORR catalytic activity of different Mn species tends to decrease in the order of MnOOH > Mn_2O_3 > Mn_3O_4 > Mn_5O_8,

which is attributed to efficiency differences in accelerating peroxide disproportionation (Reaction 2-11).[109] For MnO_2, it is reported that the ORR catalytic activities of different 1D structures decrease in the order of α-MnO_2 > β-MnO_2 > γ-MnO_2 due to a combination of the influence of conductivity and tunnel size.[110] Experiments show that the OER catalytic abilities of MnO_2 in alkaline media are strongly dependent on crystallographic structure, following the order of α-MnO_2 > amorphous MnO_2 > β-MnO_2 > δ-MnO_2.[111] The lower charge transfer resistance, combined with abundant protonation sites, contribute to the outstanding OER activity of α-MnO_2. The relatively poor electrocatalytic performance of metal oxides can be improved by adding conductive materials (e.g., graphene and carbon nanotubes),[112, 113] optimizing catalyst morphology[114, 115] or introducing defects.[116] In addition to metal oxides, nanostructured transition metal sulfides, phosphides, carbides and nitrides have shown high activity towards ORR and OER as well.[117-119]

2.2.3.2 Spinel type composite oxides

In addition to single metal oxides, different metal ions can be incorporated into composite metal oxides. Composite oxides have better structural stability and can provide both ORR and OER active sites, which are beneficial for bifunctional catalysts. Composite oxides, in the form of spinel structures, have received much attention because they allow partial cation substitution to produce various oxides and their catalytic properties can be tuned.[120] Spinels are compounds in the form of AB_2O_4, and are a face-centered cubic arrangement of O ions with metal ions occupying octahedral and tetrahedral interstitial sites.[121]

2.2.3.3 Perovskites

Perovskites are a family of compounds with the form ABO_3, in which A sites are occupied by rare-earth metal ions and B sites are occupied by transition metal ions. Both A and B site elements can

be partially substituted to create a large number of oxides with the form AA'BB'O_3.[122] For application as a catalyst, the catalytic activity of perovskites is mainly determined by the B-site cations, while the selection of A-site cations controls the valency and has a minor effect.[123]

2.2.3.4 Other transition metal compounds

In addition to above materials, it has been found that other transition metal compounds can possess excellent electrocatalytic ability. For example, a hybrid catalyst of NiFe LDH (layered double hydroxides) and carbon nanotubes was found to perform well for the OER process and was used together with CoO/N-CNT as a bifunctional catalyst in Zn-air batteries.[124] A rechargeable Zn-air battery adopting this catalyst can deliver a current density of 10 mA cm^{-2} at 1.25V and then is recharged at 1.95V. Heat-treated Fe- and Co-N/C catalysts are another option for ORR. The mechanisms for these catalysts are not fully understood, but the nitrogen content and the surface properties of the carbon-support seem to play an important role in performance.[125] Metal-organic frameworks (MOF) are a class of crystalline porous materials consisting of metal ions and organic ligands, with the pore size adjustable from several angstroms to several nanometers.[126] Their ultra-large surface-to-volume ratio and tunable active sites make them excellent catalysts for ORR and OER.[127]

2.2.4 Carbonaceous catalysts

Carbonaceous materials are good candidates for catalysts in Zn-air batteries due to their low cost and high stability in alkaline media. Carbons have two types of hybridization: sp^3 and sp^2. In sp^3 hybridized carbon, such as diamond, all valence electrons are constrained and the material has low electronic conductivity. In contrast, graphite with sp^2 hybridization, has much better conductivity

due to the π-bond on the hexagonal plane. The catalytic activity is different for the basal plane and the edge plane in graphite. The ORR capability is higher in graphite with more edge-plane sites.[128] Doping with heteroatoms like N and S also helps to improve the performance by enhancing the structural disorder. For example, doping of nitrogen can introduce defects into the graphite layer and create many edge-plane sites. However, not all doped N atoms can help increase the catalytic activity. Only the pyridinic, pyrrolic and graphitic N atoms which have a planar structure are active for ORR, while quaternary N atoms in a 3D structure are not active because of the interruption of their π-π conjugation.[129, 130] Nitrogen doping is normally obtained by the pyrolysis of nitrogen-containing hydrocarbons and it is difficult to achieve a high content of N, which is the limiting factor for catalytic ability.[131] In addition to N-doped carbon, other carbonaceous materials like carbon nanotubes (CNTs) and graphenes have received extensive attention because of their high surface area and electrical conductivity. They can either serve as the substrate for metal-based catalysts or can be used independently.

To achieve the highest discharging-charging efficiency for Zn-air batteries, the catalysts mentioned above are usually combined together and coated on the air electrode. An ORR active catalyst can be hybridized with an OER active catalyst chemically or physically to make a bifunctional catalyst. A summary of transition metal compounds and carbonaceous catalysts used in Zn-air batteries is shown in Table 2-1.

Table 2-1. Summary of transition metal catalysts used in rechargeable Zn-air batteries

Catalyst material	Battery performance	Reference
NiO/CoN	Discharge: 1.29 V at 10 mA cm^{-2} Charge: 2.30 V at 50 mA cm^{-2}	Ref.[132]
α-MnO_2/CNT	Discharge: 1.25 V at 10 mA cm^{-2} Charge: 2.10 V at 10 mA cm^{-2}	Ref.[133]
Zn-Co-mixed sulfide	Discharge: 1.18 V at 10 mA cm^{-2} Charge: 2.03 V at 10 mA cm^{-2}	Ref.[134]
MnS/Co/N-doped CNT	Discharge: 1.14 V at 10 mA cm^{-2} Charge: 2.13 V at 10 mA cm^{-2}	Ref.[135]
CoP/N-, S-, P-doped carbon	Discharge: 1.20 V at 20 mA cm^{-2} Charge: 2.00 V at 20 mA cm^{-2}	Ref.[136]
Ni-Fe nitride nanoplates	Discharge: 1.17 V at 10 mA cm^{-2} Charge: 1.94 V at 10 mA cm^{-2}	Ref.[137]
Spinel $CoMn_2O_4$/N-doped graphene	Discharge: 1.10 V at 20 mA cm^{-2} Charge: 2.00 V at 20 mA cm^{-2}	Ref.[138]
Spinel $MnCo_2O_4$/CNT	Discharge: 1.20 V at 10 mA cm^{-2} Charge: 2.05 V at 5 mA cm^{-2}	Ref.[139]
$PrBa_{0.5}Sr_{0.5}Co_{2-x}Fe_xO_{5+\delta}$	Discharge: 1.25 V at 10 mA cm^{-2} Charge: 2.05 V at 10 mA cm^{-2}	Ref.[140]
Fe-N-C/MOF	Discharge: 1.13 V at 10 mA cm^{-2} Charge: 1.95 V at 10 mA cm^{-2}	Ref.[141]

2.2.5 Fabrication methods for air electrode loaded with catalysts

Catalysts cannot work independently in a battery; they must be first loaded onto a substrate and made into an electrode. One of the major issues for air electrodes is the loading of the catalyst on a GDL/substrate. Currently, the most widely used GDL is a carbon paper that contains large amounts of hydrophobic PTFE to prevent flooding. The catalyst is not easy to load onto the hydrophobic surface of the GDL because of wettability issues. There are several ways to load the prepared catalyst onto the GDL, such as film coating, spraying and electrodeposition. The film coating method requires specific equipment like a screen printer to achieve a uniform layer. The spray method can produce relatively uniform loading, but it is difficult to control the mass loading. These methods also require adding binders like PTFE or Nafion to stick the catalyst particles onto the GDL surface. The binders are not conductive and will gradually lose their adhesion during battery cycling.

An alternative way for loading catalysts is to directly grow the active material on the GDL/substrate by chemical methods; binders are not required. For example, Lee et al. have directly grown mesoporous Co_3O_4 nanowires onto a stainless steel mesh substrate and used it as the air cathode in a Zn-air battery.[142] The assembled Zn-air cell had recharge and discharge potential retentions of 97% and 94% after 600 h of cycling, respectively.

Electrodeposition is a way to deposit metal or metal oxides onto a conductive substrate using electric current. The mass loading, as well as the uniformity, can be controlled. There are two types of electrodeposition process, cathodic and anodic. In terms of loading metal oxides onto GDL, both cathodic and anodic methods can be used. In the cathodic process, metals are first reduced at the surface of the GDL and then oxidized in a subsequent annealing process. In other words, the metals are first electroplated onto the GDL. In the anodic process, metal ions in a low valence state

are oxidized to a higher valence state and then precipitate at the GDL surface in the form of metal oxides. Electrodeposition is the primary method to prepare catalysts in this study and will be discussed in following sections.

2.3 Electrodeposition process

Electrodeposition of metals or metal oxides involves the reduction or oxidation of metal ions from aqueous or organic electrolytes. Four steps are involved in typical cathodic metal electrodeposition:[143]

(1) Ion hydration and migration.

Metal ions are hydrated in aqueous solution and migrate toward the cathode by an electric field or diffusion/convection.

(2) Ion alignment and dehydration.

Hydrated metal ions are aligned on the electrode surface by the weak electric field of the diffusion double layer. Then they enter the Helmholtz double-layer and lose their hydrated shell due to the high strength electric field.

(3) Ion reduction and adsorption.

Dehydrated metal ions are adsorbed and reduced to atoms (adatoms) on the electrode surface by electron transfer.

(4) Adatom incorporation.

Adsorbed atoms diffuse on the surface and seek low energy positions to be incorporated into the bulk crystal.

The whole process is as follows and depicted in Fig. 2-5.

$$M^{n+}(\text{solution}) \rightarrow \left[M(H_2O)_x\right]^{n+}(\text{solution}) \rightarrow M^{n+}(\text{adsorbed}) \rightarrow M(\text{lattice}) \qquad (2\text{-}26)$$

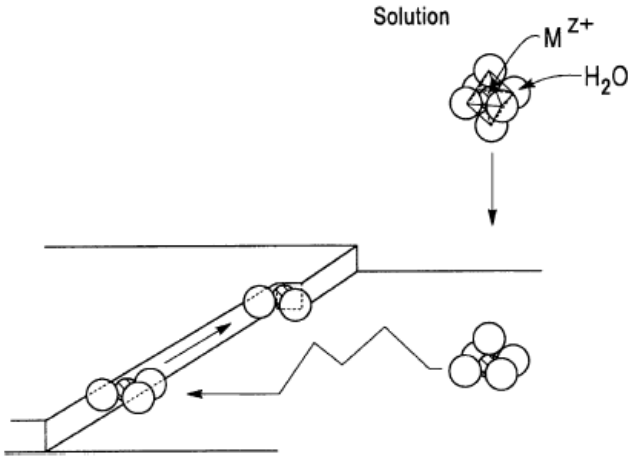

Fig. 2-5. Metal ion transfer process in cathodic electrodeposition.[143]

(Reproduced by permission of John Wiley and Sons.)

2.3.1 Cathodic electrodeposition

2.3.1.1 General mechanism

Cathodic electrodeposition or electroplating is widely used to form a coherent metal coating on a solid substrate. The reaction in the cathodic electrodeposition of a hydrated metal ion is:[144]

$$M^{n+} \cdot xH_2O + ne^- \rightarrow M^0 + xH_2O \qquad (2\text{-}27)$$

Both two-electrode galvanostatic electrodeposition and three-electrode (with a reference electrode) potentiostatic electrodeposition can be used in cathodic electrodeposition. Compared with potentiostatic electrodeposition, the issue with galvanostatic electrodeposition is the lack of a theoretical model (such as the 3D nucleation process proposed by Scharifker and Hills[145]) to help explain the nucleation mechanism during the process. However, galvanostatic electrodeposition is more practical and more common than potentiostatic electrodeposition in industry (the conditions provided in an electroplating instruction manual normally refer to current densities rather than potentials). In addition, it is easier to apply pulse electrodeposition in the galvanostatic mode. Therefore, the two-electrode setup was applied in all the electrodeposition processes in this study.

The properties of electrodeposited films are determined by a variety of factors, including applied potential/current, electrolyte additives and electrolyte agitation.

2.3.1.2 Effect of potential/current

The electrode potential must be shifted from its equilibrium value to achieve a reasonable rate of metal deposition. The value of this shift is called overpotential η. It has been reported that the size of the critical nucleus N_c depends strongly on the overpotential η.[143] In a 2D nucleation process:

$$N_c = \frac{bs\varepsilon^2}{(ne\eta)^2} \tag{2-28}$$

Where b is the shape factor ($b=P^2/4S$; P is nucleus perimeter and S is the nucleus surface area), s is the area occupied by one atom on nucleus surface, ε is the edge energy, n is the number of electrons transferred and $e=1.602 \times 10^{-19}$ C.

The steady-state nucleation rate J, is given by:[146]

$$J = K_1 \exp\left(\frac{K_2}{\eta^2}\right) \tag{2-29}$$

where K_1 and K_2 are constants that are independent of overpotential change.

As such, in theory a large number of small particles can be generated when a high overpotential is applied in electrodeposition. In fact, metals deposited at high overpotentials usually have finer grains than those deposited at low overpotentials. Metals are grouped by their overpotential value at ordinary current densities (10-100 mA cm^{-2}): high η group (η ≈ hundreds of mV; Fe, Co, Ni, Cr, Mn and Pt); intermediate η group (Cu, Bi and Zn) and low η group (η ≈ tens of mV; Pb, Sb, Ag, Sn and Cd).[144] The classification is determined by the exchange current density (j_0) measured for the reduction/oxidation of the metal. A high j_0 value leads to a low η and vice-versa.

Catalysts with small particles (nanocrystalline) are desired since they have high surface area and more active sites. In order to achieve a high overpotential, a high current density can be adopted in electrodeposition. However, a high current that lasts for a long time can decrease the current efficiency and generate a lot of heat in the cell. The use of pulsed current, in which a high current density is applied for a short time (on-time), followed by a relaxation period (off-time), is helpful in mitigating the adverse effect.[147]

2.3.1.3 Effect of additives and agitation

In addition to increasing current density, there are other ways to increase the overpotential for small-particle electrodeposition. For example, electrolyte additives (saccharin, gelatin, etc.) can adsorb on the electrode surface and slow down the metal ion discharge rate, thereby increasing the

deposition overpotential.[148, 149] The activity of the metal ions can be greatly decreased by complexing with other ions. By using a complexing agent, the decreased electrochemical reaction rate will lead to a higher overpotential and finer particles during electrodeposition.[150] The complexing agent can also help stabilize the plating bath and prevent metal hydroxide precipitation in high pH or even alkaline electrolytes.[151, 152]

The hydrogen evolution reaction (HER) is a side reaction during cathodic electrodeposition due to overlap of the potential range for metal deposition and hydrogen evolution. HER can lower the current efficiency and cause a local pH increase near the electrode. Metal ions will then precipitate as metal hydroxide, forming gels or precipitates in the cell due to the low solubility of metal hydroxide.[153] The degree of HER is determined by several factors. Several elements like Fe, Co and Ni have low overpotentials for HER. Electrodeposition of these elements is always accompanied by significant H_2 formation. The local concentration of metal ions near the electrode is another factor. Agitation of the electrolyte by stirring or sonication can facilitate metal ion diffusion towards the cathode, suppressing HER. Depleted metal ions can be replenished during the off-time of pulse electrodeposition as well.[147] Additives like boric acid can be used to suppress HER and retard the pH increase at the cathode surface.[154, 155] Sometimes, H_2 bubbles from HER can be used as a dynamic template to produce metal foams. For example, porous Cu or Ag foams have been deposited galvanostatically with a large current.[156, 157]

2.3.1.4 Electrodeposition of alloys

The co-electrodeposition of two or more metals is a useful technique to prepare alloy coatings. The composition of the alloy can be adjusted by simply changing the element ratio in the plating

bath if these elements have similar reduction potentials. However, an alloy consisting of both a noble metal with high reduction potential and a less-noble metal with a lower reduction potential is difficult to prepare by co-electrodeposition due to the large gap in their deposition potentials.[158] This will lead to the preferential deposition of the more noble metal, since a larger overpotential will be achieved for it compared with the less-noble one at the same cathodic current.[159] To solve this problem, complexing agents can be added to complex the noble metal ions or both the noble and less noble metal species. Their reduction potentials will be changed due to a change in their ionic activities, according to the Nernst equation. The complexing agents are supposed to reduce the ionic activity more for the noble metal and, thus, noble metal's reduction potential drops close to the potential of the active metal. As-deposited alloys can be further oxidized by annealing or electrochemical oxidation to acquire the desired composition. For example, $CoFe_2O_4$ thin films were prepared by the electrochemical oxidation of electrodeposited $CoFe_2$ alloy films.[160]

Not all metals or alloys can be electrodeposited from an aqueous electrolyte due to the interference of HER. Mn/Mn^{2+} has a standard reduction potential of -1.18 V vs. SHE, making Mn the least noble metal that can be electrodeposited from an aqueous electrolyte.[161] The current efficiency of Mn metal deposition is usually quite low because of its low reduction potential and electrolyte impurities (Fe, Co, Ni, etc.).[162] However, Mn metal or its alloys can be easily electrodeposited from organic electrolytes such as ionic liquids or eutectic solvents.[163, 164]

2.3.1.5 Electrodeposition of metal hydroxides/oxides

Metal hydroxides/oxides can also be electrodeposited on the cathode due to the increase in pH induced by HER. There is no direct electron transfer from the cathode to the metal species in this

case. Normally, metal nitrates are used as precursors to generate OH^- by the reduction of nitrate ions, followed by the precipitation of metal hydroxides:[165, 166]

Nitrate ion reduction: $NO_3^- + 7H_2O + 8e^- \rightarrow NH_4^+ + 10OH^-$

or $NO_3^- + H_2O + 2e^- \rightarrow NO_2^- + 2OH^-$ (2-30)

Metal hydroxide precipitation: $M^{2+} + 2OH^- \rightarrow M(OH)_2$ (2-31)

Metal oxides can be obtained by dehydration or annealing of the hydroxides. Many transition metal oxides/oxy-hydroxides, such as Co_3O_4 and MnOOH, have been prepared in this way.[167, 168]

2.3.2 Anodic electrodeposition

Due to the various limitations of cathodic electrodeposition, anodic electrodeposition was introduced to prepare some materials that are difficult to fabricate by the electrochemical reduction. For example, manganese oxides can be prepared by annealing of electroplated Mn metal, or by the direct oxidation Mn^{2+} ions at the anode. The latter method has a much higher current efficiency and is widely used in the battery industry to prepare γ-MnO_2 (electrochemical manganese dioxide, EMD) cathode material. The electrodeposition process proceeds in the following manner:[169, 170]

Anode: $Mn^{2+} + 2H_2O \rightarrow MnO_2 + 4H^+ + 2e^-$ (E^0=1.23 V vs. SHE) (2-32)

$2H_2O \rightarrow O_2 + 4H^+ + 4e^-$ (side reaction, OER, E^0=1.23 V vs. SHE) (2-33)

Cathode: $2H^+ + 2e^- \rightarrow H_2$ (2-34)

Overall: $Mn^{2+} + 2H_2O \rightarrow MnO_2 + H_2 + 2H^+$ (2-35)

It has been suggested that reaction (2-32) has two electron transfer steps. The first step is the oxidation of solvated Mn^{2+} to a soluble Mn^{3+} intermediate:[170]

$$Mn^{2+} \rightarrow Mn^{3+} + e^{-} \quad (2\text{-}36)$$

The second step is dependent on the acidity of the electrolyte. The Mn^{3+} intermediate is stable in a concentrated acidic electrolyte (e.g., 0.5 M H_2SO_4) and will undergo disproportionation to form soluble Mn^{2+} and Mn^{4+}, which will quickly hydrolyze and precipitate as MnO_2:[170]

$$2Mn^{3+} \rightarrow Mn^{2+} + Mn^{4+} \quad (2\text{-}37)$$

$$Mn^{4+} + 2H_2O \rightarrow MnO_2 + 4H^{+} \quad (2\text{-}38)$$

In an electrolyte with less acidity (e.g., 0.1 M H_2SO_4), the Mn^{3+} intermediate will first hydrolyze to a MnOOH precipitate and then transform to MnO_2 by solid-state oxidation:[171]

$$Mn^{3+} + 2H_2O \rightarrow MnOOH + 3H^{+} \quad (2\text{-}39)$$

$$MnOOH \rightarrow MnO_2 + H^{+} + e^{-} \quad (2\text{-}40)$$

Various morphologies like nanowires, flakes can be prepared by changing the experimental conditions or the use of templates.[172, 173] MnOOH, Mn_2O_3 and Mn_3O_4 can also be prepared by anodic electrodeposition directly or through a subsequent heat treatment.[174, 175]

Some conductive polymers such as polypyrrole (ppy) can be electropolymerized on electrodes through anodic oxidation, which is another form of anodic electrodeposition.[176] In addition, they can form nanocomposites with transition metals or metal oxides by electrodeposition. For example, Co-ppy and MnOx-ppy have been synthesized by electrodeposition and show some ORR activity.[177, 178]

2.4 Experimental methodology

2.4.1 Electrode fabrication

All electrodes in this study were prepared by electrodeposition methods. The typical process is described in the following sections.

2.4.1.1. Electrolyte preparation

The electrolyte contained metal precursors like metal sulfates or metal acetates. Other additives like complexing agents, buffering agents, antioxidant and surfactants were added to increase the quality of the deposited film. For example, for cathodic electrodeposition of Co-Fe alloys, $CoSO_4$ and $FeSO_4$ were the metal precursors and sodium citrate was added to complex with Co^{2+} and Fe^{2+} ions. Boric acid was used as a pH buffering reagent to suppress the HER, which could cause a rapid pH increase during cathodic electrodeposition. Any pH increase near the cathode can produce metal hydroxide precipitates, which can interfere with the reduction of metal ions on the electrode. In addition, the HER acts as a side reaction and will decrease the efficiency of cathodic electrodeposition. L-ascorbic acid acted as an antioxidant and was used to prevent the oxidation of metal ions (especially Fe^{2+} to Fe^{3+}) in preparing the electrodeposition solution. Sodium dodecyl sulfate was used to improve the wettability of the electrodeposition solution on the GDL substrate, which contains PTFE as a binder and waterproof coating (Table 2-2). The hydrophobic GDL surface hinders electrodeposition because a layer of air will be trapped between it and the electrolyte. The electrolyte was stirred at room temperature for several hours until all salts were dissolved.

2.4.1.2. Electrolytic cell setup

The GDL is a PTFE-coated carbon paper and was purchased from SGL Group. It has two layers: a microporous layer (MPL) for loading the catalysts and a fibrous backing layer for support and air diffusion (Fig. 2-6(a)). Typical properties of the GDL are listed in Table 2-2. The GDL was used as the working electrode and the microporous layer was covered by a plastic sheet to limit the area for electrodeposition. The counter electrode was Pt mesh with the same size. The distance between the electrodes was fixed by inserting two spacers. Then a certain volume of the electrolyte was added to the cell for electrodeposition. The whole setup is shown in Fig. 2-6(b).

Table 2-2. Typical properties of GDL

Properties	Unit	Values
Thickness	μm	325
Area weight	g m^{-2}	105
Porosity	%	50-52
Gas permeability (Gurley)	cm^3 cm^{-2} s^{-1}	1.0-1.5
Electric conductivity (In plane, X/Y)	S cm^{-1}	170/145
Electric conductivity (Through-plane)	S cm^{-1}	2.0-2.2
PTFE load of backing	%	5±1
PTFE content of microporous layer	%	23

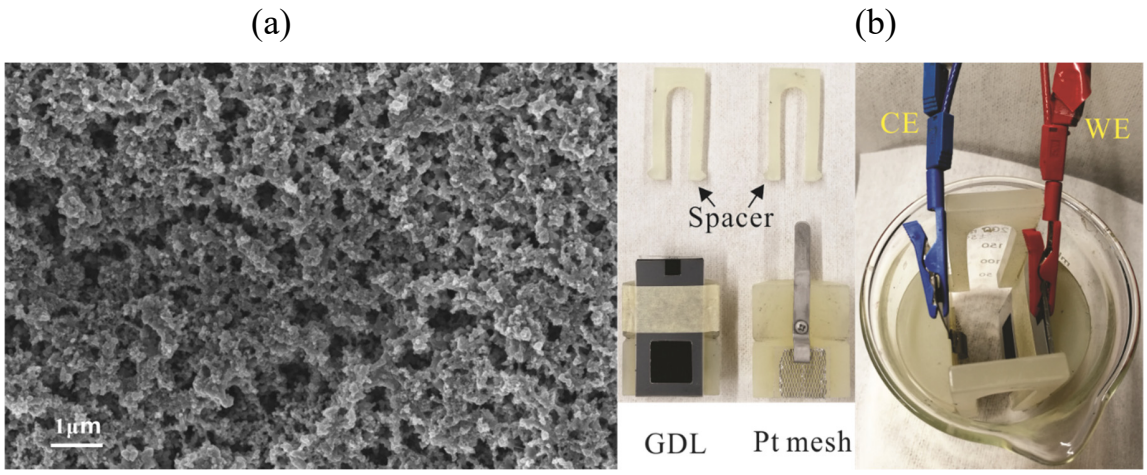

Fig. 2-6. (a) SEM secondary electron (SE) image of the MPL of the GDL. (b) Setup for the electrodeposition process.

2.4.1.3. Electrodeposition

The electrolytic cell was connected to a potentiostat for electrodeposition. A cathodic or anodic current was applied for a certain duration in the form of a constant current or pulse current. The electrolyte was stirred or sonicated at the same time. The samples were rinsed with DI water and some were annealed in a furnace to improve the electrochemical performance. To determine mass loading of the catalyst, the sample was dried in a vacuum oven at 60°C for several hours before electrodeposition and weighed. The same sample was weighed again after electrodeposition and vacuum drying. The mass loading values presented in this thesis are the average of several samples. A GDL with a catalyst deposit was then ready for electrochemical tests as the air electrode.

2.4.2 Materials characterization techniques

2.4.2.1 Morphology and composition (SEM, TEM, EDX, STEM)

The morphology and composition of electrodeposited films were examined by scanning electron microscopy (SEM), transmission electron microscopy (TEM) and energy dispersive X-ray (EDX) spectroscopy. SEM samples were prepared by attaching the electrode to conductive carbon tape or copper tape and then mounting on an aluminum stub. No carbon or gold coating was applied to samples. An acceleration voltage of 5-20 kV was used in the SEM. For TEM analysis, part of the catalyst layer was scraped from the GDL and then dispersed in ethanol by sonication. One or two drops of the suspension were placed on a copper supported carbon grid for observation in the TEM. Point analysis, line scans and maps were used in the EDX analysis. Multiple samples and regions were observed to confirm deposition uniformity. Only representative images and spectra are shown in the thesis. Scanning transmission electron microscopy (STEM) is essentially a hybrid of SEM and TEM, where images are formed by scanning the electron beam over the sample. In this study, STEM EDX analysis was used to generate X-ray maps of TEM samples for elements of interest.

2.4.2.2 Structure determination (XRD, electron diffraction)

The crystal structure of deposited catalysts films was studied by either X-ray diffraction (XRD) or electron diffraction in the TEM. For XRD analysis, Co Kα radiation (λ= 1.789 Å) was used. The d-spacing of a given lattice plane is related to the diffraction angle θ by the Bragg's law ($\lambda = 2d\sin\theta$). XRD patterns from the samples were then compared with standard powder diffraction cards for phase identification. Selected area electron diffraction (SAED) in the TEM was used to get more

detailed crystal structure of representative nanoparticles. SAED has much better spatial resolution than XRD.

2.4.2.3 Surface analysis (XPS, AES, RS)

X-ray photoelectron spectroscopy (XPS), Auger electron spectroscopy (AES) and Raman scattering spectroscopy (RS) were used to characterize the surfaces of the materials; all have small interaction volumes. XPS generally provides composition and valence state information for the elements, but cannot be used to analyze specific regions because of its poor spatial resolution. AES provides similar composition and valence state information as XPS. In addition, for a dedicated scanning Auger microscope (SAM), the electrons can be focused to a fine probe (<10 nm in diameter). The fine probe provides much better spatial resolution compared with XPS. Depth profiling can be done in both AES and XPS by using an ion beam to sputter away layers of atoms. RS is useful in differentiating different structures of metal oxides made up of the same elements, because Raman bands are very sensitive to coordination geometry and crystal symmetry.[179]

2.4.3 Electrochemical characterization

2.4.3.1 Half-cell electrochemical tests

Half-cell measurements were run in a 100 ml electrochemical cell (AKCELL1, Pine Instrument) with five ports. Three ports were used to mount a working electrode (WE), a reference electrode (RE) and a counter electrode (CE) with fixed distances between them. Oxygen or argon gas can be purged through the other ports into the electrolyte. The sample to be tested was always used as

the working electrode. The reference electrode was selected depending on the pH of the electrolyte in the tests. A Hg/HgO RE (0.098 vs. SHE at 25℃ in 1 M NaOH, CHI 152) was used in alkaline solutions, while a Hg/Hg_2SO_4 RE (0.640 V vs. SHE at 25℃ in saturated K_2SO_4, CHI 151) was used in neutral to acidic electrolytes. The RE was calibrated by comparing its open circuit voltage (OCV) with an Ag/AgCl RE (0.195 vs. SHE at 25℃ in 3 M NaCl, 012167 RE-1B) before use. The Ag/AgCl RE was calibrated to a standard hydrogen electrode (SHE) before use. The counter electrode was a coiled platinum wire mounted on an epoxy rod (AFCTR5, Pine Instrument). The Pt wire (99.99% pure) has an outside diameter of 0.5 mm and surface area of 4.7 cm^2.

A typical half-cell test was subjected to a 30 min gas purge to saturate the electrolyte with oxygen or remove O_2 (purge Ar). The purpose of purging oxygen is to ensure all the ORR/OER measurements are implemented with the same oxygen concentration for comparison. An oxygen saturated electrolyte sets the equilibrium potential of ORR/OER as well, making it possible to calculate the overpotential for the reactions. The overpotential η is defined by subtracting the equilibrium potential (E) and IR drop from measured potential ($E_{measured}$).

$$\eta = E_{measured} - E - IR \tag{2-41}$$

The equilibrium potential at different pH is calculated according to the Nernst equation:

$$E = E^0 - \frac{RT}{nF} \ln \frac{a_{Red}}{a_{Ox}} \tag{2-42}$$

E^0 is the standard equilibrium potential, R is the gas constant (8.31 J mol^{-1} K^{-1}), T is temperature (K), n is the number of electrons exchanged in the reaction and F is the Faraday constant (96485 C mol^{-1}). a_{Red} is the chemical activity of the reduced species and a_{Ox} is the chemical activity of the oxidized form, which are measured against the standard state (solute: 1 mol L^{-1}; gases: 1 atm).

At 298 K,

$$E = E^0 - \frac{0.0591}{n} \log \frac{a_{\mathrm{Red}}}{a_{Ox}} \tag{2-43}$$

For ORR/OER in an acidic electrolyte, E^0=1.229 V vs. SHE, for the following reaction:

$$\mathrm{O_2} + 4\mathrm{H^+} + 4\mathrm{e^-} \rightarrow 2\mathrm{H_2O} \tag{2-44}$$

The equilibrium potential for ORR/OER is determined by the pH of the electrolyte:[180, 181]

$$E = 1.229 - \frac{0.0591}{4} \log \frac{\left[a_{\mathrm{H_2O}}\right]^2}{p_{O2}\left[a_{\mathrm{H^+}}\right]^4} = 1.229\text{-}0.0591 \times \mathrm{pH} + 0.00147 \log p_{O2} \tag{2-45}$$

In an ORR/OER test, the entire electrolytic cell including the electrolyte is saturated by purging with pure oxygen at ~1 atm pressure (P_{O2} = 1 atm).[182, 183] In 1 M KOH electrolyte (pH=14), E=1.229 - 0.0591×14 = 0.401 V vs. SHE.[12]

Electrochemical measurements in the half-cell were performed using a Bio-logic SP-300 or VSP potentiostat with EC-lab software. Electrochemical impedance spectroscopy (EIS), cyclic voltammetry (CV), linear sweep voltammetry (LSV) and chronopotentiometry were used to characterize the performance of the catalysts. EIS was run under two different modes in this study. EIS was used to measure the ohmic resistance when measured under OCV mode. The value of the ohmic resistance was used to confirm the correct connection of the setup or to apply an IR drop correction for other voltammetry methods. EIS can also be used to demonstrate the charge transfer resistance or interfacial resistance by applying a certain potential (potentiostatic mode). The values of these resistances can be obtained by fitting EIS spectra with an equivalent circuit using Z-Fit software (Bio-logic). In a CV test, the working electrode potential is changed linearly with time,

until it reaches a designated point and the potential is varied in the opposite direction. The current resulting from the potential sweep is measured by the potentiostat and provides information about the electrochemical reactions, such as the redox potential of electroactive species.

LSV techniques are similar to CV but only scan in either the cathodic or anodic direction; no backward scan is done. In addition, the scan rate of LSV (e.g., 5 mV s^{-1}) is much slower than for CV (20 mV s^{-1}) to ensure a quasi-steady state measurement in the polarization process. The double-layer capacitance charging current (capacitive current or non-Faradaic current) is minimized in such a test so that a more precise Faradaic current from the electrochemical reaction can be detected and compared among different catalysts. The steady-state measurements obtained by LSV can be used to determine the redox potential and kinetic parameters. Tafel plots (η vs. logi), which are a measurement of electrocatalytic activity, were determined from the LSV curve in this study.

Chronopotentiometry is a technique in which the current is controlled and the potential is measured as a function of time. The potential plateaus obtained from this test reflect the redox potential of electroactive species. In this study, the measured potential ($E_{measured}$) was used to calculate the overpotential η of ORR/OER as shown in Section 2.4.3.1 and to test the durability of catalysts in long-term electrochemical reactions. Electrochemical tests were repeated at least 3 times to ensure stable and repeatable results.

2.4.3.2 Full cell (battery) electrochemical tests

A vertical two-electrode Zn-air battery is shown in Fig. 2-7 and is used in Chapters 3, 4 and 5. The air electrode prepared in Section 2.4.1 was assembled into this cell to run battery tests. The catalyst side of the air electrode contacts the KOH electrolyte directly. The other side faces the air (or

oxygen) to allow diffusion into the cell. 10 mL of electrolyte was added to the cell from the top opening. The electrolyte was 6 M KOH + 0.25 M ZnO. A commercial separator was sandwiched between two Ni plates and inserted between the air and Zn electrode, which were connected to the working electrode and counter electrode of a potentiostat, respectively. The separator (Celgard 5550) is a laminated polypropylene membrane with a thickness of 110 μm and a porosity of 55%. The cell was first tested by EIS techniques at OCV condition to confirm correct connections. Then galvanodynamic polarization, rate discharge-charge tests and galvanostatic discharge-recharge cycling were performed. In galvanodynamic polarization, the applied current, either cathodic or anodic, is scanned from 0 to 100 mA cm^{-2} at a scan rate of 1 mA s^{-1}. The cell potential was monitored and recorded for different electrodes. Rate discharge-charge tests were run at increasing current densities (e.g., 2/5/10/20 mA cm^{-2}) for 10 min each to assess the cell potential at different current densities. The discharge-charge cycling efficiency is calculated by dividing the discharge potential by the charge potential. The efficiency is calculated by the following equation:

$$\text{Efficiency} = \int_{t1}^{t2} E(t)_{discharge} I_{discharge} dt \,/\, \int_{t3}^{t4} E(t)_{charge} I_{charge} dt \tag{2-46}$$

Because the galvanostatic discharge-charge process has equal periods, i.e., $I_{discharge} = I_{charge}$ and $t_2 - t_1 = t_4 - t_3$, then:

$$\text{Efficiency} = \int_{t1}^{t2} E(t)_{discharge} dt \,/\, \int_{t3}^{t4} E(t)_{charge} dt \tag{2-47}$$

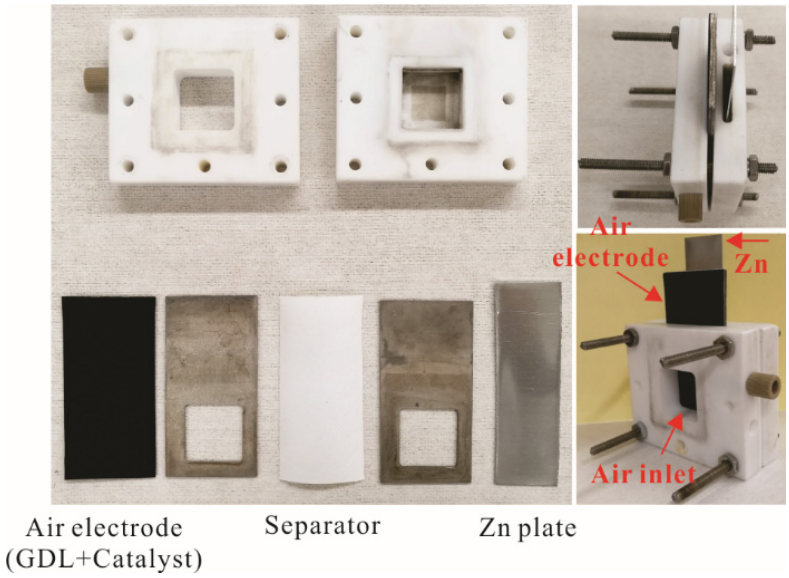

Fig. 2-7. Structure of a vertical Zn-air battery.

Unlike conventional batteries like Li-ion batteries, the charging and discharging processes for Zn-air batteries have different requirements for the electrodes. The discharge process is driven by the ORR and requires an air electrode that is not flooded by the electrolyte. The charging process (OER), on the other hand, is more favored when the electrode is submerged in the electrolyte. In addition, the ORR active sites at the electrode can be damaged by the oxidation potential of the OER process. Therefore, a design with physically decoupled electrodes for discharge and charge can avoid these adverse effects. This approach also allows for more flexibility to optimize ORR and OER electrocatalysts individually. A horizontal tri-electrode Zn-air battery with separate ORR and OER electrodes was designed and is presented in Chapter 6.

2.5 Summary

In this chapter, the reaction mechanisms for rechargeable Zn-air batteries were discussed. An in-depth analysis of the major problems that affect the electrochemical performance, along with their solutions, were covered. Different catalysts and fabrication methods for the air electrode were compared. Electrodeposition was found to be a good way of preparing air electrodes with active catalysts. The mechanisms for cathodic and anodic electrodeposition, as well as their limitations, were presented. The experimental methods including materials fabrication, characterization and electrochemical tests were summarized. In summary, the following problems should be solved for the development of rechargeable Zn-air batteries:

(1) ORR and/or OER active catalysts based on non-precious materials should be synthesized in an easy and cost-effective way.

(2) The catalysts should be combined at the air electrode via a simple method and show stable performance during battery testing.

(3) The structure of the Zn-air battery must be optimized for the best working conditions of electrodes.

Problems (1) and (2) are addressed by electrodepositing transition metal oxide catalysts directly on the GDL (Chapters 3, 4 and 5). Problem (3) is addressed by using a tri-electrode setup and depositing ORR and OER catalysts onto different substrates (Chapter 6).

Chapter 3 : Electrodeposited Co-Fe as an oxygen evolution catalyst for rechargeable Zn-air batteries

A version of this Chapter has been published in Electrochemistry Communications:

M. Xiong, D.G. Ivey, Electrodeposited Co-Fe as an oxygen evolution catalyst for rechargeable Zn-air batteries, *Electrochemistry Communications*, 75 (2017) 73-77. (10.1016/j.elecom.2016.12.018)

Graphical abstract

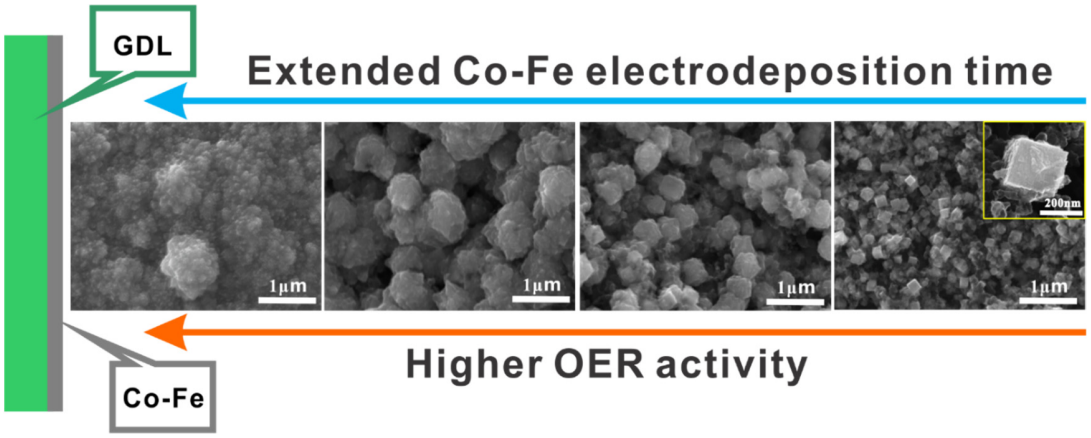

3.1 Introduction

Rechargeable Zn-air batteries are promising candidates as grid-scale energy storage devices due to their high theoretical energy density and low cost.[184-187] The efficiency of the discharge-charge cycle is largely dependent on OER catalysts at the air electrode.[188, 189] Precious metals like Ru and Ir are two of the most efficient OER catalysts,[107] but their scarcity has limited their use for large-

scale applications. Transition metal-based (Co and Fe) OER catalysts have been developed to replace noble metals, because of their low cost and high stability in alkaline solutions.[190-192] It has been reported that OER activity of Ni or Co-based catalysts can be greatly improved by doping with Fe.[193, 194] However, synthesis of these catalysts typically requires complex procedures like hydrothermal methods or high temperature annealing. In addition, conductive additives like carbon black are usually needed to improve the electronic conductivity. Polymer binders like PTFE or Nafion are needed to help combine the catalysts onto the electrode. These steps add extra cost and impair the practicality of the technology. Therefore, it is imperative to find a more efficient way to fabricate and coat catalysts onto the air electrode.

Herein, galvanostatic electrodeposition is used to produce and coat Co-Fe OER catalysts on the air electrode of a Zn-air battery in one step. The electrochemical performance is investigated and compared with commercial Pt/Ru catalysts. Electrodeposited Co-Fe is a body-centered cubic (bcc) solid solution with an oxidized surface that exhibits high catalytic activity for OER and excellent durability in battery environments. The fabrication conditions are easy to control and are scalable.

3.2 Experimental

3.2.1. Electrodeposition of Co-Fe on carbon paper

All the reagents were certified ACS grade. The GDL (SGL 35DC) was used as the substrate for Co-Fe electrodeposition. Electrodeposition was performed in a two-electrode configuration, with GDL (5 cm^2) and Pt mesh as the working electrode and the counter electrode, respectively. Co-Fe was cathodically electrodeposited on the GDL surface in an electrolyte containing $CoSO_4$ (0.15 M), $FeSO_4$ (0.05 M), sodium citrate (0.2 M), boric acid (0.2 M - buffering agent), L-ascorbic acid

(0.05 M - antioxidant) and sodium dodecyl sulfate (400 mg L^{-1} - surfactant). A constant current of 150 mA was applied for electrodeposition at room temperature. Samples were rinsed with water after electrodeposition and then dried in air. Mass loading of Co-Fe on GDL was calculated by measuring the weight before and after electrodeposition. Mass loadings of Co-Fe on GDL were 0.2, 0.4, 0.9, 1.7 and 3.2 mg cm^{-2} for 1, 2, 4, 8 and 16 min deposition times, respectively.

3.2.2. Materials characterization

The structure and composition of the samples were characterized by SEM (Tescan VEGA3 and Zeiss Sigma) and TEM (JEOL JEM-2010), along with EDX spectroscopy. The crystal structure was examined using XRD (Rigaku Ultima IV) with Co Kα radiation (λ= 1.789 Å).

3.2.3. Electrochemical measurements

LSV, chronopotentiometric measurements and CV were carried out in 1 M KOH using a potentiostat with a three-electrode configuration. The Co-Fe coated GDL, Hg/HgO and Pt mesh were used as the working electrode, the reference electrode and the counter electrode, respectively. All potentials in this study are relative to Hg/HgO unless otherwise indicated. All potentials were IR-compensated with the ohmic resistance (R_s) measured by EIS; typically R_s= 3-5 Ω. The electrolyte was agitated with a stir bar below the working electrode and the electrolyte was purged with pure O_2 gas to fix the reversible oxygen potential in all experiments.[195] The current densities were normalized to the geometric surface area. The overpotential (η) of OER was calculated from the following equation: η = E(vs. Hg/HgO) – IR – 0.303 V.[196] For comparison, a Pt/Ru catalyst ink was sprayed onto other GDL samples. The ink consisted of 50 mg of Pt/Ru powder (30% Pt and

15% Ru on carbon black, Alfa Aesar) dispersed in 2.0 mL of de-ionized water, 1.0 ml of isopropanol, 0.1 ml of 5 wt% Nafion (D-521) and 0.2 mL of 10 wt% PTFE binder (DISP30). The mass loading of the Pt/Ru ink on GDL was about 1.2 mg cm^{-2} after drying in a furnace.

3.2.4. Battery testing

Zinc-air battery tests were performed in a home-made cell, which is shown in Fig. 2-7. Briefly, Zn foil and the catalyst loaded GDL were used as the anode and the air electrode, respectively. The battery discharge and charge voltages were measured galvanostatically for 10 min at different current densities of 1, 2, 5 and 10 mA cm^{-2}. Discharge-charge cycling was done using a current density of 5 mA cm^{-2} with each cycle consisting of 30 min discharge followed by 30 min charge. Battery tests were performed in ambient air.

3.3 Results and discussion

SEM images of Co-Fe catalysts prepared for different deposition times are shown in Fig. 3-1(a)-(d) and in the supporting information (Fig. S3-4). The 1 min deposition sample features cuboidal particles that merge into the porous graphite substrate. The nanocube facets have a terraced structure (inset of Fig. 3-1(a)) and a diameter of 100-200 nm. Similar Co-Fe nanocubes have been electrodeposited previously on a flat glassy carbon surface by chronoamperometry, but showed smooth surfaces[197]. The 1 min Co-Fe deposition on gold (Au)-coated silicon (Si) wafers under the same conditions shows a different morphology compared with the one deposited on GDL (Fig. S3-5). Therefore, the carbon paper substrate has an influence on the generation of nanocubes.

The Co-Fe cuboids were further investigated by TEM; one such particle is shown in Fig. 3-1(e) attached to carbon from the substrate. A representative selected area electron diffraction (SAED) pattern (inset of Fig. 3-1(e)) reveals that each particle is a single crystal and the pattern was indexed to the bcc Co-Fe solid solution. The zone axis is [001], which indicates that the facets are {100} planes. The faint rings in the SAED pattern are from the carbon in the substrate (indexed to graphite). As the deposition time is increased, the Co-Fe nanoparticles grow in size and finally form a continuous film at 8 min (Fig. 3-1(b)-(d)). Single crystal, cuboidal deposits, with a bcc crystal structure, were also obtained for a 2 min deposition time (Fig. S3-6).

The crystal structure of the Co-Fe deposit was further studied by XRD (Fig. 3-1(f)). For the 1 min deposit, the peak at 52.90° corresponds to the (110) plane of bcc Co-Fe solid solution. The (110) peak shifts to slightly lower angles for longer deposition times, reaching 52.74° for the 4 min and 8 min deposits. A smaller diffraction angle corresponds to a larger d-spacing and lattice parameter. The increase in d-spacing for longer deposition suggests an increase in the amount of Fe, since Fe has a larger atomic radius than Co.[198] The deposit composition can be calculated from the Vegard equation, showing 30.3% of Fe in Co-Fe for the 1 min deposition time and 39.4% of Fe for longer deposition times. EDX spectra also showed a significant oxygen peak providing evidence for oxide formation, which likely occurred during electrodeposition and/or from exposure to the atmosphere after deposition.[199-201] In addition, the anodic process during OER will oxidize Co-Fe. As such, it is the oxidized surface of the Co-Fe particles that provides the active sites to catalyze OER.[98, 202] The metal interior provides high electronic conductivity for fast electron transfer between the substrate and surface OER active sites.[203]

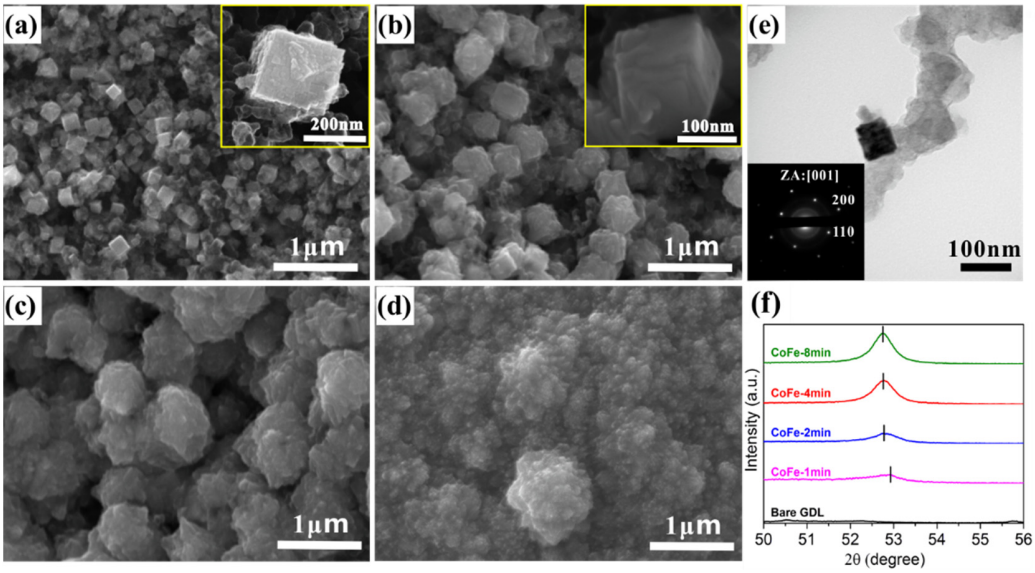

Fig. 3-1. SEM secondary electron (SE) images of Co-Fe prepared for different deposition times: (a) 1 min, (b) 2 min, (c) 4 min and (d) 8 min. (e) TEM bright field image and diffraction pattern (inset) of Co-Fe after 1 min deposition time. (f) XRD patterns of Co-Fe for different deposition times (magnified patterns).

LSV curves are shown in Fig. 3-2(a). The bare GDL substrate has negligible OER activity. However, GDL with electrodeposited Co-Fe has considerably higher OER current, which increases with increasing deposition time until 8 min. The higher OER activity is related to better coverage of the substrate (Fig. 3-1) and higher mass loading. After 8 min, the OER activity decreases due to a reduction in available active surface to the electrolyte. The CoFe-16 min film is quit dense and has reduced porosity. A layer of insulating $FeOOH/Fe(OH)_3$ was generated on the surface of the 16 min Co-Fe deposit, possibly due to the oxidation from soluble Fe^{2+} to insoluble Fe^{3+} during the long time electrodeposition (A detailed discussion is provided in Chapter 4). Co-Fe exhibits inferior OER activity in terms of onset potential and current density compared with the commercial Pt/Ru catalyst. Tafel plots are given in Fig. 3-2(b); Tafel slopes from 38.8 to 53.8 mV dec^{-1} were obtained for samples with different deposition times. Similar Tafel slopes

ranging from 33 to 67 mV dec^{-1} for transition metal-based OER catalysts have been reported in literature, where low Tafel slopes were attributed to high electronic conductivity or high electrochemically active surface areas.[204, 205] The increase in Tafel slope may be due to increased electron transport resistance or a change in the surface hydration state of the deposited film.[206, 207] Pt/Ru has a Tafel slope of 57.0 mV dec^{-1}, which is higher than the values for all the Co-Fe deposits. The surface defects (terraces) on Co-Fe (Fig. 3-1(a)) may facilitate OER by providing numerous active sites.[208]

The overpotential applied to reach a 10 mA cm^{-2} current density is presented in Fig. 3-2(c). For the 8 min deposit, the overpotential is ~0.29 V, which is higher than the 0.25 V value for Pt/Ru. However, this overpotential is comparable or even lower than those recently reported for Co-based OER catalysts.[95, 209] The durability of the OER catalysts in an alkaline solution was investigated by chronopotentiometric testing at 10 mA cm^{-2} for 20 h (inset of Fig. 3-2(c)). The overpotential for Pt/Ru increased from 0.248 to 0.279 V, or by 12.5%. In contrast, the overpotential rose from 0.309 to 0.335 V, or by 8.4%, for the 4 min deposit and rose from 0.282 to 0.295 V, or by 4.6%, for the 8 min deposit. The overpotential for the 8 min sample is only 0.016 V higher than that for Pt/Ru at the end of the test, indicating that Co-Fe exhibits good stability in alkaline media.

Since the catalyst is to be used in a Zn-air battery, it must be stable during both the charge and discharge processes, corresponding to the OER and ORR process, respectively. Therefore, the catalysts were cycled from the potential range of ORR (-0.25 V) to the potential range of OER (0.7 V) at a scan rate of 20 mV s^{-1} (Fig. 3-2(d)). Pt/Ru shows a much higher ORR current than Co-Fe, since it contains the well-known ORR catalyst Pt. Pt/Ru also has a lower onset potential than Co-Fe when scanning towards the OER operating range. However, the 8 min Co-Fe deposit has the same current density as Pt/Ru at 0.7 V. LSV curves after 50 CV cycles were acquired to assess

cyclic stability (inset of Fig. 3-2(a)). The OER current density at 0.7 V decreased by 25.8%, 37.9%, 23.3%, 5.4% and 7.4% for the 1, 2, 4 and 8 min Co-Fe deposits and Pt/Ru, respectively. Therefore, the 8 min sample has the best cycling stability among all the samples. The CV curves for the Co-Fe catalysts exhibit strong Co^{2+}/Co^{3+} redox peaks at 0.13 V and 0.25 V (Fig. 3-2(d)) that increase in intensity with increasing deposition time.[98] The increased voltammetric charge indicated by the stronger redox peaks may be responsible for the higher OER activity, since they are indicative of electrochemically active surfaces.[194]

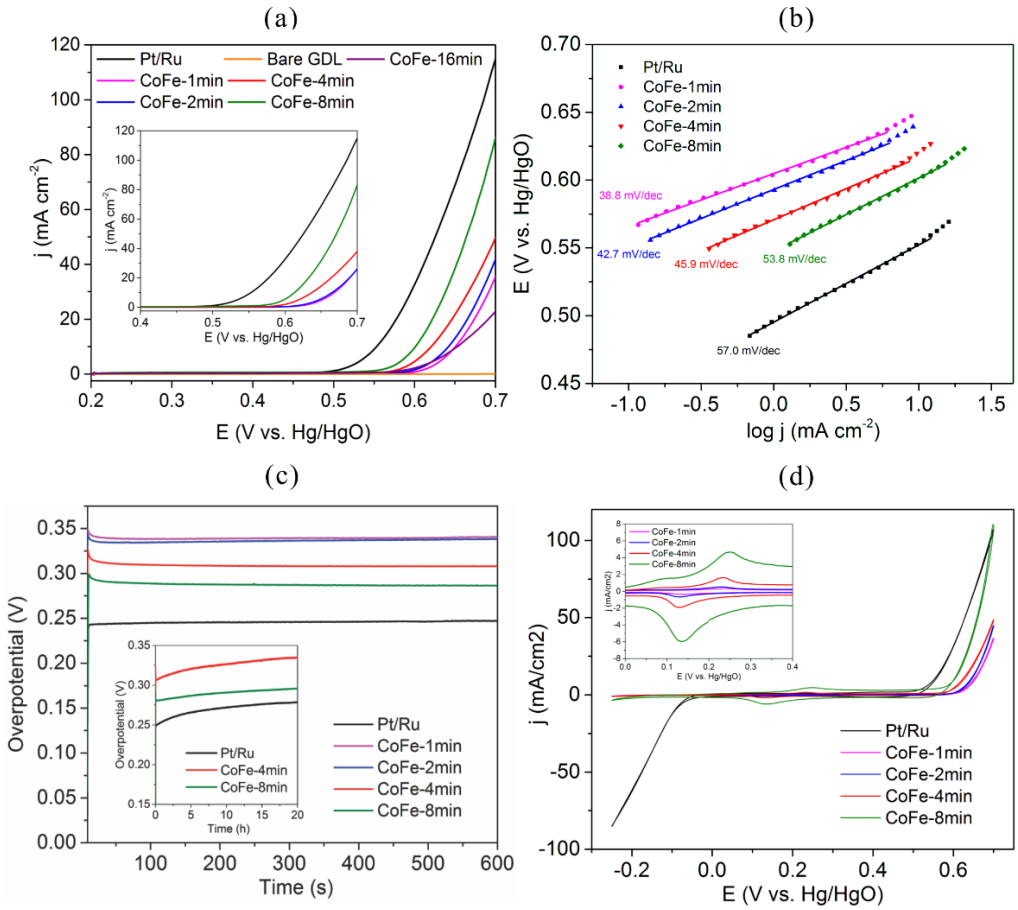

Fig. 3-2. (a) LSV plots for catalysts at a scan rate of 5 mV s^{-1} (inset: LSV plots after 50 cycles of CV testing). (b) Tafel plots derived from (a). (c) Chronopotentiometric measurements at 10 mA cm^{-2} (inset: long term stability tests). (d) CV curves for catalysts at a scan rate of 20 mV s^{-1} (inset: magnified plots for the 0.0 to 0.4 potential range).

The Co-Fe coated GDL was assembled into a Zn-air battery as the air electrode for evaluation and the performance was compared with that of Pt/Ru loaded GDL. Fig. 3-3(a) shows the discharge and charge profiles of the Zn-air battery at different current densities. Only the 4 and 8 min Co-Fe deposits were tested, since they have much higher OER activity than the 1 and 2 min deposits. The discharge voltage of Pt/Ru is higher than that for Co-Fe due to the presence of ORR active Pt. However, the gap between their charge potentials is not that significant. At 10 mA cm^{-2}, the charge potential of the 8 min Co-Fe deposit is almost the same as that for Pt/Ru. From this point forward, E vs. Zn/Zn^{2+} is used to represent the cell potential of Zn-air batteries.

Fig. 3-3(b) presents the cycling performance of Pt/Ru and Co-Fe at a current density of 5 mA cm^{-2} for 20 h using ambient air to supply O_2. Pt/Ru has better initial performance (first several cycles); however, Pt/Ru shows noticeable degradation in discharge performance due to the long-term instability (e.g., Pt agglomeration and oxidation) of Pt/C during ORR and OER.[210] Pt/Ru discharges at almost the same potential as Co-Fe after 8 cycles. The charge potential difference between Co-Fe and Pt/Ru is negligible, leading to the same discharge-charge efficiency. In contrast, Co-Fe exhibits better cycling stability in the Zn-air battery by exhibiting a consistent voltage curve. In addition, Co-Fe deposits did not delaminate from the substrate and the morphology did not change after cycling (confirmed by SEM, Fig. S3-7). Thus, electrodeposited Co-Fe is a stable catalyst with comparable performance to Pt/Ru for Zn-air batteries.

(a) (b)

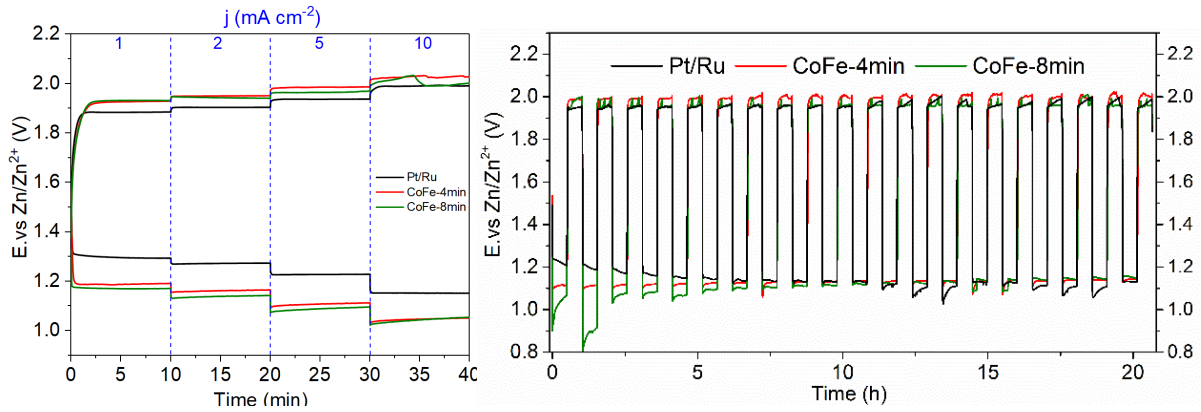

Fig. 3-3. (a) Rate discharge-recharge curves for Zn-air batteries at different current densities. (b) Galvanostatic cycling test of Zn-air batteries at a current density of 5 mA cm^{-2}.

3.4 Summary

Co-Fe OER nanocuboidal catalysts for the air electrode were fabricated by electrodeposition. The OER catalytic capacity was evaluated in alkaline media and compared with commercial Pt/Ru catalysts. Co-Fe deposits exhibited low Tafel slopes, high durability and low overpotential (0.29 V at 10 mA cm^{-2}). The Co-Fe catalysts were tested in a Zn-air battery and showed similar cycling efficiency, but better cycling stability, compared with Pt/Ru.

3.5 Supporting information

Influence of the deposition time on the morphology of electrodeposited CoFe

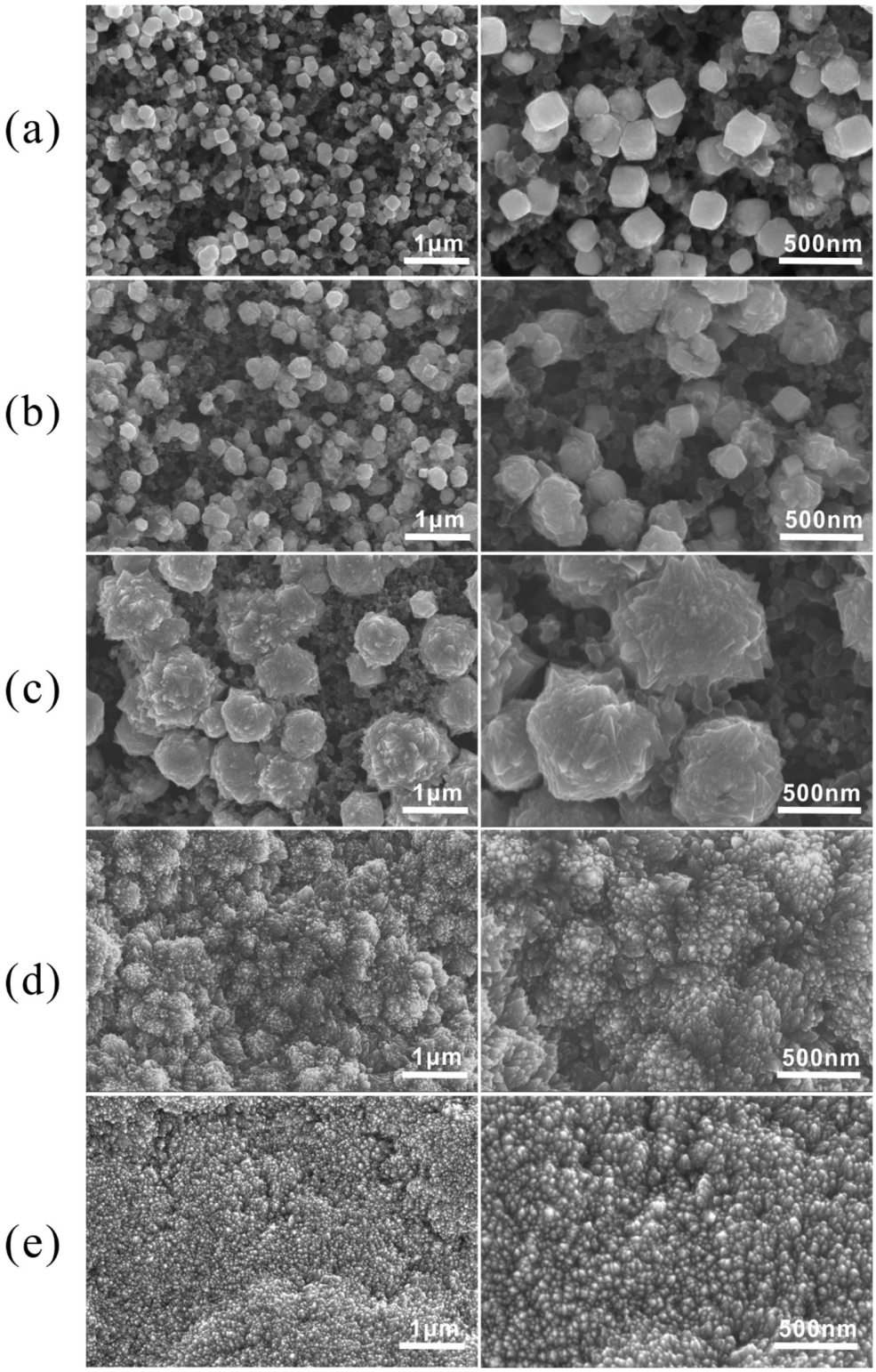

Fig. S3-4. FESEM SE images of Co-Fe electrodeposited for different deposition times: (a) 1 min, (b) 2 min, (c) 4 min, (d) 8 min and (e) 16 min.

Influence of the substrate on the morphology of electrodeposited CoFe-1min

CoFe was electrodeposited on Au-coated Si wafer to investigate the influence of the substrate on deposit morphology. The deposition was performed using the same electrolyte and current density. Fig. S3-5 shows that a 1 min deposition did not create the same nanocubes on surface of the Au-coated Si wafer as the same deposition condition for GDL (CoFe-1min, Fig. 3-1(a)). Therefore, the carbon paper substrate has an influence on the generation of nanocubes.

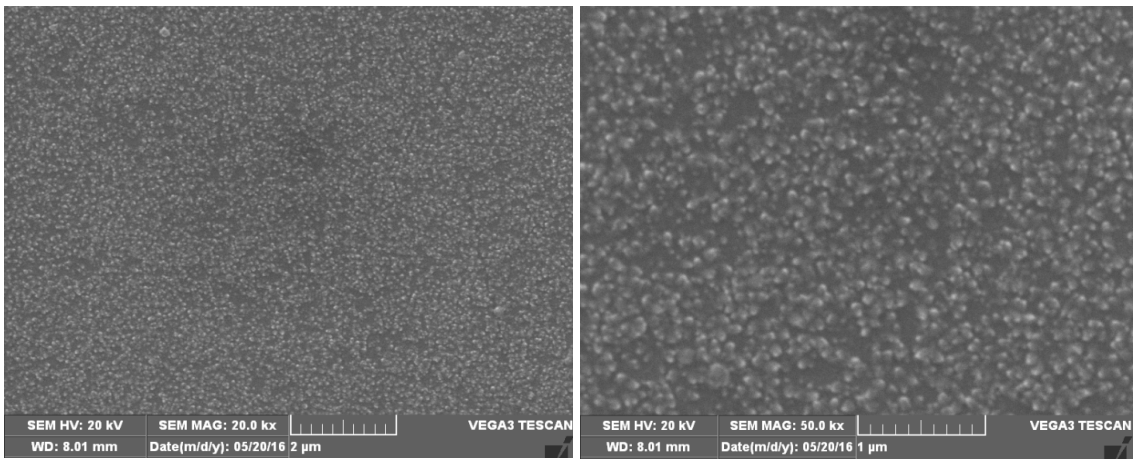

Fig. S3-5. SEM SE images of Co-Fe electrodeposited on an Au coated Si wafer at a current of 150 mA for 1 min.

TEM images of CoFe-2min

Single crystal, cuboidal deposits, with a bcc crystal structure, were also obtained for a 2 min deposition time (Fig. S3-6).

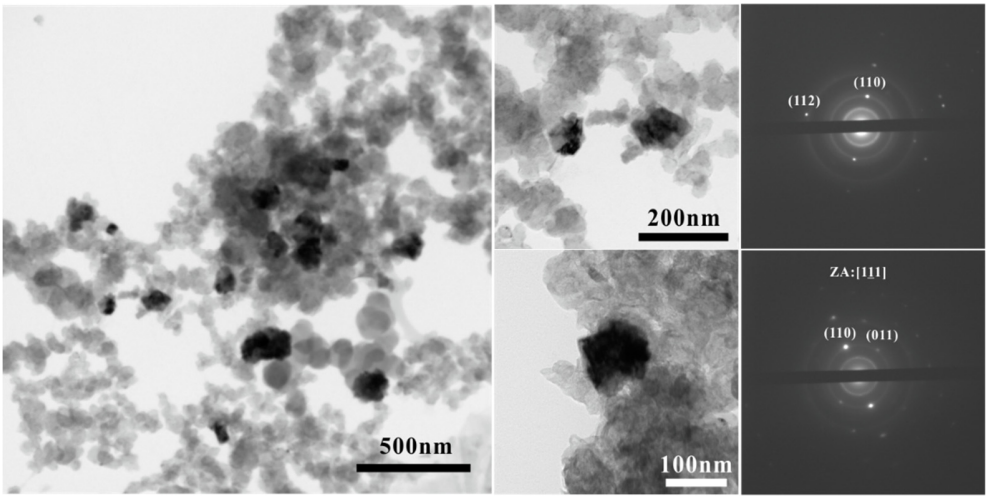

Fig. S3-6. TEM bright field images and SAED patterns of CoFe-2min deposit showing that the particles are single crystals. The faint rings in the SAED patterns are from the carbon substrate.

CoFe-4min morphology change after battery cycling

The CoFe-4min electrode was examined by SEM to investigate any morphology change after battery cycling. Fig. S3-7 shows that Co-Fe deposits did not peel away from the substrate and the morphology did not change after cycling.

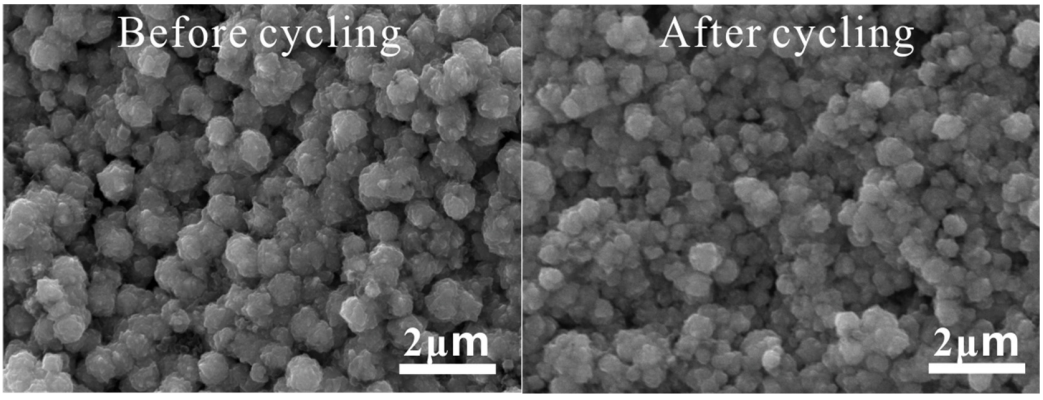

Fig. S3-7. SEM SE images of the CoFe-4min samples before and after the battery cycling test shown in Fig. 3-3(b).

Chapter 4 : Composition effects of electrodeposited Co-Fe as electrocatalysts for the oxygen evolution reaction

A version of this Chapter has been published in Electrochimica Acta:

M. Xiong, D.G. Ivey, Composition effects of electrodeposited Co-Fe as electrocatalysts for the oxygen evolution reaction, *Electrochimica Acta*, 260 (2017) 872-881. (10.1016/j.electacta.2017.12.059)

4.1 Introduction

The OER plays an important role in rechargeable metal-air batteries and water splitting processes.[211-213] Noble metal-based catalysts like IrO_2 and RuO_2 are too expensive for large-scale applications. Therefore, catalysts based on first-row transition metals, especially Ni, Co and Fe, have been developed as inexpensive replacements.[214-218] Among them, Co-Fe based OER catalysts have received significant attention due to their high OER activity and stability in alkaline solutions [219, 220]. There are several ways to fabricate Co-Fe based catalysts. $CoFe_2O_4$ and Co-Fe layered double hydroxide nanosheets can be synthesized by hydrothermal methods.[221, 222] Sol-gel methods and thermal decomposition can also be adopted to prepare binary Co-Fe OER catalysts.[190, 223-225] Electrodeposition is a simple and effective way to directly grow the active material on current collectors without any additives like binders and conductive agents. Either Co-Fe (oxy)hydroxide ((Co,Fe)OOH) or Co-Fe alloys can be deposited onto a conductive substrate by cathodic electrodeposition.[193, 226, 227]. The Co/Fe ratio can influence the OER performance of (Co,Fe)OOH; Fe tends to act as the primary active sites, while CoOOH provides an electronically conductive frame.[193] In addition, Co-Fe oxyhydroxide experiences structural changes during long-term

stability testing. In our work in Chapter 3, a Co-Fe alloy in the form of a solid solution ($Co_{0.7}Fe_{0.3}$) with an oxidized surface was electrodeposited from an electrolyte of fixed composition onto carbon paper for use in a Zn-air battery as the OER catalyst.[228] The OER activity of the Co-Fe alloy increased with increasing deposition time (for the fixed alloy composition) and the deposited Co-Fe exhibited excellent stability after various electrochemical tests.

Other factors, such as deposit Co/Fe ratio, may also have an impact on the electrochemical properties. It has been revealed that adsorption of OH^- on CoOOH is weak and can be enhanced by Fe-doping to facilitate the OER process.[223] Electrodeposited Co-Fe alloys with different bulk Co/Fe ratios have been compared in terms of OER activity, with $Co_{0.67}Fe_{0.33}$ showing much better OER activity than either $Co_{0.33}Fe_{0.67}$ and $Co_{0.25}Fe_{0.75}$.[227] However, OER activity may not be directly related to the bulk composition of the alloy, since OER occurs at the electrode-electrolyte interface. Both the surface and bulk regions of the catalyst particles can contribute to OER performance, especially for porous materials where small reacting species like OH^- ions can easily diffuse into the pores. The 'internal' and 'external' active surfaces are defined according to their accessibility to OH^- ions.[229] Inner surfaces, such as grain boundaries, pores, cracks, etc., may act as sources of bulk activity but are less accessible than external surfaces for OER processes. Co-Fe alloy catalysts are typically covered with an oxide or hydroxide layer, which is the primary location for OER rather than the bulk. Therefore, the surface composition is likely a more suitable indicator of catalyst OER performance.

In this study, the initial work done in Chapter 3 on electrodeposition of Co-Fe solid solutions on carbon paper is continued. In Chapter 3, a fixed composition ($Co_{0.7}Fe_{0.3}$) was deposited; here, different electrolyte compositions are explored so that deposits with a full range of compositions, from pure Co to pure Fe, are obtained. Deposits are characterized using XRD, electron microscopy

and Auger electron spectroscopy (AES). AES depth profiling is used to probe the composition of individual particles from the surface to the interior of the particles. Microstructural effects are correlated with OER activity through electrochemical measurements, such as LSV, chronopotentiometry, CV and EIS. Finally, the best candidates are tested in a Zn-air battery.

4.2 Experimental

4.2.1. Electrodeposition of Co-Fe on carbon paper

Teflon-coated porous carbon paper (GDL, SGL 39BC) was sectioned into 5 cm^2 pieces to be used as the substrate for electrodeposition at room temperature (25°C). Electrodeposition was performed in a two-electrode configuration, where the GDL and Pt mesh were used as the working electrode and the counter electrode, respectively. Co-Fe was cathodically electrodeposited on GDL at a constant current of 150 mA for 1 min. The solutions for Co-Fe deposition contained $CoSO_4$ and $FeSO_4$ with several different composition ratios ($CoSO_4$:$FeSO_4$ = 1, 3:1, 1:1, 1:3 and 0, with an overall $CoSO_4$+$FeSO_4$ concentration = 0.2 M). Sodium citrate (0.2 M), boric acid (0.2 M), L-ascorbic acid (0.05 M) and sodium dodecyl sulfate (400 mg L^{-1}) were added to the electrolytes to enhance the uniformity of the deposits and adhesion to the substrate. The samples are denoted in terms of the $CoSO_4$/$FeSO_4$ ratio in the electrolyte (e.g., Co-Fe-3-1 corresponds to $CoSO_4$:$FeSO_4$ = 3:1). The mass loading for all samples was measured using a balance (Mettler Toledo PB303-S) and was ~0.2 mg cm^{-2}. The current efficiency of electrodeposition is around 50% (Fig. S4-17).

4.2.2. Materials characterization

The microstructure and composition of the samples were characterized by SEM (Tescan VEGA3 and Zeiss Sigma SEMs operated at 10-20 kV) and TEM (JEOL 2010 TEM operated at 200 kV), along with EDX spectroscopy for both SEM and TEM. The crystalline state was examined by XRD (Rigaku Ultima IV) using Co Kα radiation (λ= 1.789 Å). AES (JEOL JAMP-9500F) was used for composition depth profiling of the samples. The scanning voltage and current were 15 kV and 8 nA, respectively. For depth profiling, samples were sputtered with Ar^+ at a sputtering voltage and current of 2 kV and 20 mA, respectively. The sputtering rate was calibrated as 5 nm/min using quartz samples. The atomic sensitivity factors for quantitative analysis of O, Fe and Co are 0.293, 0.252 and 0.362, respectively. The distribution of Fe, Co and O in the Co-Fe-3-1 particles in both the as-deposited condition and after OER testing was mapped out using EDX analysis in a TEM/STEM (JEOL ARM 200CF operated at 200 kV).

4.2.3. Electrochemical measurements

LSV, chronopotentiometric measurements and CV were carried out in 1 M KOH using a potentiostat with a three-electrode configuration. The catalyst-coated GDL, Hg/HgO (0.098 V vs. SHE) and Pt mesh were used as the working electrode, reference electrode and counter electrode, respectively. The electrolyte was agitated with a stir bar below the working electrode and the electrolyte was purged with pure O_2 gas. The current densities were normalized to the geometric surface area. All potentials reported are relative to Hg/HgO unless otherwise indicated and all potentials were IR-compensated (R_u= 3-5 Ω). The overpotential (η) of OER was calculated from the following equation: η = E (vs. Hg/HgO) – IR – 0.303 V. EIS was performed at 0.6 V vs. Hg/HgO with 10 mV AC potential from 100 kHz to 0.01 Hz.

4.2.4. Battery testing

Zn-air battery testing was done in a home-made cell with the same conditions reported in Chapter 3. Briefly, Zn foil and the catalyst loaded GDL were used as the anode and the air electrode, respectively. A microporous membrane (Celgard 5550) was used as the separator. Discharge-charge cycling was done using a current density of 5 mA cm^{-2} for each cycle. Battery tests were performed in ambient air.

4.3 Results and discussion

Fig. 4-1 shows SEM images of Co-Fe catalysts prepared from different solutions. The overall bulk deposit compositions in terms of the amount of Fe (determined by EDX analysis in the SEM) are shown in Table 4-1. For the Co-Fe solid solution alloys, the Fe composition relative to the total Fe and Co is 29.5 at%, 64.9 at% and 83.1 at% in Co-Fe-3-1, Co-Fe-1-1 and Co-Fe-1-3, respectively. Pure Co was electrodeposited as hexagonal crystals, while the other samples all had cuboidal shapes. According to the Co-Fe phase diagram, the stable form of pure Co is the hexagonal close-packed (hcp) crystal structure at room temperature. For the Co-Fe alloy compositions studied in this work and pure Fe, the body-centered cubic (bcc) structure is stable.[230] The Co-Fe samples have a terraced surface with tiny steps (less than 10 nm in size - Fig. 4-1(b), (c) and (d)), while the Fe nanocubes have relatively smooth facets (Fig. 4-1(e)). The facets for all the cuboidal particles (confirmed by TEM electron diffraction) correspond to the {100}-type planes of the bcc structure. All electrodeposited particles are embedded in the microporous layer of the GDL and have good contact with the carbon particles (shown by the yellow arrows in Fig. 4-1), facilitating charge transfer between the catalyst layer and the substrate. The electrodeposited Co/Fe layers on the 5

cm^2 electrodes are quite uniform, with pure Co exhibiting the best uniformity across the entire surface. The other samples had some small differences in particle density across the surface. To prevent any influence of particle density on OER tests, only the central 1 cm^2 area was used for electrochemical testing. The entire 5 cm^2 electrode, however, was used for Zn-air battery testing.

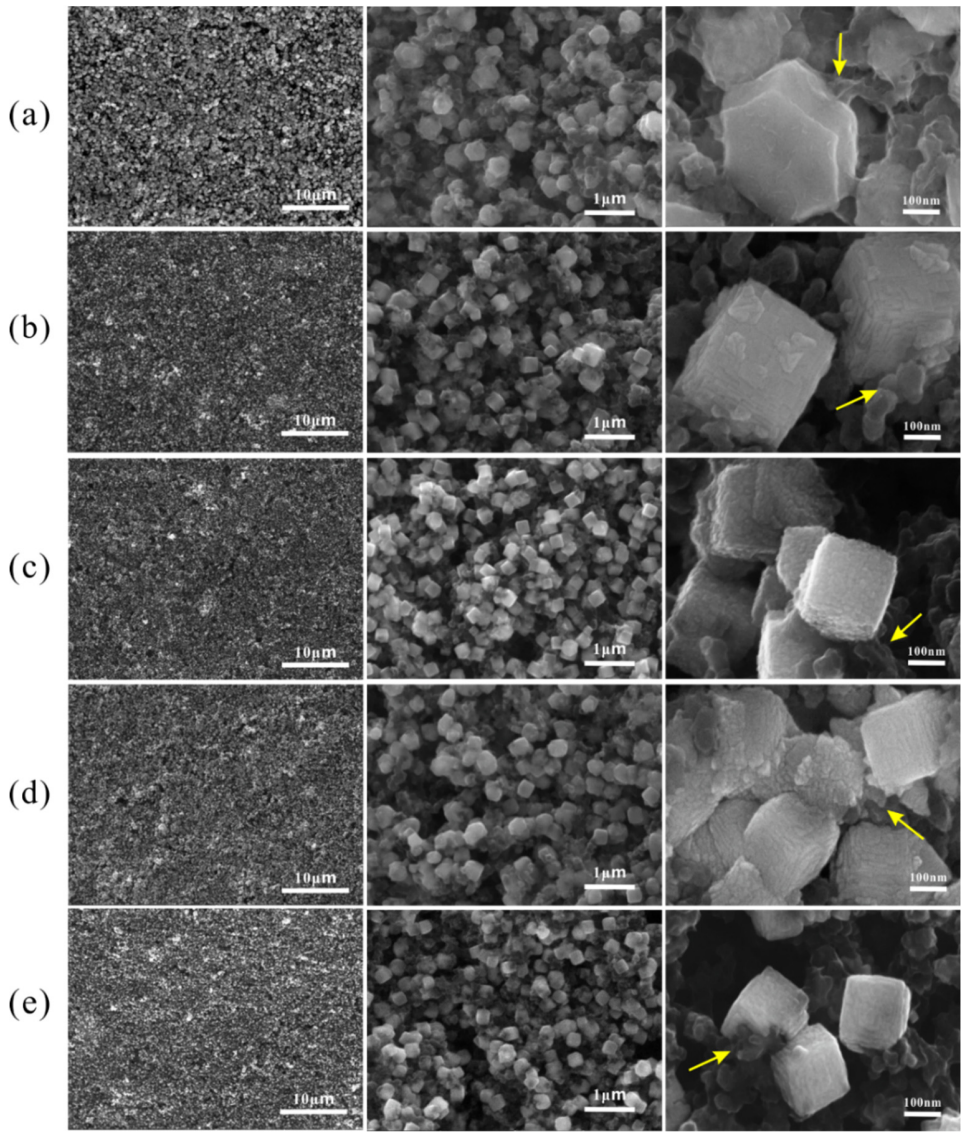

Fig. 4-1. SEM secondary electron (SE) images showing the morphology of Co-Fe catalysts on the air electrode: (a) Co; (b) Co-Fe-3-1; (c) Co-Fe-1-1; (d) Co-Fe-1-3; (e) Fe. Arrows indicate the graphite particles of the GDL.

Table 4-1. Property comparison for various Co-Fe samples

Properties	Description	Co	Co-Fe-3-1	Co-Fe-1-1	Co-Fe-1-3	Fe
Fe content (at%)- EDX	~1 μm depth	0	29.5	64.9	83.1	100
Fe content (at%)- Auger	1 nm depth	N/A	47.8	77.5	N/A	N/A
Fe content (at%)- XRD	Bulk, crystalline	0	30.0	60.0	N/A	100
j at 0.7 V ($mA\ cm^{-2}$)	More positive value (+) preferred	5.3	28.0	40.0	21.3	2.6
Δ j% after CV cycling	More positive value (+) preferred	-38.5	-33.9	-6.9	-7.0	-55.8
η at 10 mA cm^{-2} (V)	More negative value (-) preferred	0.42	0.35	0.33	0.36	0.41
Δ η% after 20 h OER	More negative value (-) preferred	N/A	11.2	7.2	4.1	N/A
Tafel slope (b/mV dec^{-1})	More negative value (-) preferred	67	46	37	37	39
j_0* ($A\ cm^{-2}$)	More positive value (+) preferred	5.8×10^{-9}	5.9×10^{-10}	9.4×10^{-12}	1.8×10^{-12}	2.3×10^{-13}
C_{dl} ($mF\ cm^{-2}$)	More positive value (+) preferred	10.4	4.5	4.5	1.4	0.7
R_s ($\Omega\ cm^2$)	More negative value (-) preferred	3.7	4.5	4.3	4.3	N/A
R_f ($\Omega\ cm^2$)	More negative value (-) preferred	1.2	1.0	1.1	2.7	N/A
R_{ct} ($\Omega\ cm^2$)	More negative value (-) preferred	92.1	23.3	15.8	44.3	N/A
Q_f ($m\Omega^{-1}\ s^n\ cm^{-2}$)		4.2 (n=0.51)	2.1 (n=0.64)	4.5 (n=0.53)	39.0 (n=0.30)	N/A
Q_{dl} ($m\Omega^{-1}\ s^n\ cm^{-2}$)		25.9 (n=0.93)	14.9 (n=0.93)	17.2 (n=0.94)	9.0 (n=0.96)	N/A

* These are estimated values from extrapolation.

Fig. 4-2(a) shows LSV curves for the different samples, as well as bare GDL. Pure Co and Fe have lower OER currents compared with all the alloys. Co-Fe-1-1 has the highest OER activity among the Co-Fe samples, even after 50 CV cycles from -0.25 V to 0.7 V (inset of Fig. 4-2(a)). The OER current at 0.7 V before and after CV cycling is plotted against Fe composition in the Co-Fe deposits (Fig. 4-2(b)). Co-Fe-1-1 and Co-Fe-1-3 have much lower degradation with cycling than the other three samples. Fig. 4-2(b) also demonstrates that the OER activity increases with increasing doping of Fe into Co up to 65 at% Fe (Co-Fe-1-1) and then declines at higher Fe concentrations. In previous studies, the optimal Fe content in Co-Fe (oxy)hydroxide for best OER performance was reported to be either 54 at% [193] or 35 at%.[231] The overpotential applied to reach a current density of 10 mA cm^{-2} is shown in Fig. 4-2(c) and exhibits the same trend as OER activity, with Co-Fe-1-1 having the lowest overpotential. The durability of the catalysts was assessed through chronopotentiometric testing at the same current density for 20 h (inset of Fig. 4-2(c)). A comparatively small overpotential rise occurred for Co-Fe-1-1 (7%) and Co-Fe-1-3 (4%).

Tafel plots derived from the LSV curves are given in Fig. 4-2(d). The Tafel slope for Co is the highest with a value of 67 mV dec^{-1}, but decreases considerably after alloying with Fe. The Tafel slopes for Co-Fe-3-1, Co-Fe-1-1 and Co-Fe-1-3 are 46, 37 and 37 mV dec^{-1}, respectively. These Tafel slopes are comparable to the values obtained for Co-Fe (oxy)hydroxide, which range from 30 to 70 mV dec^{-1}.[193, 231] The Tafel slope varies depending on the different mechanisms for OER and the adsorption of intermediates on the surface.[232, 233] A relative measure of the electrocatalyst activity cannot be made simply based on the Tafel slope, since their exchange current densities (j_0) are different. The j_0 values were calculated by extrapolating the Tafel plots to E= 0.303 V vs. Hg/HgO (η= 0) (Fig. 4-3) and the data is added to Table 4-1. It should be mentioned that the true exchange current densities can only be measured experimentally under equilibrium conditions and,

as such, the extrapolated exchange current densities are only estimates. The pure Co electrode has the highest j_0 value, 5.8×10^{-9} A cm^{-2}, which is similar to the values ranging from 0.2×10^{-9} A cm^{-2} to 4.7×10^{-9} A cm^{-2} reported for Co oxide OER catalysts.[234-236] The value of j_0 decreased after doping with Fe, which is similar to the trend reported for Fe-doped Ni electrocatalysts.[237] The Tafel plots for Co-Fe-1-3 and Fe shift to higher potentials and lower current densities relative to Co-Fe-1-1, even though they have the same slope. The lack of CoOOH, which provides a conductive framework, and the generation of an insulating FeOOH surface layer may be responsible for this effect in the high Fe-containing samples.[193]

Magnified CV curves are presented in Fig. 4-2(e) (complete curves are in Fig. 4-4). There is a redox couple for Co^{2+}/Co^{3+} at around 0.2 V for pure Co and Co-Fe-3-1 (29.5 at% Fe).[98] However, the anodic and cathodic peaks are at the same position for Co but are separated for Co-Fe-3-1. The peak-to-peak separation for Co-Fe-3-1 is $\Delta E_p = (E_p^{ox}-E_p^{red}) = 115$ mV, which is larger than the theoretical value of 59 mV (298 K) for an electrochemically reversible process.[238] Fig. 4-2(f) shows that the Co^{2+}/Co^{3+} redox peaks for Co-Fe-3-1 do not shift with increasing scan rate, meaning that the surface reaction is not kinetically limited. Therefore, the irreversibility of this surface reaction is dictated by the electronic properties of the Co^{2+}/Co^{3+} redox species in Co-Fe-3-1. The peak is suppressed and shifted for Co-Fe-1-1 (64.9 at% Fe) and Co-Fe-1-3 (83.1 at% Fe) due to stronger interaction between Co and Fe, as well as a much lower Co content in these materials.[193] For Co-Fe oxy-hydroxide, the disappearance of this redox peak happens at 80 at% Fe.[193] For the current work, the disappearance of the peak occurred at a lower concentration of ~65 at% Fe. CV cycling at various rates confirmed this difference between Co-Fe-3-1 and Co-Fe-1-1 (Fig. 4-2(f) and Fig. 4-5). The Co^{2+}/Co^{3+} peak faded after 49 cycles for Co and Co-Fe-3-1, while CV curves for other samples barely changed (Fig. 4-6). The peaks at ~0.55 V vs. Hg/HgO can be assigned to

the surface oxidation/reduction pair where Co(III) is oxidized to Co(IV) at high anodic potentials.[98] These peaks are present in the Co sample but are suppressed after adding Fe.

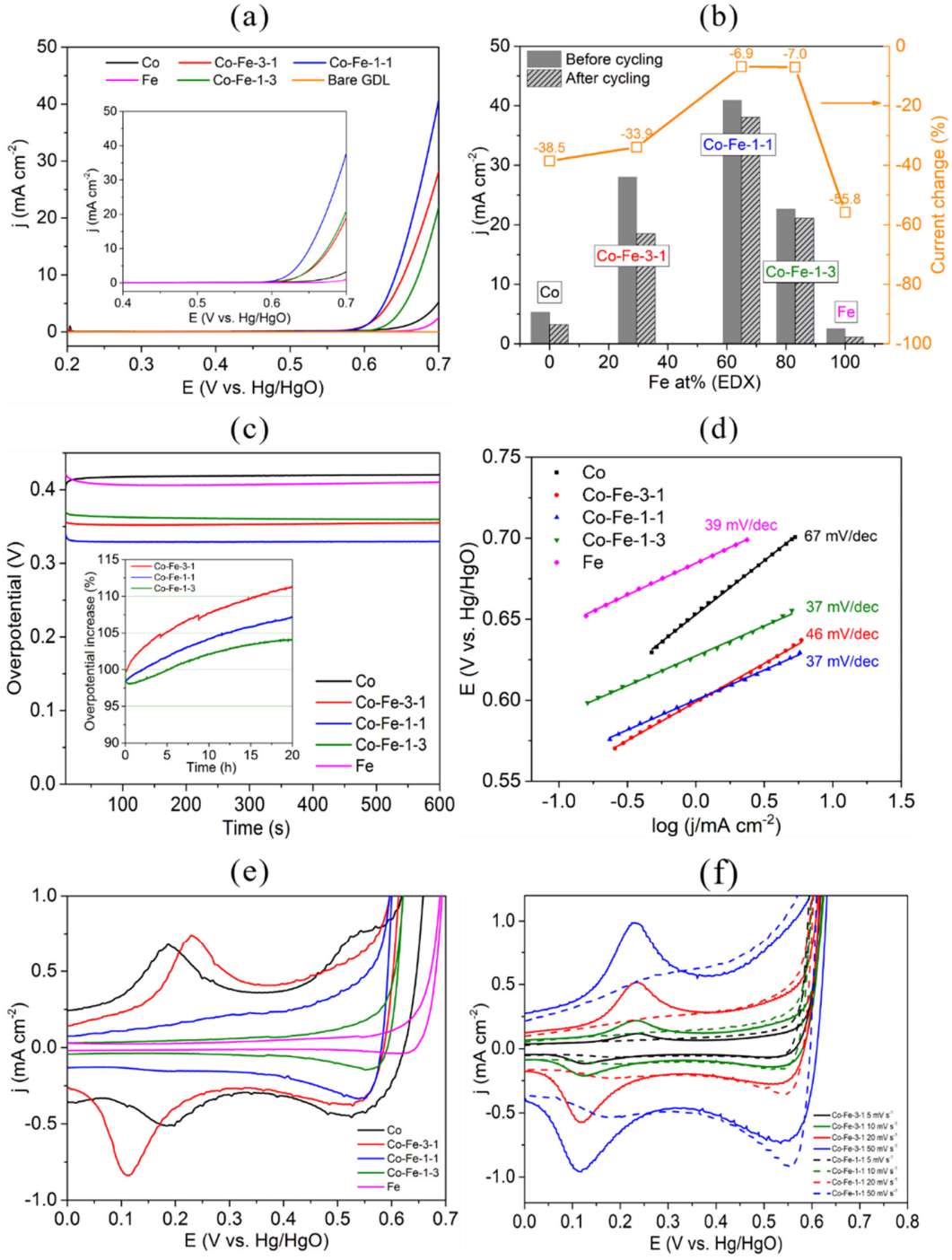

Fig. 4-2. (a) LSV plots for catalysts and bare GDL at a scan rate of 5 mV s^{-1} in oxygen saturated 1 M KOH electrolyte (inset: LSV plots after 50 cycles of CV testing). (b) Current density at 0.7 V

before and after 50 CV cycles from -0.25 V to 0.7 V. The percent loss in current density with cycling is also shown. (c) Chronopotentiometric measurements at 10 mA cm^{-2} (inset: stability tests). (d) Tafel plots derived from (a). (e) Magnified CV plots (2^{nd} cycle) for catalysts at a scan rate of 20 mV s^{-1}. (f) Comparison of CV curves (2^{nd} cycle) for Co-Fe-3-1 (solid line) and Co-Fe-1-1 (dashed line) at different scan rates of 5, 10, 20 and 50 mV s^{-1}.

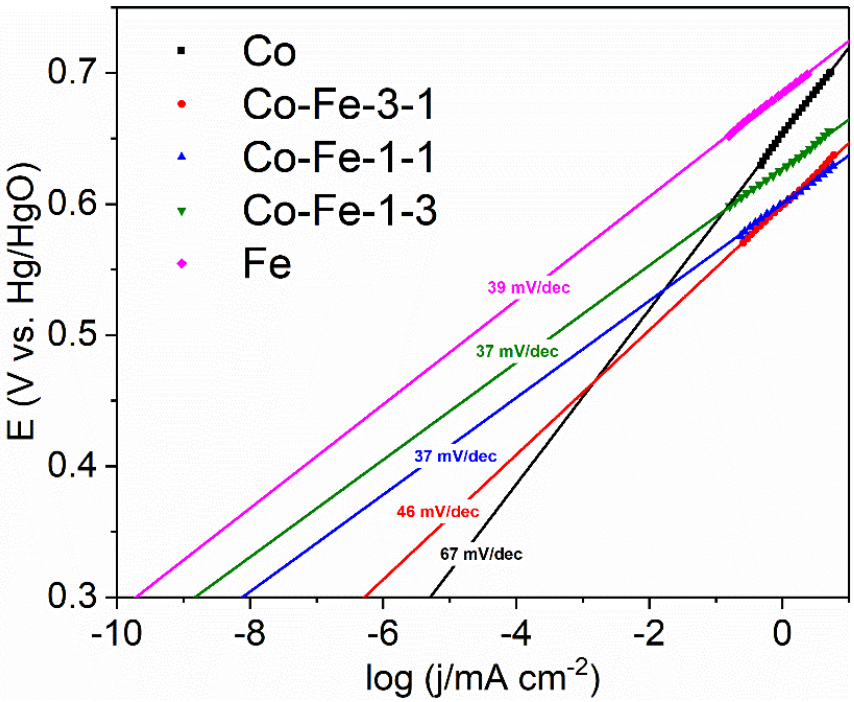

Fig. 4-3. Determination of j_0 by extrapolating the Tafel plots to E= 0.303 V vs. Hg/HgO (η= 0).

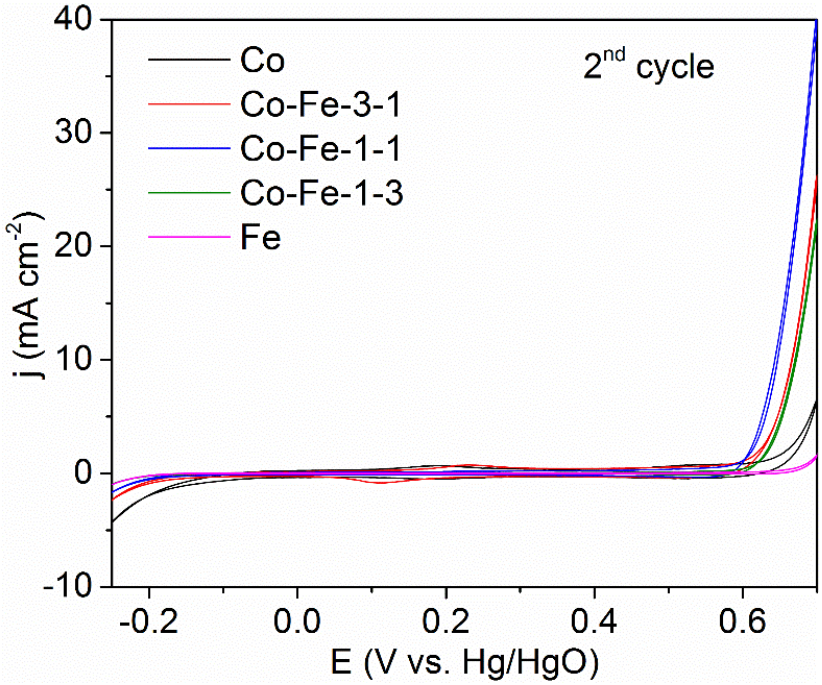

Fig. 4-4. CV curves (2nd cycle) from -0.25 V to 0.7 V for catalysts at a scan rate of 20 mV s^{-1}.

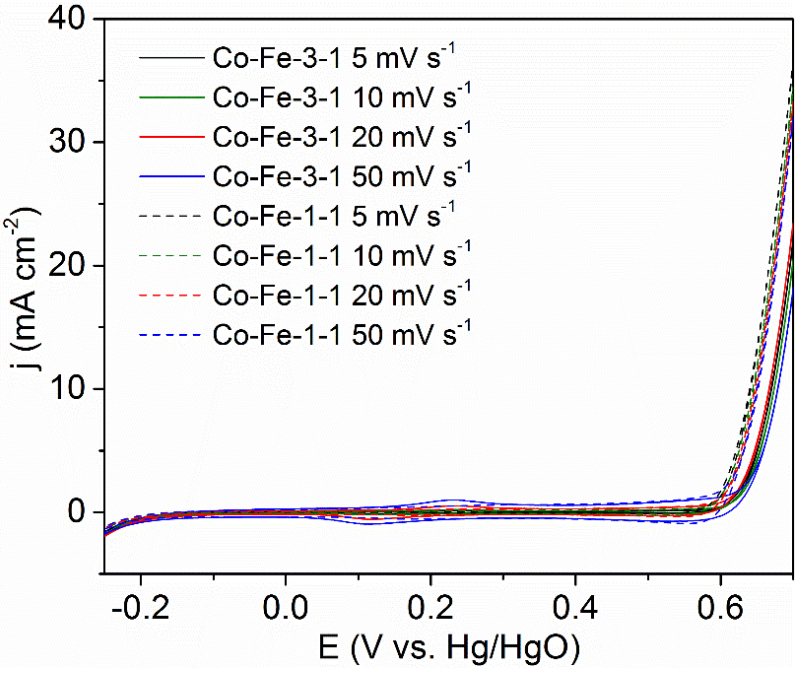

Fig. 4-5. CV curves (2nd cycle) from -0.25 V to 0.7 V for catalysts at different scan rates of 5, 10, 20 and 50 mV s^{-1}.

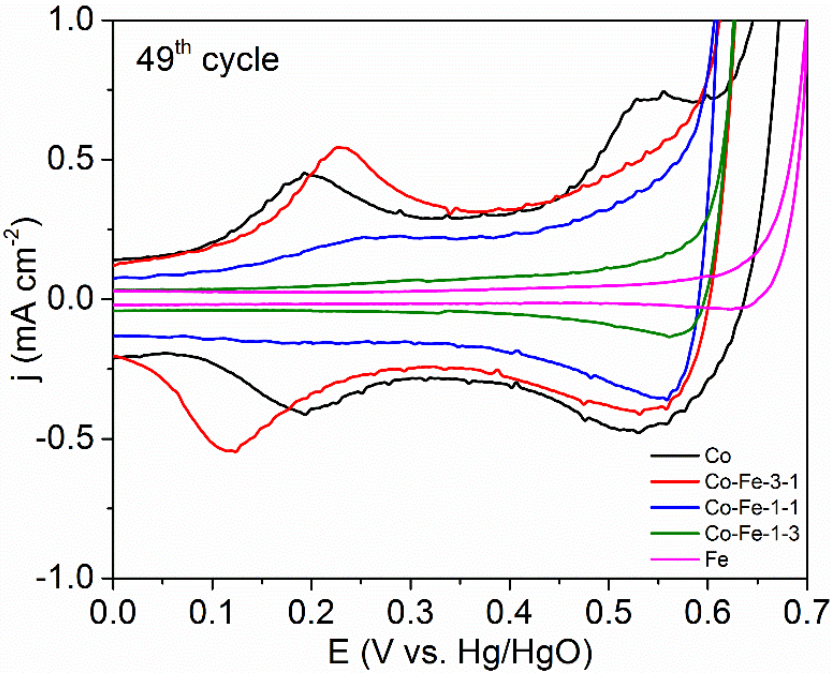

Fig. 4-6. Magnified CV plots (49th cycle) for catalysts at a scan rate of 20 mV s^{-1}.

Electrodes with different catalysts were CV cycled in the potential range of 0.3 V-0.4 V at different rates to compare their capacitive properties (Fig. 4-7). There are several ways to electrochemically characterize the surface properties of porous electrocatalysts. The "internal" and "external" surface areas of oxide electrodes, as well as the porosity, can be defined by plotting pseudocapacitive voltammetric charge (q*) versus potential scan rate.[229] Alternatively, the morphology factor of a porous electrode, which excludes the effects of solid-state surface redox transitions (SSSRT), can be obtained by plotting capacitive current against scan rate.[239, 240] The Co-Fe catalysts possess several solid-state surface redox transitions in the potential range.[98, 241] Therefore, a method was used to differentiate double-layer capacitance C_{dl} and pseudo-capacitance C_p.[242] The double layer charge q_{dl} is estimated by extrapolation of q to $v=\infty$ in a plot of q vs. $v^{-1/2}$ (Fig. 4-8(a)), where q is the voltammetric charge integrated using the CV curve and v is the scan rate. Then C_{dl} can be

obtained by dividing half of q_{dl} by the 0.1 V potential window of the CV curve; this was used to compare the electrochemically active surface area (ECSA) of the samples. Pure Co has the highest C_{dl} value of 10.4 mF cm^{-2}, which decreases after alloying with Fe. Co-Fe-3-1 and Co-Fe-1-1 have similar values of around 4.5 mF cm^{-2}, which are much higher than the capacitances for Co-Fe-1-3 (1.4 mF cm^{-2}) and Fe (0.7 mF cm^{-2}), even though the deposits are similar in terms of morphology. Therefore, the difference in ECSA must stem from differences in composition rather than morphology. The insulating layer produced at the surface by the excess Fe can change the electronic conductivity or charge density at the electrode surface, leading to different double layer capacitance or ECSA. The C_{dl} value of the carbon substrate is quite small (0.2 mF cm^{-2}), possibly due to the hydrophobicity of the PTFE binder within it.

Electrochemical impedance spectroscopy (EIS) at 0.6 V was performed for all samples, and the spectra were fit using Z-Fit software (Fig. 4-8(b)). The impedance spectra are composed of a poorly developed semi-circle in the high-frequency domain, which is related to metal/metal oxide interface, and a well-developed semi-circle in the low-frequency domain which is related to the kinetic parameters of OER.[243] An $R_s(R_f\ Q_f)(R_{ct}\ Q_{dl})$ equivalent circuit was used to fit the experimental data, where R_s, R_f and R_{ct} represent the solution resistance, the metal oxide interlayer resistance and the charge transfer resistance at the oxide/solution interface, respectively.[244] Q_f and Q_{dl} are the corresponding constant phase elements (CPE). The Nyquist plots reveal that the samples have similar R_s and R_f values but differ in R_{ct}. R_{ct} decreases in the following order: Co (92.1 Ω cm^2) > Co-Fe-1-3 (44.3 Ω cm^2) > Co-Fe-3-1 (23.3 Ω cm^2) > Co-Fe-1-1 (15.8 Ω cm^2) (Table 4-1). The results indicate that doping with Fe can effectively improve charge transfer up to a point, but too much Fe will hinder charge transfer.[222] The electrochemical properties of all three Co-Fe alloys are compared and summarized in Table 4-1.

The Co-Fe samples were assembled into Zn-air batteries and tested via galvanostatic discharge-charge cycling at 5 mA cm^{-2} (Fig. 4-8(c)). Batteries with all three Co-Fe catalysts can charge at a lower potential than the cell using bare GDL (with Co-Fe-1-1 providing the best performance). To simulate discharge-charge cycling in the battery and to exclude the effect of the Ni frame/plate, a chronopotentiometric test at 5 mA cm^{-2} current density (30 min cathodic current followed by 30 min anodic current) was performed in a three-electrode system in both 1 M KOH and 6 M KOH + ZnO (the battery electrolyte), as shown in Fig. 4-9. Both tests show that Co-Fe has much better OER activity than bare GDL, confirming the LSV test results. The difference in charge potential becomes more pronounced with battery cycling. The Co-Fe catalysts are not oxygen reduction reaction (ORR) active but can be combined with other ORR catalysts to work in Zn-air batteries. The discharge potential of the cell using Co-Fe-1-3 is lower than the cell using bare GDL, making it unsuitable for use as an OER catalyst in a Zn-air battery. As such, the rest of the discussion is focused on the Co-Fe-3-1 (29.5 at% Fe) and Co-Fe-1-1 (64.9 at% Fe) only.

The most OER active catalyst, Co-Fe-1-1, was selected to be cycled galvanostatically in both 1 M KOH and 6 M KOH + ZnO (the battery electrolyte) for 100 hours to confirm its stability (Fig. 4-8(d)). The test started with a 30 min cathodic current of 5 mA cm^{-2}, followed by a 30 min anodic current to simulate discharge-charge cycling in Zn-air batteries. The charging potential remained almost the same after 100 h of cycling.

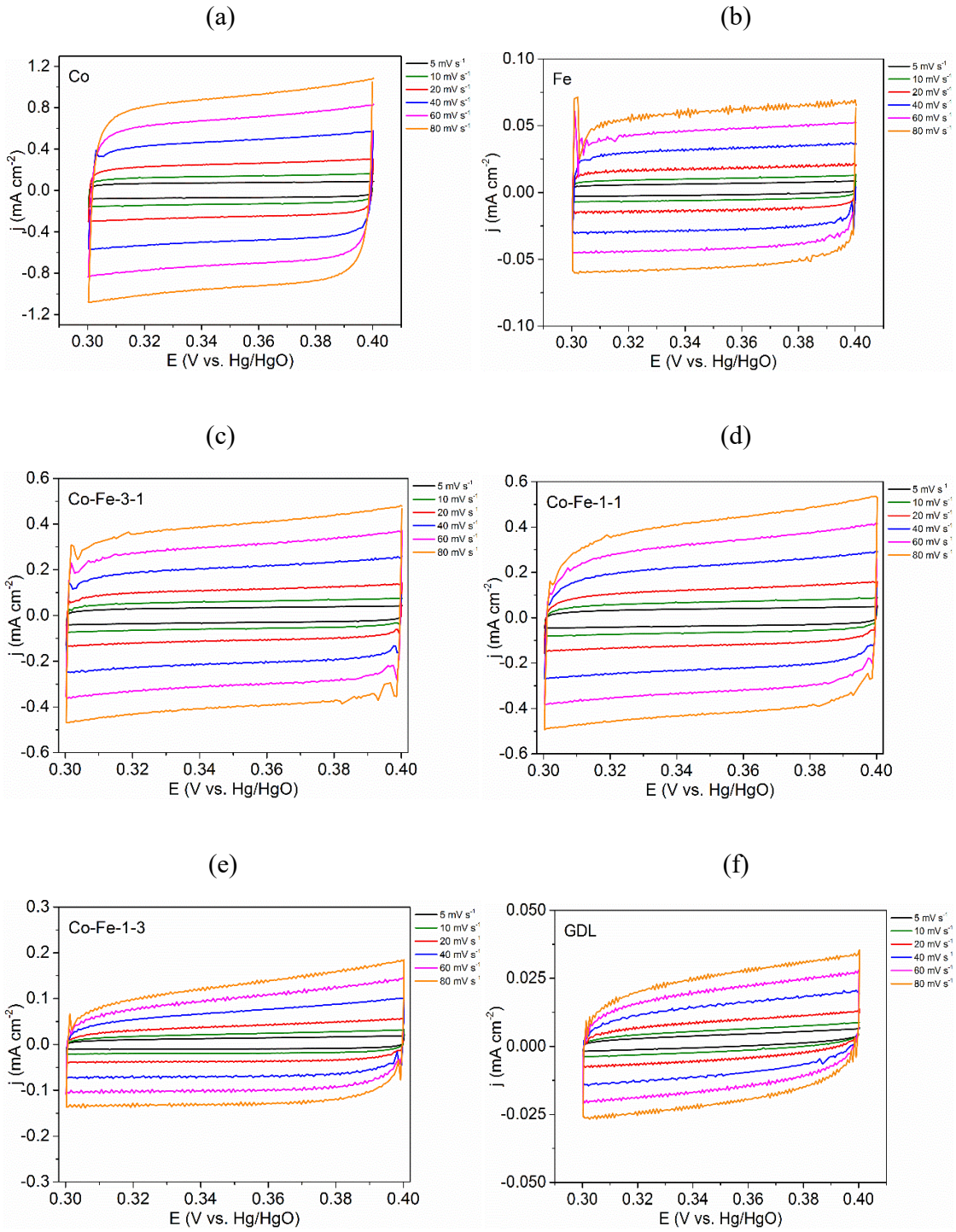

Fig. 4-7. CV curves at different scan rates in a potential window of 0.3-0.4 V vs. Hg/HgO for different samples: (a) Co; (b) Fe; (c) Co-Fe-3-1; (d) Co-Fe-1-1; (e) Co-Fe-1-3; (f) bare GDL.

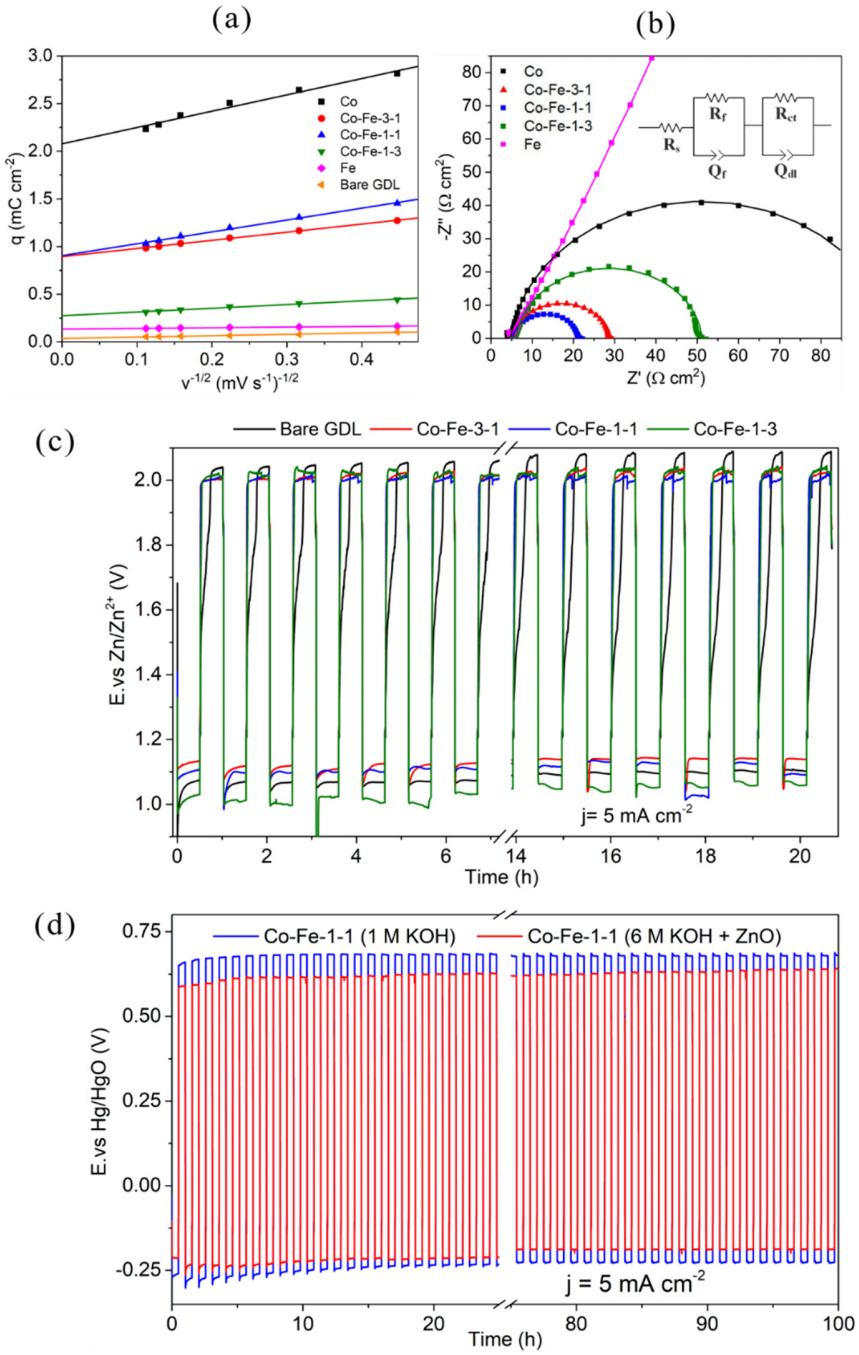

Fig. 4-8. (a) Voltammetric charge (q) plotted against scan rate where the intercept on the q-axis is equivalent to the double layer charge, q_{dl}. (b) Electrochemical impedance spectra at 0.6 V (inset: equivalent circuit diagram). (c) Galvanostatic discharge-recharge cycling for Zn-air batteries at a current density of 5 mA cm^{-2}. (d) Chronopotentiometric measurements of Co-Fe-1-1 at 5 mA cm^{-2} for 100 hours in 1 M KOH and 6 M KOH + ZnO.

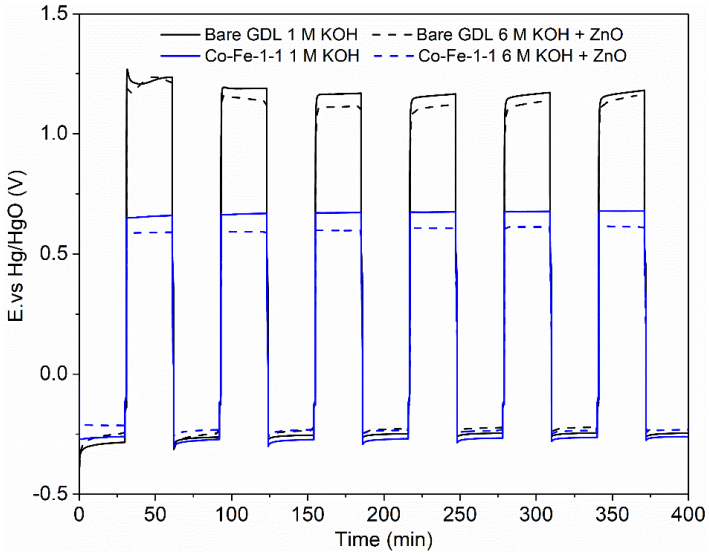

Fig. 4-9. Chronopotentiometric test for bare GDL and Co-Fe-1-1 at 5 mA cm^{-2} (30 min reduction current followed by 30 min oxidation current) in a three-electrode system in both 1 M KOH and 6 M KOH + ZnO (the battery electrolyte).

In order to determine the reasons for the disappearance of the Co^{2+}/Co^{3+} peak when the catalyst composition was changed, i.e., Co-Fe-3-1 (~30 at% Fe) vs. Co-Fe-1-1 (~65 at% Fe), AES composition depth profiling was performed on individual Co-Fe particles (Fig. 4-10). Two particles from each sample were profiled and these are labeled as 1 and 2 in Fig. 4-10(c) (Co-Fe-3-1) and Fig. 4-10(f) (Co-Fe-1-1). The particles were chosen such that a cuboid facet was perpendicular to the electron beam. In addition, AES spectra at different sputtering intervals for the two samples are shown in Fig. 4-11. The sputtering rates for Co and Fe are very close to one another since they have similar atomic masses.[245] AES peaks at 503 eV, 589 eV and 771 eV were selected to measure the concentrations of O, Fe and Co, respectively. The concentration of Fe relative to total amount of Co and Fe in the deposit is also shown for the deposits (green curves in

Fig. 4-10). For Co-Fe-3-1, the relative amount of Fe in Co-Fe is highest at the surface and decreases from 48 at% to 27 at% over a depth of ~10 nm (Fig. 4-10(a) and 4-10(b)). The Co-Fe-1-1 sample has the same Fe composition trend, but the amount of Fe is much higher. The Fe composition is 78 at% at the surface and decreases to 71 at% at ~10 nm. The surface Fe concentration (to a depth of ~1 nm) for Co-Fe-1-1 obtained from AES analysis is about 19% higher than the Fe concentration from EDX analysis (with a depth resolution of ~1 μm - Table 1), indicating segregation of Fe to the surface. Iron segregation to the surface occurs for Co-Fe-3-1 as well.

The surfaces of the particles are oxidized, which is evident from the high O levels at the surface for all samples that decrease from the surface to the interior (black line in Fig. 4-10). Therefore, both catalysts are covered by a layer of Co/Fe oxide with more Fe in the surface region than in the particle interior. From a thermodynamic point of view, Fe oxides have a more negative standard free Gibbs energy of formation (ΔG_f°) than Co oxides, which can provide the driving force for Fe segregation to the surface and subsequent oxidation.[12] Another reason for the high surface Fe concentration is Fe hydroxide generated by the hydrogen evolution reaction (HER) during cathodic electrodeposition. $Fe(OH)_3$ has low solubility in the electrolyte used for electrodeposition (pH= 4.5), facilitating formation on the newly formed Co-Fe alloy surface.[246] The average near-surface Fe concentrations (to a depth of ~10 nm) for Co-Fe-3-1 and Co-Fe-1-1 are higher than the bulk concentrations of deposited alloys as will be shown in the following XRD analysis. For example, the average near-surface Fe concentration for Co-Fe-1-1 determined by AES is 72 at%, while the bulk Fe concentration is only 60 at% ($Co_{0.4}Fe_{0.6}$) as determined by XRD. This means that some Fe exists as amorphous hydroxide, a typical by-product of cathodic electrodeposition.

The surface Fe concentration for Co-Fe-1-1 is 78 at%, which is close to the Fe concentration in the study mentioned above where the Co^{2+}/Co^{3+} redox peak started to disappear.[193] It is likely that

Co-Fe-1-3 will have an even higher surface Fe content. Previous work in Chapter 3 has shown that the oxidation states of Co and Fe on the particle surfaces are Co^{2+} and Fe^{3+} when the Co-Fe solid solution is deposited on GDL.[247] As such, a high level of Fe oxide (especially insulating Fe_2O_3/FeOOH) can block many of the active sites on the catalyst surface.

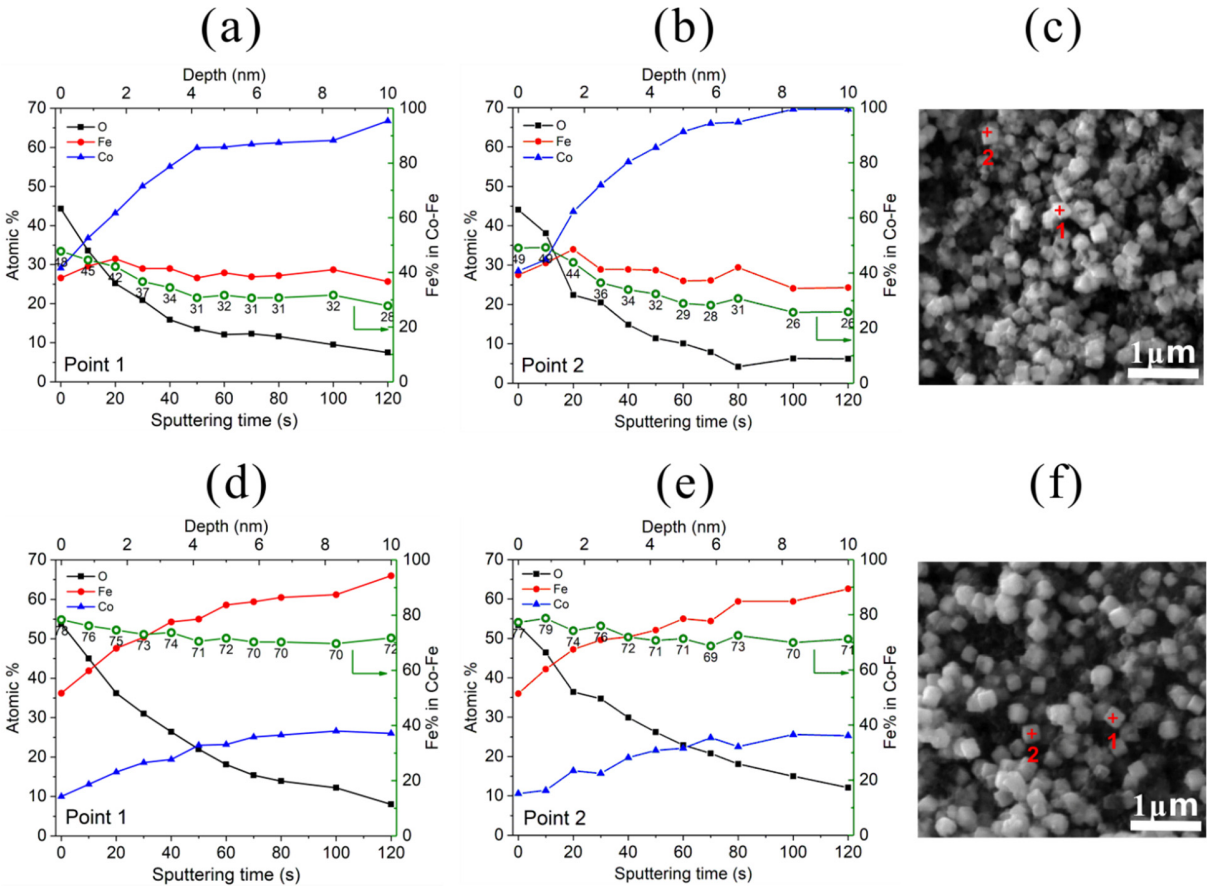

Fig. 4-10. AES depth profiles for (a) Co-Fe-3-1, point 1; (b) Co-Fe-3-1, point 2; (c) SE image of Co-Fe-3-1. AES depth profiles for (d) Co-Fe-1-1, point 1; (e) Co-Fe-1-1, point 2; (f) SE image of Co-Fe-1-1. The green curves in all cases represent the amount of Fe (in at%) relative to the total amount of Co and Fe.

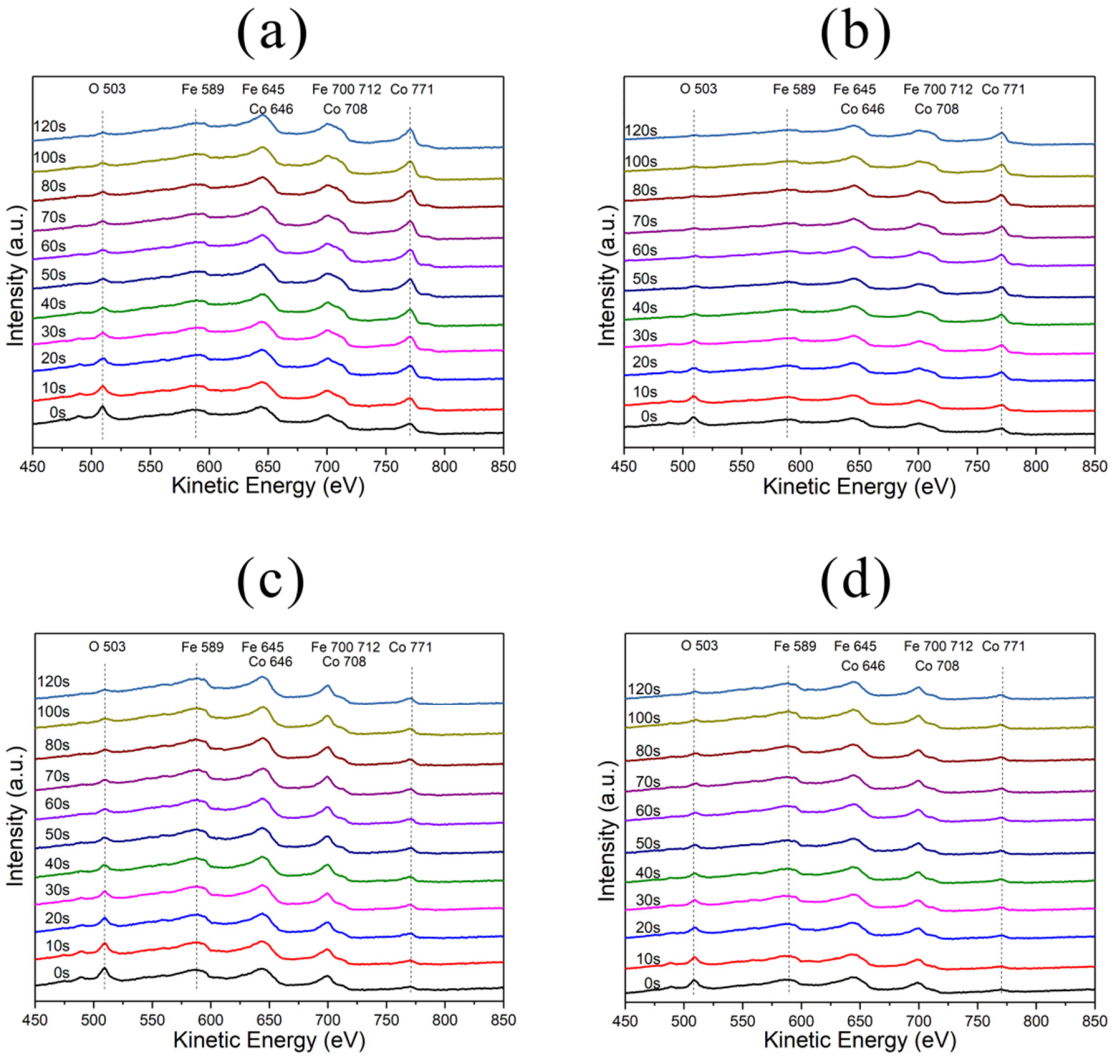

Fig. 4-11. Selected Auger electron spectra taken from Co-Fe particles shown in Fig. 4-10: (a) Co-Fe-3-1, point 1; (b) Co-Fe-3-1, point 2; (c) Co-Fe-1-1, point 1; (d) Co-Fe-1-1, point 2.

The crystal structures of the samples were studied using XRD (Fig. 4-12(a)). For each sample, the diffraction peaks at 49.52° and 64.38° are from graphite (PDF File No. 89-8487) in the GDL substrate. For the pure Co deposit, the peaks at 51.89° and 55.64° are indexed to hcp Co (PDF File No. 89-4308). For the Co-Fe alloys and pure Fe, the peaks correspond to a bcc crystal structure. There is a slight shift in the peaks to lower angles as the amount of Fe increases in the deposits.

This corresponds to an increase in the d-spacings and an increase in the lattice parameter, which is not surprising as the atomic radius for Fe (0.140 nm) is larger than that for Co (0.135 nm). Overall deposit composition can be estimated from the Vegard equation, i.e., Co-Fe-3-1 contains 30 at% Fe ($Co_{0.7}Fe_{0.3}$) and Co-Fe-1-1 contains 60 at% Fe ($Co_{0.4}Fe_{0.6}$). The compositions determined by the three methods (AES, SEM-EDX and XRD) are listed in Table 4-1 for comparison. Note that the EDX and XRD values are similar, but the Fe levels are higher for Auger analysis, due to Fe segregation to the particle surfaces.

The Co-Fe-3-1 and Co-Fe-1-1 samples were further investigated using TEM. The particles in both samples are covered by a thin amorphous oxide layer, which was confirmed by EDX point analysis. The O levels at points 1 and 2 in Fig. 4-12(c) are higher than that at the particle center (point 3 in Fig. 4-12(c)). These results corroborate the Auger depth profiles. Steps less than 10 nm in height are clearly visible at the surfaces, which correlate with the surface features visible in the SEM images (Fig. 4-1(b) and 4-1(c)). Selected area electron diffraction (SAED) patterns reveal that the bulk particles are single crystals and these are also indexed to the bcc Co-Fe solid solution (confirms the XRD results).

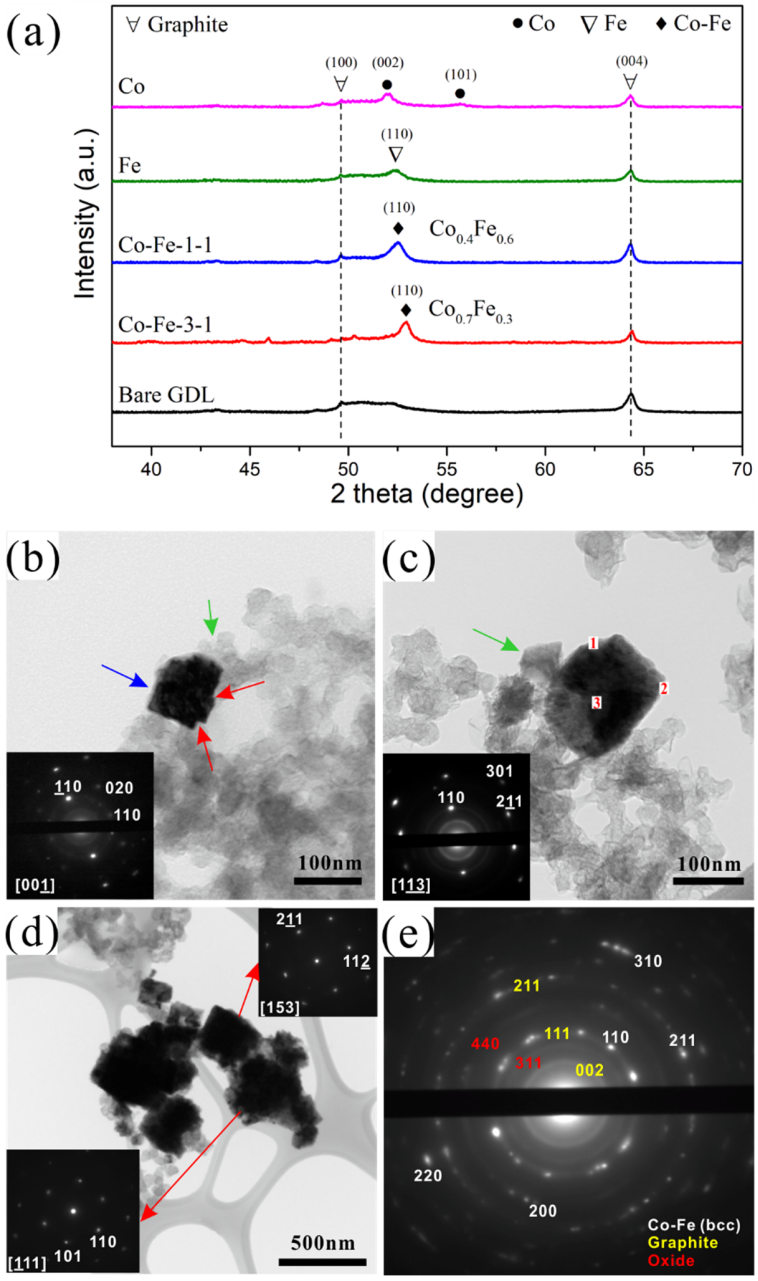

Fig. 4-12. (a) XRD patterns for Co, Fe, Co-Fe-3-1, Co-Fe-1-1 and bare GDL. (b) TEM bright field (BF) image and SAED pattern from a particle in Co-Fe-3-1, which is surrounded by carbon particles from the microporous layer (green arrow). The blue arrow indicates a thin amorphous oxide layer. Surface steps, less than 10 nm in height, are clearly visible (red arrows). (c) TEM BF image and SAED pattern from a particle in Co-Fe-1-1. The oxygen concentrations at points 1, 2 and 3 in (c) are 48%, 38% and 17%, respectively. The faint rings in the SAD patterns can be indexed to graphite in the GDL. (d) TEM bright field (BF) image and SAED pattern from a particle in Co-Fe-3-1 after 20 h OER test. (e) The SAED pattern is from the whole area in Fig. 4-12(d). The planes labeled in red ((440) and (311)) are from spinel Fe_3O_4.

AES depth profiling was used to study any composition changes in Co-Fe-3-1 after a 20 h OER test (inset in Fig. 4-2(c)) and battery testing for 20 h (Fig. 4-13 and Fig. 4-14). The relative Fe concentration (at% of Fe relative to the total amount of Co and Fe) is lower at the surface and increases towards the interior, which is the opposite of the Fe distribution before cycling (Fig. 4-10). The Fe content in the surface region (0-1 nm), relative to the total amount of Co and Fe, decreased from ~48 at% to ~16 at% after the 20 h OER test and ~26 at% after battery cycling, due to the dissolution of Fe which is chemically unstable under OER conditions from the particle surface.[193] The O levels are considerably higher than those for the original samples (Fig. 4-10(a) and 4-10(b)), even towards the interior of the particles.

TEM analysis of particles in the Co-Fe-3-1 sample after the 20 h OER test indicate that they are mostly metallic with a surface oxide layer (Fig. 4-12(d) and 4-12(e)). Single crystal patterns from individual particles (insets in Fig. 4-12(d)) can be indexed to metallic Co-Fe. The diffraction pattern obtained from entire region shown in Fig. 4-12(d) exhibits a number of rings. Most of the rings can be indexed to metallic Co-Fe and graphite from the GDL layer. There are two extra rings in Fig. 4-12(e) which can be indexed best to a spinel structure ($Co_xFe_{3-x}O_4$), but there is reasonable fit to $Fe_xCo_{1-x}O$ as well. Therefore, for Co-Fe-3-1 after the 20 h OER test, the increase in O content is due to the increased degree of surface oxidation. TEM analysis shows that the particles have metal cores that are inaccessible to electrolyte, while the Co/Fe-oxyhydroxide outer shell acts as the active structure for the OER process. Previous studies have shown that a $Co/CoO/Co(OH)_2$ "sandwich type" structure can be generated at low potentials due to the hydrous nature of the anodic oxide formed on a metallic Co electrode in alkaline solutions.[248] At high anodic potentials, a second passive layer is formed outside the Co(II) layer and consists of Co(III) and Co(IV) species.[98] A similar $M/MO_x/MO_a(OH)_b(OH_2)_c$ structure was found for Fe electrodes anodized in

alkaline solutions as well, where MO_x represents the inner compact layer that passivates during the anodic sweep.[249] STEM imaging and X-ray mapping show that there is a thin oxide layer around the as-deposited particles, which indicates limited oxidation (Fig. S4-18(a)). After the 20 h OER test, the oxide layer is thicker (~20 nm thick), while the core remains unoxidized (Fig. S4-18(b)). These results corroborate the Auger results.

After battery cycling, the increase in the amount of O is at least partially due to KOH, K_2CO_3 and ZnO residues precipitating from the battery electrolyte (Fig. 4-13(d) and (e)).[13] Peaks for K and Zn are present in the AES survey spectra in Fig. 4-15 (after cycling), even after sputtering for 180 s. The metal peaks (Fe and Co) are suppressed as a result of the residues coating the surface. The particle morphology did not change after cycling, i.e., compare Fig. 4-1(b) with Fig. 4-13(f) and Fig. 4-16. Therefore, the Co-Fe-3-1 deposit is stable in terms of morphology during Zn-air battery cycling.

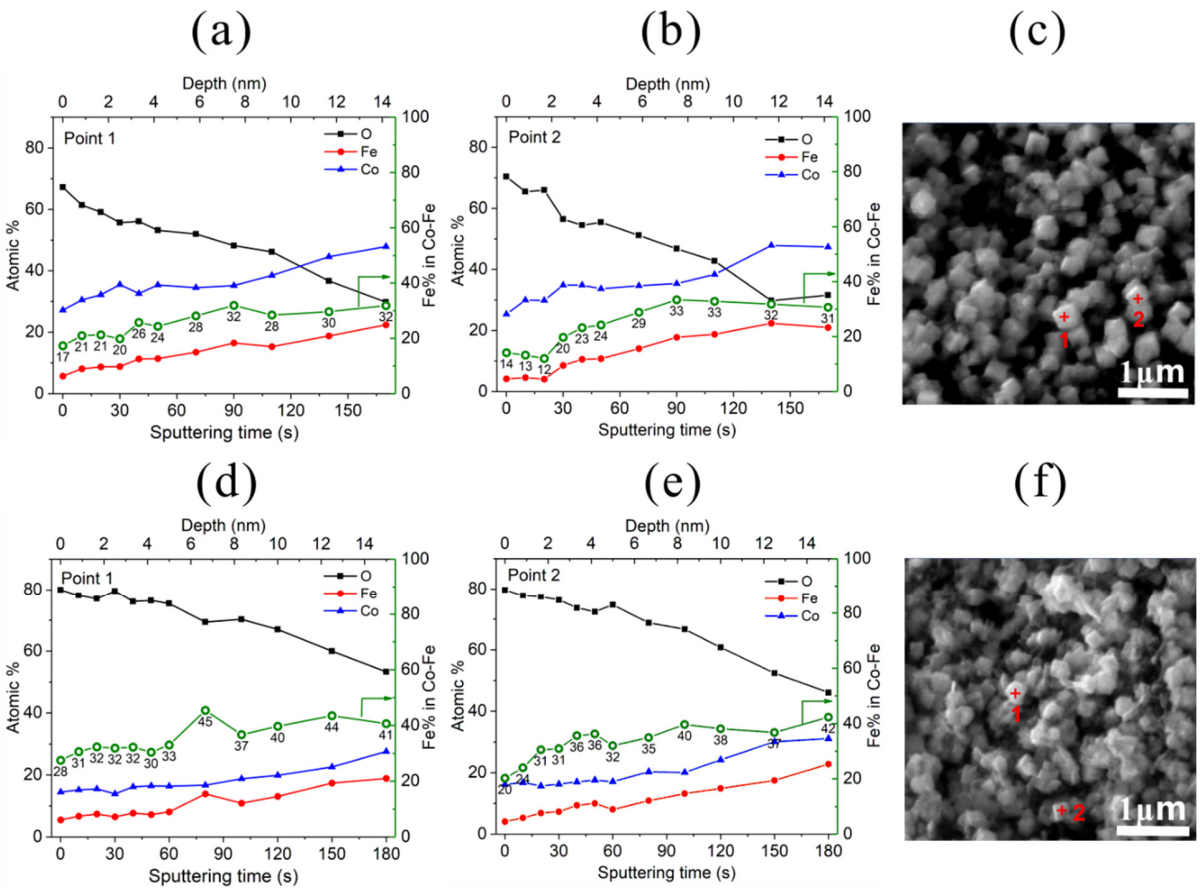

Fig. 4-13. Auger electron spectroscopy (AES) results for Co-Fe-3-1 after the 20 h OER test (a-c) and battery cycling (d-f). (a) Depth profile at point 1 in (c). (b) Depth profile at point 2 in (c). (c) SE image of Co-Fe-3-1 after 20 h OER test. (d) Depth profile at point 1 in (f). (e) Depth profile at point 2 in (f). (f) SE image of Co-Fe-3-1 after battery cycling. The green curves in (a), (b), (d) and (e) represent the amount of Fe (in at%) relative to the total amount of Co and Fe.

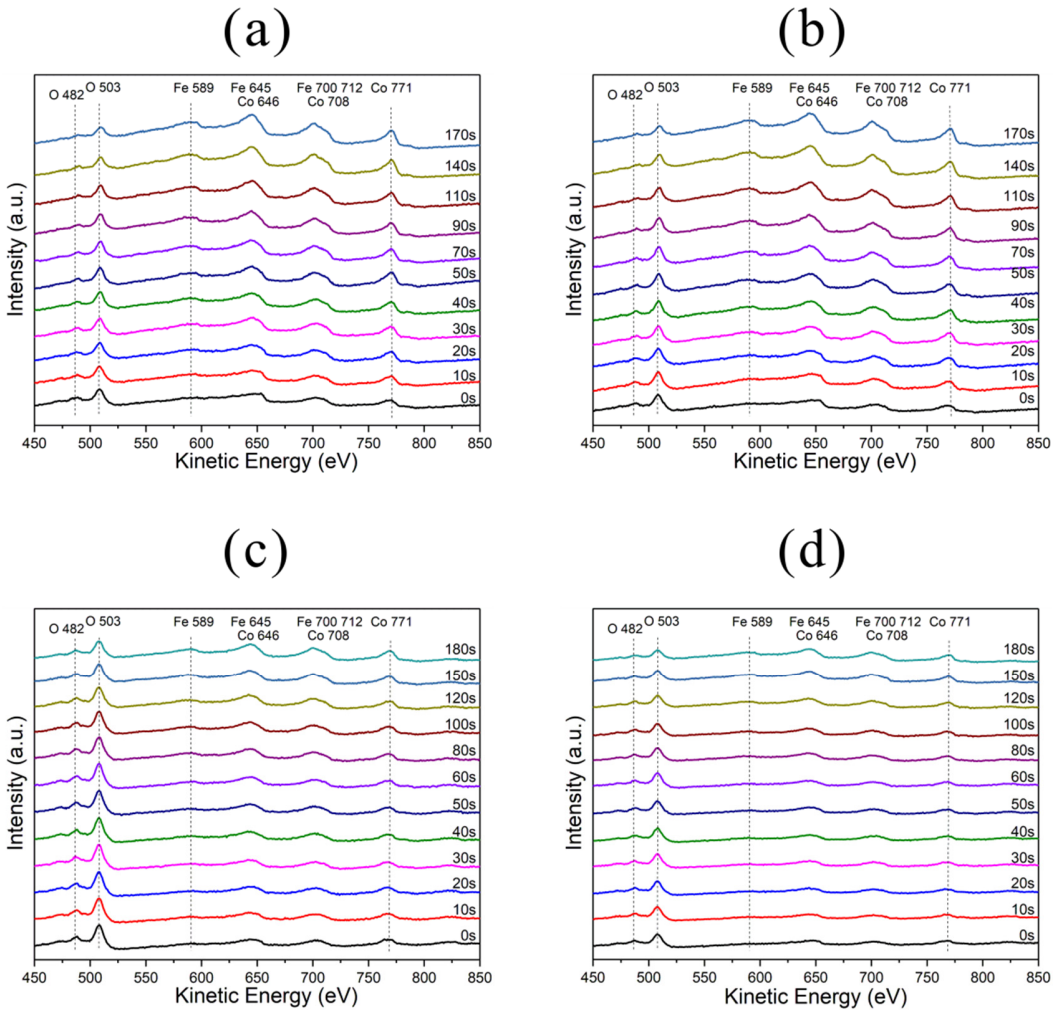

Fig. 4-14. Selected Auger spectra during depth profiling of Co-Fe-3-1 particles after 20 h OER ((a) and (b)) and after battery cycling ((c) and (d)). (a) Spectra from point 1 in Fig. 4-13(c); (b) spectra from point 2 in Fig. 4-13(c); (c) spectra from point 1 in Fig. 4-13(f); (d) spectra from point 2 in Fig. 4-13(f).

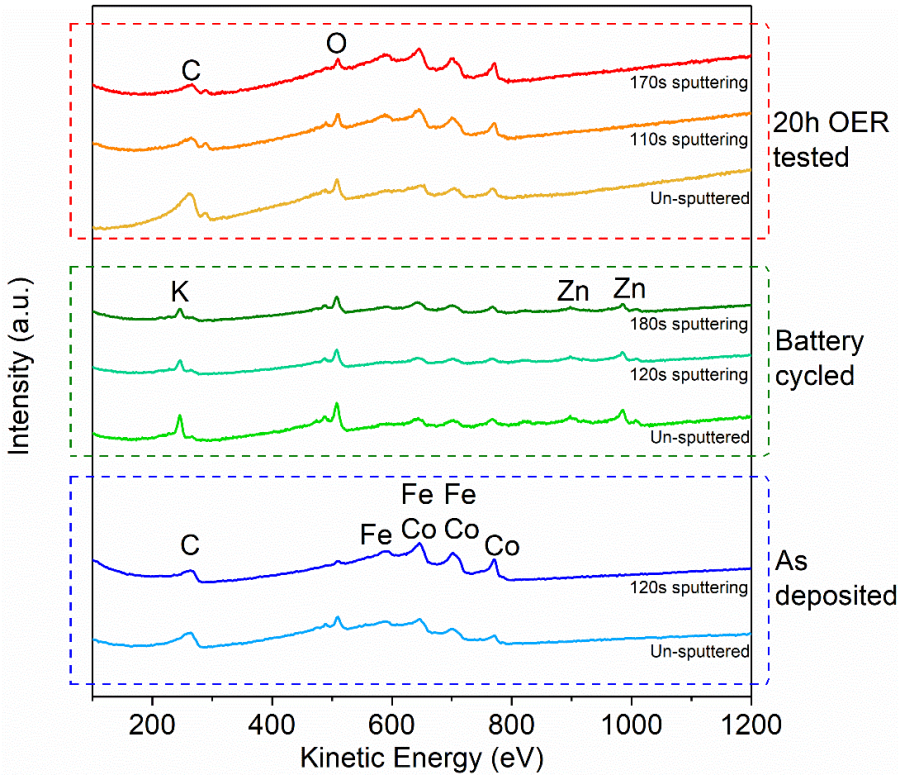

Fig. 4-15. AES survey spectra for Co-Fe-3-1 before and after 20 h OER test and battery cycling.

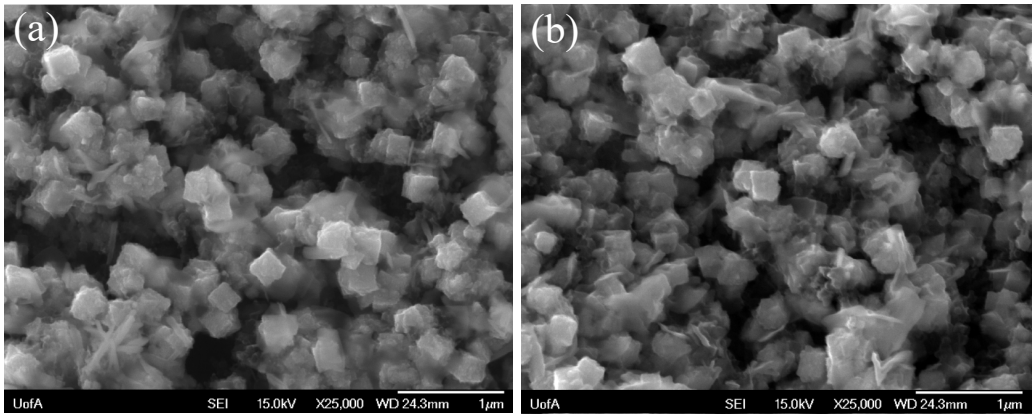

Fig. 4-16. Auger SE images of Co-Fe-3-1 after battery cycling for 20 h. (a) Surface un-sputtered; (b) after 3 min of sputtering. The particle morphology did not change after cycling (compare with Fig. 4-1(b)).

4.4 Summary

Co-Fe alloys with oxidized surfaces have been studied as potential electrocatalysts for the oxygen evolution reaction (OER) in Zn-air batteries. Co-Fe was directly electrodeposited onto carbon paper (gas diffusion layer or GDL) from electrolytes with different Co/Fe ratios ($CoSO_4$:$FeSO_4$ = 3:1, 1:1, 1:3 - denoted as Co-Fe-3-1, Co-Fe-1-1 and Co-Fe-1-3, respectively). The amount of Fe in the deposits increased with increasing Fe in the electrolyte, but the deposit morphology remained essentially the same (with the exception of pure Co) as single crystal, cuboidal nanoparticles. The deposited catalysts were metallic in nature (bcc solid solution) with oxidized surfaces that were rich in Fe relative to the bulk. The OER activity increased with increasing Fe levels, up to ~65 at% Fe (Co-Fe-1-1), with an overpotential of 0.33 V at 10 mA cm^{-2} in 1 M KOH. Zn-air batteries fabricated using the Co-Fe catalysts at the air electrode had lower charging potentials than the charging potential for the bare GDL substrate. The catalyst particles were stable in terms of morphology and performance after 100 h of galvanostatic cycling and 20 h of battery testing, although additional oxidation of the particle surfaces occurred.

4.5 Supporting information

Study of the electrodeposition process and current efficiency

The current efficiency for Co-Fe electrodeposition is primarily determined by the hydrogen evolution reaction (HER) during the process. A 0.2 M Na_2SO_4 solution was used to replace $CoSO_4$/$FeSO_4$ in the plating bath to estimate the degree of HER. This solution, together with the Co-Fe plating bath, was CV cycled with a 5 cm^2 GDL electrode (Fig. S4-17). A Hg/Hg_2SO_4 (0.64 V vs SHE) reference electrode was used. The electrodeposition of Co-Fe starts at around -1.6 V to

-1.7 V (confirmed by SEM), accompanied by the HER. The current for the Co-Fe solution is around 85 mA at -2.0 V while that for the Na_2SO_4 solution is 38 mA (derived from the HER), giving a 55% current efficiency ((85-38)/85). At -2.5 V, the average current for the Co-Fe solution is 144 mA with an HER current of 71 mA, giving a theoretical current efficiency of around 50%. The actual deposition efficiency could be even lower considering the relatively low pH and ionic conductivity of the Co-Fe plating bath compared with the Na_2SO_4 solution.

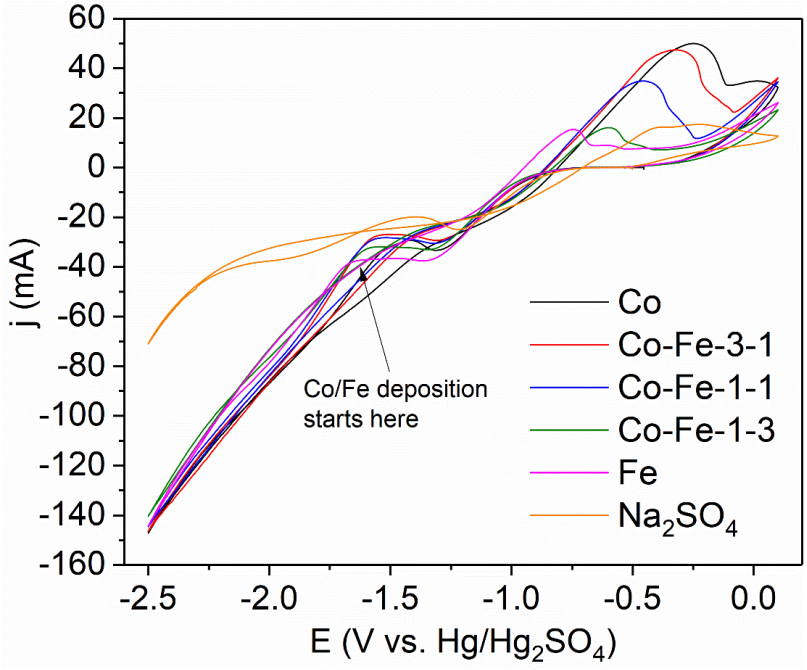

Fig. S4-17. CV curves for the 5 cm^2 GDL electrode in different electrolytes.

STEM mapping of element distribution in Co-Fe-3-1

EDX analysis in a STEM was used to map out the distribution of Fe, Co and O for the Co-Fe-3-1 particles in both the as-deposited condition (Fig. S4-18(a)) and after OER testing (Fig. S4-18(b)). There is a thin oxide layer (red colour) around the as-deposited particle shown in Fig. S4-18(a).

which indicates limited oxidation. After the 20 h OER test, the oxide layer is thicker (~20 nm thick), while the core remains unoxidized (Fig. S4-18(b)). These results corroborate the Auger results in Fig. 4-10 and Fig. 4-13.

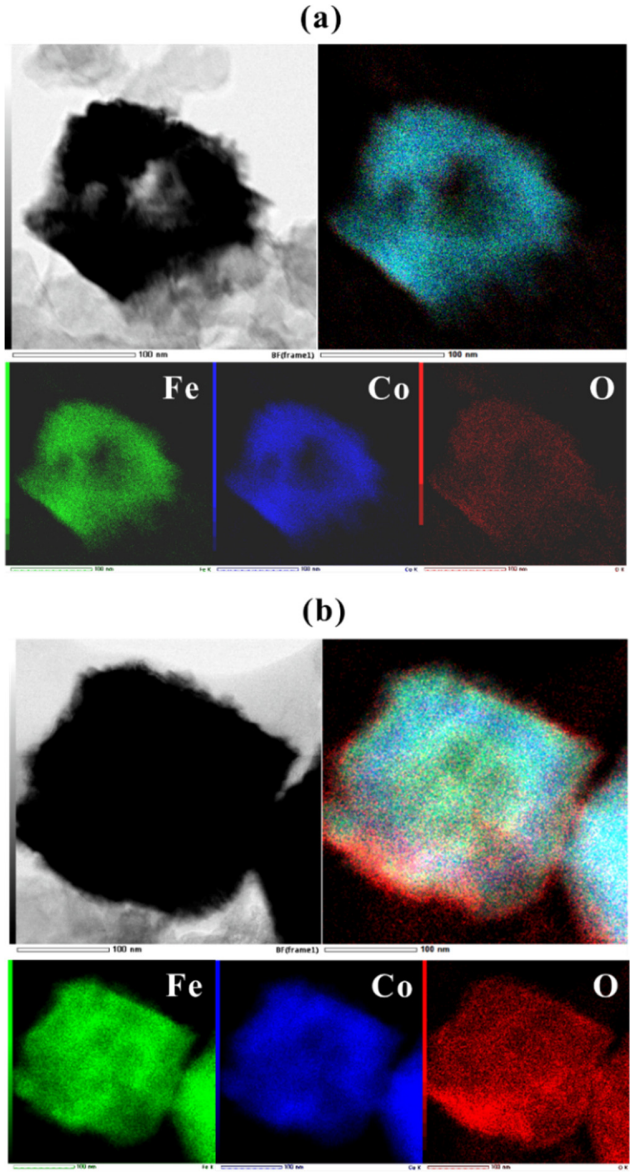

Fig. S4-18. STEM high angle annular dark field (HAADF) images and X-ray maps for Co-Fe-3-1. (a) As-deposited; (b) after 20 h OER test.

Chapter 5 : Sequentially electrodeposited MnOx/Co-Fe as bifunctional electrocatalysts for rechargeable Zn-air batteries

A version of this Chapter has been published in ECS Transactions and the Journal of The Electrochemical Society:

M. Xiong, D.G. Ivey, Electrodeposited MnOx-CoFe as Bifunctional Electrocatalysts for Rechargeable Zinc-Air Batteries, *ECS Transactions*, 75 (2017) 1-7. (10.1149/07536.0001ecst)

M. Xiong, D.G. Ivey, Sequentially Electrodeposited MnOx/Co-Fe as Bifunctional Electrocatalysts for Rechargeable Zinc-Air Batteries, *Journal of The Electrochemical Society*, 164 (2017) A1012-A1021. (10.1149/2.0481706jes)

5.1 Introduction

Electrochemically rechargeable Zn-air batteries are one of the best candidates to store large amounts of electrical energy.[250, 251] However, due to the sluggish ORR and OER at the air electrode, the efficiency of Zn-air batteries is comparatively low, leading to energy losses.[10] Also, catalyst stability is a problem, because the catalyst can detach from the current collector or pulverize during battery cycling.[185] Currently, some precious metals such as Pt, Ru and Ir are recognized as the most active ORR or OER electrocatalysts.[107, 252] However, their application in Zn-air batteries is limited by their high cost and low abundance. Also, Pt is vulnerable during battery cycling, because it can oxidize or agglomerate.[210] Hence, the fabrication of cheap and stable bifunctional electrocatalysts/electrodes that are active for both ORR and OER is of great importance to the application of Zn-air batteries.

Extensive efforts have been devoted to the development of transition metal (Mn, Co, Ni and Fe) based ORR and OER electrocatalysts, since they are abundant and stable in alkaline solutions.[253] Manganese oxides are active towards ORR and are used in commercial primary Zn-air batteries.[254-258] However, their ORR activity is limited by the low electrical conductivity of the oxides, which can be improved by adding carbon blacks or hybridizing with conductive agents like carbon nanotubes or graphenes.[259-261] In addition, manganese oxides do not have appreciable OER activity and should be combined with another OER electrocatalyst. Co and Fe-based materials have been shown to be excellent OER catalysts and are stable in alkaline solutions.[190, 193, 221] The proper combination of the ORR and OER electrocatalysts is critical to electrochemical performance. This can be achieved by using a single layer of bifunctional catalysts or by using multiple catalytic layers.[262] The catalysts for a single layer structure are usually synthesized as powders and mixed with binders (e.g., Nafion and PTFE) and conductive agents (e.g., carbon black) to coat onto the GDL substrate.[263, 264] Alternatively, catalysts can be directly electrodeposited onto the GDL substrate, without using any binders and conductive agents. However, anodic electrodeposition of binary or ternary metal (oxides) is difficult due to the gap in redox potentials. For anodic deposition of Mn, Co and Fe oxides, starting from their metal sulfates, the redox potential increases in the order (assuming the electrolyte for electrodeposition has a pH of 5): Fe^{2+}/Fe_2O_3 (0.25 V vs. SHE) < Mn^{2+}/MnO_2 (0.80 V vs. SHE) < $Co^{2+}/Co(OH)_3$ (1.35 V vs. SHE).[265-267] Therefore, the generation of mixed oxides is difficult because Fe oxide would deposit first.[206] Cathodic electrodeposition of binary or ternary metal alloys containing both Mn and Co/Fe is impossible for the same reason, since the redox potentials increase in the following order: Mn/Mn^{2+} (-1.19 V vs. SHE) < Fe/Fe^{2+} (-0.60 V vs. SHE) < Co/Co^{2+} (-0.35 V vs. SHE). Thermodynamically favored Co/Fe deposition

will lead to a strong hydrogen evolution reaction (HER) on the substrate, making it impossible to produce Mn metal.[161]

One solution to this problem is the use of multiple layers. For example, an air electrode consisting of two parts was reported to present superior performance in a Zn-air battery.[187] ORR and OER catalyzing layers were fabricated independently, i.e., α-MnO_2 loaded on carbon paper and $Fe_{0.1}Ni_{0.9}Co_2O_4$ coated onto Ti mesh. These were then pressed together to form a bifunctional electrode. For electrodeposition, several layers of catalysts can be fabricated by simply dipping the substrate into different electrolytes. The layer thickness, as well as the morphology and composition, can be tuned by adjusting the deposition conditions.

In this study, an ORR active MnOx film and an OER active Co-Fe layer are sequentially electrodeposited onto GDL substrates to produce bifunctional electrocatalysts for rechargeable Zn-air batteries (Fig. 5-1). In this double-layered electrode, the first layer of ORR active MnOx is combined with the porous GDL, allowing access to the air supply to favor ORR, while the second layer of OER active Co-Fe is deposited by immersion into a second electrolyte. The Co-Fe layer is composed of nanoparticles, which not only provide OER active sites but also decrease the charge transfer resistance of the electrode. The nanoscale amalgamation of the two materials is able to generate an efficient bi-functional catalyst that is better than either layer alone. The whole fabrication process only includes two electrodeposition steps, which is cost effective, scalable and easy to control.

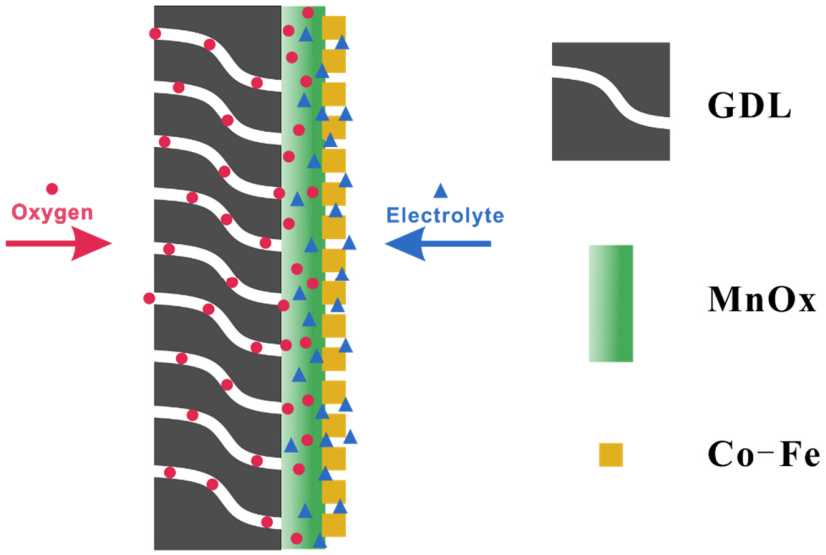

Fig. 5-1. Schematic illustration of the structure of bifunctional catalysts on GDL (cross-section view).

5.2 Experimental

5.2.1. Electrodeposition of MnOx, Co-Fe and MnOx/Co-Fe on GDL

All reagents were certified ACS grade without further purification. GDL (SGL 35DC, 5 cm^2 pieces) was used as the substrate for electrodeposition at room temperature (25°C). Electrodeposition was performed in a two-electrode configuration, where the GDL and Pt mesh were used as the working electrode and the counter electrode, respectively. Sodium dodecyl sulfate (surfactant), L-ascorbic acid (antioxidant) and boric acid (buffering agent) were added to the baths to enhance the uniformity of the coating and its adhesion to the substrate. MnOx was anodically electrodeposited onto GDL at a constant current of 40 mA for 10 min in an electrolyte containing $MnSO_4$ (0.1 M), sodium acetate (0.1 M) and sodium dodecyl sulfate (100 mg L^{-1}). Co-Fe was cathodically electrodeposited on GDL at a constant current of 200 mA for 2 min. The solution for

Co-Fe deposition included $CoSO_4$ (0.15 M), $FeSO_4$ (0.05 M), sodium citrate (0.2 M), boric acid (0.2 M), L-ascorbic acid (0.05 M) and sodium dodecyl sulfate (400 mg L^{-1}). For sequentially deposited MnOx/Co-Fe, a layer of MnOx was anodically deposited first, followed by a layer of cathodically deposited Co-Fe. After electrodeposition, the GDL was rinsed several times with de-ionized water and dried in air. The mass loading of catalysts on GDL was determined by measuring the mass with a microbalance before and after electrodeposition. Mass loadings were 1, 0.6 and 1.2 mg cm^{-2} for MnOx, Co-Fe and MnOx/Co-Fe, respectively.

5.2.2. Materials characterization

The microstructure and composition of the samples were characterized by SEM (Tescan VEGA3 and Zeiss Sigma operated at 10-20 kV) and TEM (JEOL 2010 operated at 200 kV), along with EDX spectroscopy. The crystalline state was examined by XRD (Rigaku Ultima IV) using Co Kα radiation (λ= 1.789 Å). XPS using an Al X-ray source (Kratos AXIS 165) was conducted to determine the oxidation state of the different species. All XPS spectra were corrected using the C 1s line at 284.8 eV. Casa XPS software (Version 2.3.17 PR1.1) was used for curve fitting and background subtraction.

5.2.3. Electrochemical measurements

Electrochemical tests were carried out in 6 M KOH at room temperature using a potentiostat with a three-electrode configuration. The catalyst-coated GDL, Hg/HgO and Pt mesh were used as the working electrode, reference electrode and counter electrode, respectively. All potentials are relative to Hg/HgO unless otherwise indicated. CV measurements were scanned from -0.25 V to 0.7 V at 10 mV s^{-1}. The electrolyte was agitated with a stir bar below the working electrode and

the electrolyte was purged with pure O_2 gas or Ar gas. The current densities were normalized to the geometric surface area. For comparison, a Pt/C catalyst ink was sprayed onto separate GDL substrates. The ink consisted of 50 mg of Pt/C powder (40% Pt, Alfa Aesar) dispersed in 2.0 mL of de-ionized water, 1.0 mL of isopropanol, 0.1 mL of 5 wt% Nafion (D-521) and 0.2 mL of 10 wt% PTFE binder (DISP30). The mass loading of Pt/C ink on the GDL was about 0.6 mg cm^{-2} after drying in a furnace.

5.2.4. Cell testing

Zinc-air battery testing was done in a home-made cell with the same conditions reported in chapter 3. Briefly, a Zn foil and the catalyst loaded GDL were used as the anode and the air electrode, respectively. A microporous membrane (Celgard 5550) was used as the separator. The battery discharge and charge voltages were measured by a galvanostatic method for 10 min at different current densities of 1, 2, 5 and 10 mA cm^{-2}. Discharge-charge cycling was done using a current density of 5 mA cm^{-2} for each cycle. The back side of the GDL was purged with pure oxygen at 20 mL min^{-1} and the catalytic active side (5 cm^2) was in contact with the electrolyte. The discharge-charge efficiency was calculated by dividing the average discharge potential by the average charge potential. EIS was performed at 1.1 V vs. Zn/Zn^{2+} with 20 mV AC potential from 1 MHz to 0.1 Hz.

5.3 Results and discussion

Catalyst characterization

SEM secondary electron (SE) images of the catalyst layers on GDL are shown in Fig. 5-2. The MnOx film deposited on GDL has an irregular surface (Fig. 5-2(a) and 5-2(b)). SEM imaging revealed a porous structure (inset in Fig. 5-2(b)). The pores within the film may have been generated by the removal of water within the deposit during drying, since the MnOx deposit is significantly hydrated after electrodeposition.[169] The porous structure can provide a large surface area for the electrochemical reaction and facilitate the diffusion of oxygen into the ORR reaction zone. Co-Fe, as a separate layer on the GDL, was deposited as individual particles with diameters of several hundred nanometers or less (Fig. 5-2(c) and 5-2(d)). The inset image (Fig. 5-2(d)) shows that individual Co-Fe particles have a terraced surface, which can provide numerous surface defects for the OER reaction.[268]

Sequentially deposited MnOx/Co-Fe consists of a MnOx layer covered with Co-Fe particles (Fig. 5-2(e) and 5-2(f)). In order to confirm the presence of Co-Fe particles on the MnOx film, EDX mapping was done on the MnOx/Co-Fe sample (Fig. 5-3) and showed that MnOx is uniformly coated on GDL. Co and Fe are distributed across the MnOx surface, but are concentrated at the Co-Fe particle locations. Therefore, a MnOx film coupled with Co-Fe nanoparticles was successfully synthesized through sequential electrodeposition. The KOH electrolyte still has access to the MnOx for ORR.

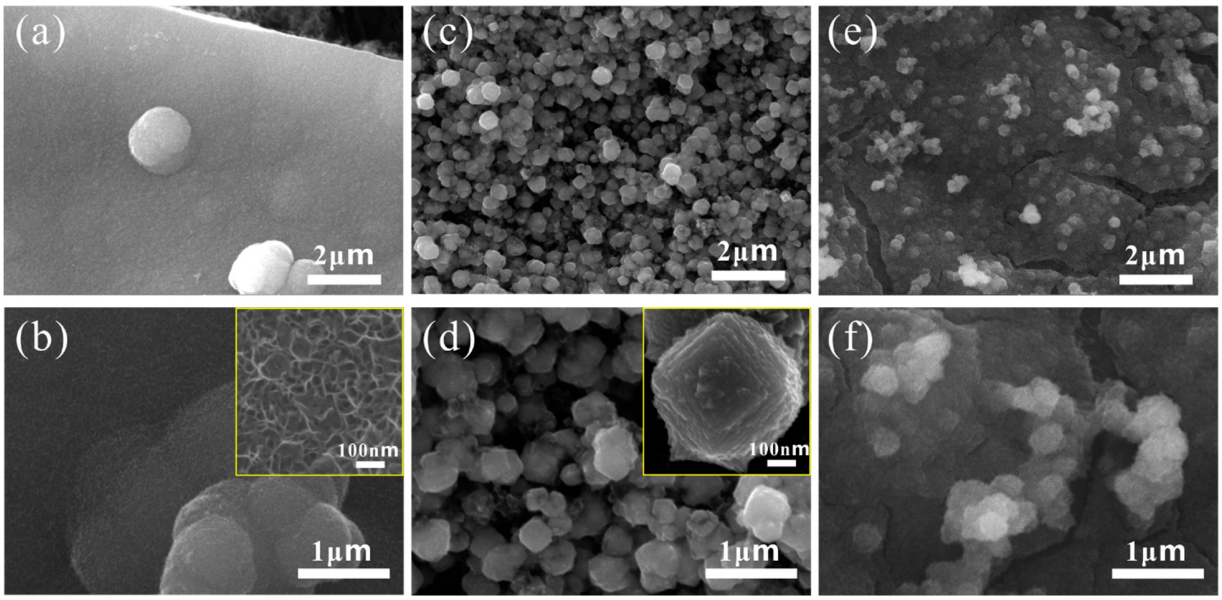

Fig. 5-2. SEM SE images of (a, b) MnOx on GDL; (c, d) Co-Fe on GDL; (e, f) MnOx/Co-Fe on GDL.

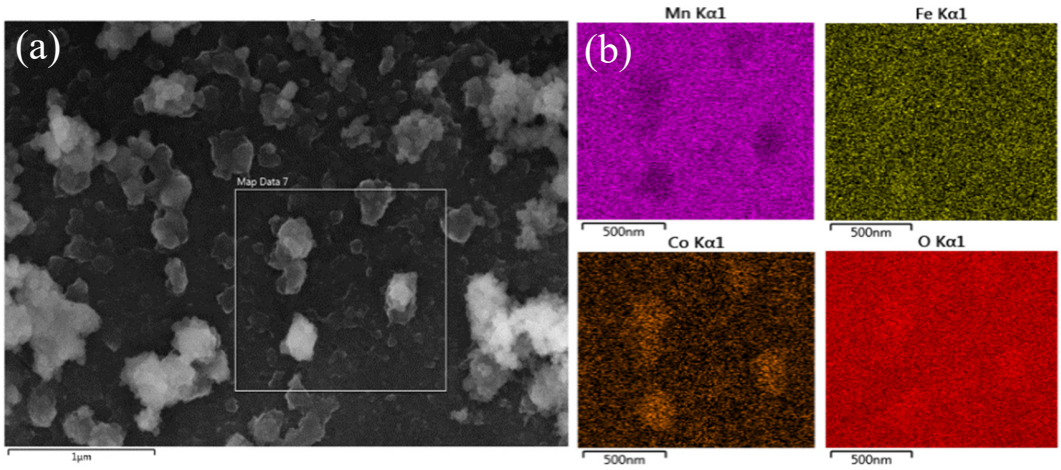

Fig. 5-3. (a) SEM SE image of MnOx/Co-Fe sequential deposit on GDL. (b) EDX elemental mapping images for Mn, Fe, Co and O obtained from the indicated region in (a).

The crystal structures of the separate MnOx and Co-Fe deposits were studied using XRD (Fig. 5-4). The diffraction peaks at 21.0° and 30.82° are from the PTFE (PDF File No. 54-1595) and graphite (PDF File No. 89-8487) in the GDL substrate, respectively. For the Co-Fe deposit on GDL, the peak at 52.80° corresponds to the (110) plane of the bcc Co-Fe solid solution. The deposit composition can be estimated from the Vegard equation, i.e., ~36 at% Fe in Co-Fe or $Co_{0.64}Fe_{0.36}$. There is only a weak, broad peak at 43.05° to 43.37° corresponding to MnOx, indicating its amorphous or nanocrystalline structure. There are several Mn dioxides with a major peak at or near the same angle (e.g., PDF File No. 53-0633, tetragonal Hollandite), so MnOx may be one form of α-MnO_2[269]. XPS data, presented later in this chapter, confirms that a significant portion of MnOx consists of Mn with a valence of 4+.

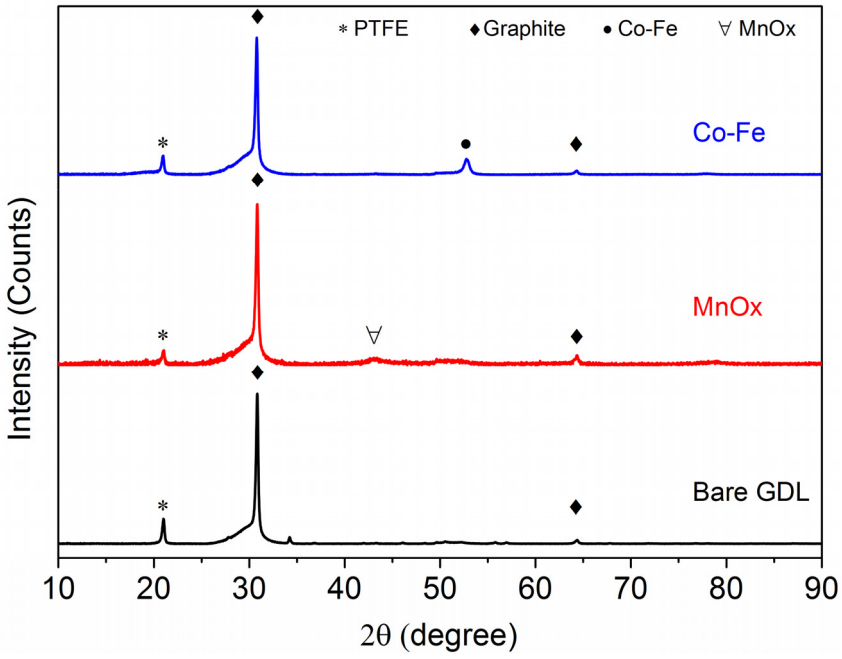

Fig. 5-4. XRD patterns for MnOx, Co-Fe and bare GDL.

Further investigation by TEM confirmed the amorphous nature of MnOx (Fig. 5-5). The SAED pattern only shows diffuse rings, which can be indexed to graphite; there are no separate, distinct rings for MnOx (Fig. 5-5(a)). It has been reported that the extent of disorder within electrodeposited MnOx will increase for depositions at higher current density, while a relatively dense deposit is generated with a low current density.[270]

The hybrid structure (MnOx/Co-Fe) was investigated by TEM. Co-Fe exists in two different forms: metallic nanoparticles and an amorphous mesh (Fig. 5-6(a)). The metallic particles are ~100 nm in size (red arrow) with the same crystal structure (bcc) as the Co-Fe electrodeposited separately (SAED pattern in Fig. 5-6(a)). The three concentric diffraction rings can be indexed to the (110), (200) and (211) planes of bcc Co-Fe. The Co/Fe ratio is ~2 (EDX spectrum in Fig. 5-6(b)), which is similar to the composition for the Co-Fe particles deposited separately. The particles contain a small amount of oxygen, due to surface oxidation when the deposit is exposed to air.[271] The amorphous region has a mesh-like appearance (yellow arrow and SAED pattern in Fig. 5-6(a)) and is more Fe-rich than the crystalline Co-Fe regions (compare the EDX spectra from the crystalline and amorphous Co-Fe regions in Fig. 5-6(c)). The oxygen level is significantly higher in the amorphous region, possibly due to the formation of metal hydroxide caused by the HER during cathodic electrodeposition of Co-Fe. The amorphous Co-Fe contains low levels of Mn, implying some degree of MnOx dissolution (less than 40%) and replacement with Co and Fe during Co-Fe deposition on MnOx. Co-Fe was also found in the form of extremely fine (~5 nm) nanocrystalline particles (Fig. 5-6(d)). The three concentric diffraction rings can be indexed to the (311), (400) and (440) planes of cubic spinel $(Co,Fe)_3O_4$. The Co/Fe ratio (1.22) can be estimated from the Vegard equation, giving a composition corresponding to $(Co_{0.55}Fe_{0.45})_3O_4$ which agrees with the EDX results in Fig. 5-6(e).

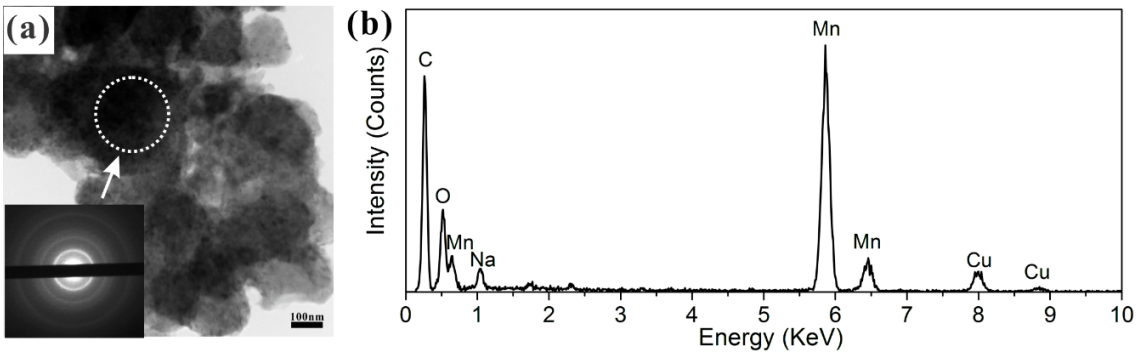

Fig. 5-5. (a) TEM bright field (BF) image of MnOx and SAED pattern (inset) of the region indicated. (b) EDX spectrum of the region indicated in (a).

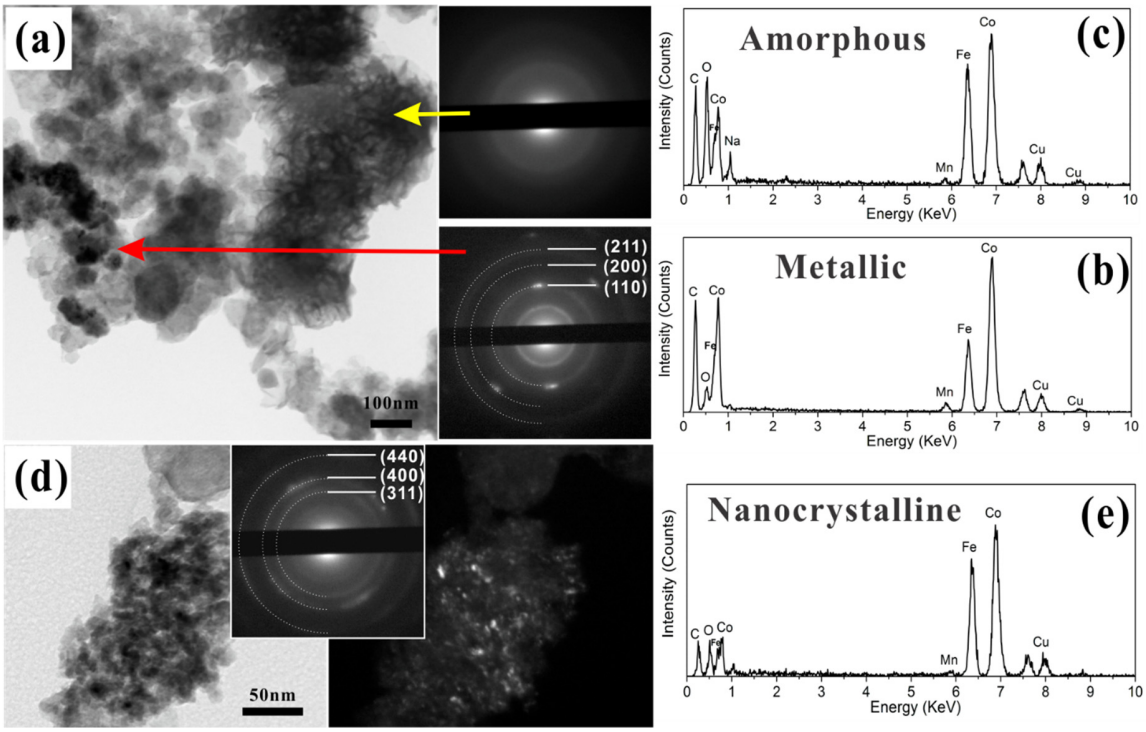

Fig. 5-6. (a) TEM BF image and SAED patterns from MnOx/Co-Fe deposit. (b) EDX spectrum from the metallic Co-Fe region (red arrow). (c) EDX spectrum from the amorphous Co-Fe region (yellow arrow). (d) BF image, SAED pattern and DF image from Co-Fe nanoparticles in MnOx/Co-Fe deposit. The DF image was obtained from part of the first two rings in the SAED pattern. (e) EDX spectrum from the Co-Fe nanoparticles in (d).

Normally, crystalline spinel M_3O_4 coatings (M= Co, Ni or Fe) can be prepared by electrodeposition through three different ways: (1) Anodic electrodeposition;[272, 273] (2) cathodic electrodeposition of metal followed by electrochemical oxidation (anodization) in an alkaline solution;[160, 274] (3) cathodic electrodeposition of metal hydroxide followed by thermal annealing at high temperature.[275, 276] In this study, the nanocrystalline spinel phase $(Co_{0.55}Fe_{0.45})_3O_4$ is generated by a different mechanism, since neither anodization nor thermal annealing was used after cathodic electrodeposition. According to the Ellingham diagrams for Mn, Co and Fe oxides, the standard Gibbs free energy changes at 300 K for the oxidation of Co and Fe to the spinel phases are as follows:[277]

$$3/2\ Co + O_2 \rightarrow 1/2\ Co_3O_4 \qquad \Delta G° = -390\ kJ \qquad (5\text{-}1)$$

$$3/2\ Fe + O_2 \rightarrow 1/2\ Fe_3O_4 \qquad \Delta G° = -520\ kJ \qquad (5\text{-}2)$$

The oxide in this work is a mixed Co-Fe spinel, so the standard free energy change will be between the above two values:

$$3/2\ [0.55\ Co + 0.45\ Fe] + O_2 \rightarrow 1/2\ (Co_{0.55}Fe_{0.45})_3O_4 \qquad \Delta G° = -450\ kJ \qquad (5\text{-}3)$$

The standard free energy for the reduction of MnO_2 to Mn_2O_3 is:[278]

$$4\ MnO_2 \rightarrow 2\ Mn_2O_3 + O_2 \qquad \Delta G° = 90\ kJ \qquad (5\text{-}4)$$

MnO_2 was chosen as the initial form of MnOx based on the XPS results presented later in this section. Therefore, the free energy change for the reduction of MnO_2 to Mn_2O_3 by Co and Fe is

given by the sum of the standard free energies for reactions (5-3) and (5-4). Note, that this is the free energy change for standard state conditions; however, the large negative free energy change indicates that there will still be a significant driving force for the reduction of MnO_2 in the presence of Co and Fe even under non-standard state conditions.

$$8\ MnO_2 + 3\ [0.55\ Co + 0.45\ Fe] \rightarrow (Co_{0.55}Fe_{0.45})_3O_4 + 4\ Mn_2O_3 \qquad \Delta G° = -720\ kJ \qquad (5\text{-}5)$$

The surface compositions of the MnOx, Co-Fe and MnOx/Co-Fe deposits were investigated using XPS (Fig. 5-7). The O 1s spectrum for the MnOx deposit was deconvoluted into three components: O-M(Mn)-O, M(Mn)-O-H and H-O-H (Fig. 5-7(a)).[279] Quantitative calculations (Fig. 5-7(a)) show more oxide than hydroxide with an oxide/hydroxide ratio of 3.6. The binding energy for the H_2O peak is 532.45 eV, suggesting chemisorbed or structurally bound water.[280] The fitting procedure for Mn $2p_{3/2}$ is based on the data reported in the literature.[281] Mn $2p_{3/2}$ was deconvoluted into different components belonging to Mn^{+4} and Mn^{+3} after considering the binding energy, the full width at half maximum (FWHM) and the relative intensity. The normalized compositions of Mn^{+4} and Mn^{+3} are 62.9 at% and 37.1 at%, respectively. Therefore, the MnOx film should be a mixture of MnO_2 and $MnOOH/Mn_2O_3$, with more MnO_2. It has been reported that the pathway for MnO_2 electrodeposition is dependent on the acidity of the supporting electrolyte.[171] Accordingly, initial precipitation of MnOOH on the GDL surface, followed by incomplete solid state oxidation to MnO_2 should be favored in this work since a near neutral electrolyte (pH= 6.7) was used.[170]

For the Co-Fe deposit, a weak O-M-O peak and a relatively strong M-O-H peak with an oxide/hydroxide ratio of 0.4 indicate a hydroxide-like environment that dominates the surface (Fig. 5-7(b)). The fitting procedure for the Co-Fe deposit is based on the data reported in the literature.[282]

The Co $2p_{3/2}$ peak of the Co-Fe deposit is composed of Co^{2+} components and Co^{0} metal (778.35 eV), indicating that the surface was not fully oxidized after electrodeposition. In addition, the Co LMM Auger peak at 775.87 eV is visible in the XPS spectrum.[282] The Fe LMM Auger peak at 786.69 eV (green arrow) is also present and contributes to the Co $2p_{3/2}$ spectrum. The Fe $2p_{3/2}$ peak can be deconvoluted into Fe^{3+} (710.79 eV) and Fe^{0} metal (706.55 eV). Therefore, Co-Fe (oxy)hydroxide generated on the surface of the Co-Fe alloy will provide the primary active sites to catalyze OER.

Cathodic electrodeposition of Co-Fe on MnOx changed the XPS spectra for both materials (Fig. 5-7(c)). The O 1s peak for the MnOx/Co-Fe sequential deposit shows an oxide/hydroxide ratio of 0.5, which is between the values for the separate MnOx and the Co-Fe samples. The Mn $2p_{3/2}$ spectrum shows that the Mn^{4+} was reduced to Mn^{3+} after cathodically depositing a layer of Co-Fe on MnOx. The metal phase disappeared in both the Co $2p_{3/2}$ and Fe $2p_{3/2}$ spectra, but the oxidation states for Co (Co^{2+}) and Fe (Fe^{3+}) remained unchanged. In addition, the peak at 786.63 eV in the Co $2p_{3/2}$ part of the spectrum became stronger compared with the Co-Fe sample. This component was attributed to the Fe LMM Auger line as explained before. The same trend was reported in the literature, with a stronger shoulder in the Co $2p_{3/2}$ peak when more Fe^{3+} was incorporated into $Co(OH)_2$.[193] As such, these results suggest that there is more Fe in Co-Fe when it is deposited onto MnOx. The TEM analysis in Fig. 5-6 is consistent with the XPS results, i.e., the amorphous Co-Fe hydroxide and nanocrystalline spinel ($(Co_{0.55}Fe_{0.45})_3O_4$) which form in the MnOx/Co-Fe deposit are more Fe-rich compared with the solid solution phase that forms in the separate Co-Fe deposit ($Co_{0.64}Fe_{0.36}$).

(a) MnOx

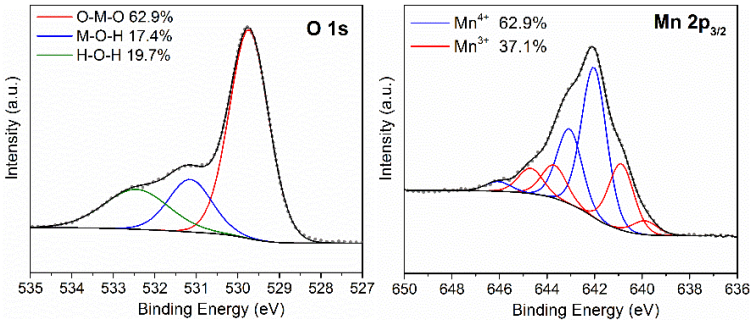

(b) CoFe

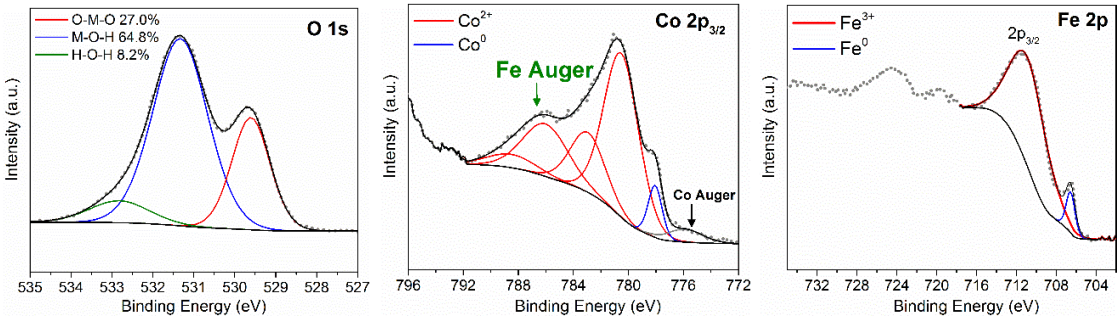

(c) MnOx/Co-Fe

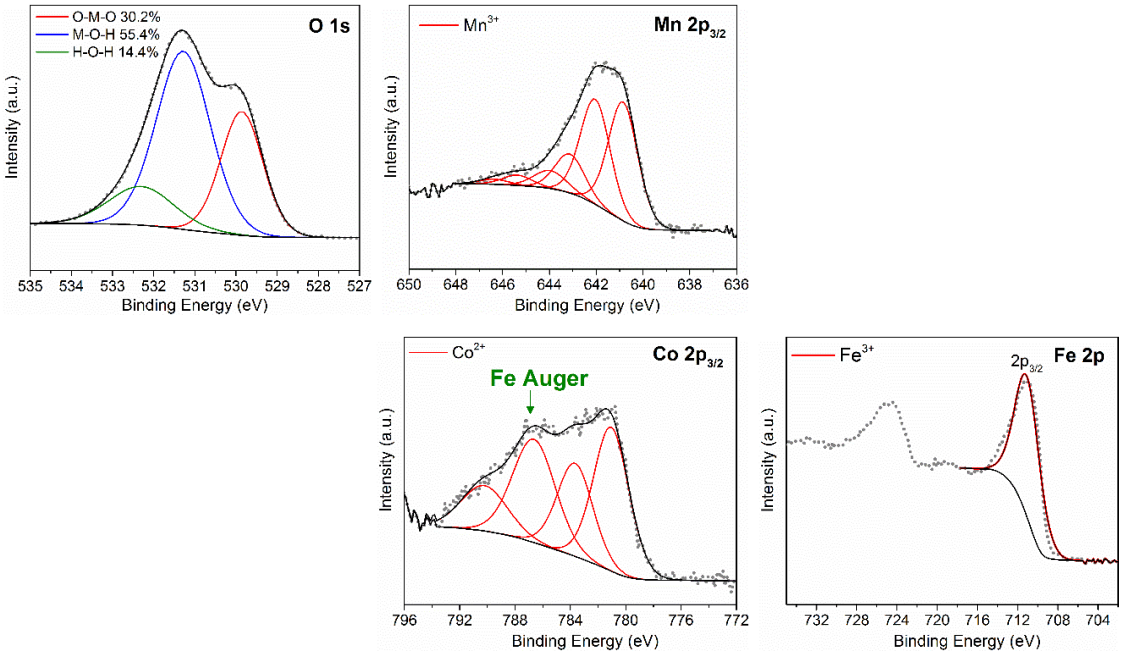

Fig. 5-7. XPS spectra for the three types of deposits, i.e., (a) MnOx, (b) Co-Fe and (c) MnOx/Co-Fe.

Electrochemical performance

Fig. 5-8(a) shows CV curves for the catalysts cycled in oxygen saturated 6 M KOH solution. The current at -0.25 V is derived from ORR and the current at 0.7 V is produced by OER. Thus, this test can provide information for both ORR and OER electrocatalytic capabilities of the catalysts. The ORR and OER activities of MnOx, Co-Fe and MnOx/Co-Fe are compared. In terms of ORR activity, MnOx has better performance than Co-Fe as expected and its performance is improved by sequentially depositing a Co-Fe layer (MnOx/Co-Fe). For MnOx/Co-Fe compared with MnOx the mass loading increased by 0.2 mg cm^{-2} or 20%, but the ORR current density at -0.25 V increased by 44% from 12.5 mA cm^{-2} to 18 mA cm^{-2}. The OER current density at 0.7 V increased by 54% from 17.5 mA cm^{-2} to 27 mA cm^{-2}, with a more negative onset potential. In addition, the shape of the MnOx/Co-Fe CV curve changed with a bump appearing at 0.1 V. MnOx may experience some dissolution during cathodic electrodeposition of Co-Fe, meaning less MnOx is present in MnOx/Co-Fe. However, MnOx/Co-Fe still performs better than the MnOx sample in terms of ORR activity. If it is assumed that the mass of MnOx does not change during Co-Fe deposition, then only 0.2 mg cm^{-2} of Co-Fe was coated onto the MnOx, but the OER performance was much better compared with pure MnOx. These observations indicate that the improvements for MnOx/Co-Fe relative to MnOx are not simply from the increase in mass loading, but also from a synergistic effect of the two materials. Amorphous MnOx can provide numerous active sites for oxygen adsorption and deliver discharge power comparable to 20% Pt/C in a Zn-air battery after combining with Ketjenblack carbon to improve its electrical conductivity.[283]

The improved ORR activity for MnOx/Co-Fe, relative to MnOx alone, may be related to the reduced oxidation state of Mn. The specific ORR electrocatalytic activity of MnOx increases exponentially with the potential of the Mn^{4+}/Mn^{3+} redox couple and $MnOOH/Mn_2O_3$ has a higher

formal potential than MnO_2 for this transition.[87] Therefore, the better ORR activity of MnOx/Co-Fe compared with MnOx may be due to the change in oxidation state from Mn^{4+} to Mn^{3+} as demonstrated in the XPS analysis. The addition of $Ni(OH)_2$ into MnOx by reducing an amorphous MnO_2/C suspension, in the presence of Ni^{2+} with $NaBH_4$, has also been reported to stabilize the morphology and phase of the active material.[284] ORR activity was improved due to the higher MnOOH content after adding the reducing agent $NaBH_4$.[285] An increasing level of Mn^{3+} may be expected to decrease the conductivity of MnOx; however, EIS results demonstrate that the electrical properties of MnOx/Co-Fe are enhanced by the Co-Fe coating, as will be shown later.

The CV curves for MnOx and MnOx/Co-Fe show typical behavior for an electrochemical capacitor, due to pseudocapacitive reactions occurring on the surface of Mn oxide (Fig. 5-8(a)).[286] In contrast, Co-Fe shows no obvious capacitive current but has a Co^{2+}/Co^{3+} redox peak at around 0.1 V.[98] Co-Fe is a much better OER catalyst than MnOx, as confirmed in Chapter 3. The large active surface area of the Co-Fe nanoparticles, as shown by SEM and TEM analysis, can facilitate the OER reaction. MnOx/Co-Fe has higher OER activity than pure Co-Fe. According to the literature, amorphous MnOx can act as an OER catalyst as well.[287] The Pourbaix diagram of Mn shows that MnO_2 tends to dissolve under high anodic potential, even in alkaline solutions[265]. Therefore, a low OER potential or charging voltage is desired when using MnO_2 in the bifunctional catalysts, which was achieved by coating the Co-Fe OER active layer onto MnO_2 in this work. In addition, the Co-Fe layer covering MnO_2 has more contact with the KOH electrolyte and acts as the primary OER active sites, reducing the negative impact of the oxygen evolution process. Therefore, in terms of both ORR and OER activity, MnOx/Co-Fe performs better than either MnOx or Co-Fe alone, making it a promising bifunctional catalyst. CV scans for Ar saturated electrolyte and oxygen saturated electrolyte (both 6 M KOH) are compared in Fig. 5-8(e) and 5-

8(f). The ORR current was diminished when Ar was purged into the electrolyte for all three samples, while the OER current increased for Co-Fe and MnOx/Co-Fe (dashed line). The CV scan for the Ar saturated electrolyte shows that MnOx/Co-Fe has a higher capacity than MnOx (dashed line in Fig. 5-8(e)), so the better ORR activity may be partly from the larger surface area.

The MnOx/Co-Fe sample was cycled 100 times to test its durability and compared with commercial Pt/C (Fig. 5-8(b)). The ORR current density for MnOx/Co-Fe at -0.25 V decreased by 16% from the 10^{th} to the 100^{th} cycle, while the ORR current density for Pt/C dropped by 73%. The plot in Fig. 5-8(c) shows that the ORR current for Pt/C decreased rapidly after 30 cycles, possibly due to the detachment of active material from GDL or catalyst particle agglomeration.[288] In contrast, the ORR current for MnOx/Co-Fe was stable during cycling. The OER performance of MnOx/Co-Fe was much better in terms of both activity and durability than Pt/C (Fig. 5-8(d)). These results indicate the combined MnOx/Co-Fe catalysts are more stable than Pt/C during cycling from the ORR to the OER potential range and are good candidates as bifunctional catalysts in Zn-air batteries.

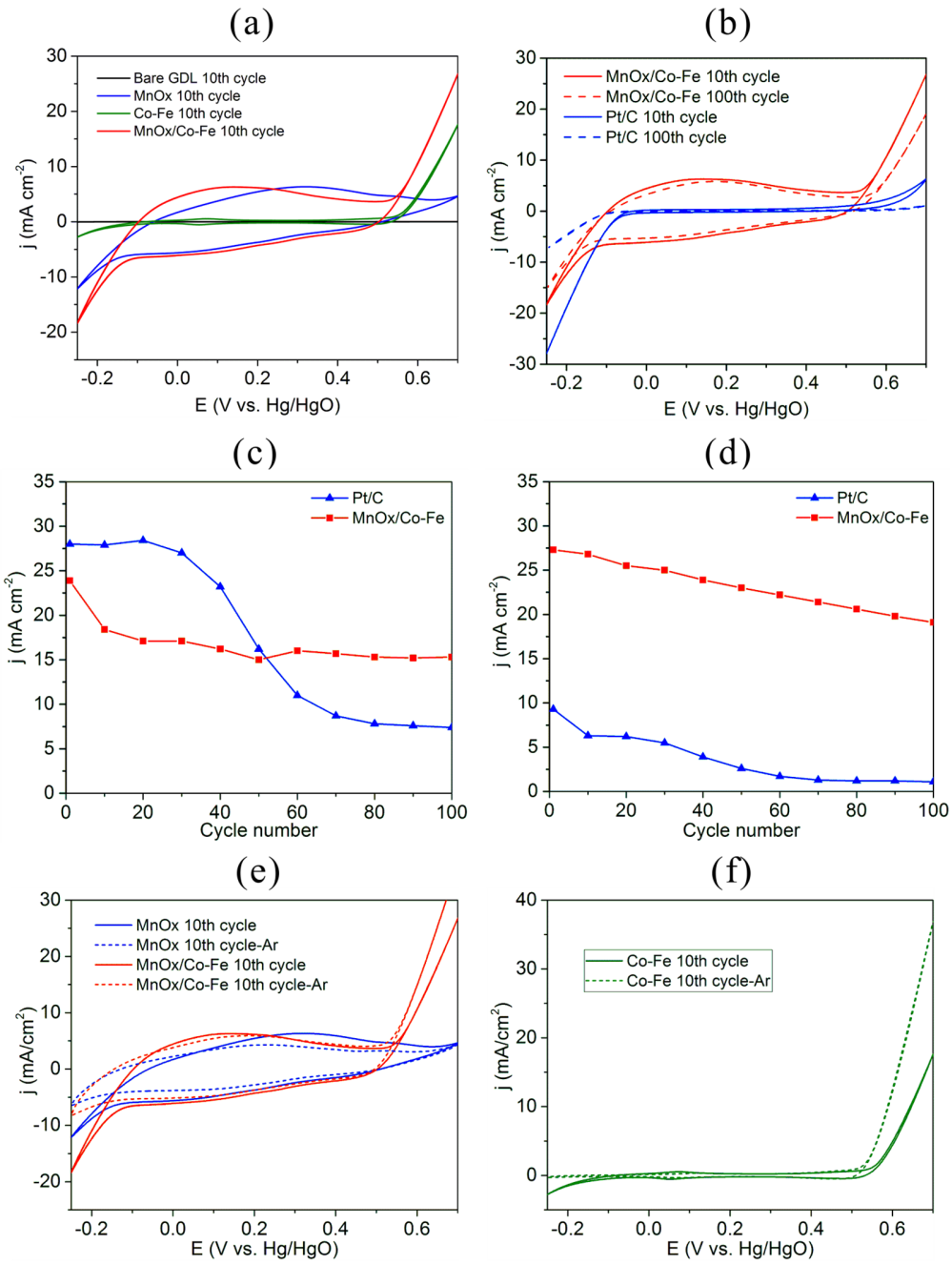

Fig. 5-8. (a) CV curves for different catalysts in oxygen saturated 6 M KOH, cycled from -0.25 V to 0.7 V. (b) CV curves for MnOx/Co-Fe and Pt/C at the 10th and 100th cycles in oxygen saturated 6 M KOH. (c) Current density as a function of cycle number at -0.25 V. (d) Current density as a function of cycle number at 0.7 V. (e) CV scans for MnOx and MnOx/Co-Fe in oxygen and Ar saturated 6 M KOH. (f) CV scans of Co-Fe in oxygen and Ar saturated 6 M KOH.

Battery performance

Three different catalyst materials (MnOx, MnOx/Co-Fe and Pt/C)) were assembled into Zn-air batteries for discharge-charge tests at different current densities (1, 2, 5 and 10 mA cm^{-2}). Fig. 5-9(a) shows that Pt/C has the highest discharge potential, because its ORR activity is the highest, followed by MnOx/Co-Fe. At a current density of 10 mA cm^{-2}, the cell with MnOx/Co-Fe catalysts is able to discharge at 1.24 V vs. Zn/Zn^{2+}, which is higher than the discharge potential for either MnOx (1.16 V) or Co-Fe (1.08 V). Moreover, MnOx/Co-Fe has the lowest charge potential among all samples. This performance confirms the CV results in Fig. 5-8(a). The efficiencies calculated from Fig. 5-9(a) are plotted for different current densities (Fig. 5-9(b)). The cell with MnOx/Co-Fe catalysts has the highest efficiency at nearly all current densities. The efficiency is 62% at 10 mA cm^{-2}, which is higher than the 60% efficiency of Pt/C. Fig. 5-9(c) shows that Pt/C performs the best during discharge polarization, followed by MnOx/Co-Fe, which has the lowest charge polarization potential. The above battery tests were performed with pure oxygen. Battery performance with MnOx/Co-Fe and Pt/C were compared in ambient air as well (Fig. S5-12). Batteries with both catalysts have lower discharge potential in ambient air due to the lower oxygen concentration. The discharge-charge efficiency of MnOx/Co-Fe is almost the same as Pt/C in ambient air.

Potentiostatic EIS was performed at 1.1 V vs. Zn/Zn^{2+} for the Zn-air battery, with different catalysts, to evaluate the electrical properties of the electrodes. The impedance data were fit using Z-Fit software, with the equivalent circuit shown in Fig. 5-9(d), and the values of fitted parameters are listed in Table 5-1. The Nyquist plots reveal that the three samples have similar solution resistances (R_s), but have different solid-electrolyte interface resistances (R_{int}) and charge transfer resistances (R_{ct}).[289] The R_{int} value of MnOx/Co-Fe is half that of MnOx, indicating easier

interfacing with the electrolyte after coating with Co-Fe.[142] In addition, R_{ct} for MnOx/Co-Fe is greatly reduced compared with MnOx, showing almost the same value as Pt/C. The enhanced electrical properties of MnOx/Co-Fe relative to MnOx can be attributed to the thin layer of conductive Co-Fe nanoparticles.

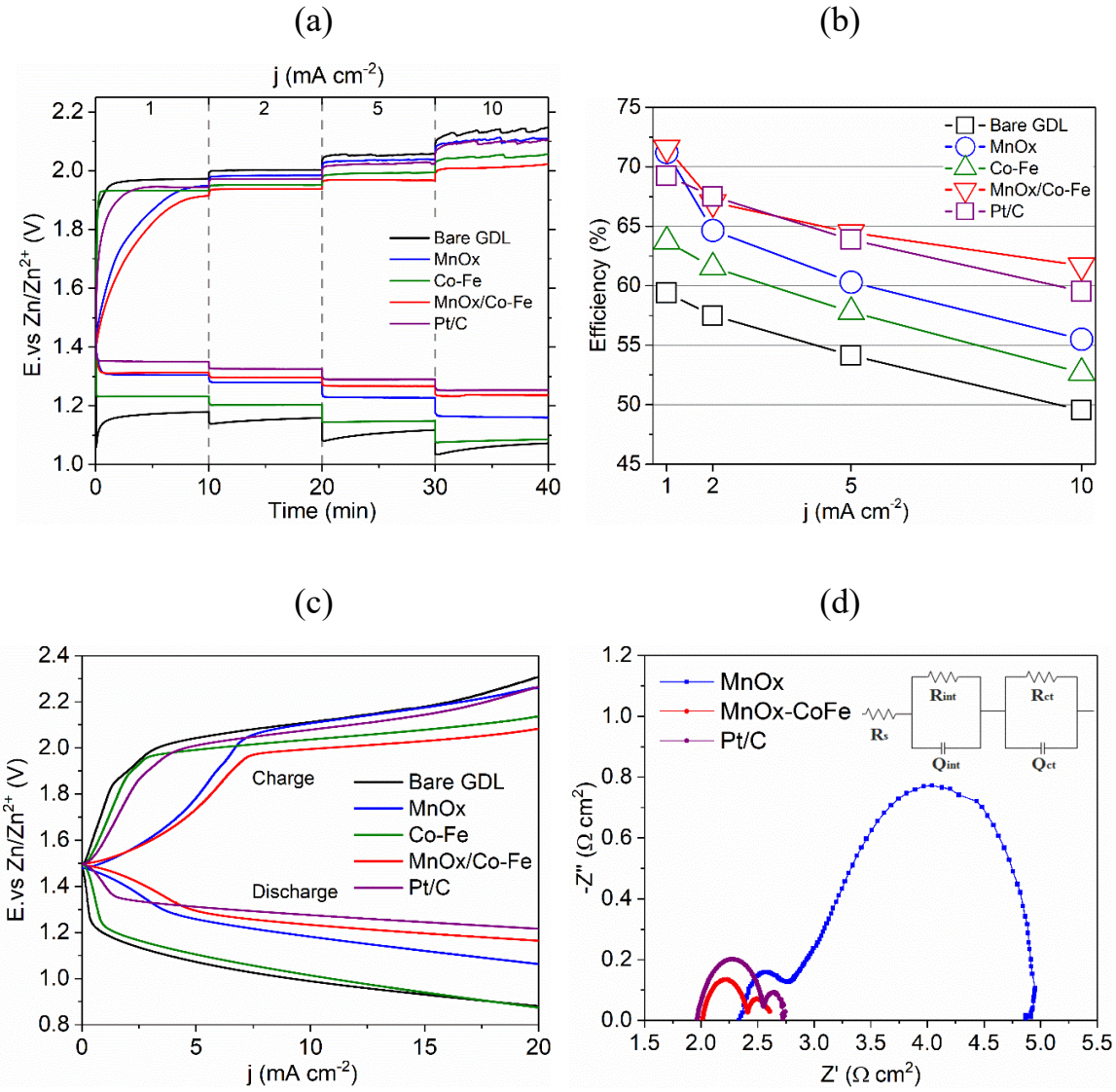

Fig. 5-9. (a) Rate discharge-charge curves for Zn-air batteries. (b) Discharge-charge efficiencies for Zn-air batteries at various current densities. (c) Discharge-charge polarization curves for Zn-air batteries. (d) Electrochemical impedance spectra for Zn-air batteries at 1.1 V vs. Zn/Zn^{2+}.

Table 5-1. Equivalent circuit elements based on EIS analysis of Pt/C, MnOx/Co-Fe and MnOx

	Pt/C	MnOx/Co-Fe	MnOx
R_s (Ω cm^2)	1.96	2.00	2.27
R_{int} (Ω cm^2)	0.61	0.40	0.81
R_{ct} (Ω cm^2)	0.17	0.21	1.89

During discharge-charge cycling at 5 mA cm^{-2} (Fig. 5-10(a)), the cell with MnOx/Co-Fe had an average discharge potential of 1.18 V vs. Zn/Zn^{2+}, which is slightly lower than the cell with Pt/C with an average discharge potential of 1.21 V vs. Zn/Zn^{2+}. Due to the better OER activity of MnOx/Co-Fe, its cell can charge at an average potential of 1.98 V vs. Zn/Zn^{2+}, which is lower than the 2.03 V vs. Zn/Zn^{2+} for the cell with Pt/C. The declining discharge potential for the Pt/C cell can be attributed to two factors. The first is the poor stability of Pt/C particles when cycled between cathodic and anodic potentials, which was confirmed by the CV cycling test in Fig. 5-8(b). The second reason relates to flooding of the electrolyte into the pores of the air electrode, which limits diffusion of air and impairs the three-phase reaction zone for ORR. This influences the MnOx/Co-Fe sample as well.[22] For the OER part, the charge potential of Pt/C increases with cycling, while the charge potential of MnOx/Co-Fe remains almost the same throughout the whole test. Therefore, both the MnOx/Co-Fe and Pt/C cells have almost the same efficiency of 59.6%.

Discharge-charge polarization was conducted again after the cycling tests and shows that MnOx/Co-Fe performs better than Pt/C (Fig. 5-10(b)). The cell with MnOx/Co-Fe catalysts was then cycled for 40 h to test the catalyst's durability in a Zn-air battery. Fig. 5-11(a) presents the galvanostatic discharge-charge curve for the cell. The discharge potential gradually decreased after 20 h of cycling. One possible reason for the decrease is blocking of oxygen diffusion caused by flooding of electrolyte into the air electrode.[290] There was no obvious peeling of the MnOx/Co-

Fe layer from the GDL substrate (insets of Fig. 5-11(b) and 5-11(d)). SEM images show that there are more cracks on the electrode surface after cycling, but no obvious morphology changes, other than the cracking, were observed (Fig. 5-11(b)-(e)). The cracks may be produced by MnOx phase changes when cycled between ORR and OER potentials.[291] EDX analysis of the GDL surface demonstrates that the composition did not change much after cycling, other than the presence of small amounts of Zn and K from the electrolyte (Table 5-2). Thus, the MnOx/Co-Fe bifunctional catalysts exhibit excellent structural stability in terms of morphology and composition during battery cycling.

(a)

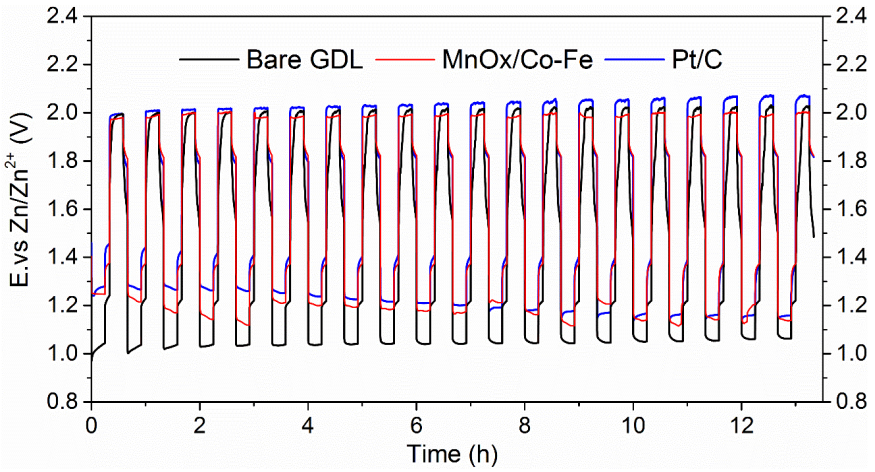

(b)

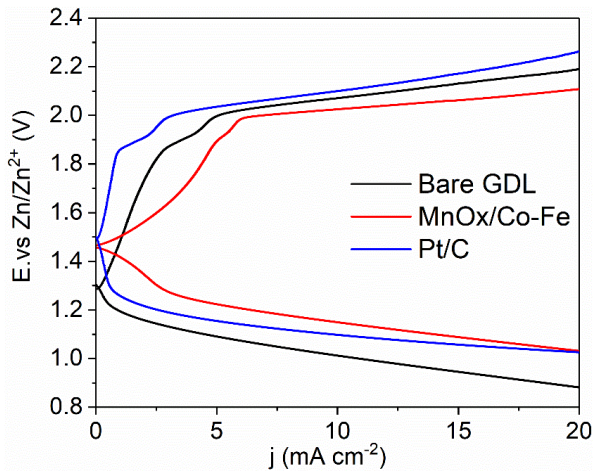

Fig. 5-10. (a) Discharge-charge cycling performance for Zn-air batteries at 5 mA cm^{-2}. (b) Discharge-charge polarization curves after cycling.

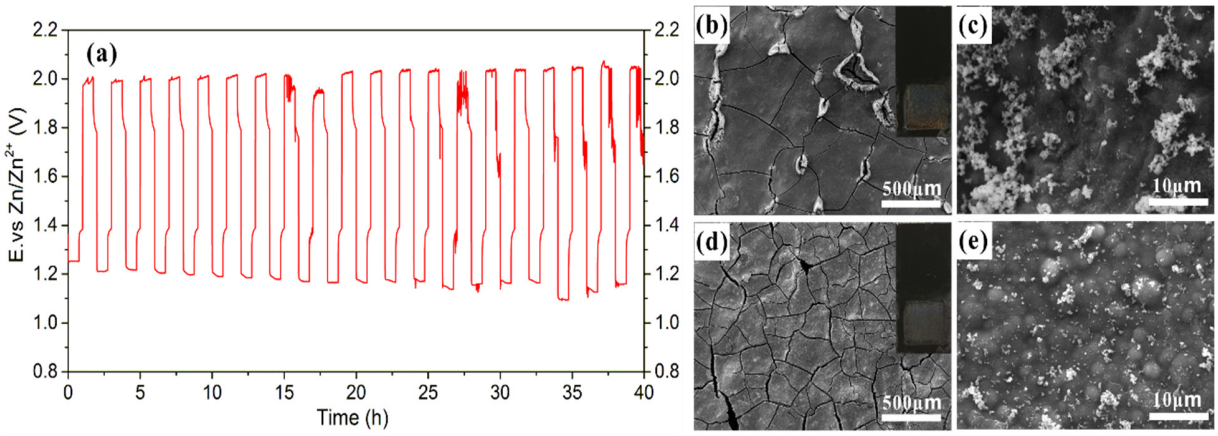

Fig. 5-11. (a) Discharge-charge cycling at 5 mA cm^{-2} for Zn-air battery with MnOx/Co-Fe catalysts. (b, c) SEM SE images of MnOx/Co-Fe catalyst layer before cycling. (d, e) SEM SE images of MnOx/Co-Fe catalyst layer after cycling. The insets show the visual appearance of MnOx/Co-Fe catalyst layer on GDL before and after cycling.

Table 5-2. Composition of catalyst layer before and after 40 h cycling test (at%)

Condition	Mn	Co	Fe	C	O	Na	K	Zn
Before cycling	21.6%	0.7%	0.5%	6.5%	67.6%	3.2%	0	0
After cycling	20.8%	0.6%	0.3%	0	68.7%	0	7.8%	1.9%

The MnOx/Co-Fe sample was immersed into the Zn-air battery electrolyte (6 M KOH + 2% ZnO) for 6 days to further confirm its stability. The same location at the center of the electrode was selected for analysis. Other than cracks on the surface, there were no major changes in the morphology (Fig. S5-13 and Table S5-3).

5.4 Summary

MnOx and Co-Fe were sequentially electrodeposited on carbon paper to fabricate bifunctional catalysts MnOx/Co-Fe for Zn-air batteries. The MnOx, Co-Fe and MnOx/Co-Fe structures were confirmed by SEM, TEM, XRD and XPS analysis. MnOx was initially deposited as an amorphous mixture (MnO_2/MnOOH) and was then reduced to Mn_2O_3/MnOOH after coating with Co-Fe nanoparticles. The electrochemical properties of the hybrid MnOx/Co-Fe catalysts were measured, showing higher ORR and OER activity compared with MnOx and Co-Fe alone. The synergistic effect is related to the reduced Mn oxidation state, higher surface area and lower charge transfer resistance. A Zn-air battery using MnOx/Co-Fe catalysts exhibited good discharge-recharge performance and a cycling efficiency of 59.6% (at 5 mA cm^{-2}) that is comparable with Pt/C catalysts . Electrodeposited MnOx/Co-Fe showed strong adhesion to GDL and was stable throughout 40 h of battery cycling.

5.5 Supporting information

Comparison of discharge-charge performance in oxygen and in air

In this study, the battery tests were run with a constant flow of oxygen to prevent the influence of oxygen concentration on performance and to avoid K_2CO_3 precipitation in the air electrode. Battery performance with MnOx/Co-Fe and Pt/C were compared in ambient air as well, as shown in Fig. S5-12. Batteries with both catalysts have lower discharge potential in ambient air due to the lower oxygen concentration. The discharge-charge efficiency of MnOx/Co-Fe is still almost the same as Pt/C in ambient air.

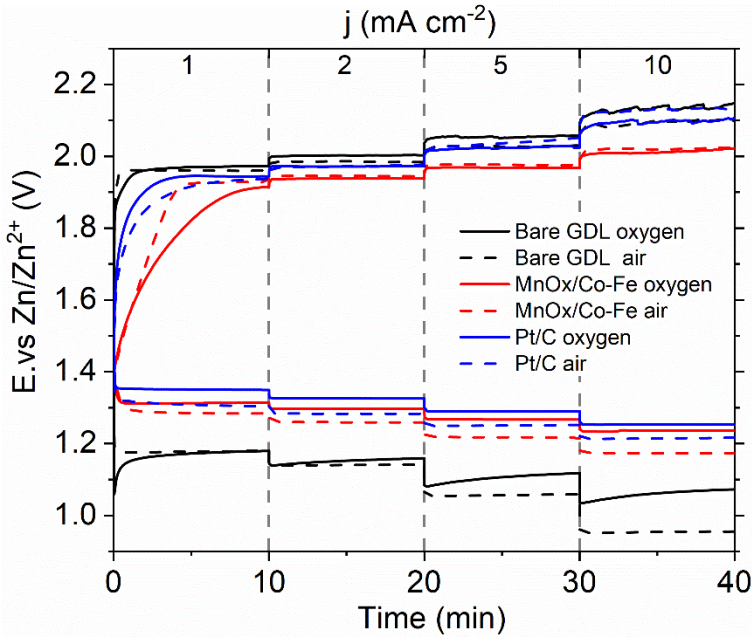

Fig. S5-12. Comparison of rate discharge-charge performance in oxygen and in air.

Morphology and composition change of MnOx/Co-Fe after 6 days of immersion in electrolyte

The MnOx/Co-Fe sample was immersed into the Zn-air battery electrolyte (6 M KOH + 2% ZnO) for 6 days to further confirm its stability. The same location at the center of the electrode was selected for analysis. Other than cracks on the surface, there were no major changes in the morphology (Fig. S5-13).

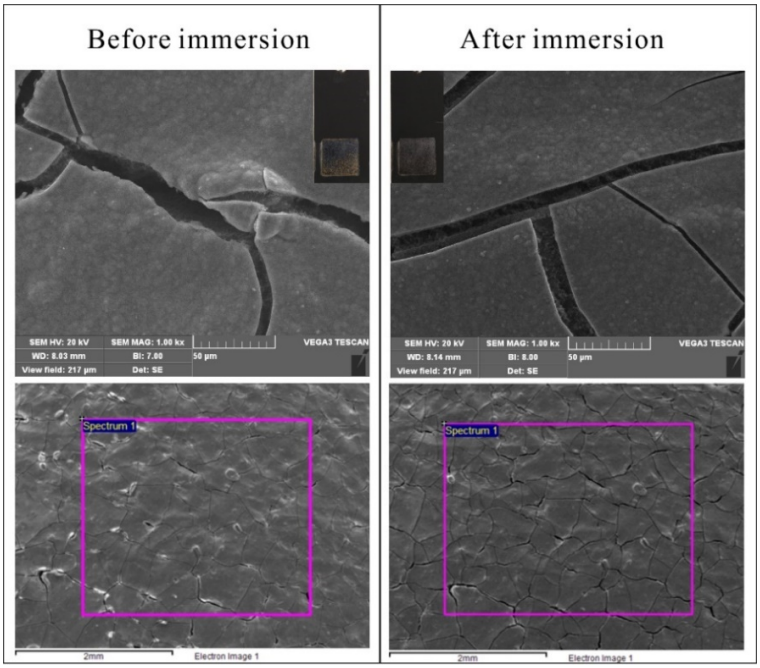

Fig. S5-13. Morphology of MnOx/Co-Fe sample before and after 6 days of immersion; the regions in the square were selected for EDX analysis (Table S5-3).

Table S5-3. Composition of MnOx/Co-Fe sample catalyst layer before and after immersion in 6 M KOH + 2% ZnO for 6 days (at%)

Condition	Mn	Co	Fe	C	O	Na	K	Zn
Before immersion	22.5%	0.7%	0.5%	9.9%	64.6%	1.9%	0	0
After immersion	19.1%	0.8%	0.5%	13.6%	60.2%	0	5.4%	0.5%

Chapter 6 : A horizontal Zn-Air battery with physically decoupled OER and ORR electrodes

A version of this Chapter has been published in the Journal of Power Sources:

M. Xiong, M.P. Clark, M. Labbe, D.G. Ivey, A horizontal zinc-air battery with physically decoupled oxygen evolution/reduction reaction electrodes, *Journal of Power Sources*, 393 (2018) 108-118. (10.1016/j.jpowsour.2018.05.004)

6.1 Introduction

Electrically rechargeable Zn-air batteries have gained renewed interest among the various technologies available because of their high theoretical energy density and low cost.[54, 292] As an open system, Zn-air batteries need to work in an environment where the air quality can be monitored and controlled. Humid air can cause air electrode flooding while dry air can cause rapid electrolyte evaporation.[293] A Zn-air battery cannot last very long in ambient air due to the presence of CO_2 in the atmosphere. CO_2 can react with KOH and precipitate as K_2CO_3 that gradually blocks the pores in the gas diffusion layer.[18] Therefore, the most suitable application for a Zn-air battery is stationary energy storage. Several start-up Zn-air companies in stationary energy storage have entered the market in recent years, such as EOS Energy, Fluidic Energy, WatTech Power and ZincNyx Energy Solutions. All these companies emphasize the advantages of Zn-air batteries, such as safety, affordability and scalability from kW to MW systems. The most important consideration then is to extend the lifetime as much as possible.

The large-scale industrial deployment of zinc-air batteries has been hampered by several problems, i.e., low round-trip energy efficiency and poor cycling stability. A rechargeable Zn-air battery

requires active catalysts for the ORR and OER to improve discharge-charge efficiency. The catalysts for ORR and OER can be integrated into one electrode or can work separately.[247, 294, 295] An electrode integrated with both ORR and OER catalysts or bifunctional catalysts has several problems. Firstly, synthesis of bifunctional catalysts with high catalytic activity toward both ORR and OER is difficult, requiring complex fabrication procedures. However, catalysts that are active for either ORR or OER can be synthesized by relatively simple methods. Some are made from non-precious metals, like carbon-based materials (e.g., N-doped carbon), transition metal oxides (e.g., Co_3O_4) or perovskites,[296-298] with higher activity and/or durability than some noble metal-based catalysts (e.g., Pt, Ru, IrO_2). Secondly, the support materials also have a significant influence on the performance of catalysts.[299] Carbon-based substrates, which are often used for ORR catalyst loading, are vulnerable during the high-voltage charge process.[300] An electrode with a carbon substrate will gradually lose its function during the charging process due to corrosion of the carbon. Finally, the charging and discharging processes for Zn-air batteries have different requirements for the electrodes. The discharge process is driven by ORR and requires an air electrode that is not flooded by the electrolyte. The charging process during which OER happens, on the other hand, is more favored when the electrode is submerged in the electrolyte. As such, it is beneficial from a cycling efficiency point of view if the ORR and OER catalysts are synthesized and loaded on separate substrates. The high voltage during charging is detrimental to many materials due to their high solubility in alkaline solutions, according to Pourbaix diagrams.[301] These materials include carbonaceous materials that are used as the support material for ORR catalysts and conductive agents (carbon black, graphite, etc.), several transition metal oxide catalysts like MnOx and noble metals such as Pt. All these materials are damaged by high charge potentials and would be more durable if they were only subjected to reducing discharge potentials. Other metal oxides like Ni-

Fe or Co-Fe (oxy)hydroxide are stable and OER active under high charge potentials, making them good candidates as an independent electrode for charging.[302, 303] Therefore, a design that incorporates physically decoupled electrodes for discharging and charging is able to provide more flexibility to optimize ORR and OER electrocatalytic behavior.[304]

Several attempts have been made to use physically decoupled electrodes in Li-air and Zn-air batteries.[305-307] Most of these use a traditional setup with vertically deployed electrodes.[308] This configuration allows for easy assembly of the electrodes but does not tailor the environment for the needs of each electrode. A vertical Zn anode will have the reaction product (Zn dendrites) deposited mostly at the bottom of the cell due to gravity effects, leading to a higher risk of short-circuiting. A vertical ORR electrode will have the same liquid pressure on its surface as that on an OER electrode. Such a high pressure could easily cause flooding of the ORR electrode by the electrolyte and reduce the amount of three-phase boundaries, even if hydrophobic carbon paper is used as the substrate.[309] In practical terms, the high pressure induced by a large quantity of electrolyte could lead to physical destruction of the fragile carbon paper. Zn-air batteries with all the electrodes in a horizontal configuration have been reported to improve cycle life and performance durability.[310-312] In this study we have developed a Zn-air battery hybrid design with a horizontally arranged ORR electrode and Zn electrode, but with a vertical OER electrode (Fig. 6-1(a) and (b)). The ORR electrode is placed on top of the cell to reduce the electrolyte pressure on it. The OER electrode is vertically immersed in the electrolyte to enable full contact with the electrolyte and ensure easy exhaust of generated oxygen during OER.[313] Internal short-circuiting caused by Zn dendrite formation during repeated cycling is the primary failure mode of rechargeable Zn-air batteries.[314] Zinc dendrites can grow progressively on repeated cycling and cause an internal short circuit.[315, 316] Sufficient space was left between the electrodes to prevent

this from happening. In order to avoid manual switching between the ORR and OER electrodes, two channels of a potentiostat are synchronized to perform discharge and charge alternately (Fig. 6-1(b)).

MnOx is anodically electrodeposited on carbon paper as the ORR catalyst and Co-Fe is cathodically electrodeposited on Ni foam as the OER catalyst. The MnOx layer has been identified as a combination of Mn_3O_4 (hausmannite) and α-Mn_2O_3 (bixbyite), both of which have been reported as highly active ORR catalysts.[317, 318] Mn_3O_4 has been synthesized as an ORR catalyst in several studies.[319, 320] However, most of the studies use a solution based method such as solvothermal or thermal decomposition.[87, 321] The synthesized catalyst particles are then mixed with a binding agent (PTFE or Nafion) and a conductive agent (carbon black, carbon nanotube, graphene, etc.) and then sprayed on the air electrode. Other methods include sputtering of MnOx followed by thermal oxidation.[317] In our work, all the above steps are simplified into one-step electrodeposition. The active material is grown directly on the gas diffusion layer without any additives. The direct growth results in lower contact resistance and shorter oxygen diffusion paths between the current collector and the active material. Therefore, fabrication is simpler and lower cost than other reported methods. This is important for large-scale applications such as stationary batteries. In addition, annealed Mn_3O_4 is more active than as-deposited Mn_3O_4, showing comparable ORR activity to noble metal catalysts.

The electrodeposited Co-Fe catalyst is, in fact, a solid solution of Fe and Co with the surface oxidized. It has been shown to be an active and durable OER catalyst according to our research in Chapter 3 and Chapter 4. Electrodeposited Co-Fe based catalysts have been reported in the literature, but most of these are deposited as Co-Fe oxyhydroxide.[322] In this study, Co-Fe is electrodeposited on Ni foam to take advantage of nickel's high conductivity and stability in alkaline

solutions. Electrochemical tests show that both catalysts have comparable or even better activity than their commercial Pt-Ru catalyst counterpart. The durability of the MnOx catalyst is significantly enhanced by using it exclusively for ORR instead of as an ORR-OER bifunctional catalyst. Finally, MnOx and Co-Fe are assembled into a Zn-air battery as decoupled electrodes for discharge and charge tests.

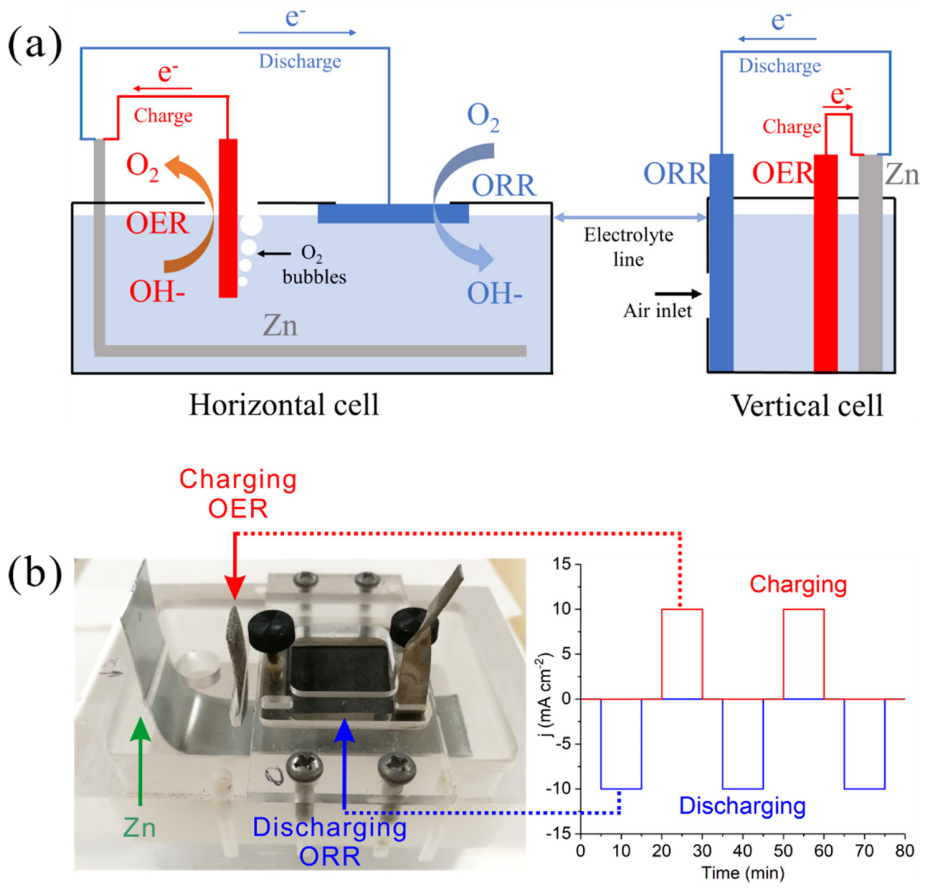

Fig. 6-1. (a) Comparison of assembly structure between tri-electrode horizontal cell and vertical cell. (b) Photograph of Zn-air battery with physically decoupled electrodes for discharge and charge (left). Current waveform for discharge-charge cycling of Zn-air battery (right).

6.2 Experimental

6.2.1. Electrodeposition of MnOx and Co-Fe catalysts

Electrodeposition of MnOx was performed in a two-electrode configuration, where Teflon-coated porous carbon paper (GDL: SGL 39BC) and Pt mesh were used as the working electrode and the counter electrode, respectively. The substrate area for anodic MnOx electrodeposition was 5.1 cm^2 (1.7 cm × 3 cm). Pulse electrodeposition at a current of 6 mA was applied with a 0.25 s ON-time and a 0.5 s OFF-time for each cycle with 2400 cycles in total (Fig. 6-2(a)). The solution for MnOx deposition contained 0.02 M manganese acetate, 0.02 M sodium acetate and 100 mg L^{-1} sodium dodecyl sulfate. The Co-Fe OER catalysts were cathodically electrodeposited on Ni foam with an area of 4.2 cm^2 (1.6 cm × 2.6 cm) at a constant current of 300 mA for 4 min. The Ni foam was cleaned prior to electrodeposition with acetone, followed by 1 M HCl and then isopropanol by sonication. The Ni foam was finally rinsed several times with de-ionized water. The electrolyte was the same as the one used in Chapter 4, containing $CoSO_4$ (0.1 M), $FeSO_4$ (0.1 M), sodium citrate (0.2 M), boric acid (0.2 M), L-ascorbic acid (0.05 M) and sodium dodecyl sulfate (400 mg L^{-1}). Co-Fe was electrodeposited on both sides of the Ni foam by placing the Ni foam between two counter electrodes of Pt mesh (Fig. 6-2(b)). The mass loading of MnOx on GDL was ~0.2 mg cm^{-2} and that for Co-Fe on Ni foam (Co-Fe/Ni) was ~0.8 mg cm^{-2}. The electrolyte was agitated for both electrodeposition processes by placing the electrolytic cell in an ultrasonic bath (Branson 2510, 40 kHz). All as-deposited samples were rinsed with deionized water and dried in air. The MnOx sample was also annealed at 300°C in air for 0.5 h to enhance ORR activity.

6.2.2. Materials characterization

The microstructure and composition of the samples were characterized by SEM (Zeiss Sigma) and TEM (JEOL JEM-ARM 200CF and JEOL 2010), along with EDX spectroscopy for both SEM and TEM. XRD (Rigaku Ultima IV) using Co Kα radiation (λ= 0.1789 nm) and XPS (Kratos AXIS 165, Al X-ray source) were used to investigate the crystal structure and oxidation states of the catalysts. All XPS spectra were calibrated using the C 1s line at 284.8 eV and analyzed with Casa XPS software (Version 2.3.17 PR1.1). Raman scattering spectra were obtained between 100 and 1000 cm^{-1} at room temperature (Thermo DXR2 Raman microscope, excitation at 532 nm^{-1}). Each Raman spectrum shown is the average of 20 scans to increase the signal-noise ratio.

6.2.3. Electrochemical measurements

A potentiostat (Bio-logic SP-300) was used to perform LSV, chronopotentiometric measurements and CV in 1 M KOH. MnOx coated GDL or Co-Fe coated Ni foam, Hg/HgO (0.098 V vs. SHE) and Pt mesh were used as the working electrode, reference electrode and counter electrode, respectively. The electrolyte was agitated with a stir bar below the working electrode and the electrolyte was purged with pure O_2 gas or Ar gas. The current densities were normalized to the geometric surface area. All potentials in the voltammetric tests (LSV and CV) were IR-compensated and are reported relative to Hg/HgO unless otherwise indicated. EIS was performed at -0.1 V vs. Hg/HgO for the ORR tests and 0.6 V vs. Hg/HgO for the OER tests with 10 mV AC potential from 100 kHz to 0.01 Hz. A bifunctional Pt/Ru catalyst ink, sprayed onto bare GDL, was used for comparison. The ink consisted of 50 mg of Pt-Ru powder (30% Pt and 15% Ru on carbon black, Alfa Aesar) dispersed in a suspension of 2 mL of deionized water, 1 mL of isopropanol, 0.1

mL of 5% Nafion (D-521) and 0.2 mL of 5% PTFE binder. The mass loading of the Pt/Ru ink on GDL was ~0.5 mg cm^{-2} after drying in a furnace.

6.2.4. Battery testing

Zn-air battery testing was performed in a home-made cell with physically decoupled electrodes for discharge and charge (Fig. 6-1(b)). MnOx-coated GDL acted as the discharge electrode with an area of 2 cm^2 exposed to the electrolyte (6 M KOH + 0.25 M ZnO). The electrode was placed horizontally on top of the cell with the uncoated side exposed to air. Co-Fe coated Ni foam was utilized as the charge electrode and was vertically submerged into the electrolyte with an area of 2 cm^2 (both sides inclusive). The Zn electrode was bent into an L-shape with one arm placed horizontally at the bottom of the cell. The distance between the horizontal Zn plate and the air electrode was ~17 mm. A blueprint of the cell with critical dimensions is provided in Fig. 6-2(c). No separator is needed in this configuration and an outlet is included for electrolyte refilling. Two channels of the potentiostat (Bio-logic, VSP) were synchronized to perform discharge-charge cycling at a current density of 10 mA cm^{-2}. For comparison, separate Pt-Ru loaded GDL electrodes were used for discharge and charge in the same battery configuration. The discharge and charge processes were performed sequentially for a total time of 50 h with 10 min for each process and 5 min rest time (Fig. 6-1(b)). A syringe pump was used to add de-ionized water into the cell at a rate of 0.2 mL/h to compensate for water evaporated from the cell. The total volume of electrolyte in the cell was ~80 mL.

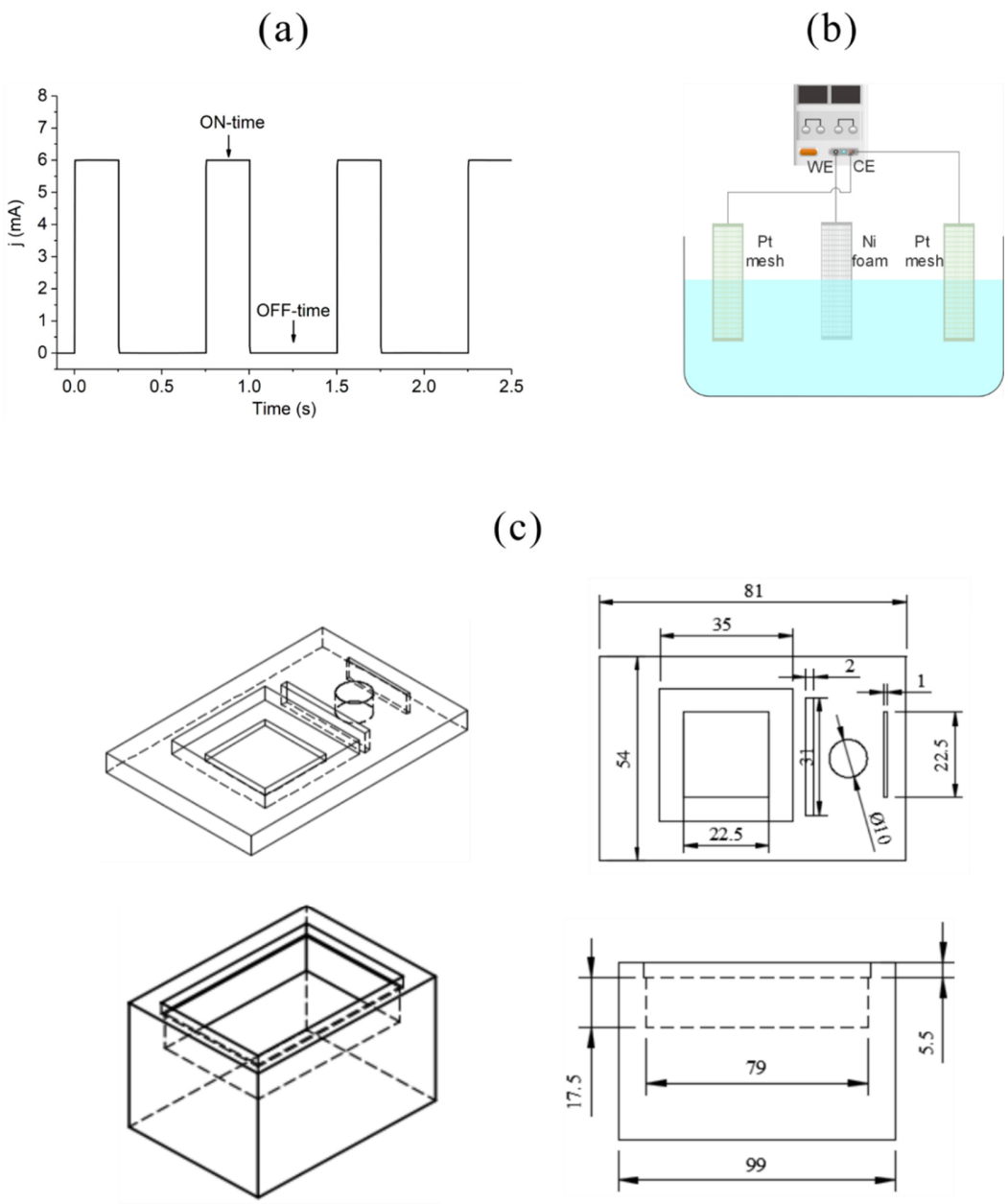

Fig. 6-2. (a) Current waveform and pulse electrodeposition parameters for MnOx. (b) Electrolytic cell setup for double-sided electrodeposition of Co-Fe on Ni foam. (c) Blueprint of cell design with critical dimensions (units: mm).

6.3 Results and discussion

Catalyst characterization

SEM secondary electron (SE) images and XPS spectra of MnOx layers on GDL are shown in Fig. 6-3. The as-deposited or unannealed MnOx (Fig. 6-3(a) and (b)) shows a porous structure composed of mostly nanorods (>90%) with spherical particles distributed throughout the layer (indicated by the arrows). The nanorods are 10-20 nm in diameter (the average diameter is 11.0 ± 2.5 nm) and the spheres are micrometer-sized. After annealing, the well-dispersed nanorods twisted together to form bundles, leaving large spaces between these bundles (Fig. 6-3(c) and (d)). As such, the pores on the surface became larger, but the nanorods and spheres generally maintained their size and shape. The diameter of the nanorods slightly increased to 12.8 ± 2.6 nm. The length of the nanorods varies between 0.2 μm and 1 μm. The nanorods form before the spheres during electrodeposition (Fig. S6-17).

XPS spectra from unannealed and annealed MnOx were compared to investigate the effect of annealing. Fig. 6-3(e) shows the survey spectra for each condition with peak labels for each of the strong signals, as well as high-resolution O 1s, Mn 3s and Mn 2p spectra. Elements Mn, O and F are present in the survey scan of both samples, while the annealed sample has a stronger F signal from the Teflon in the substrate (Teflon-coated porous carbon paper). The O 1s spectrum was deconvoluted into three components: lattice oxygen (O-M(Mn)-O, 529.8 eV), surface adsorbed oxygen or OH groups (M(Mn)-O-H, 531.2 eV) and water (H-O-H, 532.7 eV).[279, 323] Quantitative calculations show that the relative abundance of lattice oxygen for annealed MnOx (~70%) is higher than that for unannealed MnOx (~46%). The amount of OH groups decreased after annealing. A linear relation has been reported between the Mn oxidation state and the multiplet splitting widths of the Mn 3s peak.[324] The splitting width (ΔE) decreases when the oxidation state

of the Mn cations increases. Annealed MnOx has a lower value of ΔE (5.12 eV) than unannealed MnOx (5.39 eV), which indicates an increase in the average Mn valence from 2.9 to 3.2. The Mn oxidation state can also be determined by deconvoluting the Mn $2p_{3/2}$ peak into the various valence states (Mn^{2+}, Mn^{3+} and Mn^{4+}).[325, 326] The unannealed MnOx spectrum is characterized by the presence of Mn^{2+} (~23%), Mn^{3+} (~63%) and Mn^{4+} (~14%), giving an average valence of 2.9. Deconvolution of the same peak for annealed MnOx shows the presence of Mn^{2+} (~5%), Mn^{3+} (~77%) and Mn^{4+} (~18%), giving an average valence of 3.1. The results from the Mn 3s and Mn 2p spectra corroborate one another. The main change to MnOx during annealing is oxidation of Mn^{2+} to Mn^{3+}.

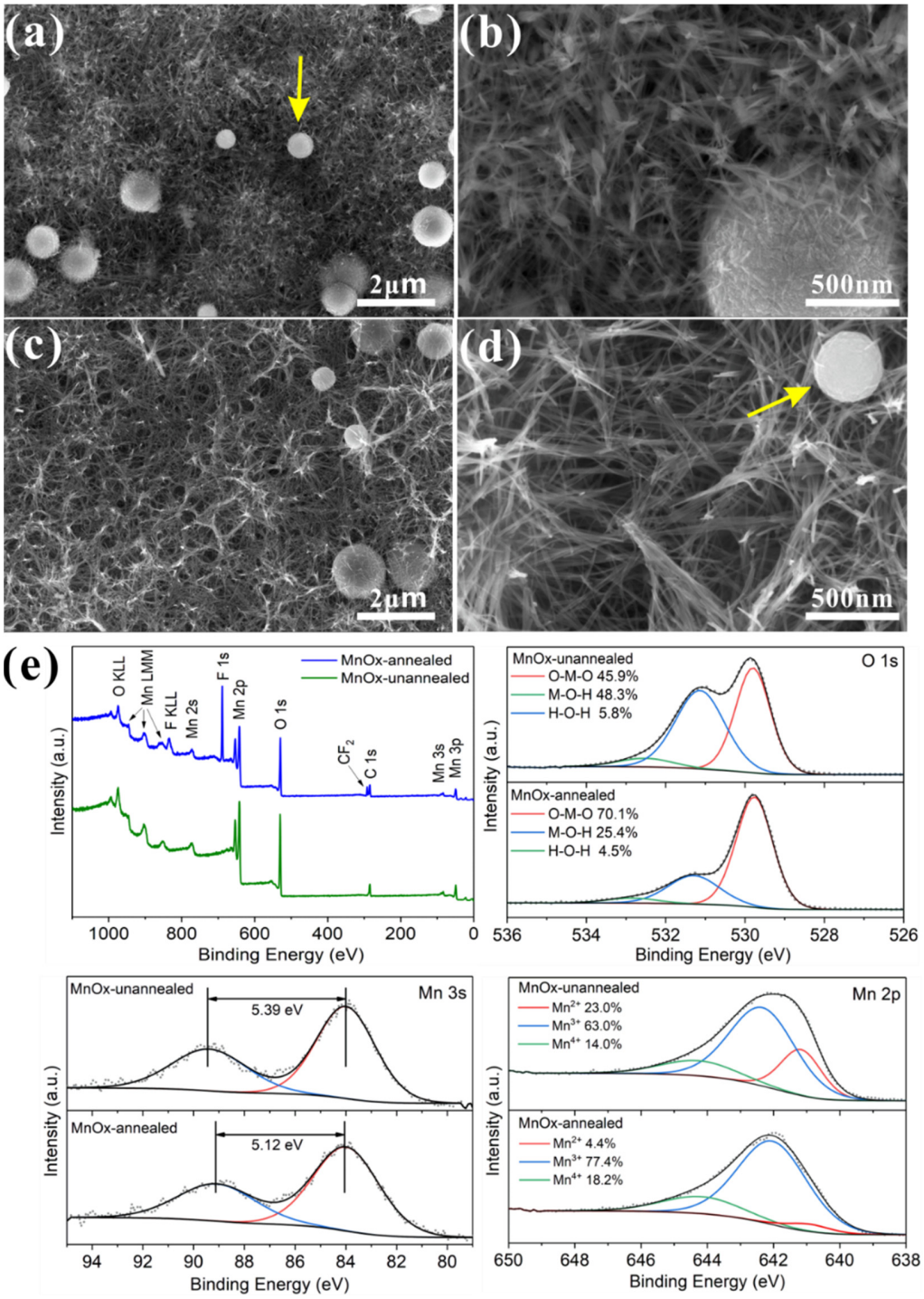

Fig. 6-3. SEM SE images showing the morphology of MnOx catalysts on the air electrode: (a, b) unannealed MnOx; (c, d) annealed MnOx; (e) XPS spectra for unannealed and annealed MnOx.

The electrodeposited MnOx layer was further investigated by TEM. Both morphologies (nanorods and spheres) of unannealed MnOx were visible and were confirmed to contain Mn and O through EDX analysis (not shown) (Fig. 6-4(a)). Several electron diffraction patterns were obtained from the two morphologies at various orientations (one example for each morphology is shown in Fig. 6-4(a)). The diffraction patterns from the spherical particles were all indexed to cubic α-Mn_2O_3 (bixbyite - PDF 76-0150). The diffraction patterns from the nanorods were more difficult to index, as the patterns could be indexed to multiple Mn oxide phases. However, tetragonal Mn_3O_4 (hausmannite - PDF 24-0734) was the only phase that could be matched with all the diffraction patterns from the rods. Note that the overall Mn valence of unannealed MnOx was 2.9; α-Mn_2O_3 has a Mn valence of 3+, while Mn_3O_4 (hausmannite) has a mixed Mn valence of 2+/3+ (average of 2.67). The inset in Fig. 6-4(a) shows a high-resolution TEM (HRTEM) image of part of one nanorod. Lattice spacings of ~0.31 nm and ~0.29 nm for adjacent grains correspond to the (112) and (200) planes of hausmannite Mn_3O_4, respectively. Each nanorod is polycrystalline, so that only part of the rod imaged in high resolution at a given orientation.

The annealed MnOx sample was very similar in appearance to the unannealed sample (Fig. 6-4(b)). Spherical particles are present and were identified through electron diffraction as the same α-Mn_2O_3 (bixbyite) found in the unannealed sample. Diffraction patterns from the annealed nanorods were also obtained (an example is shown in Fig. 6-4(b)) and are streaked in the direction perpendicular to the nanorod axis. These were indexed to Mn_3O_4 (hausmannite), as was the case for the unannealed sample, which suggests that there is no structural change on annealing. However, based on the XPS analysis discussed above, the annealed sample has a higher Mn oxidation state (a shift in Mn valence from 2.9 to 3.2); the main change during annealing is a shift from Mn^{2+} to Mn^{3+}. This change in valence can be accommodated by the formation of another

Mn_2O_3 phase from Mn_3O_4 (hausmannite). This phase is γ-Mn_2O_3, which is isostructural with hausmannite[327-329] with slightly different lattice parameters. γ-Mn_2O_3 is considered to be a defect structure,[330] i.e., there must be some Mn vacancies to accommodate oxidation of Mn (from 2+ to 3+) while still retaining the tetragonal hausmannite structure.

Raman scattering spectra are useful for distinguishing between different metal oxides with the same elements, such as Mn_2O_3, Mn_3O_4 and MnO_2, because the Raman bands are very sensitive to crystal symmetry and coordination geometry.[179] Raman spectra for the unannealed and annealed MnOx layer (as well as bare GDL) are shown in Fig. 6-4(c). Both MnOx samples are composed primarily of nanorods, so the spectra are likely mainly from the nanorods. The Raman spectra and band frequencies for MnOx are in good agreement with those of Mn_3O_4 (hausmannite) or its isostructural γ-Mn_2O_3 counterpart.[321, 331-333] The unannealed MnOx is characterized by a sharp peak at about 644 cm^{-1} and two peaks at 360 cm^{-1} and 292 cm^{-1}. After annealing, there are slight shifts of these bands to lower wavenumbers. These downward shifts may indicate the partial transformation of hausmannite (Mn_3O_4) to γ-Mn_2O_3, as a similar shift has been reported.[331] To summarize, unannealed MnOx is composed of Mn_3O_4 (hausmannite) nanorods and α-Mn_2O_3 (bixbyite) spheres. After annealing at 300°C in the air, some of the Mn_3O_4 is partially oxidized to γ-Mn_2O_3, while the spheres maintain their α-Mn_2O_3 structure.

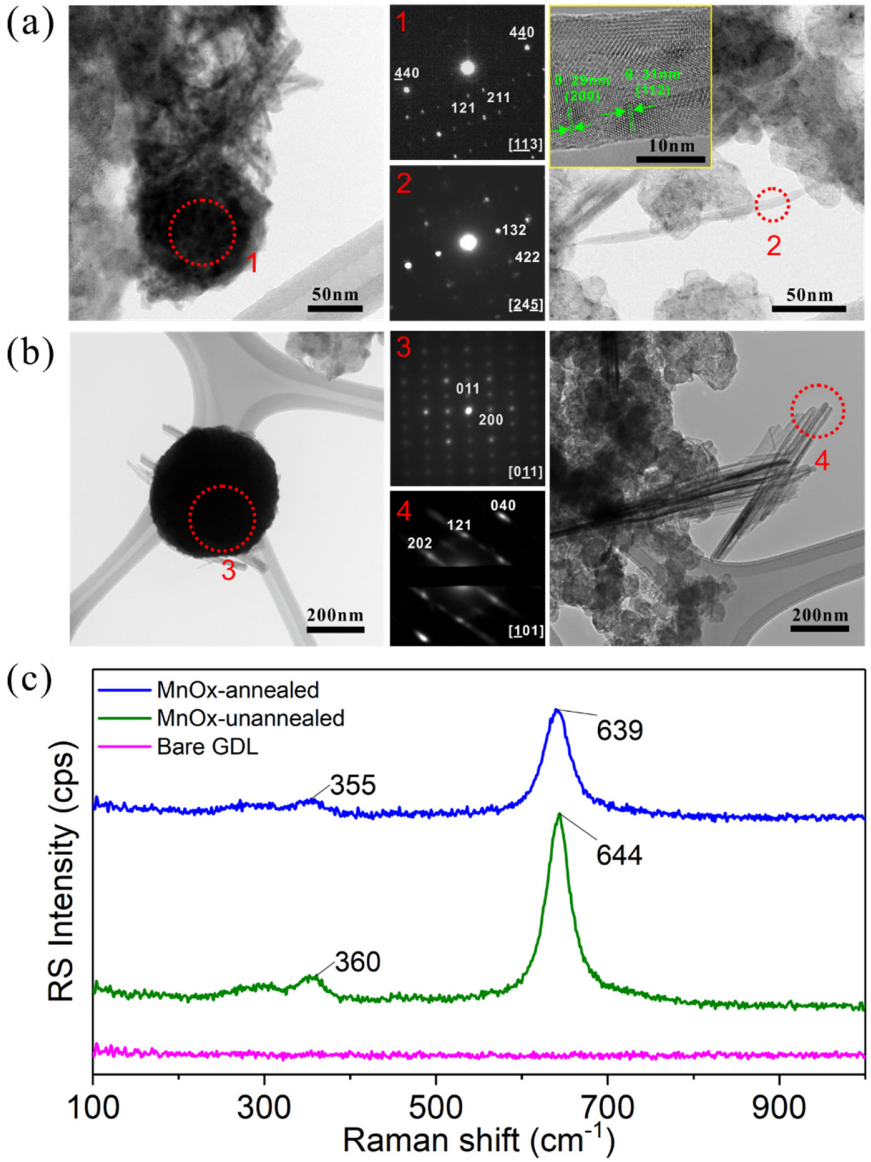

Fig. 6-4. (a) TEM bright field (BF) images and electron diffraction patterns from the areas shown of unannealed MnOx. The inset in (a) is a HRTEM image of part of one nanorod. (b) TEM BF images and diffraction patterns from the areas shown of annealed MnOx. For the spheres, both the unannealed and annealed MnOx patterns can be indexed to bixbyite α-Mn_2O_3 (PDF 76-0150). Note that the patterns (with the exception of #3) are only near the zone axes shown. For the nanorods, both the unannealed and annealed patterns can be indexed to hausmannite Mn_3O_4 (PDF 24-0734). (c) Raman scattering spectra of bare GDL and MnOx before and after annealing.

For the OER electrode, Co and Fe were electrodeposited on Ni foam. The crystal structure of the Co-Fe deposit was studied using XRD (Fig. 6-5(a)). The intense diffraction peaks at 52.24°, 61.14° and 91.86° are from the Ni foam ((111), (200) and (220) - PDF 65-2586). The weak and broad peaks at around 77.0° and 99.4° (see inset in Fig. 6-5(a)) correspond to the (200) and (211) planes of bcc Co-Fe solid solution (PDF 65-7519). The strong (110) peak of Co-Fe is at 52.4° but overlaps the (111) peak of Ni. The composition of the Co-Fe film from EDX analysis (not shown here) was ~73 at% Fe and the surface was oxidized. According to results in Chapter 4, the electrodeposited Co-Fe layer is mostly metallic with a surface oxide layer, even after a 20 h OER test. There is a small peak at ~55° that can be matched to Co(Fe)OOH. The Co-Fe layer (~1.5 μm thick) with an OER active Co/Fe-oxyhydroxide surface layer is uniformly distributed on the Ni foam with a grain size of 20-50 nm (Fig. 6-5(b) and (c)).

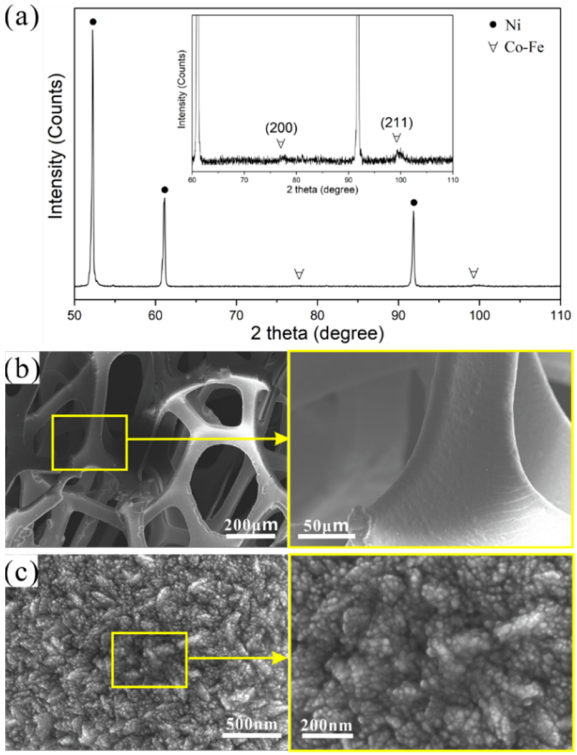

Fig. 6-5. (a) XRD pattern from as-deposited Co-Fe on Ni. (b, c) SEM SE images of Co-Fe layer on Ni.

Electrochemical performance

Fig. 6-6(a) shows CV curves for MnOx catalysts cycled in Ar and O_2 saturated 1 M KOH electrolyte. Both unannealed and annealed MnOx show much higher current in O_2 than in Ar, confirming their ORR activity. The ORR activity of the different catalysts is compared through LSV scans in Fig. 6-6(b), which shows that annealed MnOx has nearly the same performance as Pt-Ru at a low overpotential of -0.1 V. Both CV and LSV results demonstrate that annealed MnOx has higher ORR activity than unannealed MnOx for the specific fabrication process (2400 deposition cycles in this case). Simply increasing the number of deposition cycles will not increase the ORR activity of MnOx (Fig. S6-18 and Fig. S6-19).

Electrodes with different catalysts were CV cycled in the potential range of 0.1 V to 0.2 V at different rates to evaluate their double-layer capacitance (C_{dl} - Fig. 6-7). The double-layer charge q_{dl} is estimated by extrapolation of q to $v=\infty$ (v is the scan rate) in a plot of q vs. $v^{-1/2}$, according to the method reported in the literature (Fig. 6-6(c)).[242] The C_{dl} values can be obtained by dividing half of q_{dl} by the potential window of the CV curve. Annealed MnOx has a higher C_{dl} value (8.3 mF cm^{-2}) than unannealed MnOx (6.2 mF cm^{-2}), indicating that a higher electrochemically active surface area (ECSA) was achieved by annealing. The carbon paper substrate contributes negligible capacitance (0.2 mF cm^{-2}) due to its hydrophobic surface.

The total capacitance C_t and pseudocapacitance C_p were also estimated using the same method (Fig. 6-8(a)) and the results are summarized in Table 6-1. The pseudocapacitance C_p derived from the redox reaction of MnOx is higher for the unannealed sample. Therefore, unannealed MnOx is a better supercapacitor, but not as good an ORR electrocatalyst, as annealed MnOx. The source of higher ORR activity was further investigated by the potentiostatic EIS testing under ORR reaction conditions at -0.1 V (Fig. 6-8(b)). An R_s (R_f Q_f) (R_{ct} Q_{dl}) equivalent circuit was used to fit the

experimental data, where R_s, R_f and R_{ct} represent the solution resistance, the catalyst interlayer resistance and the charge transfer resistance, respectively.[334] The charge transfer resistance, represented by the semi-circle, is lower for annealed MnOx (2.7 Ω cm^2) compared with unannealed MnOx (13.0 Ω cm^2) (Table 6-2). This effect may be related to the higher Mn oxidation state after annealing. It has been reported that a mixed valence of Mn^{4+} and Mn^{3+} may facilitate ORR, because the presence of Mn^{3+}, possibly including some Mn^{4+}, is key to catalyzing the four-electron process and increasing the fraction of hydroxide relative to peroxide.[87, 88] Hence, only the more active annealed MnOx is discussed in the following electrochemical tests.

Fig. 6-6(d) shows that the OER activity of Ni foam is improved after coating with Co-Fe. The onset potential for OER on Ni foam is 0.67 V, which is 90 mV higher than that for Co-Fe/Ni (0.58 V). The onset potential here is defined as the potential corresponding to a current density of 10 mA cm^{-2}. There is a Ni^{2+}/Ni^{3+} oxidation peak at 0.42 V for bare Ni foam which disappears for Co-Fe/Ni, indicating that NiOx active sites are screened by the Co-Fe coating.[196] Co-Fe/Ni has a higher onset potential for OER than Pt-Ru but performs better at high current densities. MnOx cannot compete with Co-Fe in catalyzing OER and, as such, is only used as the ORR catalyst.

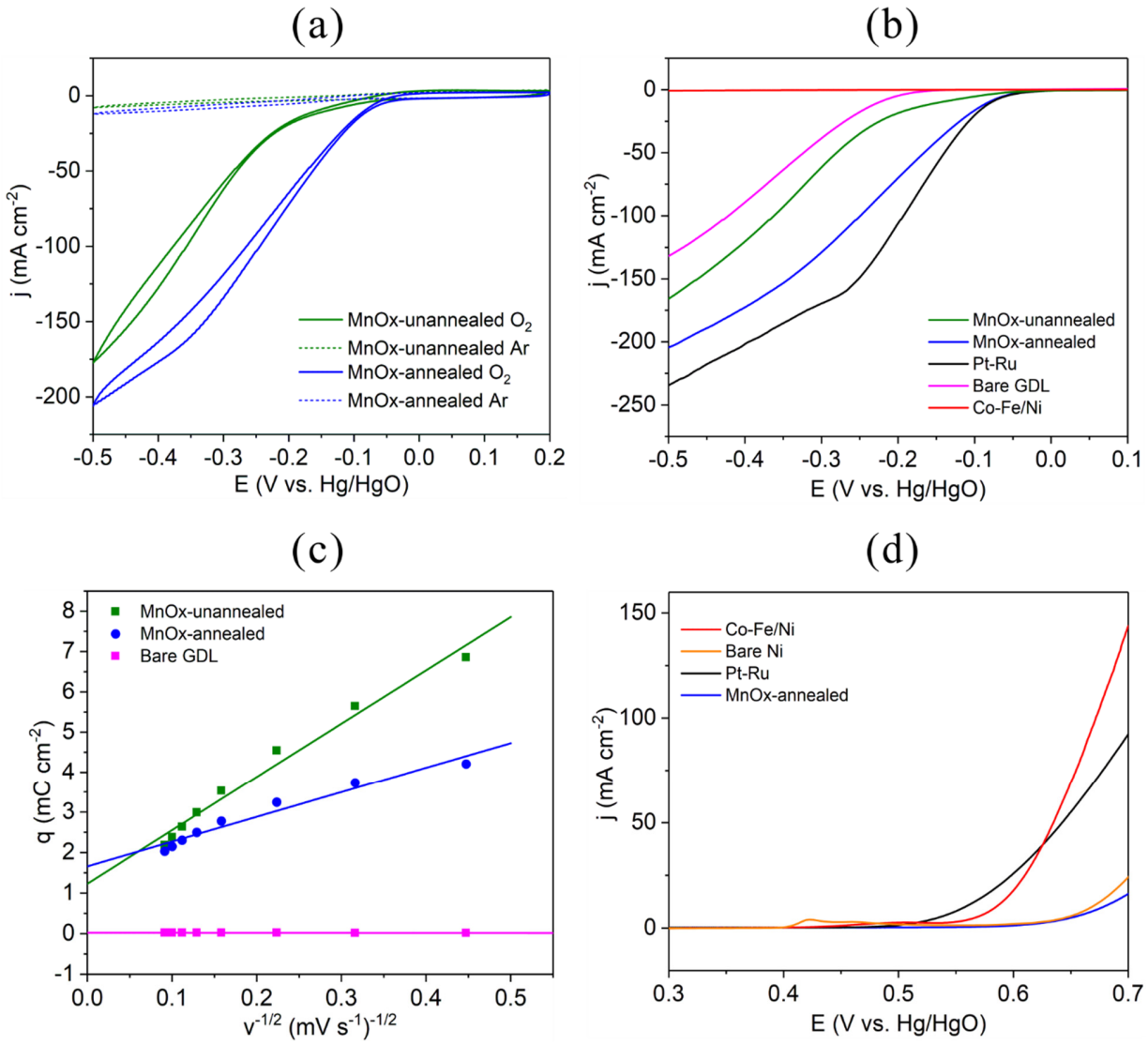

Fig. 6-6. (a) CV plots for MnOx catalysts at a scan rate of 20 mV s^{-1} in Ar and O_2 saturated 1 M KOH electrolyte. (b) ORR LSV plots for catalysts at a scan rate of 5 mV s^{-1} in O_2 saturated 1 M KOH electrolyte. (c) Voltammetric charge (q) plotted against the square root of the scan rate ($v^{1/2}$), where the intercept on the q-axis is equivalent to the double layer charge, q_{dl}. (d) OER LSV plots for catalysts at a scan rate of 5 mV s^{-1} in O_2 saturated 1 M KOH electrolyte.

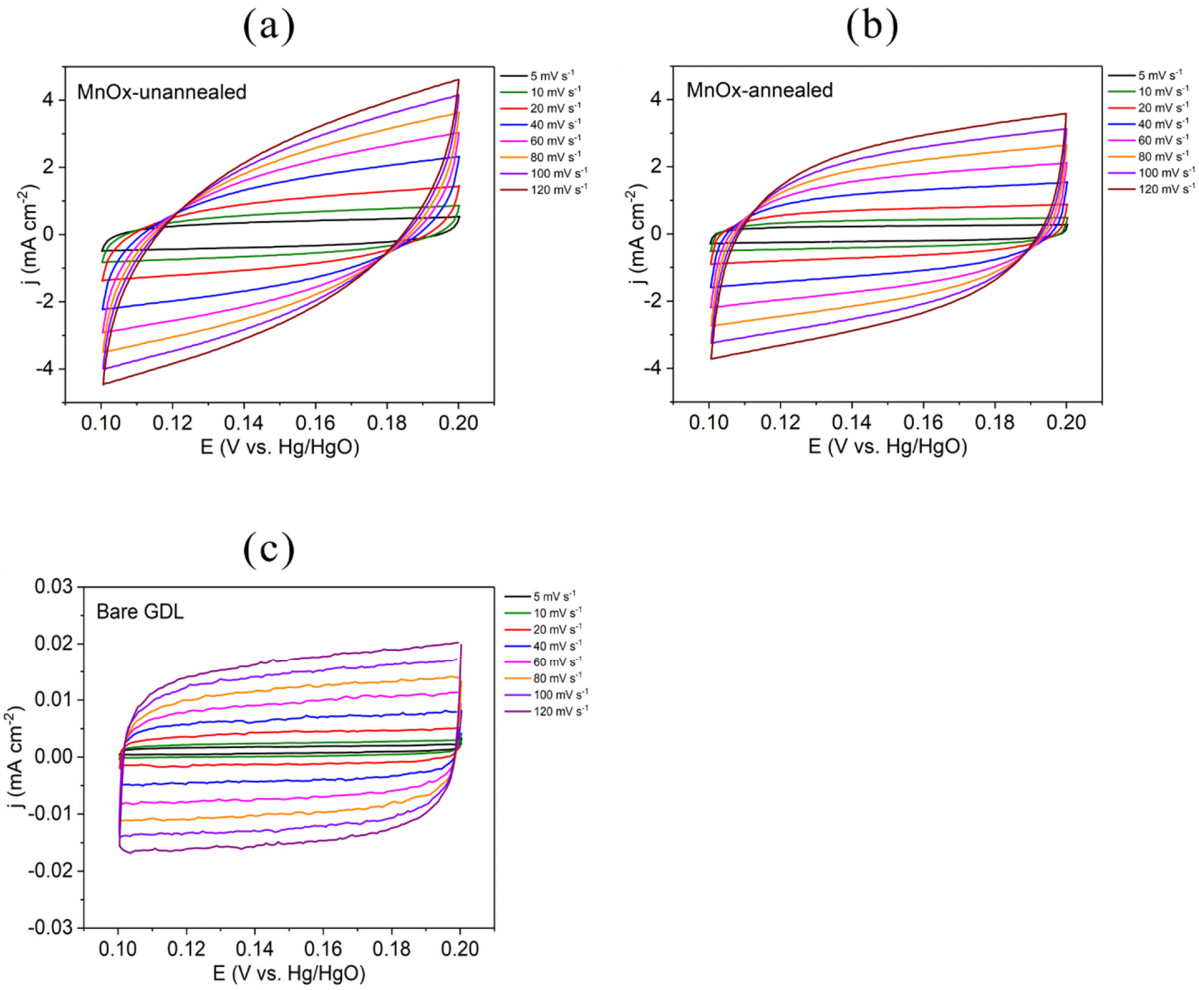

Fig. 6-7. CV curves at different scan rates in a potential window of 0.1 to 0.2 V vs. Hg/HgO in Ar saturated 1 M KOH for different samples: (a) unannealed MnOx; (b) annealed MnOx; (c) bare GDL.

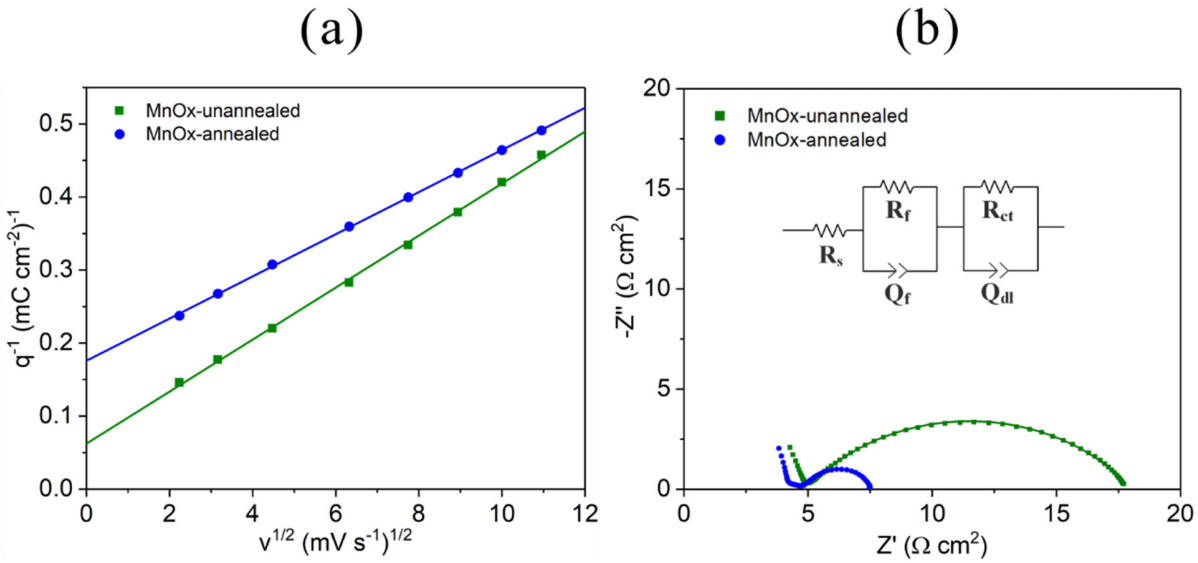

Fig. 6-8. The reciprocal of voltammetric charge (q^{-1}) plotted against square root of the scan rate ($v^{1/2}$), where the intercept on the q^{-1}-axis is equivalent to the total voltammetric charge, for MnOx. (b) Electrochemical impedance spectra at -0.1 V for MnOx in oxygen saturated 1 M KOH (inset: equivalent circuit).

Table 6-1. Capacitance values of unannealed MnOx, annealed MnOx and bare GDL

Sample	q_t	q_{dl}	C_t	C_{dl}	C_p
	mC cm^{-2}	mC cm^{-2}	mF cm^{-2}	mF cm^{-2}	mF cm^{-2}
MnOx-unannealed	16.0	1.24	80.0	6.2	73.8
MnOx-annealed	5.7	1.66	28.5	8.3	20.2
Bare GDL	N/A	0.03	N/A	0.2	N/A

Table 6-2. Equivalent circuit parameters according to the EIS spectra shown in Fig. 6-8(b) and Fig. 6-10; the equivalent circuit is R_s (R_f Q_f) (R_{ct} Q_{dl})

Sample	R_s Ω cm^2	R_f Ω cm^2	Q_f mΩ^{-1} s^n cm^{-2}	R_{ct} Ω cm^2	Q_{dl} mΩ^{-1} s^n cm^{-2}
MnOx unannealed	4.2	0.8	0.5 (n=0.67)	13.0	12.8 (n=0.61)
MnOx annealed (before ORR cycling)	3.5	1.4	5.2 (n=0.45)	2.7	82.9 (n=0.81)
MnOx annealed after ORR cycling	3.4	1.5	4.9 (n=0.44)	2.8	77.9 (n=0.78)
Pt-Ru before ORR cycling	3.8	1.1	32.4 (n=0.28)	2.9	33.1 (n=0.82)
Pt-Ru after ORR cycling	3.8	1.1	40.6 (n=0.29)	2.5	39.7 (n=0.82)
Co-Fe/Ni before OER cycling	1.2	0.1	193.2 (n=0.49)	1.1	47.6 (n=0.91)
Co-Fe/Ni after OER cycling	1.1	0.2	248.8 (n=0.42)	1.6	44.0 (n=0.91)
Pt-Ru before OER cycling	3.6	0.6	82.6 (n=0.44)	2.5	25.0 (n=0.88)
Pt-Ru after OER cycling	3.0	1.3	70.4 (n=0.31)	4.1	22.7 (n=0.89)

All catalysts were cycled in 1 M KOH at 20 mA cm^{-2} to confirm their stability (Fig. 6-9(a)). The ORR performance of MnOx was compared with Pt-Ru through a test that started with a 5 min cathodic current followed by a 5 min open circuit voltage (OCV) period which was repeated for

50 cycles. MnOx (annealed) had with a potential of -0.179 V for the first cycle and ended with -0.184 V after 50 cycles, which is almost the same as the potential for Pt-Ru (remained at -0.181 V). Co-Fe/Ni was compared with Pt-Ru in terms of OER performance during a test starting with a 5 min anodic current followed by a 5 min OCV period which was repeated for 50 cycles. The original potential for Co-Fe/Ni was 0.649 V and the final potential was 0.668 V; Pt-Ru started at 0.661 V and ended at 0.691 V. To show the influence of cycling potential on the durability of the catalysts, all the above catalysts were cycled from the ORR potential to the OER potential using sequential cathodic-anodic currents (ORR-OER cycling). Both MnOx and Pt-Ru exhibited significant performance degradation during the cycling process, showing a continuous decrease in ORR potential and an increase in OER potential. Co-Fe/Ni was not affected very much by the same cycling test.

LSV tests before and after cycling (Fig. 6-9(b)) show that both MnOx and Pt-Ru perform well when cycled as ORR catalysts. Co-Fe/Ni performs better than Pt-Ru when both are cycled as OER catalysts. In fact, both MnOx and Co-Fe/Ni show almost no degradation after cycling, while Pt/Ru does. Potentiostatic EIS tests were performed at -0.1 V for the ORR catalysts MnOx and Pt-Ru and at 0.6 V for OER catalysts Co-Fe/Ni and Pt-Ru (Fig. 6-10). The charge transfer resistance (R_{ct}) values were obtained from the fitted equivalent circuit of R_s ($R_f Q_f$) (R_{ct} Q_{dl}) and are listed in Table 6-2.[335] MnOx has the same R_{ct} value as Pt-Ru before ORR cycling and its value changes very little on cycling. Co-Fe/Ni has a lower R_{ct} value than Pt-Ru after OER cycling, although both materials exhibit increases in R_{ct}.

LSV testing shows that MnOx exhibits a significant loss in ORR activity after cycling in the ORR-OER potential range (Fig. 6-9(c)), indicating the importance of selecting a suitable working potential range. The morphology of MnOx after ORR and ORR-OER cycling was examined by

SEM (Fig. 6-11(a) and (b)). Both samples showed a morphology change from discrete nanorods to aggregated flakes, but the sample cycled in the ORR-OER range also had structural damage in the form of detachment (indicated by the arrow). The electrolyte turned to a brown color after ORR-OER cycling and contained particulates. The particulates were collected and examined by SEM (Fig. 6-11(c) and (d)). EDX analysis showed that the particles are primarily composed of Mn and O, which indicates some delamination of MnOx from the substrate during ORR-OER cycling. In comparison, no particulates or color change were observed after only ORR cycling of MnOx. The anodic potential is also detrimental to the Pt-Ru catalyst, since Pt is not stable at high potentials, especially in alkaline solutions.[336] The loss of electrocatalytic activity may be caused by catalyst layer detachment as well, due to mechanical damage from oxygen bubble formation during OER.[337, 338]

SEM SE images of the Co-Fe catalysts after 50 cycles of OER cycling at 20 mA cm^{-2} are provided in Fig. 6-12. The Co-Fe layer is still firmly attached to the Ni foam and the morphology shows almost no change compared with the as-deposited sample before cycling (Fig. 6-5). This demonstrates the stability of the Co-Fe catalyst under OER conditions.

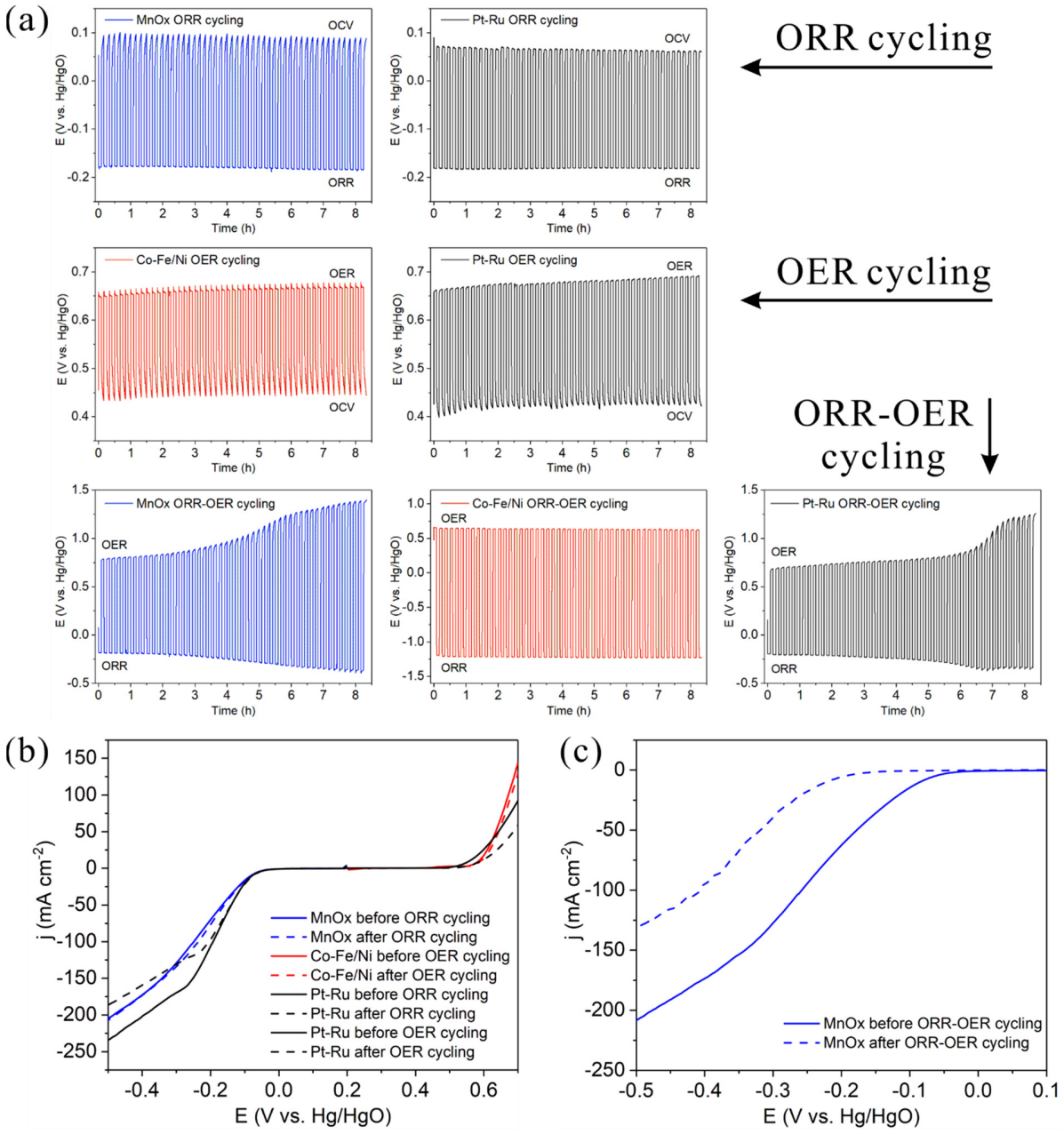

Fig. 6-9. (a) Chronopotentiometric measurements for catalysts at 20 mA cm^{-2} for 50 cycles in 1 M KOH. (b) LSV plots for catalysts before and after ORR or OER cycling (scan rate is 5 mV s^{-1}). (c) LSV plots for MnOx before and after ORR-OER cycling.

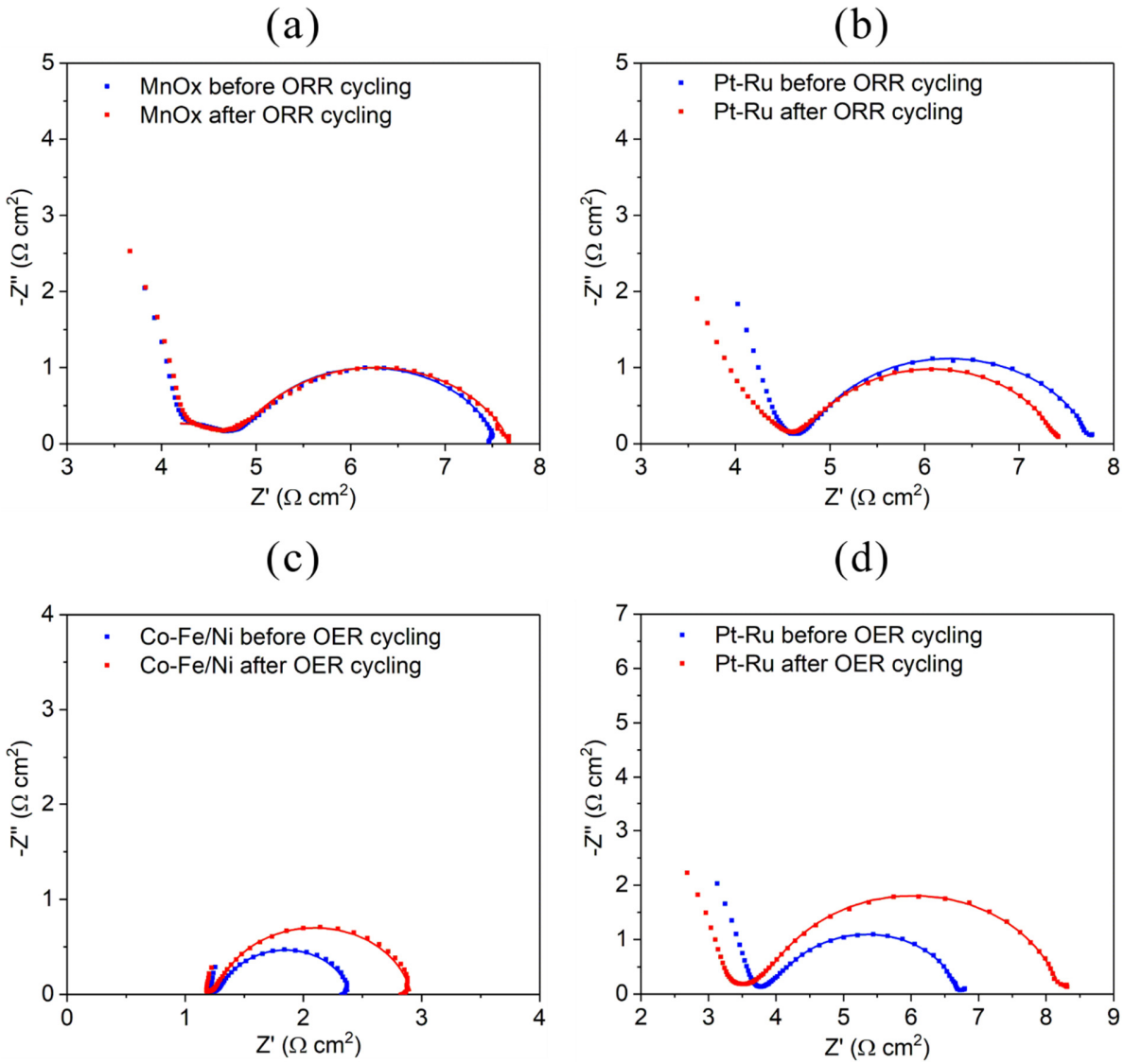

Fig. 6-10. Electrochemical impedance spectra (EIS) for catalysts at different potentials: (a) EIS at -0.1 V for MnOx before and after cycling; (b) EIS at -0.1 V for Pt-Ru before and after cycling; (c) EIS at 0.6 V for Co-Fe/Ni before and after cycling; (d) EIS at 0.6 V for Pt-Ru before and after cycling.

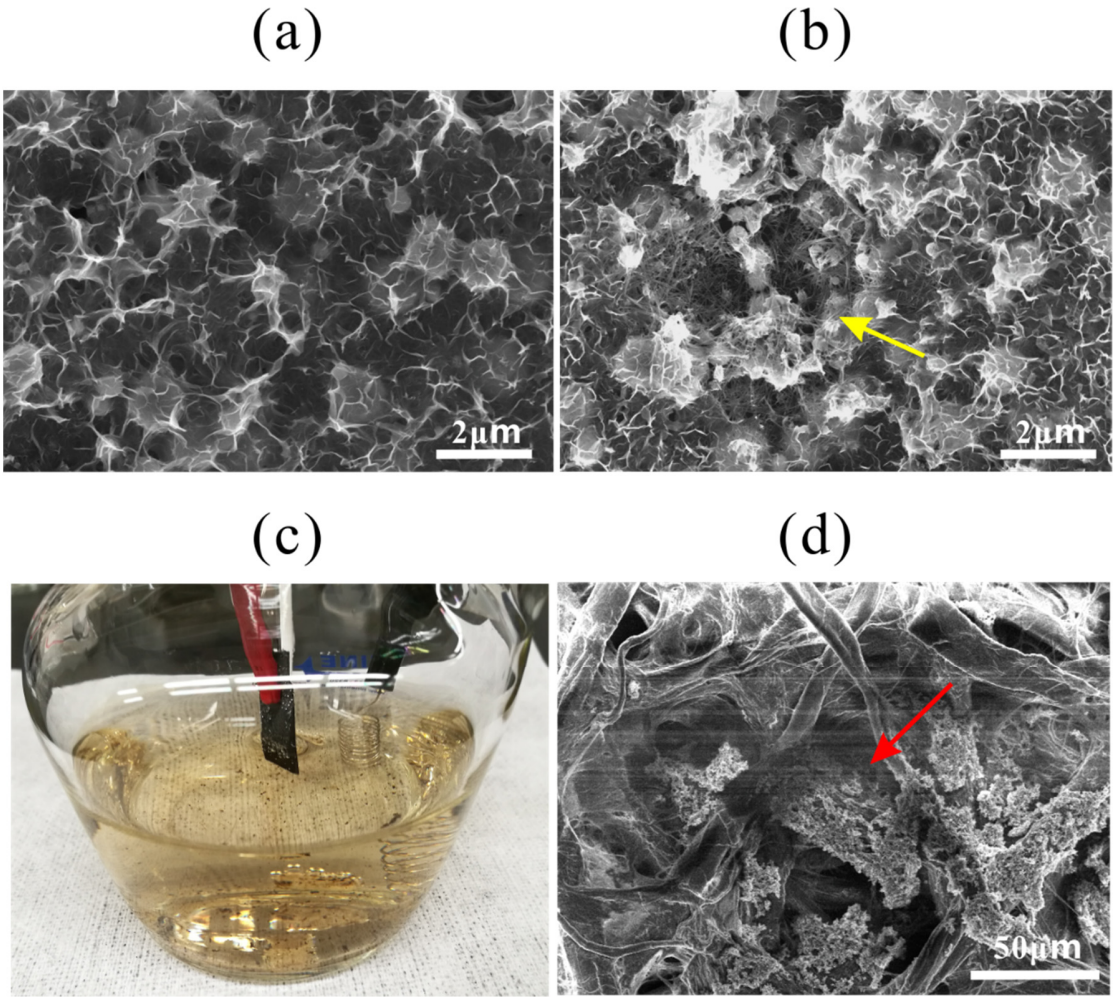

Fig. 6-11. (a, b, d) SEM SE images showing the morphology of MnOx catalysts on the air electrode after different cycling durability tests: (a) MnOx after ORR cycling; (b) MnOx after ORR-OER cycling. (c) The electrolyte after ORR-OER cycling, showing a color change and particulates. (d) SEM SE image of particulates in (c) collected on filter paper (indicated by arrow); identified as MnOx.

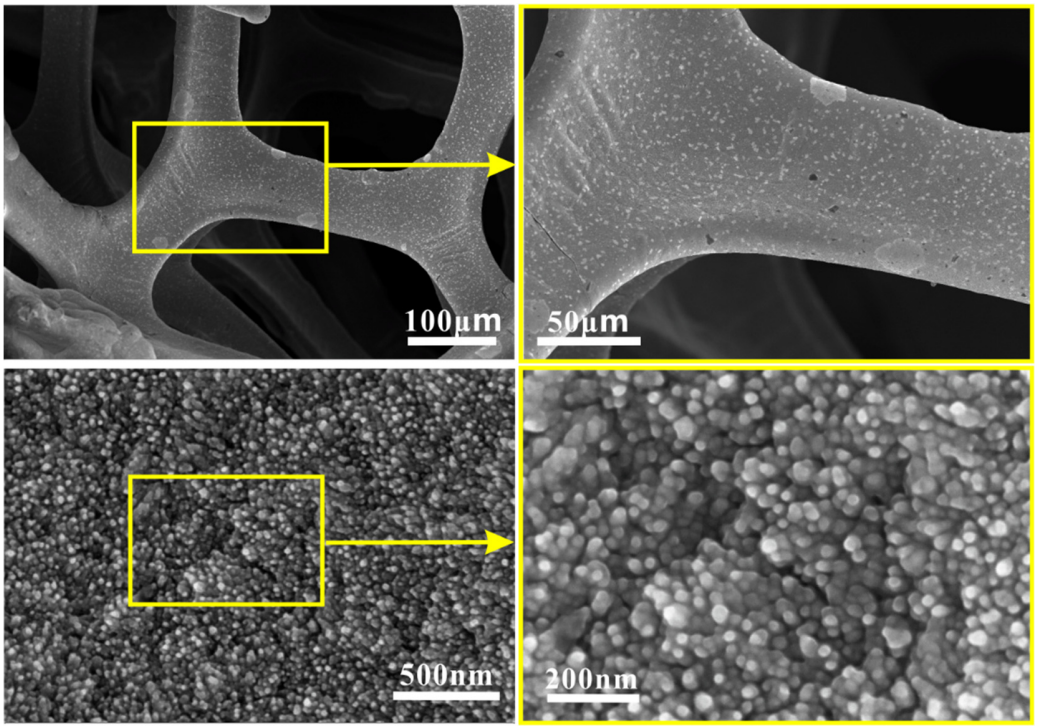

Fig. 6-12. SEM SE images of Co-Fe layer on Ni, shown in Fig. 6-9(a), after the 50 cycles of OER cycling at 20 mA cm^{-2}.

Battery performance

The electrodes were assembled in the Zn-air battery setup for testing. The ORR electrode (MnOx or Pt-Ru) for discharging and the OER electrode (Co-Fe/Ni or Pt-Ru) for charging were physically decoupled to work independently. Fig. 6-13(a) shows that MnOx has nearly the same performance as Pt-Ru during discharge polarization. Co-Fe/Ni has a lower charging voltage than Pt-Ru at high current densities during charge polarization. This performance confirms the LSV results in Fig. 6-9. All catalysts were assembled into Zn-air batteries for testing at different current densities of 2, 5, 10 and 20 mA cm^{-2} (Fig. 6-13(b)). The results again verify that both MnOx and Co-Fe/Ni have comparable or even better activity than their commercial Pt-Ru catalyst counterparts.

Potentiostatic EIS of the ORR electrode was performed at 1.1 V vs. Zn/Zn^{2+} for the Zn-air battery to evaluate the electrical properties of the electrodes (Fig. 6-13(c)). The fitted impedance data show that the solution resistance between the ORR electrode and the Zn foil is ~1 Ω. This value is comparable or even smaller to the values reported in the literature.[339] The distance between the two electrodes is 17 mm, but the resistance is low due to the high conductivity of the electrolyte and the absence of a separator.

Discharge-charge cycling tests at 10 mA cm^{-2} are presented in Fig. 6-13(d). At the beginning of the test, the cell using bare GDL and bare Ni foam can discharge at 0.98 V and charge at 2.07 V, giving an efficiency of 47.2%. A 50.5% efficiency was reached at the end of the test, with discharge and charge potentials of 1.02 V and 2.01 V, respectively. The improved efficiency was primarily caused by a decrease in charging potential, possibly due to the activation of Ni foam during cycling (e.g., more Ni metal converted to OER active Ni (oxy)hydroxide during repeated redox cycling).

After coating the substrates with catalysts by electrodeposition (MnOx on GDL and Co-Fe on Ni), the initial and final efficiencies were increased to 60.2% (discharge at 1.18 V, charge at 1.96 V) and 55.5% (discharge at 1.11 V, charge at 2.00 V), respectively (Fig. 6-13(d) and Fig. 6-14). The Pt-Ru catalyst performed well when used as an ORR catalyst for discharging, but the charge potential continuously increased with cycling. Efficiencies of 58.8% and 56.9% were achieved at the beginning (discharge at 1.20 V, charge at 2.04 V) and the end (discharge at 1.19 V, charge at 2.09 V) of the test. Both the discharge and charge branches of Pt-Ru demonstrated faster degradation when used as bifunctional ORR-OER catalysts during battery cycling, compared with the setup where the ORR or OER reactions were decoupled (Fig. 6-15). The battery test results generally confirm the electrochemical behavior of the catalysts shown in previous sections. The

combination of MnOx + Co-Fe/Ni demonstrates the same average efficiency (~58%) as Pt-Ru + Pt-Ru and both are superior to bare-GDL + bare Ni (~49%).

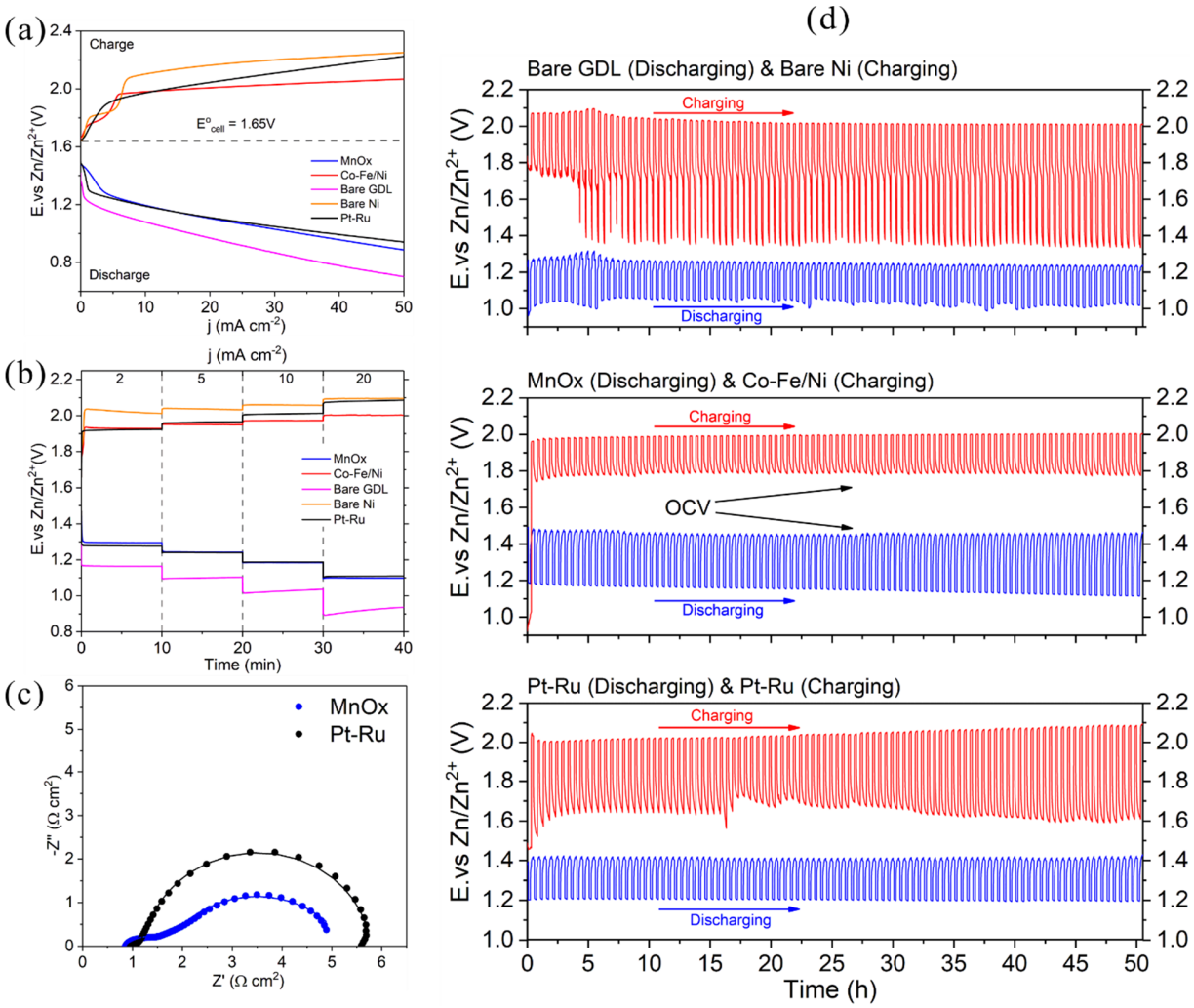

Fig. 6-13. (a) Discharge-charge polarization curves for various Zn-air batteries. (b) Rate discharge-charge curves for various Zn-air batteries. (c) Electrochemical impedance spectra for Zn-air batteries at 1.1 V. (d) Discharge-charge cycling performance for Zn-air batteries at 10 mA cm^{-2}.

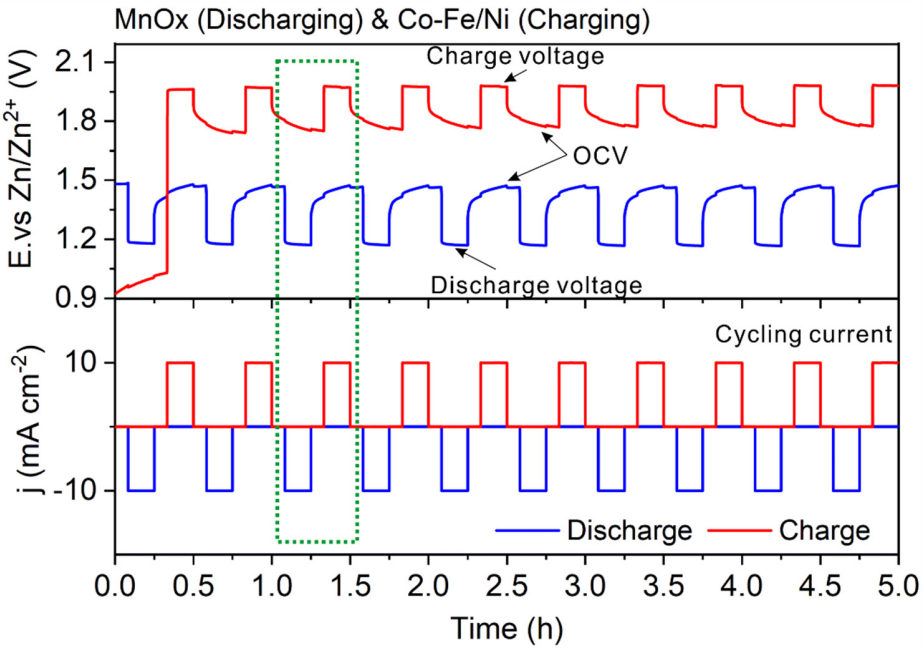

Fig. 6-14. First 5 h of discharge-charge cycle testing of the MnOx/Co-Fe combination. The green square indicates a single discharge-charge cycle.

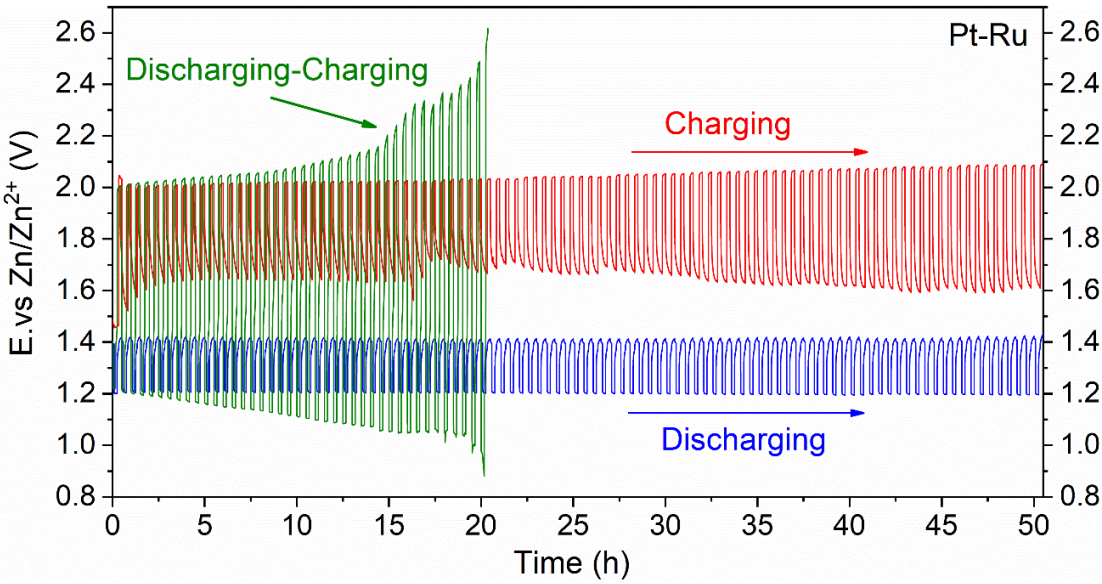

Fig. 6-15. Pt-Ru as bifunctional ORR-OER catalysts for both discharge and charge (green line), showing faster performance degradation compared with the test in Fig. 6-13(d) (red and blue lines).

A discharge–charge voltage gap (Δη) was used to appraise the cell performance of a Zn-air battery and to compare this performance with the literature.[340] For the MnOx/Co-Fe catalysts in this study, the initial overpotential difference between charge and discharge ($\Delta\eta_{initial}$) is 0.78 V. The overpotential difference ($\Delta\eta_{end}$) was increased to 0.89 V at the end of cycling. The small gap of 0.11 V, between the initial and final states, indicates the MnOx/Co-Fe combination is as stable as or better than other Zn-air battery catalysts reported in the literature (Fig. 6-16 and Table 6-3). Only references with similar current densities and cycling times are compared here.

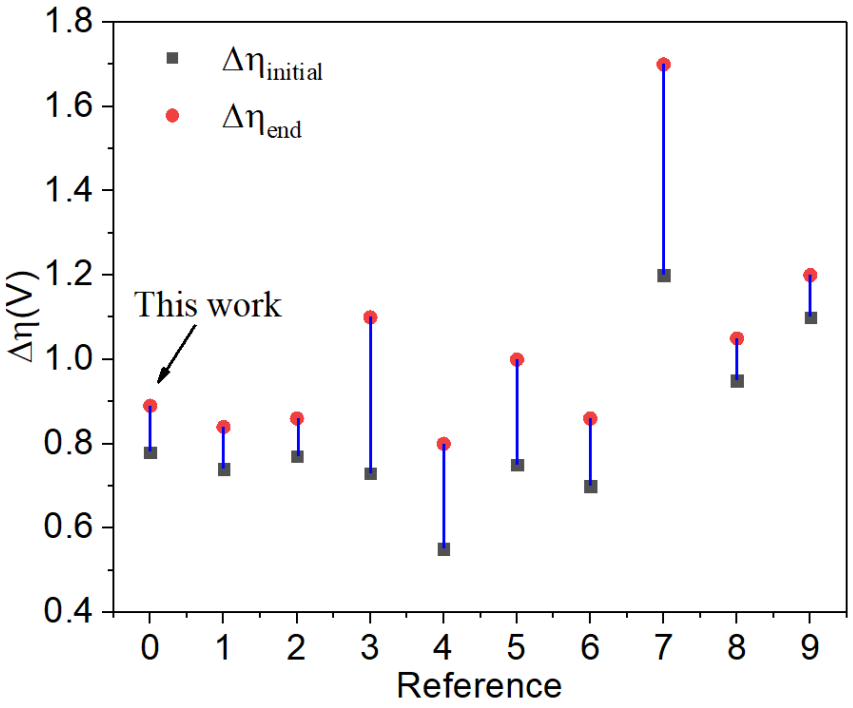

Fig. 6-16. Comparison of discharge-charge voltage gap (Δη) between this work and the literature (reference numbers are shown in Table 6-3).

Table 6-3. Comparison of discharge-charge voltage gap (Δη) between this work and the literature

No.	Battery test condition and Battery performance	Reference
0	10 mA cm^{-2} for 50 h $\Delta\eta_{initial}$= 0.78 V $\Delta\eta_{end}$= 0.89 V $\Delta\eta_{end}$-$\Delta\eta_{initial}$= 0.11 V	This work
1	10 mA cm^{-2} for 33.3 h $\Delta\eta_{initial}$= 0.74 V $\Delta\eta_{end}$= 0.84 V $\Delta\eta_{end}$-$\Delta\eta_{initial}$= 0.10 V	Ref.[341]
2	10 mA cm^{-2} for 55 h $\Delta\eta_{initial}$= 0.77 V $\Delta\eta_{end}$=0.86 V $\Delta\eta_{end}$-$\Delta\eta_{initial}$= 0.09 V	Ref.[342]
3	10 mA cm^{-2} for 64 h $\Delta\eta_{initial}$= 0.73 V $\Delta\eta_{end}$= 1.10 V $\Delta\eta_{end}$-$\Delta\eta_{initial}$= 0.37 V	Ref.[343]
4	10 mA cm^{-2} for 33.3 h $\Delta\eta_{initial}$= 0.55 V $\Delta\eta_{end}$= 0.80 V $\Delta\eta_{end}$-$\Delta\eta_{initial}$= 0.25 V	Ref.[344]
5	10.5 mA cm^{-2} for 33.3 h $\Delta\eta_{initial}$= 0.75 V $\Delta\eta_{end}$= 1.0 V $\Delta\eta_{end}$-$\Delta\eta_{initial}$= 0.25 V	Ref.[340]
6	10 mA cm^{-2} for 16.7 h $\Delta\eta_{initial}$= 0.70 V $\Delta\eta_{end}$= 0.86 V $\Delta\eta_{end}$-$\Delta\eta_{initial}$= 0.16 V	Ref.[345]
7	16 mA cm^{-2} for 13.3 h $\Delta\eta_{initial}$= 1.20 V $\Delta\eta_{end}$= 1.70 V $\Delta\eta_{end}$-$\Delta\eta_{initial}$= 0.50 V	Ref.[346]
8	15 mA cm^{-2} for 14 h $\Delta\eta_{initial}$= 0.95 V $\Delta\eta_{end}$= 1.05 V $\Delta\eta_{end}$-$\Delta\eta_{initial}$= 0.10 V	Ref.[347]
9	10 mA cm^{-2} for 50 h $\Delta\eta_{initial}$= 1.10 V $\Delta\eta_{end}$= 1.20 V $\Delta\eta_{end}$-$\Delta\eta_{initial}$= 0.10 V	Ref.[348]

Separation of the electrodes for the charge and discharge processes led to separation of reaction sites on the Zn electrode. After cycling, the Zn surface close to the vertical OER electrode became thicker, because it is favored for Zn deposition during charging. The region close to the horizontal ORR electrode underwent a decrease in thickness since, more Zn dissolution occurred. However, the thickness change in both areas was very small compared with the total thickness of Zn plate (~650 μm) (Fig. S6-22). After the 50 h cycling test, the thickness of the region near OER electrode increased by a maximum of 30 μm or 4.6%, while the thickness of the region near the ORR electrode decreased by ~10 μm or 1.6%. Therefore, the cycle life of the Zn-air battery is not limited by Zn consumption near the ORR electrode. The thickness changes are caused by current density differences between the discharge and the charge process at the same Zn surface sites. The process has been simulated using COMSOL Multiphysics® software (Fig. S6-23 and Fig. S6-24). This effect can be alleviated by reducing the distance between the ORR and OER electrodes, which is the subject of future work (Fig. S6-25). Other battery design enhancements, such as decreasing the distance between the ORR/OER electrode and the Zn electrode, will also be introduced to enhance battery performance.

6.4 Summary

In summary, an ORR active catalyst was synthesized by electrodepositing a combination of Mn_3O_4 nanorods and α-Mn_2O_3 spheres on carbon paper. An OER active Co-Fe (oxy)hydroxide film was electrodeposited on Ni foam. Both electrodes displayed ORR/OER activity that is comparable or even better than the commercial bifunctional Pt-Ru catalyst. It was demonstrated that both MnOx and Pt-Ru are more durable during cycling if they are used exclusively for ORR instead of as ORR-OER bifunctional catalysts. The electrodeposited materials were directly used in a modified Zn-

air battery as physically decoupled electrodes. The combination of MnOx and Co-Fe/Ni showed the same overall discharge-charge efficiency as Pt-Ru. The results indicate that the horizontal tri-electrode battery, together with separately synthesized electrocatalysts, can be a cost-effective way to improve efficiency and cycling stability of Zn-air batteries.

6.5 Supporting information

Influence of deposition time on MnOx morphology

The number of deposition cycles was changed to investigate the influence of deposition time on MnOx morphology. Nanorods preferentially grow at the beginning of electrodeposition (Fig. S6-17).

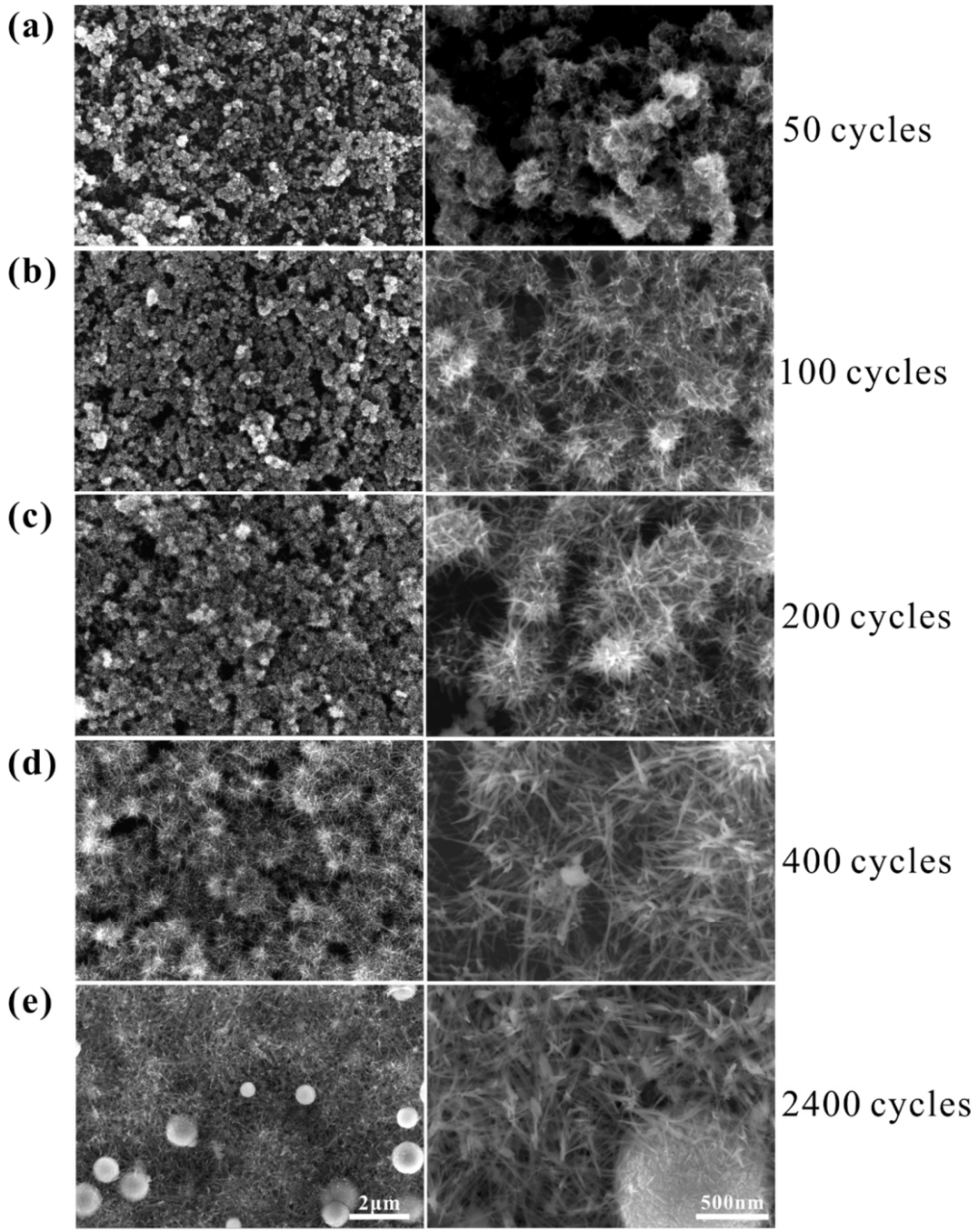

Fig. S6-17. SEM SE images showing the morphology of air electrode MnOx catalysts (unannealed), deposited with different electrodeposition cycles: (a) 50 cycles; (b) 100 cycles; (c) 200 cycles; (d) 400 cycles; (e) 2400 cycles (Fig. 6-3a and 6-3b). Note that there are no spherical particles for the shorter cycles.

Influence of deposition time on MnOx electrochemical performance

The relative number of spheres increases with increasing deposition time, leading to a composition change in the as deposited film (Fig. S6-18). LSV plots show that MnOx fabricated with 2400 deposition cycles has the highest ORR activity among all samples (Fig. S6-19). Increasing the deposition time from 2400 to 3600 or 4800 cycles does not enhance the ORR activity. The 2400 cycle and 3600 cycle samples have very similar activities, while there is a significantly activity drop off for the 4800 cycle sample. The 4800 cycle sample appears to contain more spheres that may reduce the surface area of active materials. MnOx fabricated with 1200 deposition cycles does not have good coverage on the GDL. As such, MnOx with 2400 deposition cycle was chosen for further electrochemical testing.

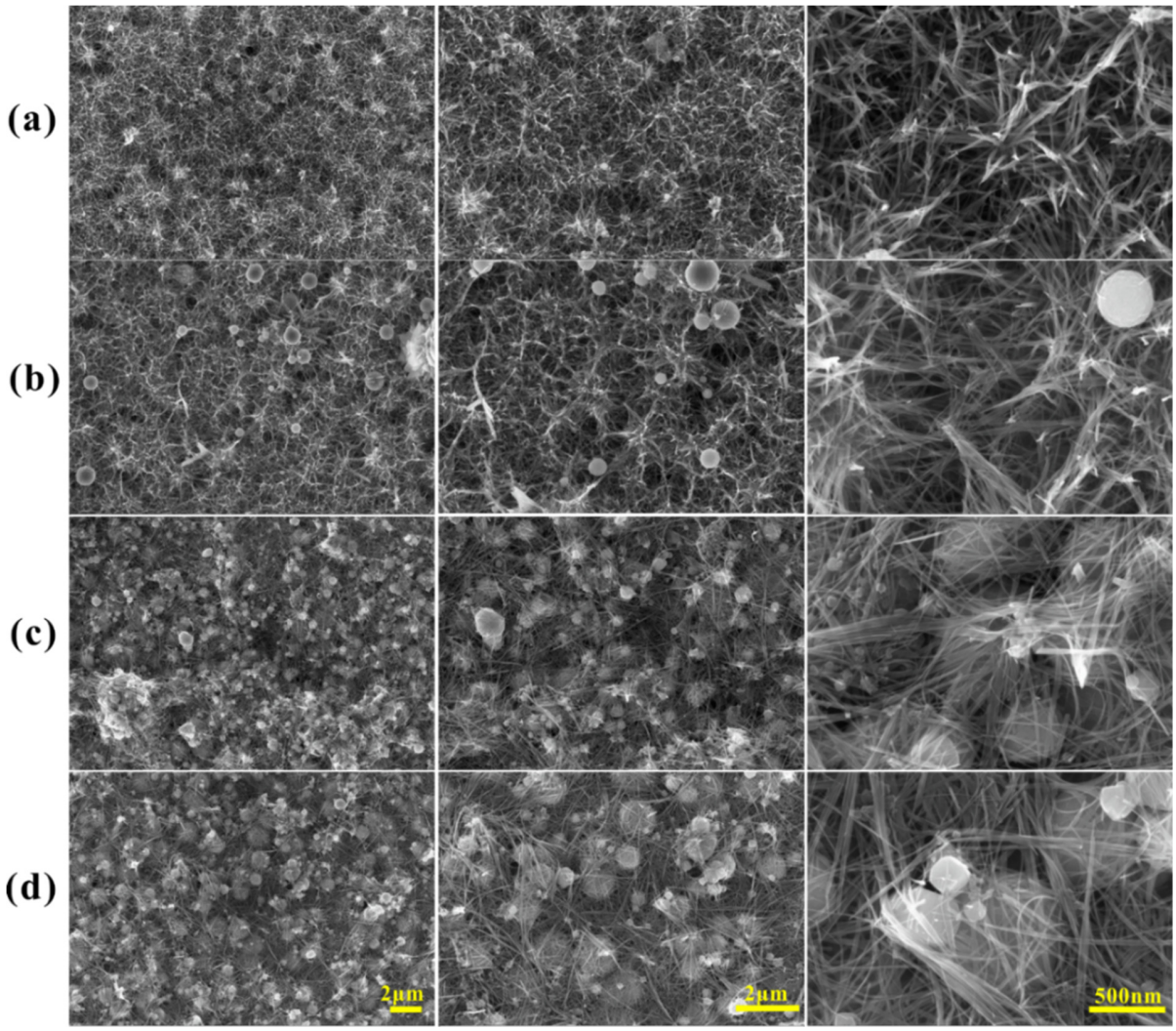

Fig. S6-18. SEM SE images showing the morphology of air electrode MnOx catalysts, deposited with different electrodeposition cycles: (a) 1200 cycles; (b) 2400 cycles; (c) 3600 cycles; (d) 4800 cycles. The images were taken after annealing.

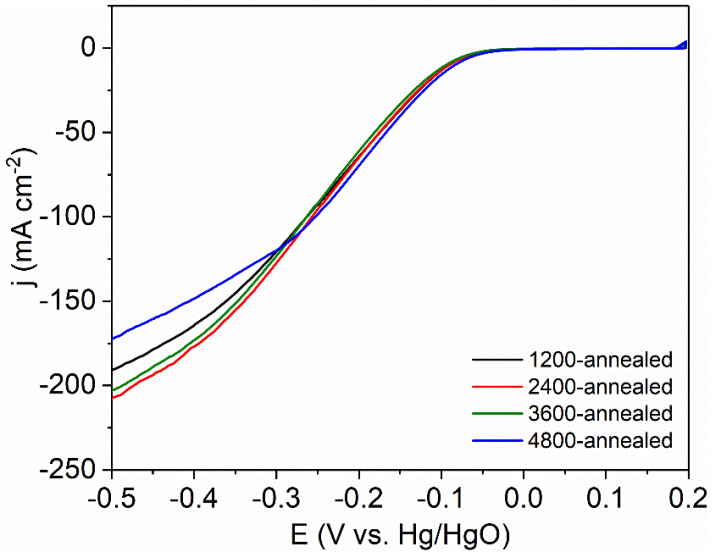

Fig. S6-19. LSV plots for MnOx-annealed catalysts with different deposition cycles in oxygen saturated 1 M KOH (scan rate is 5 mV s^{-1}).

Influence of Co doping into MnOx on electrochemical performance

It has been reported that Co oxides such as Co_3O_4 or amorphous CoOx are active OER catalysts and show a certain degree of ORR activity.[349, 350] Mixed Mn-Co oxides such as $MnCo_2O_4$ or $CoMn_2O_4$ have been reported as bifunctional catalysts.[351, 352] Therefore, it is possible to have Mn-Co oxides co-electrodeposited as bifunctional catalysts. Here, various amounts of Co precursor were added to the Mn electrodeposition electrolyte to form a mixed Mn-Co oxide catalyst layer under the same deposition conditions. The solutions for Mn-Co oxides deposition contained Mn acetate and Co acetate with several different composition ratios (Mn acetate:Co acetate = 1, 9:1, 1:4, 1:9 and 0, with an overall concentration of 0.02 M). These samples were labeled as pure Mn, Mn-Co-9-1, Mn-Co-1-4, Mn-Co-1-9 and pure Co, respectively.

SEM images show that the Mn oxide films start to become more dense after doping with Co (Fig. S6-20). EDX analysis shows that the Co content in Mn-Co oxide deposits increases in the following order: Mn (Mn:Co=∞) < Mn-Co-9-1 (Mn:Co=10:1) < Mn-Co-1-4 (Mn:Co=2:1) < Mn-Co-1-9 (Mn:Co=1.2:1) < Co (Mn:Co=0). Preferential deposition of MnOx results in a higher Mn content in the film relative to the electrolyte composition (Mn-Co-1-4 and Mn-Co-1-9).

The morphology of the deposits changed with increased doping of Co. Pure Mn oxide is composed mainly of nanorods (Fig. S6-20a), while a granular morphology appeared when a small amount of Co was added (Mn-Co-9-1, Fig. S6-20b). The porosity of the film decreased as more Co was added (Mn-Co-1-4, Fig. S6-20c and Mn-Co-1-9, Fig. S6-20d). The pure Co oxide sample had a dense, granular appearance (Fig. S6-20e).

LSV test show that the ORR activity decreases with increasing Co doping, while the OER activity increased with increasing Co doping (Fig. S6-21). The lower ORR activity is most likely caused by the lower porosity and the presence of CoOx (CoOx is not as active as MnOx in catalyzing ORR). It is interesting that Mn-Co-1-4 and Mn-Co-1-9 have the highest OER activity, not the pure Co oxide. The dense structure of the Co oxide deposit may be the reason for this difference. Therefore, the co-electrodeposition of mixed Mn-Co oxides is not a viable way to synthesize bifunctional catalysts, since too much ORR activity is sacrificed for a limited increase in OER activity.

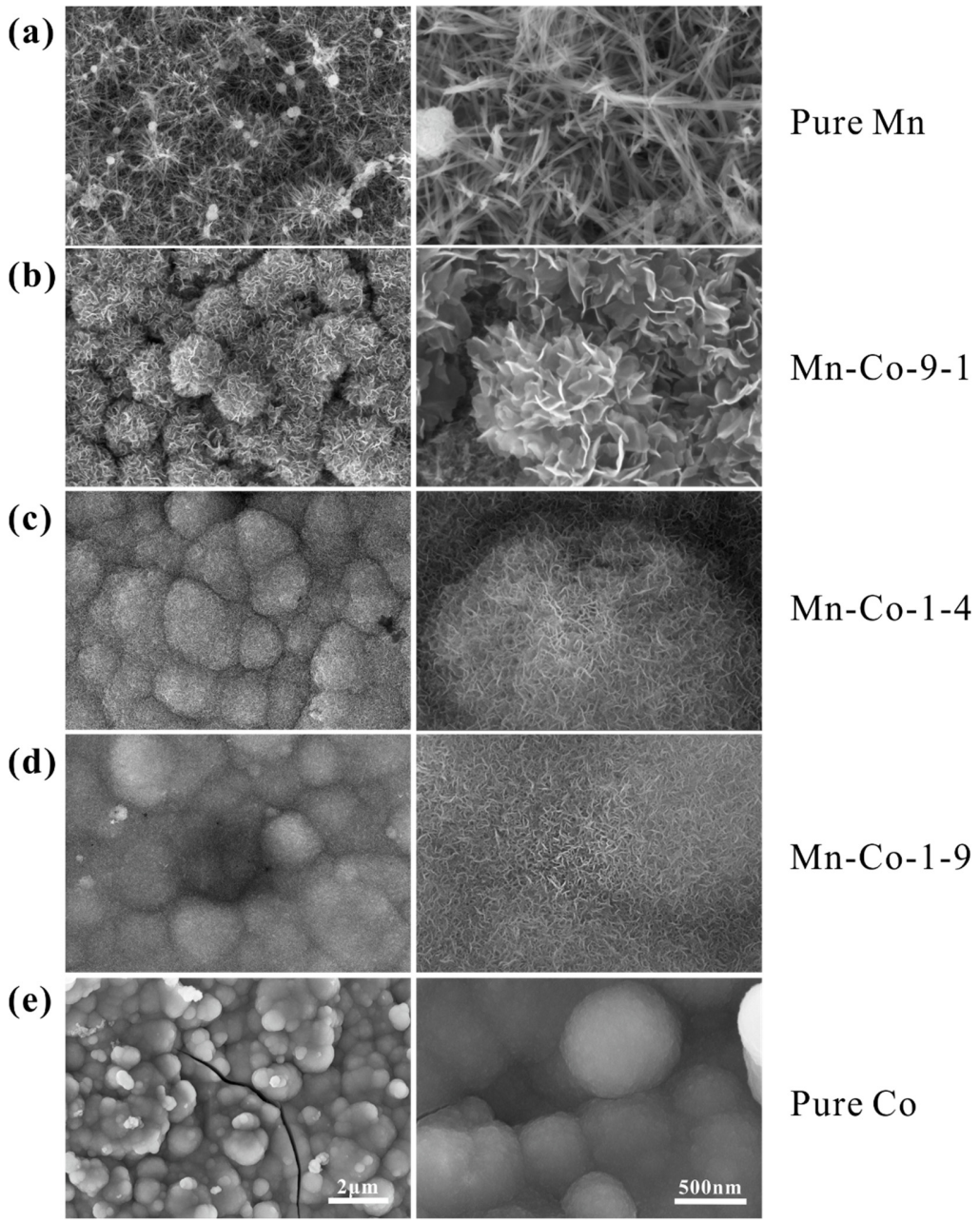

Fig. S6-20. SEM SE images showing the morphology of Mn-Co oxides with different Mn/Co ratios in the electrolyte.

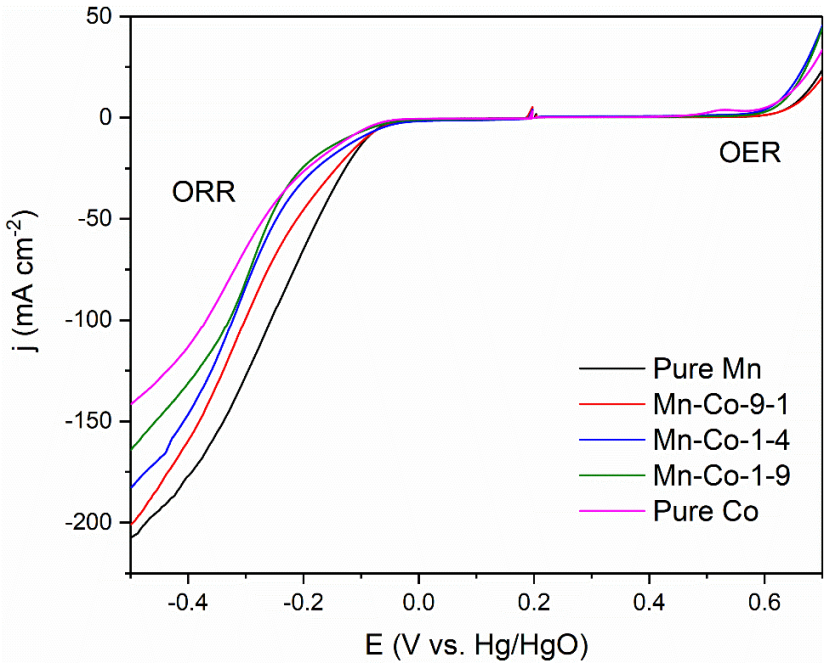

Fig. S6-21. LSV plots for Mn-Co oxides catalysts with different composition in oxygen saturated 1 M KOH (scan rate is 5 mV s^{-1}).

Simulation of Zn-air batteries by COMSOL Multiphysics® software

The reaction sites on the Zn electrode are different for the discharge and charge process. Two cycled Zn plates used in discharge-charge cycling tests (Fig. 6-13(d)) were compared with a fresh Zn plate, as shown in Fig. S6-22(a). The cycled Zn surface is essentially divided into two regions with the centre dividing line located about 3 cm from the left side. The dark region on the left of the centre dividing line faces the OER electrode, while the bright region on the right faces the ORR electrode (here the ORR electrode is represented by a 1 cm × 2 cm piece of GDL to indicate the actual reaction site). The Zn thickness at different locations was measured with a digital micrometer (0.001 mm accuracy) and compared with the fresh Zn plate (Fig. S6-22(b)). The dark

region of the cycled Zn is thicker than the fresh Zn, because it is favored for Zn deposition during the charging process. The brighter region on the right undergoes a decrease in thickness since more Zn dissolution happens there. However, the thickness change in both areas is very small compared with the total thickness of the Zn plate (~646 μm). After the 50 h cycling test or 100 cycles, the dark region thickness increased by a maximum of 30 μm or 4.6% (1 cm location), while the bright region thickness decreased by ~10 μm or 1.6% (5 cm location). Therefore, the cycle life of a Zn-air battery will not be limited by the continuous consumption of Zn near the ORR electrode. The thickness is predicted to decrease by ~50% after 3000 cycles or 1500 h of testing with the current consumption rate. Degradation of the air electrode or electrolyte is more likely to limit the battery lifetime.

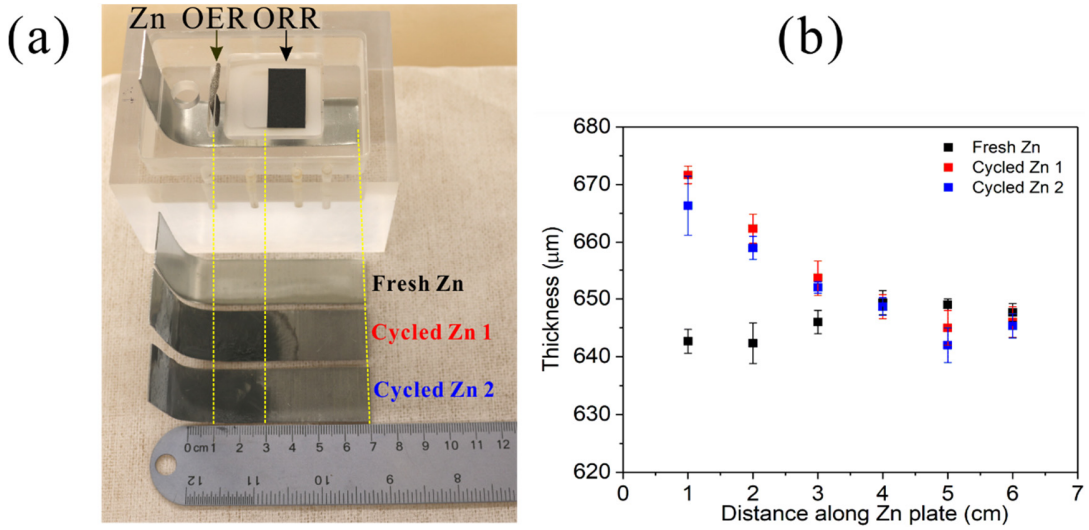

Fig. S6-22. (a) Image of fresh Zn plate and cycled Zn plate. (b) Thickness at various points along the Zn plate.

The current density distribution across the Zn surface during the discharge and charge process has been simulated using COMSOL Multiphysics® software. First, a geometric model of the tri-

electrode cell with the same dimensions and electrode layout was constructed (Fig. S6-23(a)). A secondary current distribution interface was used to simulate the electrochemical process, where only the effects of the electrode kinetics and solution resistance are taken into account. It is assumed that there are no diffusion or convection effects on the transport of electrolyte ions because the electrolyte is concentrated and static. The electrode reaction is controlled by the charge transfer process, according to the Butler-Volmer function:[353]

$$j = j_0 \left[\exp\left(\frac{\alpha_a n F \eta}{RT} \right) - \exp\left(\frac{-\alpha_c n F \eta}{RT} \right) \right] \quad (6\text{-}1)$$

where j_0 is the exchange current density, α_a and α_c are the dimensionless anodic and cathodic charge transfer coefficients, respectively, n is the number of electrons transferred, j is the reaction current density and η is the overpotential.

The exchange current density and charge transfer coefficient are key factors that determine the kinetics of the electrochemical process. However, these values from the literature vary significantly for different catalysts and experimental conditions (e.g., electrolyte concentration and temperature) and no values were found for our system.[354-358] Also, the appropriate values for our catalysts are not experimentally obtainable due to interference from the carbon paper substrate. As such, the kinetic parameters were adjusted from literature values to ensure that the simulated results were close to the experimental tests results. Other conditions were set according to the actual test environment, such as the temperature (25°C), electrolyte composition (6 M KOH + 0.25 M ZnO) and conductivity of the electrolyte/electrode. These parameters are shown in Table S6-4. Discharge-charge polarization and rate tests were simulated and showed similar behavior to actual cell tests, especially at a current density of 10 mA cm^{-2} (Fig. S6-23(b) and (c)).

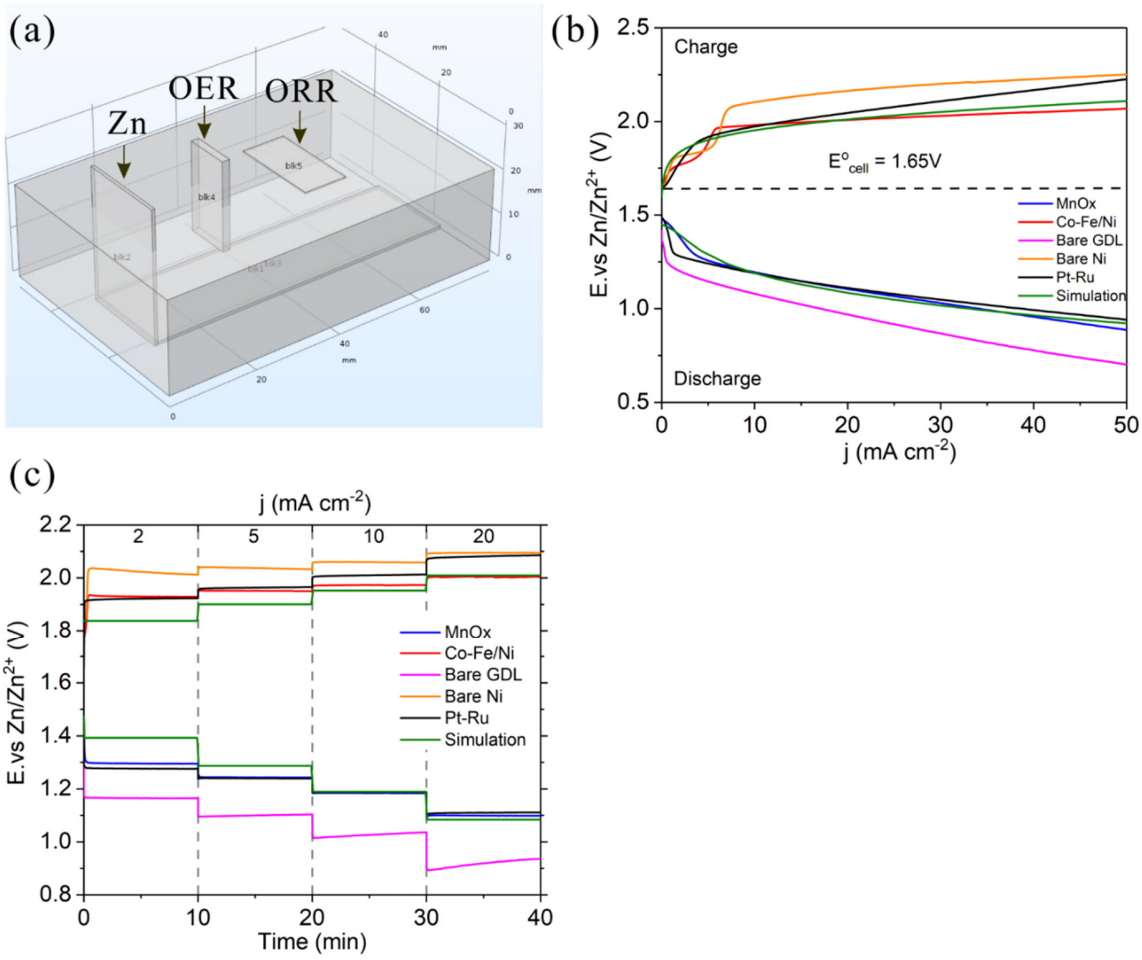

Fig. S6-23. (a) Geometry of Zn-air battery using COMSOL Multiphysics® software. (b) Comparison between simulated and experimental polarization curves. (c) Comparison between simulated and experimental discharge-charge rate test curves.

Table S6-4. Parameters used in modeling of the horizontal Zn-air battery at 25°C

Parameters	Unit	Value
Electric conductivity of ORR electrode (GDL)	S cm^{-1}	2.2
Electric conductivity of OER electrode (Ni)	S cm^{-1}	1.38×10^7
Electric conductivity of Zn	S cm^{-1}	1.66×10^7
Ionic conductivity of KOH electrolyte	S cm^{-1}	0.63
Diffusion coefficient of nitrogen in air	cm^2 s^{-1}	0.056
Diffusion coefficient of oxygen in air	cm^2 s^{-1}	0.045
Standard electrode potential of ORR/OER	V	0.401
Standard electrode potential of $Zn/Zn(OH)_2$	V	-1.25
Exchange current density of ORR	mA cm^{-2}	0.028
Anodic charge transfer coefficient of ORR	N/A	0.8
Cathodic charge transfer coefficient of ORR	N/A	0.2
Exchange current density of OER	mA cm^{-2}	0.06
Anodic charge transfer coefficient of OER	N/A	0.4
Cathodic charge transfer coefficient of OER	N/A	0.6
Exchange current density of $Zn/Zn(OH)_2$	mA cm^{-2}	10
Anodic charge transfer coefficient of $Zn/Zn(OH)_2$	N/A	0.5
Cathodic charge transfer coefficient of $Zn/Zn(OH)_2$	N/A	0.5

The same current density of 10 mA cm^{-2} applied in the experimental discharge-charge cycling tests (Fig. 6-13(d)) was applied to the modeled ORR and OER electrodes, respectively, to simulate the actual electrochemical process. The Zn region close to the ORR electrode has a higher current density than the OER side during discharge (Fig. 6-24(a)) and has a lower current density than the OER side during charge (Fig. 6-24(b)). As such, the higher discharge current density relative to the charge current density results in a higher Zn dissolution rate than deposition rate (Fig. 6-24(c)), which is the reason for the thickness decrease in Fig. S6-22. The magnitude of current density

across the Zn surface is between 0.8 and 1.3 mA cm^{-2}, due to the much larger area of Zn electrode compared with the ORR/OER electrode. The rate of Zn thickness change is thus very slow due to this low current density. The degree of uneven Zn surface current distribution can be alleviated by simply reducing the distance between the ORR and OER electrodes. For example, the simulation predicts that the gap between discharge and charge current density at the same location will be decreased by moving the OER electrode 1 cm towards the ORR electrode (Fig. S6-25).

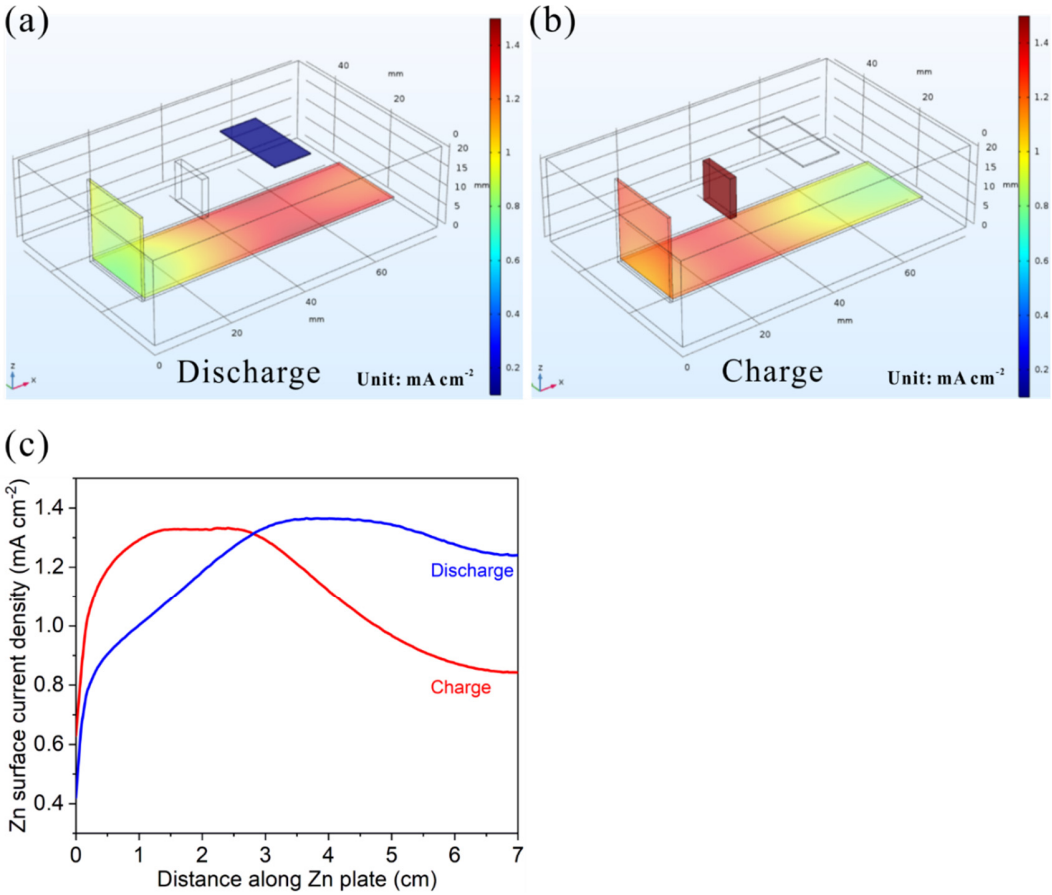

Fig. S6-24. (a) Zn surface current density distribution during the discharge process. (b) Zn surface current density distribution during the charge process. (c) Simulated average Zn surface current density from left to right.

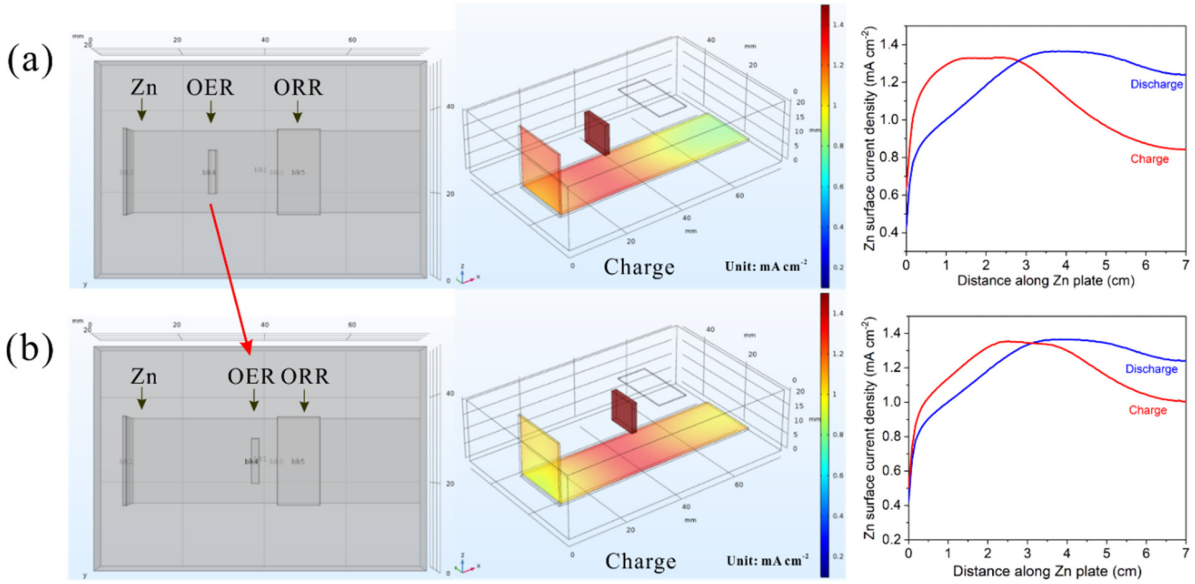

Fig. S6-25. Simulated Zn surface current density distribution: (a) Before adjustment of the OER electrode location. (b) After adjustment of the OER electrode location.

Chapter 7 : Conclusions and future work

7.1. Conclusions

This thesis has presented efforts in developing transition metal oxide catalysts through electrodeposition for Zn-air batteries. Co-Fe with an oxidized surface was electrodeposited on GDL carbon paper or Ni foam as the OER catalyst, while MnOx was electrodeposited on GDL as the ORR catalyst. The influence of deposition time and composition on OER activity of Co-Fe was systematically studied. Then Co-Fe was combined with ORR active MnOx catalysts for use in a rechargeable Zn-air battery. By sequentially depositing Co-Fe over the MnOx layer, a bifunctional MnOx/Co-Fe catalyst was realized. As an alternative, MnOx and Co-Fe were deposited on GDL and Ni foam separately and tested as physically decoupled electrodes (MnOx and Co-Fe/Ni) in Zn-air batteries. This study showed that transition metal catalysts prepared by electrodeposition can have comparable or even better ORR/OER activity than the state-of-art catalysts. In addition, catalysts electrodeposited on electrodes displayed good durability and stable performance in Zn-air batteries. Therefore, electrodeposition is an effective way to fabricate Zn-air battery catalysts.

The main achievements and conclusions of this work are listed in the following.

Co-Fe OER catalysts: influence of deposition time

Co-Fe OER nanocuboidal catalysts for the air electrode were fabricated by cathodic electrodeposition. The electrolyte for deposition was controlled at $CoSO_4$:$FeSO_4$ = 3:1 while the deposition time was increased from 1 to 16 min. The deposits evolved from single crystal nanocubes for the 1 min deposition into a continuous film for the 8 min deposition. The crystal

structure of the Co-Fe deposit was studied by XRD, showing a bcc Co-Fe solid solution but with different Fe levels. The Fe amount was 30.3% Co-Fe for the 1 min deposition time and 39.4% for longer deposition times. EDX analysis showed that all the particles had oxidized surfaces, which provided active sites to catalyze OER. The OER catalytic capacity was evaluated in alkaline media and compared with commercial Pt/Ru catalysts. The OER activity increased with increasing deposition time until 8 min, after which the activity decreased. Co-Fe deposits exhibited low Tafel slopes, high durability and low overpotential (0.29 V at 10 mA cm^{-2} for CoFe-8min). The Co-Fe catalysts were tested in a Zn-air battery and showed similar cycling efficiency, but better cycling stability, compared with Pt/Ru.

Co-Fe OER catalyst: influence of composition

Following the study on Co-Fe catalysts, deposited for different deposition times, different electrolyte compositions were explored to generate deposits with a full range of compositions, from pure Co to pure Fe. The composition ratio in the solution was changed ($CoSO_4$:$FeSO_4$ = 1, 3:1, 1:1, 1:3 and 0, with an overall $CoSO_4$+$FeSO_4$ concentration = 0.2 M). Co-Fe was cathodically electrodeposited on GDL at a constant current of 150 mA for 1 min. The amount of Fe in the deposits increased with increasing Fe in the electrolyte, but the deposit morphology remained essentially the same (with the exception of pure Co) as single crystals, cuboidal nanoparticles. The pure Co deposits were in the form of hexagonal plates. The deposited catalysts were metallic in nature (bcc solid solution) with oxidized surfaces that were rich in Fe relative to the bulk. The OER activity increased with increasing Fe levels, up to ~65 at% Fe (Co-Fe-1-1), with an overpotential of 0.33 V at 10 mA cm^{-2} in 1 M KOH. The catalyst particles were stable in terms of

morphology and performance after 100 h of galvanostatic cycling and 20 h or battery testing, although additional oxidation of the particle surfaces occurred.

MnOx/Co-Fe sequentially electrodeposited bifunctional catalyst

MnOx and Co-Fe were sequentially electrodeposited on carbon paper to fabricate bifunctional catalysts MnOx/Co-Fe for Zn-air batteries. MnOx was initially deposited as an amorphous mixture (MnO_2/MnOOH) and was then reduced to Mn_2O_3/MnOOH after coating with Co-Fe nanoparticles. The electrochemical properties of the hybrid MnOx/Co-Fe catalysts were measured, showing higher ORR and OER activity compared with MnOx and Co-Fe alone. The synergistic effect is related to the reduced Mn oxidation state, higher surface area and lower charge transfer resistance. A Zn-air battery using MnOx/Co-Fe catalysts exhibited good discharge-recharge performance and a cycling efficiency of 59.6% that is comparable with Pt/C catalysts at 5 mA cm^{-2} current density. Electrodeposited MnOx/Co-Fe showed strong adhesion to GDL and was stable throughout 40 h of battery cycling.

MnOx and Co-Fe separately electrodeposited as physically decoupled electrodes

An ORR active catalyst was synthesized by electrodepositing a combination of Mn_3O_4 nanorods and α-Mn_2O_3 spheres on carbon paper. An OER active Co-Fe (oxy)hydroxide film was electrodeposited on Ni foam. Both electrodes displayed ORR/OER activity that was comparable or even better than the commercial bifunctional Pt-Ru catalyst. It was demonstrated that both MnOx and Pt-Ru are more durable during cycling if they are used exclusively for ORR instead of as an ORR-OER bifunctional catalyst. The fabricated catalysts were assembled into a Zn-air

battery for discharge-charge cycling tests and showed the same average efficiency (58%) as commercial Pt-Ru catalysts at 10 mA cm^{-2} current density. The results indicate that the horizontal tri-electrode battery, together with separately synthesized electrocatalysts, can be a cost-effective way to improve efficiency and cycling stability of Zn-air batteries.

7.2. Future work

Co-Fe

Cathodic electrodeposition was used to deposit Co-Fe nanocubes with a diameter of 100-200 nm. Changing the deposition electrolyte and other parameters, such as complexing agent, additives and current densities, may help reduce the particle size further and increase the surface area. Electrodeposition can be done in a non-aqueous electrolyte (e.g., eutectic solvent) to avoid the HER and result in a change in morphology or crystal structure. Doping of other elements may help increase the OER activity and durability.

MnOx

The MnOx nanorods/spheres in Chapter 6 have a high ORR activity. However, their nucleation and growth mechanisms are still unknown. It may be beneficial to sort out the mechanism(s) and then control the process to achieve higher ORR activity and stability. It may be worthwhile to deposit MnOx on other substrates like Ni-foam or stainless steel mesh to improve conductivity and durability. However, the structure of the substrate would need to be modified (e.g., pore size

and porosity) and a hydrophobic surface is required to prevent flooding, possibly by introducing PTFE.

Battery design

The battery structure needs to be optimized to achieve better cycle life. The three major problems for aqueous cell system are flooding, K_2CO_3 precipitation and electrolyte evaporation. These problems could be solved by using a solid-state electrolyte. A possible approach to reduce the interfacial resistance is to polymerize the solid-state electrolyte (ionic conductor) with catalyst particles. The catalysts need to be accessed by both electrons and ions to catalyze ORR and OER. The electrodes need to be properly arranged for uniform Zn deposition and to avoid shape change of the Zn electrode. Battery modeling may help explore the best configurations and to optimize other parameters such as temperature, humidity and air/oxygen flow rate.

References

1. M. Aneke and M. Wang, *Applied Energy,* **179** 350-377 (2016).
2. S. Xin, Y. X. Yin, Y. G. Guo, and L. J. Wan, *Advanced Materials,* **26** (8), 1261-1265 (2014).
3. Á. Cunha, J. Martins, N. Rodrigues, and F. P. Brito, *International Journal of Energy Research,* **39** (7), 889-918 (2015).
4. C. Zhang, Y.-L. Wei, P.-F. Cao, and M.-C. Lin, *Renewable and Sustainable Energy Reviews,* **82** 3091-3106 (2018).
5. T. Zhang, Z. Tao, and J. Chen, *Materials Horizons,* **1** (2), 196-206 (2014).
6. A. C. Luntz and B. D. McCloskey, *Chemical Reviews,* **114** (23), 11721-11750 (2014).
7. M. A. Hannan, M. M. Hoque, A. Mohamed, and A. Ayob, *Renewable and Sustainable Energy Reviews,* **69** 771-789 (2017).
8. D. O. Akinyele and R. K. Rayudu, *Sustainable Energy Technologies and Assessments,* **8** 74-91 (2014).
9. M. Guarnieri, P. Mattavelli, G. Petrone, and G. Spagnuolo, *IEEE Industrial Electronics Magazine,* **10** (4), 20-31 (2016).
10. M. Prabu, P. Ramakrishnan, H. Nara, T. Momma, T. Osaka, and S. Shanmugam, *ACS Applied Materials & Interfaces,* **6** (19), 16545-16555 (2014).
11. X. Zhang, in *Encyclopedia of Electrochemical Power Sources*, p. pp. 454-468, Academic Press, Amsterdam (2009).
12. D. R. Lide, *CRC Handbook of Chemistry and Physics*, CRC Press, New York (2009).
13. A. R. Mainar, O. Leonet, M. Bengoechea, I. Boyano, I. de Meatza, A. Kvasha, A. Guerfi, and J. Alberto Blázquez, *International Journal of Energy Research,* **40** (8), 1032-1049 (2016).
14. T. Reddy, *Handbook of batteries*, McGraw-Hill Pub. (2002).
15. J.-S. Lee, S. T. Kim, R. Cao, N.-S. Choi, M. Liu, K. T. Lee, and J. Cho, *Advanced Energy Materials,* **1** 34-50 (2011).
16. X. Yu and S. Ye, *Journal of Power Sources,* **172** (1), 145-154 (2007).
17. F. C. Porter, *Zinc handbook: properties, processing, and use in design*, CRC Press (1991).
18. J. F. Drillet, F. Holzer, T. Kallis, S. Müller, and V. M. Schmidt, *Physical Chemistry Chemical Physics,* **3** (3), 368-371 (2001).

19. H.-H. Cheng and C.-S. Tan, *Journal of Power Sources,* **162** (2), 1431-1436 (2006).
20. J. T. Nichols, F. R. McLARNON, and E. J. Cairns, *Chemical engineering communications,* **37** (1-6), 355-379 (1985).
21. H. Kim, G. Jeong, Y.-U. Kim, J.-H. Kim, C.-M. Park, and H.-J. Sohn, *Chemical Society Reviews,* **42** (23), 9011-9034 (2013).
22. Y. Li and H. Dai, *Chemical Society Reviews,* **43** (15), 5257-5275 (2014).
23. L. O. Valøen and M. I. Shoesmith, *PHEV 2007 Conference,* 4-5 (2007).
24. Y. Li and H. Dai, *Chemical Society Reviews,* **43** (15), 5257-5275 (2014).
25. A. R. Mainar, L. C. Colmenares, J. Alberto Blazquez, and I. Urdampilleta, *International Journal of Energy Research,* **42** (3), 903-918 (2018).
26. R. Gilliam, J. Graydon, D. Kirk, and S. Thorpe, *International Journal of Hydrogen Energy,* **32** (3), 359-364 (2007).
27. J. M. Wang, L. Zhang, C. Zhang, and J. Q. Zhang, *Journal of Power Sources,* **102** (1-2), 139-143 (2001).
28. S. J. Banik and R. Akolkar, *Electrochimica Acta,* **179** 475-481 (2015).
29. C. W. Lee, K. Sathiyanarayanan, S. W. Eom, H. S. Kim, and M. S. Yun, *Journal of Power Sources,* **159** (2), 1474-1477 (2006).
30. J. Zhu, Y. Zhou, and C. Gao, *Journal of Power Sources,* **72** (2), 231-235 (1998).
31. C. Yang, Z. Zhang, Z. Tian, K. Zhang, J. Li, and Y. Lai, *Journal of The Electrochemical Society,* **163** (9), A1836-A1840 (2016).
32. R. Shivkumar, G. P. Kalaignan, and T. Vasudevan, *Journal of power sources,* **55** (1), 53-62 (1995).
33. M. Kar, B. Winther-Jensen, M. Forsyth, and D. R. MacFarlane, *Physical Chemistry Chemical Physics,* **15** (19), 7191-7197 (2013).
34. T. J. Simons, A. A. J. Torriero, P. C. Howlett, D. R. MacFarlane, and M. Forsyth, *Electrochemistry Communications,* **18** 119-122 (2012).
35. M. Xu, D. G. Ivey, W. Qu, Z. Xie, E. Dy, and X. Z. Yuan, *Journal of The Electrochemical Society,* **161** (1), A128-A136 (2014).
36. X. Z. Yuan, V. Alzate, Z. Xie, D. G. Ivey, E. Dy, and W. Qu, *Journal of The Electrochemical Society,* **161** (4), A458-A466 (2014).
37. M. C. Buzzeo, R. G. Evans, and R. G. Compton, *Chemphyschem,* **5** (8), 1106-1120 (2004).

38. X. Z. Yuan, V. Alzate, Z. Xie, D. G. Ivey, and W. Qu, *Journal of The Electrochemical Society,* **161** (4), A451-A457 (2014).
39. S. X. Qu, Z. S. Song, J. Liu, Y. B. Li, Y. Kou, C. Ma, X. P. Han, Y. D. Deng, N. Q. Zhao, W. B. Hu, and C. Zhong, *Nano Energy,* **39** 101-110 (2017).
40. C. Y. Su, H. Cheng, W. Li, Z. Q. Liu, N. Li, Z. F. Hou, F. Q. Bai, H. X. Zhang, and T. Y. Ma, *Advanced Energy Materials,* **7** (13), (2017).
41. M. F. Wang, S. S. Liu, N. Xu, T. Qian, and C. L. Yan, *Advanced Sustainable Systems,* **1** (10), (2017).
42. S. S. Liu, M. F. Wang, X. Y. Sun, N. Xu, J. Liu, Y. Z. Wang, T. Qian, and C. L. Yan, *Advanced Materials,* **30** (4), (2018).
43. X. Zhu, H. Yang, Y. Cao, and X. Ai, *Electrochimica Acta,* **49** (16), 2533-2539 (2004).
44. Z. Zhang, C. C. Zuo, Z. H. Liu, Y. Yu, Y. X. Zuo, and Y. Song, *Journal of Power Sources,* **251** 470-475 (2014).
45. A. Sumboja, M. Lubke, Y. Wang, T. An, Y. Zong, and Z. L. Liu, *Advanced Energy Materials,* **7** (20), (2017).
46. G. M. Wu, S. J. Lin, and C. C. Yang, *Journal of Membrane Science,* **280** (1-2), 802-808 (2006).
47. Y. F. Xu, Y. Zhang, Z. Y. Guo, J. Ren, Y. G. Wang, and H. S. Peng, *Angewandte Chemie-International Edition,* **54** (51), 15390-15394 (2015).
48. R. Othman, W. J. Basirun, A. H. Yahaya, and A. K. Arof, *Journal of Power Sources,* **103** (1), 34-41 (2001).
49. A. A. Mohamad, *Journal of Power Sources,* **159** (1), 752-757 (2006).
50. J. Park, M. Park, G. Nam, J. S. Lee, and J. Cho, *Advanced Materials,* **27** (8), 1396-+ (2015).
51. J. Fu, J. Zhang, X. P. Song, H. Zarrin, X. F. Tian, J. L. Qiao, L. Rasen, K. C. Li, and Z. W. Chen, *Energy & Environmental Science,* **9** (2), 663-670 (2016).
52. J. Zhang, J. Fu, X. Song, G. Jiang, H. Zarrin, P. Xu, K. Li, A. Yu, and Z. Chen, *Advanced Energy Materials,* **6** (14), 1600476 (2016).
53. A. Puapattanakul, S. Therdthianwong, A. Therdthianwong, and N. Wongyao, *Energy Procedia,* **34** 173-180 (2013).
54. J. Fu, Z. P. Cano, M. G. Park, A. Yu, M. Fowler, and Z. Chen, *Advanced Materials,* **29** (7), (2017).

55. P. Tan, B. Chen, H. R. Xu, H. C. Zhang, W. Z. Cai, M. Ni, M. L. Liu, and Z. P. Shao, *Energy & Environmental Science,* **10** (10), 2056-2080 (2017).
56. P. Arora and Z. Zhang, *Chemical Reviews,* **104** (10), 4419-4462 (2004).
57. G. M. Wu, S. J. Lin, and C. C. Yang, *Journal of Membrane Science,* **284** (1-2), 120-127 (2006).
58. G. M. Wu, S. J. Lin, J. H. You, and C. C. Yang, *Materials Chemistry and Physics,* **112** (3), 798-804 (2008).
59. R. Franke-Lang, T. Arlt, I. Manke, and J. Kowal, *Journal of Power Sources,* **370** 45-51 (2017).
60. H. J. Hwang, W. S. Chi, O. Kwon, J. G. Lee, J. H. Kim, and Y. G. Shul, *ACS Applied Materials & Interfaces,* **8** (39), 26298-26308 (2016).
61. H. W. Kim, J. M. Lim, H. J. Lee, S. W. Eom, Y. T. Hong, and S. Y. Lee, *Journal of Materials Chemistry A,* **4** (10), 3711-3720 (2016).
62. H. J. Lee, J. M. Lim, H. W. Kim, S. H. Jeong, S. W. Eom, Y. T. Hong, and S. Y. Lee, *Journal of Membrane Science,* **499** 526-537 (2016).
63. P. Sapkota and H. Kim, *Journal of Industrial and Engineering Chemistry,* **16** (1), 39-44 (2010).
64. Z. Q. Wang, X. Y. Meng, Z. Q. Wu, and S. Mitra, *Journal of Energy Chemistry,* **26** (1), 129-138 (2017).
65. H. Saputra, R. Othman, A. G. E. Sutjipto, and R. Muhida, *Journal of Membrane Science,* **367** (1-2), 152-157 (2011).
66. X. W. Yu, M. M. Gross, S. F. Wang, and A. Manthiram, *Advanced Energy Materials,* **7** (11), (2017).
67. Y. Shen and K. Kordesch, *Journal of Power Sources,* **87** (1-2), 162-166 (2000).
68. R. Y. Wang, D. W. Kirk, and G. X. Zhang, *Journal of The Electrochemical Society,* **153** (5), (2006).
69. J. W. Diggle, A. R. Despic, and J. O. M. Bockris, *Journal of The Electrochemical Society,* **116** (11), (1969).
70. A. R. Despić and M. M. Purenović, *Journal of The Electrochemical Society,* **121** (3), (1974).
71. R. E. F. Einerhand, *Journal of The Electrochemical Society,* **138** (1), (1991).

72. F. R. McLarnon, *Journal of The Electrochemical Society,* **138** (2), (1991).
73. K. Wang, P. Pei, Z. Ma, H. Xu, P. Li, and X. Wang, *Journal of Power Sources,* **271** 65-75 (2014).
74. C. W. Lee, K. Sathiyanarayanan, S. W. Eom, H. S. Kim, and M. S. Yun, *Journal of Power Sources,* **160** (1), 161-164 (2006).
75. J. McBreen and E. Gannon, *Journal of Power Sources,* **15** (2-3), 169-177 (1985).
76. C. W. Lee, K. Sathiyanarayanan, S. W. Eom, and M. S. Yun, *Journal of Power Sources,* **160** (2), 1436-1441 (2006).
77. Y.-D. Cho and G. T.-K. Fey, *Journal of Power Sources,* **184** (2), 610-616 (2008).
78. S.-M. Lee, Y.-J. Kim, S.-W. Eom, N.-S. Choi, K.-W. Kim, and S.-B. Cho, *Journal of Power Sources,* **227** 177-184 (2013).
79. Y. N. Jo, S. H. Kang, K. Prasanna, S. W. Eom, and C. W. Lee, *Applied Surface Science,* **422** 406-412 (2017).
80. M. Schmid and M. Willert-Porada, *Journal of Power Sources,* **351** 115-122 (2017).
81. M. Schmid and M. Willert-Porada, *Electrochimica Acta,* **260** 246-253 (2018).
82. W. T. Hong, M. Risch, K. A. Stoerzinger, A. Grimaud, J. Suntivich, and Y. Shao-Horn, *Energy & Environmental Science,* **8** (5), 1404-1427 (2015).
83. Y. Jiao, Y. Zheng, M. Jaroniec, and S. Z. Qiao, *Chemical Society Reviews,* **44** (8), 2060-2086 (2015).
84. S. Maass, F. Finsterwalder, G. Frank, R. Hartmann, and C. Merten, *Journal of Power Sources,* **176** (2), 444-451 (2008).
85. L. Mao, *Electrochimica Acta,* **48** (8), 1015-1021 (2003).
86. Y. L. Cao, H. X. Yang, X. P. Ai, and L. F. Xiao, *Journal of Electroanalytical Chemistry,* **557** 127-134 (2003).
87. A. S. Ryabova, F. S. Napolskiy, T. Poux, S. Y. Istomin, A. Bonnefont, D. M. Antipin, A. Y. Baranchikov, E. E. Levin, A. M. Abakumov, G. Kerangueven, E. V. Antipov, G. A. Tsirlina, and E. R. Savinova, *Electrochimica Acta,* **187** 161-172 (2016).
88. K. A. Stoerzinger, M. Risch, B. H. Han, and Y. Shao-Horn, *ACS Catalysis,* **5** (10), 6021-6031 (2015).
89. N. T. Suen, S. F. Hung, Q. Quan, N. Zhang, Y. J. Xu, and H. M. Chen, *Chemical Society Reviews,* **46** (2), 337-365 (2017).

90. H. Dau, C. Limberg, T. Reier, M. Risch, S. Roggan, and P. Strasser, *Chemcatchem,* **2** (7), 724-761 (2010).
91. D. U. Lee, P. Xu, Z. P. Cano, A. G. Kashkooli, M. G. Park, and Z. W. Chen, *Journal of Materials Chemistry A,* **4** (19), 7107-7134 (2016).
92. S. P. Mehandru, *Journal of The Electrochemical Society,* **136** (1), (1989).
93. J. O. M. Bockris, *Journal of The Electrochemical Society,* **131** (2), (1984).
94. L. Han, S. J. Dong, and E. K. Wang, *Advanced Materials,* **28** (42), 9266-9291 (2016).
95. J. H. Wang, W. Cui, Q. Liu, Z. C. Xing, A. M. Asiri, and X. P. Sun, *Advanced Materials,* **28** (2), 215-230 (2016).
96. H. Willems, A. Kobussen, J. De Wit, and G. Broers, *Journal of Electroanalytical Chemistry and Interfacial Electrochemistry,* **170** (1-2), 227-242 (1984).
97. E. B. Castro, C. A. Gervasi, and J. R. Vilche, *Journal of Applied Electrochemistry,* **28** (8), 835-841 (1998).
98. M. E. G. Lyons and M. P. Brandon, *International Journal of Electrochemical Science,* **3** (12), 1425-1462 (2008).
99. R. A. van Santen, *Novel Concepts in Catalysis and Chemical Reactors: Improving the Efficiency for the Future,* 1-30 (2010).
100. Y. Shao, G. Yin, and Y. Gao, *Journal of Power Sources,* **171** (2), 558-566 (2007).
101. Y. Nie, L. Li, and Z. Wei, *Chemical Society Reviews,* **44** (8), 2168-2201 (2015).
102. X. Huang, Z. Zhao, L. Cao, Y. Chen, E. Zhu, Z. Lin, M. Li, A. Yan, A. Zettl, and Y. M. Wang, *Science,* **348** (6240), 1230-1234 (2015).
103. D. Y. Chung, S. W. Jun, G. Yoon, S. G. Kwon, D. Y. Shin, P. Seo, J. M. Yoo, H. Shin, Y.-H. Chung, and H. Kim, *Journal of the American Chemical Society,* **137** (49), 15478-15485 (2015).
104. D. S. Choi, A. W. Robertson, J. H. Warner, S. O. Kim, and H. Kim, *Advanced Materials,* **28** (33), 7115-7122 (2016).
105. L. Xiao, L. Zhuang, Y. Liu, J. Lu, and H. D. Abruña, *Journal of the American Chemical Society,* **131** (2), 602-608 (2009).
106. J. Guo, A. Hsu, D. Chu, and R. Chen, *The Journal of Physical Chemistry C,* **114** (10), 4324-4330 (2010).
107. T. Reier, M. Oezaslan, and P. Strasser, *ACS Catalysis,* **2** (8), 1765-1772 (2012).

108. M. S. Faber and S. Jin, *Energy & Environmental Science,* **7** (11), 3519-3542 (2014).
109. L. Mao, D. Zhang, T. Sotomura, K. Nakatsu, N. Koshiba, and T. Ohsaka, *Electrochimica Acta,* **48** (8), 1015-1021 (2003).
110. F. Cheng, Y. Su, J. Liang, Z. Tao, and J. Chen, *Chemistry of Materials,* **22** (3), 898-905 (2010).
111. Y. Meng, W. Song, H. Huang, Z. Ren, S.-Y. Chen, and S. L. Suib, *Journal of the American Chemical Society,* **136** (32), 11452-11464 (2014).
112. Y. Liang, Y. Li, H. Wang, J. Zhou, J. Wang, T. Regier, and H. Dai, *Nature materials,* **10** (10), 780 (2011).
113. N. I. Andersen, A. Serov, and P. Atanassov, *Applied Catalysis B: Environmental,* **163** 623-627 (2015).
114. C. Shi, G.-L. Zang, Z. Zhang, G.-P. Sheng, Y.-X. Huang, G.-X. Zhao, X.-K. Wang, and H.-Q. Yu, *Electrochimica Acta,* **132** 239-243 (2014).
115. H. S. Jeon, M. S. Jee, H. Kim, S. J. Ahn, Y. J. Hwang, and B. K. Min, *ACS Applied Materials & Interfaces,* **7** (44), 24550-24555 (2015).
116. F. Cheng, T. Zhang, Y. Zhang, J. Du, X. Han, and J. Chen, *Angewandte Chemie International Edition,* **52** (9), 2474-2477 (2013).
117. Z. F. Huang, J. Wang, Y. C. Peng, C. Y. Jung, A. Fisher, and X. Wang, *Advanced Energy Materials,* **7** (23), 21 (2017).
118. Y. Zhong, X. H. Xia, F. Shi, J. Y. Zhan, J. P. Tu, and H. J. Fan, *Advanced Science,* **3** (5), (2016).
119. P. W. Menezes, A. Indra, C. Das, C. Walter, C. Göbel, V. Gutkin, D. Schmeiβer, and M. Driess, *ACS Catalysis,* **7** (1), 103-109 (2016).
120. F. Cheng and J. Chen, *Chemical Society Reviews,* **41** (6), 2172-2192 (2012).
121. R. W. Grimes, A. B. Anderson, and A. H. Heuer, *Journal of the American Chemical Society,* **111** (1), 1-7 (1989).
122. J. Suntivich, H. A. Gasteiger, N. Yabuuchi, H. Nakanishi, J. B. Goodenough, and Y. Shao-Horn, *Nat Chem,* **3** (7), 546-550 (2011).
123. H. Tanaka and M. Misono, *Current Opinion in Solid State and Materials Science,* **5** (5), 381-387 (2001).

124. Y. Li, M. Gong, Y. Liang, J. Feng, J.-E. Kim, H. Wang, G. Hong, B. Zhang, and H. Dai, *Nature Communications,* **4** (2013).
125. C. W. B. Bezerra, L. Zhang, K. Lee, H. Liu, A. L. B. Marques, E. P. Marques, H. Wang, and J. Zhang, *Electrochimica Acta,* **53** (15), 4937-4951 (2008).
126. Y. V. Kaneti, J. Tang, R. R. Salunkhe, X. C. Jiang, A. B. Yu, K. C. W. Wu, and Y. Yamauchi, *Advanced Materials,* **29** (12), (2017).
127. W. Wang, X. M. Xu, W. Zhou, and Z. P. Shao, *Advanced Science,* **4** (4), (2017).
128. M. Gara and R. G. Compton, *New Journal of Chemistry,* **35** (11), 2647-2652 (2011).
129. W. Ding, Z. Wei, S. Chen, X. Qi, T. Yang, J. Hu, D. Wang, L.-J. Wan, S. F. Alvi, and L. Li, *Angewandte Chemie-International Edition,* **125** (45), 11971-11975 (2013).
130. L. Lai, J. R. Potts, D. Zhan, L. Wang, C. K. Poh, C. Tang, H. Gong, Z. Shen, J. Lin, and R. S. Ruoff, *Energy & Environmental Science,* **5** (7), 7936-7942 (2012).
131. Y. Zheng, Y. Jiao, M. Jaroniec, Y. Jin, and S. Z. Qiao, *Small,* **8** (23), 3550-3566 (2012).
132. J. Yin, Y. X. Li, F. Lv, Q. H. Fan, Y. Q. Zhao, Q. L. Zhang, W. Wang, F. Y. Cheng, P. X. Xi, and S. J. Guo, *ACS Nano,* **11** (2), 2275-2283 (2017).
133. P. C. Li, C. C. Hu, T. H. You, and P. Y. Chen, *Carbon,* **111** 813-821 (2017).
134. X. Y. Wu, X. P. Han, X. Y. Ma, W. Zhang, Y. D. Deng, C. Zhong, and W. B. Hu, *ACS Applied Materials & Interfaces,* **9** (14), 12574-12583 (2017).
135. Y. Wang, J. Fu, Y. N. Zhang, M. Li, F. M. Hassan, G. Li, and Z. W. Chen, *Nanoscale,* **9** (41), 15865-15872 (2017).
136. S. H. Ahn and A. Manthiram, *Small,* **13** (40), (2017).
137. Y. C. Fan, S. Ida, A. Staykov, T. Akbay, H. Hagiwara, J. Matsuda, K. Kaneko, and T. Ishihara, *Small,* **13** (25), (2017).
138. M. Prabu, P. Ramakrishnan, and S. Shanmugam, *Electrochemistry Communications,* **41** 59-63 (2014).
139. X. M. Ge, Y. Y. Liu, F. W. T. Goh, T. S. A. Hor, Y. Zong, P. Xiao, Z. Zhang, S. H. Lim, B. Li, X. Wang, and Z. L. Liu, *ACS Applied Materials & Interfaces,* **6** (15), 12684-12691 (2014).
140. Y. F. Bu, O. Gwon, G. Nam, H. Jang, S. Kim, Q. Zhong, J. Cho, and G. Kim, *ACS Nano,* **11** (11), 11594-11601 (2017).

141. M. F. Wang, T. Qian, J. Q. Zhou, and C. L. Yan, *ACS Applied Materials & Interfaces,* **9** (6), 5213-5221 (2017).
142. D. U. Lee, J.-Y. Choi, K. Feng, H. W. Park, and Z. Chen, *Advanced Energy Materials,* **4** (6), (2014).
143. P. Milan and S. Mordechay, *Fundamentals of Electrochemical Deposition, 2nd edition*, Wiley, New Jersey (2006).
144. Y. D. Gamburg and G. Zangari, *Theory and Practice of Metal Electrodeposition*, p. 1-378 (2011).
145. B. R. Scharifker and J. Mostany, *Journal of Electroanalytical Chemistry and Interfacial Electrochemistry,* **177** (1-2), 13-23 (1984).
146. K. Popov, B. Grgur, and S. S. Djokić, *Fundamental aspects of electrometallurgy*, Springer (2007).
147. F. Lallemand, L. Ricq, E. Deschaseaux, L. De Vettor, and P. Berçot, *Surface and Coatings Technology,* **197** (1), 10-17 (2005).
148. L. Ricq, F. Lallemand, M. P. Gigandet, and J. Pagetti, *Surface and Coatings Technology,* **138** (2-3), 278-283 (2001).
149. C. Meudre, L. Ricq, J.-Y. Hihn, V. Moutarlier, A. Monnin, and O. Heintz, *Surface and Coatings Technology,* **252** 93-101 (2014).
150. E. J. Podlaha, C. Bonhôte, and D. Landolt, *Electrochimica Acta,* **39** (18), 2649-2657 (1994).
151. Y. Zhang and D. G. Ivey, *Chemistry of Materials,* **16** (7), 1189-1194 (2004).
152. I. G. Casella and M. Gatta, *Journal of Electroanalytical Chemistry,* **534** (1), 31-38 (2002).
153. M. S. Oncel, A. Muhcu, E. Demirbas, and M. Kobya, *Journal of Environmental Chemical Engineering,* **1** (4), 989-995 (2013).
154. Y. Tsuru, M. Nomura, and F. R. Foulkes, *Journal of Applied Electrochemistry,* **32** (6), 629-634 (2002).
155. N. Zech and D. Landolt, *Electrochimica Acta,* **45** (21), 3461-3471 (2000).
156. H.-C. Shin and M. Liu, *Chemistry of Materials,* **16** (25), 5460-5464 (2004).
157. S. Cherevko, X. Xing, and C.-H. Chung, *Electrochemistry Communications,* **12** (3), 467-470 (2010).
158. S. G. Bratsch, *Journal of Physical and Chemical Reference Data,* **18** (1), 1-21 (1989).
159. A. Brenner, in *Electrodeposition of Alloys*, p. 331-387, Academic Press, (1963).

160. S. D. Sartale and C. D. Lokhande, *Ceramics International,* **28** (5), 467-477 (2002).
161. J. Lu, D. Dreisinger, and T. Glück, *Hydrometallurgy,* **141** 105-116 (2014).
162. S. K. Padhy, P. Patnaik, B. C. Tripathy, and I. N. Bhattacharya, *Materials Science and Engineering B-Advanced Functional Solid-State Materials,* **193** 83-90 (2015).
163. P.-Y. Chen and C. L. Hussey, *Electrochimica Acta,* **52** (5), 1857-1864 (2007).
164. S. Fashu, C. D. Gu, J. L. Zhang, H. Zheng, X. L. Wang, and J. P. Tu, *Journal of Materials Engineering and Performance,* **24** (1), 434-444 (2015).
165. T. Nguyen, M. João Carmezim, M. Boudard, and M. Fátima Montemor, *International Journal of Hydrogen Energy,* **40** (46), 16355-16364 (2015).
166. C.-W. Kung, H.-W. Chen, C.-Y. Lin, R. Vittal, and K.-C. Ho, *Journal of Power Sources,* **214** 91-99 (2012).
167. A. D. Jagadale, V. S. Kumbhar, R. N. Bulakhe, and C. D. Lokhande, *Energy,* **64** 234-241 (2014).
168. Y. Zhang, Z. Hu, Y. An, B. Guo, N. An, Y. Liang, and H. Wu, *Journal of Power Sources,* **311** 121-129 (2016).
169. M. P. Owen, G. A. Lawrance, and S. W. Donne, *Electrochimica Acta,* **52** (14), 4630-4639 (2007).
170. M. F. Dupont and S. W. Donne, *Electrochimica Acta,* **120** 219-225 (2014).
171. C. J. Clarke, G. J. Browning, and S. W. Donne, *Electrochimica Acta,* **51** (26), 5773-5784 (2006).
172. W. Yan, T. Ayvazian, J. Kim, Y. Liu, K. C. Donavan, W. Xing, Y. Yang, J. C. Hemminger, and R. M. Penner, *ACS Nano,* **5** (10), 8275-8287 (2011).
173. A. Biswal, M. Minakshi, and B. C. Tripathy, *Dalton Transactions,* **45** (13), 5557-5567 (2016).
174. M. S. El-Deab and T. Ohsaka, *Journal of The Electrochemical Society,* **155** (1), (2008).
175. A. Ramírez, P. Hillebrand, D. Stellmach, M. M. May, P. Bogdanoff, and S. Fiechter, *The Journal of Physical Chemistry C,* **118** (26), 14073-14081 (2014).
176. G. Sabouraud, S. Sadki, and N. Brodie, *Chemical Society Reviews,* **29** (5), 283-293 (2000).
177. P. Bocchetta, A. Gianoncelli, M. K. Abyaneh, M. Kiskinova, M. Amati, L. Gregoratti, D. Jezeršek, C. Mele, and B. Bozzini, *Electrochimica Acta,* **137** 535-545 (2014).

178. B. Bozzini, P. Bocchetta, B. Aleman, M. Amati, A. Gianoncelli, L. Gregoratti, H. Sezen, A. Taurino, and M. Kiskinova, *Journal of Materials Chemistry A,* **3** (37), 19155-19167 (2015).
179. R. Baddour-Hadjean and J. P. Pereira-Ramos, *Chemical Reviews,* **110** (3), 1278-1319 (2010).
180. I. Katsounaros, W. B. Schneider, J. C. Meier, U. Benedikt, P. U. Biedermann, A. A. Auer, and K. J. Mayrhofer, *Phys Chem Chem Phys,* **14** (20), 7384-7391 (2012).
181. B. B. Blizanac, P. N. Ross, and N. M. Markovic, *Electrochimica Acta,* **52** (6), 2264-2271 (2007).
182. U. A. Paulus, T. J. Schmidt, H. A. Gasteiger, and R. J. Behm, *Journal of Electroanalytical Chemistry,* **495** (2), 134-145 (2001).
183. M. Chatenet, L. Genies-Bultel, M. Aurousseau, R. Durand, and F. Andolfatto, *Journal of Applied Electrochemistry,* **32** (10), 1131-1140 (2002).
184. H. Wu, H. Li, X. Zhao, Q. Liu, J. Wang, J. Xiao, S. Xie, R. Si, F. Yang, S. Miao, X. Guo, G. Wang, and X. Bao, *Energy & Environmental Science,* (2016).
185. F. Meng, H. Zhong, D. Bao, J. Yan, and X. Zhang, *Journal of the American Chemical Society,* **138** (32), 10226-10231 (2016).
186. D. U. Lee, M. G. Park, H. W. Park, M. H. Seo, V. Ismayilov, R. Ahmed, and Z. W. Chen, *Electrochemistry Communications,* **60** 38-41 (2015).
187. P.-C. Li, Y.-J. Chien, and C.-C. Hu, *Journal of Power Sources,* **313** 37-45 (2016).
188. B. Li, S.-W. Chien, X. Ge, J. Chai, X.-Y. Goh, K.-T. Nai, T. S. Andy Hor, Z. Liu, and Y. Zong, *Materials Chemistry Frontiers,* (2017).
189. T. Y. Ma, J. L. Cao, M. Jaroniec, and S. Z. Qiao, *Angewandte Chemie-International Edition,* **55** (3), 1138-1142 (2016).
190. S. Luo and D. B. Zhou, *Journal of The Electrochemical Society,* **161** (1), A23-A27 (2013).
191. J. Ahmed, B. Kumar, A. M. Mugweru, P. Trinh, K. V. Ramanujachary, S. E. Lofland, and A. K. Ganguli, *The Journal of Physical Chemistry C,* **114** (44), 18779-18784 (2010).
192. W. Bian, Z. Yang, P. Strasser, and R. Yang, *Journal of Power Sources,* **250** 196-203 (2014).
193. M. S. Burke, M. G. Kast, L. Trotochaud, A. M. Smith, and S. W. Boettcher, *Journal of the American Chemical Society,* **137** (10), 3638-3648 (2015).
194. C.-C. Hu and Y.-R. Wu, *Materials Chemistry and Physics,* **82** (3), 588-596 (2003).

195. M. B. Stevens, L. J. Enman, A. S. Batchellor, M. R. Cosby, A. E. Vise, C. D. M. Trang, and S. W. Boettcher, *Chemistry of Materials,* (2016).
196. M. E. G. Lyons and M. P. Brandon, *International Journal of Electrochemical Science,* **3** (12), 1386-1424 (2008).
197. M. x. Li, J. l. Ou, Y. x. Chen, S. p. Chen, P. Wang, B. b. Xu, and S. g. Sun, *Journal of Electrochemistry,* **2** 007 (2013).
198. X.-W. Wei, G.-X. Zhu, Y.-J. Liu, Y.-H. Ni, Y. Song, and Z. Xu, *Chemistry of Materials,* **20** (19), 6248-6253 (2008).
199. M. D. Merrill and R. C. Dougherty, *The Journal of Physical Chemistry C,* **112** (10), 3655-3666 (2008).
200. B. H. R. Suryanto, X. Y. Lu, H. M. Chan, and C. Zhao, *Rsc Advances,* **3** (43), 20936-20942 (2013).
201. S. R. Brankovic, N. Vasiljevic, T. J. Klemmer, and E. C. Johns, *Journal of The Electrochemical Society,* **152** (4), C196 (2005).
202. M. E. G. Lyons and M. P. Brandon, *International Journal of Electrochemical Science,* **3** (12), 1463-1503 (2008).
203. J. X. Feng, H. Xu, Y. T. Dong, S. H. Ye, Y. X. Tong, and G. R. Li, *Angewandte Chemie-International Edition,* **55** (11), 3694-3698 (2016).
204. F. Song and X. Hu, *Nat Commun,* **5** 4477 (2014).
205. L. Trotochaud, J. K. Ranney, K. N. Williams, and S. W. Boettcher, *Journal of the American Chemical Society,* **134** (41), 17253-17261 (2012).
206. C. G. Morales-Guio, L. Liardet, and X. L. Hu, *Journal of the American Chemical Society,* **138** (28), 8946-8957 (2016).
207. R. L. Doyle and M. E. G. Lyons, *Journal of The Electrochemical Society,* **160** (2), H142-H154 (2013).
208. S. Gottesfeld and S. Srinivasan, *Journal of Electroanalytical Chemistry and Interfacial Electrochemistry,* **86** (1), 89-104 (1978).
209. L. Han, S. Dong, and E. Wang, *Adv Mater,* (2016).
210. O. Gwon, C. Kim, O. Kwon, H. Y. Jeong, H.-K. Park, J. Shin, Y.-W. Ju, and G. Kim, *Journal of The Electrochemical Society,* **163** (9), A1893-A1897 (2016).

211. L. C. Seitz, D. Nordlund, A. Gallo, and T. F. Jaramillo, *Electrochimica Acta,* **193** 240-245 (2016).
212. A. Grimaud, O. Diaz-Morales, B. H. Han, W. T. Hong, Y. L. Lee, L. Giordano, K. A. Stoerzinger, M. T. M. Koper, and Y. Shao-Horn, *Nature Chemistry,* **9** (5), 457-465 (2017).
213. J. Fu, Z. P. Cano, M. G. Park, A. Yu, M. Fowler, and Z. Chen, *Advanced Materials,* **29** (7), 1604685 (2017).
214. Y. Jia, L. Z. Zhang, G. P. Gao, H. Chen, B. Wang, J. Z. Zhou, M. T. Soo, M. Hong, X. C. Yan, G. R. Qian, J. Zou, A. J. Du, and X. D. Yao, *Advanced Materials,* **29** (17), 1700017 (2017).
215. M. Gorlin, P. Chernev, J. F. de Araujo, T. Reier, S. Dresp, B. Paul, R. Krahnert, H. Dau, and P. Strasser, *Journal of the American Chemical Society,* **138** (17), 5603-5614 (2016).
216. Y. Q. Zhang, B. Ouyang, J. Xu, G. C. Jia, S. Chen, R. S. Rawat, and H. J. Fan, *Angewandte Chemie-International Edition,* **55** (30), 8670-8674 (2016).
217. S. Cai, Z. Meng, H. Tang, Y. Wang, and P. Tsiakaras, *Applied Catalysis B: Environmental,* **217** 477-484 (2017).
218. Q. Chen, R. Wang, M. Yu, Y. Zeng, F. Lu, X. Kuang, and X. Lu, *Electrochimica Acta,* **247** 666-673 (2017).
219. X. Zhang, X. Zhang, H. Xu, Z. Wu, H. Wang, and Y. Liang, *Advanced Functional Materials,* **27** (24), 1606635 (2017).
220. Y. L. Zhu, W. Zhou, Y. B. Chen, J. Yu, M. L. Liu, and Z. P. Shao, *Advanced Materials,* **27** (44), 7150-7155 (2015).
221. X. F. Lu, L. F. Gu, J. W. Wang, J. X. Wu, P. Q. Liao, and G. R. Li, *Advanced Materials,* **29** (3), 1604437 (2016).
222. Y. Wang, Y. Zhang, Z. Liu, C. Xie, S. Feng, D. Liu, M. Shao, and S. Wang, *Angewandte Chemie-International Edition,* **56** (21), 5867–5871 (2017).
223. B. Zhang, X. L. Zheng, O. Voznyy, R. Comin, M. Bajdich, M. Garcia-Melchor, L. L. Han, J. X. Xu, M. Liu, L. R. Zheng, F. P. G. de Arquer, C. T. Dinh, F. J. Fan, M. J. Yuan, E. Yassitepe, N. Chen, T. Regier, P. F. Liu, Y. H. Li, P. De Luna, A. Janmohamed, H. L. L. Xin, H. G. Yang, A. Vojvodic, and E. H. Sargent, *Science,* **352** (6283), 333-337 (2016).
224. P. W. Cai, S. Q. Ci, E. H. Zhang, P. Shao, C. S. Cao, and Z. H. Wen, *Electrochimica Acta,* **220** 354-362 (2016).

225. C.-Y. Su, H. Cheng, W. Li, Z.-Q. Liu, N. Li, Z. Hou, F.-Q. Bai, H.-X. Zhang, and T.-Y. Ma, *Advanced Energy Materials,* **7** (13), 1602420 (2017).
226. X. Zhao, X. Shang, Y. Quan, B. Dong, G. Q. Han, X. Li, Y. R. Liu, Q. Chen, Y. M. Chai, and C. G. Liu, *Electrochimica Acta,* **230** 151-159 (2017).
227. J. Ahmed, B. Kumar, A. M. Mugweru, P. Trinh, K. V. Ramanujachary, S. E. Lofland, and A. K. Ganguli, *The Journal of Physical Chemistry C,* **114** (44), 18779-18784 (2010).
228. M. Xiong and D. G. Ivey, *Electrochemistry Communications,* **75** 73-77 (2017).
229. S. Ardizzone, G. Fregonara, and S. Trasatti, *Electrochimica Acta,* **35** (1), 263-267 (1990).
230. H. Okamoto. ASM International, Materials Park, OH, 2000.
231. F. Yang, K. Sliozberg, I. Sinev, H. Antoni, A. Bahr, K. Ollegott, W. Xia, J. Masa, W. Grunert, B. R. Cuenya, W. Schuhmann, and M. Muhler, *Chemsuschem,* **10** (1), 156-165 (2017).
232. R. Guidelli, R. G. Compton, J. M. Feliu, E. Gileadi, J. Lipkowski, W. Schmickler, and S. Trasatti, *Pure and Applied Chemistry,* **86** (2), 245-258 (2014).
233. S. Giménez and J. Bisquert, *Photoelectrochemical Solar Fuel Production*, Springer, Switzerland (2016).
234. J. A. Koza, Z. He, A. S. Miller, and J. A. Switzer, *Chemistry of Materials,* **24** (18), 3567-3573 (2012).
235. Y. Li, P. Hasin, and Y. Wu, *Advanced Materials,* **22** (17), 1926-1929 (2010).
236. B. Lu, D. Cao, P. Wang, G. Wang, and Y. Gao, *International Journal of Hydrogen Energy,* **36** (1), 72-78 (2011).
237. D. A. Corrigan, *Journal of The Electrochemical Society,* **134** (2), 377 (1987).
238. A. J. Bard and L. R. Faulkner. Wiley, New York, 2001.
239. L. M. Da Silva, L. A. De Faria, and J. F. C. Boodts, *Electrochimica Acta,* **47** (3), 395-403 (2001).
240. J. J. Teles, E. R. Faria, D. V. Franco, and L. M. Da Silva, *Int. J. Electrochem. Sci,* **12** 1755-1773 (2017).
241. W. K. Behl and J. E. Toni, *Journal of Electroanalytical Chemistry and Interfacial Electrochemistry,* **31** (1), 63-75 (1971).
242. Y.-H. Lee, K.-H. Chang, and C.-C. Hu, *Journal of Power Sources,* **227** 300-308 (2013).

243. T. Lassali, J. Boodts, and L. Bulhoes, *Journal of applied electrochemistry,* **30** (5), 625-634 (2000).
244. L. Da Silva, L. De Faria, and J. Boodts, *Journal of Electroanalytical Chemistry,* **532** (1), 141-150 (2002).
245. N. Laegreid and G. K. Wehner, *Journal of Applied Physics,* **32** (3), 365-369 (1961).
246. S. R. Brankovic, S.-E. Bae, and D. Litvinov, *Electrochimica Acta,* **53** (20), 5934-5940 (2008).
247. M. Xiong and D. G. Ivey, *Journal of The Electrochemical Society,* **164** (6), A1012-A1021 (2017).
248. H. G. Meier, J. R. Vilche, and A. J. Arvía, *Journal of Electroanalytical Chemistry and Interfacial Electrochemistry,* **138** (2), 367-379 (1982).
249. M. E. G. Lyons, R. L. Doyle, and M. P. Brandon, *Physical Chemistry Chemical Physics,* **13** (48), 21530-21551 (2011).
250. J. Zhang, Z. Zhao, Z. Xia, and L. Dai, *Nature Nanotechnology,* **10** (5), 444-452 (2015).
251. S. Suren and S. Kheawhom, *Journal of The Electrochemical Society,* **163** (6), A846-A850 (2016).
252. Y.-J. Wang, N. Zhao, B. Fang, H. Li, X. T. Bi, and H. Wang, *Chemical Reviews,* **115** (9), 3433-3467 (2015).
253. L. Han, S. Dong, and E. Wang, *Advanced Materials,* **28** (42), 9266-9291 (2016).
254. A. R. Mainar, L. C. Colmenares, O. Leonet, F. Alcaide, J. J. Iruin, S. Weinberger, V. Hacker, E. Iruin, I. Urdanpilleta, and J. A. Blazquez, *Electrochimica Acta,* **217** 80-91 (2016).
255. A. Sumboja, X. M. Ge, F. W. T. Goh, B. Li, D. S. Geng, T. S. A. Hor, Y. Zong, and Z. L. Liu, *Chempluschem,* **80** (8), 1341-1346 (2015).
256. P. C. Li, C. C. Hu, H. Noda, and H. Habazaki, *Journal of Power Sources,* **298** 102-113 (2015).
257. S. Lee, G. Nam, J. Sun, J. S. Lee, H. W. Lee, W. Chen, J. Cho, and Y. Cui, *Angewandte Chemie-International Edition,* **55** (30), 8599-8604 (2016).
258. T. Reddy, *Handbook of batteries*, McGraw-Hill Pub. (2011).
259. K. B. Liew, W. R. W. Daud, M. Ghasemi, K. S. Loh, M. Ismail, S. S. Lim, and J. X. Leong, *International Journal of Hydrogen Energy,* **40** (35), 11625-11632 (2015).

260. K. H. Wu, Q. C. Zeng, B. S. Zhang, X. Leng, D. S. Su, I. R. Gentle, and D. W. Wang, *Chemsuschem,* **8** (19), 3331-3339 (2015).
261. D. Guo, S. Dou, X. Li, J. T. Xu, S. Y. Wang, L. Lai, H. K. Liu, J. M. Ma, and S. X. Dou, *International Journal of Hydrogen Energy,* **41** (10), 5260-5268 (2016).
262. L. Jörissen, *Journal of Power Sources,* **155** (1), 23-32 (2006).
263. P.-C. Li, C.-C. Hu, T.-H. You, and P.-Y. Chen, *Carbon,* (2016).
264. X. Liu, M. Park, M. G. Kim, S. Gupta, X. Wang, G. Wu, and J. Cho, *Nano Energy,* **20** 315-325 (2016).
265. B. Messaoudi, S. Joiret, M. Keddam, and H. Takenouti, *Electrochimica Acta,* **46** (16), 2487-2498 (2001).
266. E. M. Garcia, J. S. Santos, E. C. Pereira, and M. B. J. G. Freitas, *Journal of Power Sources,* **185** (1), 549-553 (2008).
267. B. Beverskog and I. Puigdomenech, *Corrosion Science,* **38** (12), 2121-2135 (1996).
268. F. Cheng, J. Shen, B. Peng, Y. Pan, Z. Tao, and J. Chen, *Nature Chemistry,* **3** (1), 79-84 (2011).
269. J. H. Albering, *Handbook of Battery Materials, Second Edition,* 92 (2011).
270. A. D. Cross, A. Morel, T. F. Hollenkamp, and S. W. Donne, *Journal of The Electrochemical Society,* **158** (10), A1160 (2011).
271. T. L. Wee, B. D. Sherman, D. Gust, A. L. Moore, T. A. Moore, Y. Liu, and J. C. Scaiano, *Journal of the American Chemical Society,* **133** (42), 16742-16745 (2011).
272. K. Nakaoka, M. Nakayama, and K. Ogura, *Journal of The Electrochemical Society,* **149** (3), C159-C163 (2002).
273. J. A. Koza, Z. He, A. S. Miller, and J. A. Switzer, *Chemistry of Materials,* **24** (18), 3567-3573 (2012).
274. S. D. Sartale, C. D. Lokhande, M. Giersig, and V. Ganesan, *Journal of Physics-Condensed Matter,* **16** (6), 773-784 (2004).
275. Z. H. Bi, J. H. Zhu, and J. L. Batey, *Journal of Power Sources,* **195** (11), 3605-3611 (2010).
276. X. H. Xia, J. P. Tu, J. Zhang, J. Y. Xiang, X. L. Wang, and X. B. Zhao, *ACS Applied Materials & Interfaces,* **2** (1), 186-192 (2010).
277. B. D. Kernan, E. M. Sachs, M. A. Oliveira, and M. J. Cima, *International Journal of Refractory Metals and Hard Materials,* **25** (1), 82-94 (2007).

278. N. A. Godshall, *Journal of The Electrochemical Society,* **131** (3), 543 (1984).
279. W. Wei, X. Cui, W. Chen, and D. G. Ivey, *The Journal of Physical Chemistry C,* **112** (38), 15075-15083 (2008).
280. H. W. Nesbitt and D. Banerjee, *American Mineralogist,* **83** (3-4), 305-315 (1998).
281. E. S. Ilton, J. E. Post, P. J. Heaney, F. T. Ling, and S. N. Kerisit, *Applied Surface Science,* **366** 475-485 (2016).
282. M. C. Biesinger, B. P. Payne, A. P. Grosvenor, L. W. M. Lau, A. R. Gerson, and R. S. C. Smart, *Applied Surface Science,* **257** (7), 2717-2730 (2011).
283. J. S. Lee, G. S. Park, H. I. Lee, S. T. Kim, R. Cao, M. Liu, and J. Cho, *Nano Letters,* **11** (12), 5362-5366 (2011).
284. Q. Wu, L. Jiang, Q. Tang, J. Liu, S. Wang, and G. Sun, *Electrochimica Acta,* **91** 314-322 (2013).
285. Q. Wu, L. Jiang, L. Qi, E. Wang, and G. Sun, *International Journal of Hydrogen Energy,* **39** (7), 3423-3432 (2014).
286. W. Wei, X. Cui, W. Chen, and D. G. Ivey, *Chemical Society Rviews,* **40** (3), 1697-1721 (2011).
287. Y. T. Meng, W. Q. Song, H. Huang, Z. Ren, S. Y. Chen, and S. L. Suib, *Journal of the American Chemical Society,* **136** (32), 11452-11464 (2014).
288. X. Yu and S. Ye, *Journal of Power Sources,* **172** (1), 145-154 (2007).
289. Z. Chen, A. Yu, D. Higgins, H. Li, H. Wang, and Z. Chen, *Nano Letters,* **12** (4), 1946-1952 (2012).
290. X. Z. Yuan, W. Qu, X. Zhang, P. Yao, and J. Fahlman, *Ecs Transactions,* **45** (29), 105-112 (2013).
291. Y. Gorlin, B. Lassalle-Kaiser, J. D. Benck, S. Gul, S. M. Webb, V. K. Yachandra, J. Yano, and T. F. Jaramillo, *Journal of the American Chemical Society,* **135** (23), 8525-8534 (2013).
292. E. Davari and D. G. Ivey, *Sustainable Energy & Fuels,* **2** (1), 39-67 (2018).
293. D. Schröder and U. Krewer, *Electrochimica Acta,* **117** 541-553 (2014).
294. B. Pichler, S. Weinberger, L. Reščec, I. Grimmer, F. Gebetsroither, B. Bitschnau, and V. Hacker, *Electrochimica Acta,* **251** 488-497 (2017).
295. Q. Wang, Y. Xue, S. Sun, S. Li, H. Miao, and Z. Liu, *Electrochimica Acta,* **254** 14-24 (2017).

296. Q. Tang, L. Wang, M. Wu, N. Xu, L. Jiang, and J. Qiao, *Journal of Power Sources,* **365** 348-353 (2017).
297. R. Li, D. Zhou, J. Luo, W. Xu, J. Li, S. Li, P. Cheng, and D. Yuan, *Journal of Power Sources,* **341** 250-256 (2017).
298. Y.-Q. Zhang, H.-B. Tao, J. Liu, Y.-F. Sun, J. Chen, B. Hua, T. Thundat, and J.-L. Luo, *Nano Energy,* **38** 392-400 (2017).
299. M. Gorlin, J. Ferreira de Araujo, H. Schmies, D. Bernsmeier, S. Dresp, M. Gliech, Z. Jusys, P. Chernev, R. Kraehnert, H. Dau, and P. Strasser, *Journal of the American Chemical Society,* **139** (5), 2070-2082 (2017).
300. L. Li and A. Manthiram, *Nano Energy,* **9** 94-100 (2014).
301. N. Takeno, *Geological survey of Japan open file report,* **419** 102 (2005).
302. L. J. Enman, M. S. Burke, A. S. Batchellor, and S. W. Boettcher, *ACS Catalysis,* **6** (4), 2416-2423 (2016).
303. L. Han, C. Dong, C. Zhang, Y. Gao, J. Zhang, H. Gao, Y. Wang, and Z. Zhang, *Nanoscale,* **9** (42), 16467-16475 (2017).
304. Y. Li and J. Lu, *ACS Energy Letters,* **2** (6), 1370-1377 (2017).
305. J. Zhang, Z. Zhao, Z. Xia, and L. Dai, *Nature Nanotechnology,* **10** (5), 444-452 (2015).
306. G.-P. Kim, H.-H. Sun, and A. Manthiram, *Nano Energy,* **30** 130-137 (2016).
307. Z. Yan, E. Wang, J. Gao, J. Yang, C. Wu, L. Jiang, M. Zhu, and G. Sun, *ChemElectroChem,* **4** (9), 2190-2195 (2017).
308. S. H. Ahn, X. Yu, and A. Manthiram, *Advanced Materials,* **29** (26), (2017).
309. B. Amunátegui, A. Ibáñez, M. Sierra, and M. Pérez, *Journal of Applied Electrochemistry,* pp 1–11 (2017).
310. S. Amendola, M. Binder, P. J. Black, S. Sharp-Goldman, L. Johnson, M. Kunz, M. Oster, T. Chciuk, and R. Johnson. US20130115531 A1, 2012.
311. P. Pei, K. Wang, and Z. Ma, *Applied Energy,* **128** 315-324 (2014).
312. W. Hong, *International Journal of Electrochemical Science,* 3843-3851 (2016).
313. K. Wang, P. Pei, Z. Ma, H. Chen, H. Xu, D. Chen, and H. Xing, *Journal of Power Sources,* **296** 40-45 (2015).
314. D. Desai, X. Wei, D. A. Steingart, and S. Banerjee, *Journal of Power Sources,* **256** 145-152 (2014).

315. Y. Ito, X. Wei, D. Desai, D. Steingart, and S. Banerjee, *Journal of Power Sources,* **211** 119-128 (2012).
316. D. E. Turney, J. W. Gallaway, G. G. Yadav, R. Ramirez, M. Nyce, S. Banerjee, Y.-c. K. Chen-Wiegart, J. Wang, M. J. D'Ambrose, S. Kolhekar, J. Huang, and X. Wei, *Chemistry of Materials,* **29** (11), 4819-4832 (2017).
317. Y. Gorlin, C.-J. Chung, D. Nordlund, B. M. Clemens, and T. F. Jaramillo, *ACS Catalysis,* **2** (12), 2687-2694 (2012).
318. H. Y. Su, Y. Gorlin, I. C. Man, F. Calle-Vallejo, J. K. Norskov, T. F. Jaramillo, and J. Rossmeisl, *Physical Chemistry Chemical Physics,* **14** (40), 14010-14022 (2012).
319. J. Liu, L. H. Jiang, T. R. Zhang, J. T. Jin, L. Z. Yuan, and G. Q. Sun, *Electrochimica Acta,* **205** 38-44 (2016).
320. T. Li, B. Xue, B. Wang, G. Guo, D. Han, Y. Yan, and A. Dong, *Journal of the American Chemical Society,* **139** (35), 12133-12136 (2017).
321. P. R. Jothi, M. Pramanik, C. L. Li, S. Kannan, V. Malgras, R. R. Salunkhe, and Y. Yamauchi, *Chemistry-an Asian Journal,* **11** (5), 667-673 (2016).
322. M. S. Burke, M. G. Kast, L. Trotochaud, A. M. Smith, and S. W. Boettcher, *Journal of the American Chemical Society,* **137** (10), 3638-3648 (2015).
323. V. P. Santos, M. F. R. Pereira, J. J. M. Órfão, and J. L. Figueiredo, *Applied Catalysis B: Environmental,* **99** (1-2), 353-363 (2010).
324. V. R. Galakhov, M. Demeter, S. Bartkowski, M. Neumann, N. A. Ovechkina, E. Z. Kurmaev, N. I. Lobachevskaya, Y. M. Mukovskii, J. Mitchell, and D. L. Ederer, *Physical Review B,* **65** (11), (2002).
325. C.-C. Hu and C.-C. Wang, *Journal of The Electrochemical Society,* **150** (8), A1079 (2003).
326. A. Ramírez, P. Hillebrand, D. Stellmach, M. M. May, P. Bogdanoff, and S. Fiechter, *The Journal of Physical Chemistry C,* **118** (26), 14073-14081 (2014).
327. J. O. Besenhard, *Handbook of battery materials*, John Wiley & Sons (2008).
328. T. E. Moore, M. Ellis, and P. W. Selwood, *Journal of the American Chemical Society,* **72** (2), 856-866 (1950).
329. S. Kim, B. Choi, G. Lee, S. Oh, B. Kim, H. Choi, J. Park, and Y. Chang, *Journal of the Korean Physical Society,* **46** (4), 941-944 (2005).
330. J. B. Goodenough and A. L. Loeb, *Physical Review,* **98** (2), 391 (1955).

331. C. M. Julien, M. Massot, and C. Poinsignon, *Spectrochimica Acta Part A: Molecular and Biomolecular Spectroscopy,* **60** (3), 689-700 (2004).
332. J. H. Jiang and A. Kucernak, *Electrochimica Acta,* **47** (15), 2381-2386 (2002).
333. M. C. Bernard, A. H. L. Goff, B. V. Thi, and S. C. Detorresi, *Journal of the Electrochemical Society,* **140** (11), 3065-3070 (1993).
334. Y. Meng, W. Song, H. Huang, Z. Ren, S. Y. Chen, and S. L. Suib, *Journal of the American Chemical Society* **136** (32), 11452-11464 (2014).
335. J. Wu, J. Subramaniam, Y. Liu, D. Geng, and X. Meng, *Journal of Alloys and Compounds,* **731** 766-773 (2018).
336. A. Holewinski, J. C. Idrobo, and S. Linic, *Nature Chemistry,* **6** (9), 828-834 (2014).
337. S. Chen, J. Duan, M. Jaroniec, and S. Z. Qiao, *Advanced Materials,* **26** (18), 2925-2930 (2014).
338. C. Spori, J. T. H. Kwan, A. Bonakdarpour, D. P. Wilkinson, and P. Strasser, *Angewandte Chemie International Edition,* **56** (22), 5994-6021 (2017).
339. Z. Chen, A. Yu, D. Higgins, H. Li, H. Wang, and Z. Chen, *Nano Lett,* **12** (4), 1946-1952 (2012).
340. J. I. Jung, M. Risch, S. Park, M. G. Kim, G. Nam, H. Y. Jeong, Y. Shao-Horn, and J. Cho, *Energy & Environmental Science,* **9** (1), 176-183 (2016).
341. J. Park, M. Park, G. Nam, M. G. Kim, and J. Cho, *Nano Lettters,* **17** (6), 3974-3981 (2017).
342. Z. Pei, H. Li, Y. Huang, Q. Xue, Y. Huang, M. Zhu, Z. Wang, and C. Zhi, *Energy & Environmental Science,* **10** (3), 742-749 (2017).
343. B. Chen, X. He, F. Yin, H. Wang, D.-J. Liu, R. Shi, J. Chen, and H. Yin, *Advanced Functional Materials,* **27** (37), 1700795 (2017).
344. D. Bin, Z. Guo, A. G. Tamirat, Y. Ma, Y. Wang, and Y. Xia, *Nanoscale,* **9** (31), 11148-11157 (2017).
345. J. Wang, H. Wu, D. Gao, S. Miao, G. Wang, and X. Bao, *Nano Energy,* **13** 387-396 (2015).
346. Y. Liu, S. Chen, X. Quan, H. Yu, H. Zhao, Y. Zhang, and G. Chen, *The Journal of Physical Chemistry C,* **117** (29), 14992-14998 (2013).
347. G. Du, X. Liu, Y. Zong, T. S. Hor, A. Yu, and Z. Liu, *Nanoscale,* **5** (11), 4657-4661 (2013).
348. Y. Zhan, C. Xu, M. Lu, Z. Liu, and J. Y. Lee, *Journal of Materials Chemistry A,* **2** (38), 16217-16223 (2014).

349. M. Favaro, J. Yang, S. Nappini, E. Magnano, F. M. Toma, E. J. Crumlin, J. Yano, and I. D. Sharp, *Journal of the American Chemical Society,* **139** (26), 8960-8970 (2017).
350. D. Chen, C. L. Dong, Y. Zou, D. Su, Y. C. Huang, L. Tao, S. Dou, S. Shen, and S. Wang, *Nanoscale,* **9** (33), 11969-11975 (2017).
351. W. Wang, L. Kuai, W. Cao, M. Huttula, S. Ollikkala, T. Ahopelto, A.-P. Honkanen, S. Huotari, M. Yu, and B. Geng, *Angewandte Chemie-International Edition,* **129** (47), 15173-15177 (2017).
352. M. Prabu, P. Ramakrishnan, H. Nara, T. Momma, T. Osaka, and S. Shanmugam, *ACS Applied Materials & Interfaces,* **6** (19), 16545-16555 (2014).
353. X. Ge, A. Sumboja, D. Wuu, T. An, B. Li, F. W. T. Goh, T. S. A. Hor, Y. Zong, and Z. Liu, *ACS Catalysis,* **5** (8), 4643-4667 (2015).
354. J. Qiao, L. Xu, L. Ding, P. Shi, L. Zhang, R. Baker, and J. Zhang, *International Journal of Electrochemical Science,* **8** (1), 1189 (2013).
355. J. M. Bockris, Z. Nagy, and A. Damjanovic, *Journal of The electrochemical society,* **119** (3), 285-295 (1972).
356. Y.-C. Liu, J. A. Koza, and J. A. Switzer, *Electrochimica Acta,* **140** 359-365 (2014).
357. E. Yu, K. Scott, and R. Reeve, *Fuel Cells,* **3** (4), 169-176 (2003).
358. G. Wu, N. Li, D.-R. Zhou, K. Mitsuo, and B.-Q. Xu, *Journal of Solid State Chemistry,* **177** (10), 3682-3692 (2004).